Experimental Investigation of the Thermomechanical Properties and Suitability of Elastomers from Additive Manufacturing

Vivianne Marie Bruère de Carvalho Paiva

Vollständiger Abdruck der von der Fakultät für Luft- und Raumfahrttechnik

der Universität der Bundeswehr München zur Erlangung des akademischen Grades eines

Doktor-Ingenieurs (Dr.-Ing.)

angenommenen Dissertation.

Vorsitzender: Univ.-Prof. Dr.-Ing. Alexander Koch

1. Gutachter: Univ.-Prof. Dr.-Ing. habil. Alexander Lion

2. Gutachter: PD Dr.-Ing. habil. Jens Holtmannspötter

Die Dissertation wurde am 6. Juni 2023 bei der Universität der Bundeswehr München eingereicht und durch die Fakultät für Luft- und Raumfahrttechnik am 26. September 2023 angenommen. Die mündliche Prüfung fand am 11. Oktober 2023 statt.

To my family, who are always with me,
no matter the ocean between us.

Acknowledgements

Last but not least, I thank all those who are dear to my heart outside the work environment. My old and new friends, especially Catharina, Daniele, Lays, Leandro, Maria Clara, Marinna, Thais and Vicky. And finally, my family: my parents, my sister, my brother-in-law, my nephew and my grandmothers (by blood and by heart). I cannot thank you enough for your unconditional support and cheering. You are the foundation of my life and the reason why I persevere in any challenge I dare to face. Amo vocês até a lua... ida e volta!

"We keep moving forward, opening new doors
and doing new things, because we're curious,
and curiosity keeps leading us down new paths."

(Walt Disney)

Kurzfassung

Die vielfältige Verwendung von Elastomeren in Alltagsgegenständen und in der Industrie macht sie zu einem attraktiven Material, das in Kombination mit den zunehmend beliebten Technologien der additiven Fertigung (AM) erforscht werden sollte. Im Vergleich zu steifen Polymeren befindet sich der 3D-Druck von Elastomeren derzeit noch in der Anfangsphase, wozu die Einschränkungen der Maschinen bezüglich der mechanischen Verarbeitung und die begrenzte Auswahl an kompatiblen Materialien beitragen. Die Anwendungsmöglichkeiten von elastischen Teilen, die durch AM hergestellt werden, über Prototypen und Ausstellungsstücke hinaus, ist ebenfalls ein Thema, das berücksichtigt werden muss. In diesem Kontext befasst sich diese Arbeit mit dem 3D-Druck von Elastomeren und gibt einen Einblick in deren Anwendbarkeit für die Herstellung von Betriebskomponenten. Ziel ist es zu verstehen, was heutzutage mit 3D-gedruckten Elastomeren erreicht werden kann. Es wird eine Marktuntersuchung zu verfügbaren AM-Technologien sowie eine Übersicht über kommerzielle gummiähnliche Materialien, die für 3D-Drucker geeignet sind, durchgeführt. Die physikalischen Eigenschaften ausgewählter Materialoptionen aus verschiedenen Klassen werden durch thermomechanische Tests untersucht. Dazu wurden thermoplastische Polyurethane, Silikone und UV-härtbare Polymere kalorischen, quasistatischen und dynamischen mechanischen Versuchen unterzogen. Die Auswertung von Eigenschaften wie Zugfestigkeit, Bruchdehnung und Elastizität zusammen mit der Quantifizierung der Hysterese und des Mullins-Effekts unter zyklischer Belastung und der Spannungsrelaxation unter Zug sowie die Charakterisierung des viskoelastischen Verhaltens ermöglichten die Entwicklung einer Datenbank für gummiartigen Materialien, die mit verschiedenen AM-Technologien verarbeitet wurden. Das mechanische Verhalten der betrachteten Materialien wird vergleichend analysiert und ihre Eignung für funktionelle Anwendungen untersucht. Das breite Spektrum an Eigenschaften, einschließlich Dämpfungsfähigkeit, Rückprallelastizität und Betriebstemperaturen, sowie die möglichen Einsatzbereiche werden anschließend diskutiert.

x

Abstract

The wide use of elastomers in daily objects as well as in the industry makes them an attractive material to be explored in combination with the increasingly popular Additive Manufacturing (AM) technologies. Compared to stiff polymers, 3D printing of elastomers is currently in its early stages, with the mechanical processing limitations of the machines and the restricted range of compatible materials contributing to this scenario. The potential applications of elastic parts produced by AM beyond prototypes and display pieces is also an issue that needs to be considered. In this context, this work addresses the 3D printing of elastomers and provides an insight into their applicability for the production of operational components. The goal is to understand what can be done nowadays with 3D printed elastomers. An examination of the AM technologies available in the market is conducted, along with an overview of commercial rubber-like materials suitable for 3D printers. Physical properties of selected material options from different classes are investigated through thermomechanical testing. To this end, thermoplastic polyurethanes, silicones and UV-curable polymers were submitted to caloric, quasi-static and dynamic mechanical experiments. The evaluation of properties such as tensile strength, elongation a break and elasticity together with the quantification of hysteresis and Mullins effect under cyclic loading and stress relaxation under tension, as well as the characterisation of viscoelastic behaviour, allowed the development of a database of rubber-like materials processed with various AM technologies. The mechanical behaviour of materials investigated is comparatively analysed and their suitability for functional applications is assessed. The broad range of properties, including damping capabilities, resilience and service temperatures, as well as the feasible operating uses are then discussed.

Contents

Nomenclature and Abbreviations

Operators:

Grad: material gradient (with respect to the reference configuration)

grad: spatial gradient (with respect to the current configuration)

det (*): determinant of a second-order tensor

|*|: length of a vector

$\mathbf{k} \cdot \mathbf{z}$: dot (scalar) product of two vectors

$\mathbf{K} \cdot \mathbf{z}$: (single) dot product of a second-order tensor and a vector [multiplication of a matrix and a vector]

$\mathbf{K} \cdot \mathbf{Z}$: (single) dot product of two second-order tensors [multiplication of matrices]

$\mathbf{K} : \mathbf{Z}$: double contraction of two second-order tensors [double dot product]

$(\dot{*})$: material time derivative

Continuum Mechanics Quantities:

$\mathcal{B}$: continuum body

P, P_1, P_2: material points

t: time

Ω_0, Ω: region of a continuum body in the reference and current configurations, respectively

$\mathcal{O}$: origin of coordinate system

$\mathbf{e}_1, \mathbf{e}_2, \mathbf{e}_3$: orthonormal basis vectors

$\mathbf{X}$, $\mathbf{Y}$: position vectors in the reference configuration

$\mathbf{x}$, $\mathbf{y}$: position vectors in the current configuration

$\Delta \mathbf{X}$, $\Delta \mathbf{x}$: difference vector between position vectors in the reference and current configurations, respectively

$\chi(\mathbf{X}, t)$: motion vector field

$\mathcal{U}$, **u**: displacement field in the reference and current configurations, respectively.

F: deformation gradient

d**X**, d**x**: material and spatial line elements, respectively

I: identity tensor

J: Jacobian determinant

dV, dv: infinitesimal volume elements in the reference and current configurations, respectively

d**A**, d**a**: infinitesimal area elements in the reference and current configurations, respectively

C: right Cauchy-Green strain tensor

$\mathbf{C}^{-1}$: Piola deformation tensor

E: Green-Lagrange strain tensor

0: zero tensor or vector

B: left Cauchy-Green strain tensor

A: Euler-Almansi strain tensor

ε: small-train tensor

λ: stretch ratio

U, **V**: right and left stretch tensors, respectively

R: rotation tensor

$\mathcal{V}$, **v**: material and spatial velocity fields, respectively

$\dot{\mathbf{F}}(\mathbf{X}, t)$: material time derivative of the deformation gradient

L: spatial velocity gradient

D: rate of deformation tensor

W: spin tensor

dS, ds: surface element areas in the reference and current configurations, respectively

N, **n**: normal vectors of surface element areas dS and ds, respectively

d**f**: infinitesimal resultant force acting on a surface element area

T: first Piola-Kirchhoff traction vector

t: Cauchy traction vector

P: first Piola-Kirchhoff stress tensor (PK1 stress)

σ: Cauchy stress tensor

S: second Piola-Kirchhoff stress tensor (PK2 stress)

$d\bar{\mathbf{f}}$: corresponding infinitesimal force $d\mathbf{f}$ acting on the reference configuration

$\psi(\mathbf{x}, t)$: physical quantity

$\partial\Omega_0, \partial\Omega$: boundary surface of the region Ω_0 and Ω of a continuum body, respectively

$\phi(\mathbf{x}, t, \mathbf{n})$: flux of physical quantity ψ

$\Sigma(\mathbf{x}, t)$: source term

$\widehat{\psi}(\mathbf{x}, t)$: production term

dm: infinitesimal mass element

ρ_0, ρ: mass density in the reference and current configurations, respectively

$\mathcal{L}(t)$: linear momentum

$\mathcal{F}(t)$: resultant force

$\bar{\mathbf{b}}(\mathbf{X}, t), \mathbf{b}(\mathbf{x}, t)$: body force vector

$\mathcal{A}(t)$: angular momentum

$\boldsymbol{r}(\mathbf{x})$: position vector relative to a fixed point $\mathbf{x}_0$

$\mathcal{M}(t)$: resultant moment

$\boldsymbol{\epsilon}$: third-order permutation tensor

$\mathcal{P}_{\text{ext}}(t)$: rate of external mechanical work

$\mathcal{Q}(t)$: rate of thermal work

$\mathcal{K}(t)$: kinetic energy

$\mathcal{E}(t)$: total internal energy

$e(\mathbf{X}, t), e_c(\mathbf{x}, t)$: internal energy (per unit volume) in the reference and current configurations, respectively

$Q_N(\mathbf{X}, t, \mathbf{N}), q_n(\mathbf{x}, t, \mathbf{n})$: heat flux (heat per unit time and unit area) in the reference and current configurations, respectively

$\mathbf{q}(\mathbf{x}, t)$: Cauchy heat flux

$\mathbf{Q}(\mathbf{X}, t)$: Piola-Kirchhoff heat flux

R, r: heat source (per unit time and unit volume) in the reference and current configurations, respectively

$\mathcal{S}(t)$: total entropy of a continuum body

$s(\mathbf{X}, t), s_c(\mathbf{x}, t)$: entropy (per unit volume) in the reference and current configurations, respectively

$\tilde{\mathcal{Q}}(t)$: rate of entropy input

$\mathbf{H}(\mathbf{X}, t)$: Piola-Kirchhoff entropy flux

$\mathbf{h}(\mathbf{x}, t)$: Cauchy entropy flux

$\tilde{R}, \tilde{r}$: entropy source (per unit time and unit volume) in the reference and current configurations, respectively

$\Gamma(t)$: total production of entropy (per unit time)

$\hat{s}$: spatial production of entropy per unit volume

Θ: absolute temperature

$\mathcal{D}_{int}$: local production of entropy

Ψ: Helmholtz free-energy function

II_i: invariants of the Cauchy-Green deformation tensor

λ_i: principal stresses

Mechanical Behaviour Variables:

σ: stress

E: elastic modulus

ε: strain

η: viscosity

σ_0: maximum stress from the stress relaxation

τ: relaxation time

ε_a, σ_a: amplitude of sinusoidal strain and stress, respectively

f, ω: frequency in Hz and in rad/s, respectively

δ: phase angle

E': storage modulus

E'': loss modulus

ε^*, σ^*: complex strain and stress, respectively

E^*: complex modulus

$\tan \delta$: loss factor

T_R: reference temperature

C_1, C_2: WLF equation constants

T-f: temperature-frequency (sweep)

xx

(c), (h) : "cold" and "hot" temperature sweeps

c_p: isobaric specific heat capacity

ΔH_f: heat of fusion

T: temperature (in °C)

α_1, α_0: slope and y-intercept coefficients of the linear equation

Abbreviations:

AM: additive manufacturing

ABS: acrylonitrile butadiene styrene

AM: Additive Manufacturing

ASTM: American Society for Testing and Materials

BR: polybutadiene

CAD: computer-aided design

CAT: computed axial tomography

CDLM: Continuous Digital Light Manufacturing

cDLP: continuous Digital Light Processing

CLIP: Continuous Liquid Interface Production

CNC: Computer Numerical Control

DLP: Digital Light Processing

DLP: Digital Light Processing

DLS: Digital Light Synthesis

DMA: Dynamic Mechanical Analysis

DOD: Drop-On-Demand

DSC: Differential Scanning Calorimetry

EPDM: ethylene-propylene-diene monomer

EPU: elastomeric polyurethane

FDM: Fused Deposition Modelling

FFF: Fused Filament Fabrication

FPU: flexible polyurethane

IM: Injection Moulding

IR: infrared light

LAM: Liquid Additive Manufacturing

LOM: Laminated Object Manufacturing

LSR: liquid silicone rubber

LVR: Linear Viscoelastic Region

MDI: methylene diphenyl diisocyanate

MJF: Multi Jet Fusion

MJM: Multi Jet Modelling

MJP: MultiJet Printing

MPP: Multiphoton Polymerisation

MRI: magnetic resonance imaging

NBR: acrylonitrile-butadiene rubber

NIR: Near-Infrared

NR: natural rubber

PA: polyamide

PC: polycarbonate

PLA: polylactic acid

SBR: styrene-butadiene rubber

SBS: styrene-butadiene-styrene

SEBS: styrene-ethylene-butylene-styrene

SiR: silicone rubber

SIS: styrene-isoprene-styrene

SLA: Stereolithography

SLS: Selective Laser Sintering

STL: Standard Triangle Language

TDI: toluene diisocyanate

Tg: glass transition temperature

TPA: thermoplastic polyamide

TPC: thermoplastic copolyester

TPE: thermoplastic elastomer

TPO: thermoplastic polyolefin elastomer

TPS: thermoplastic polystyrene elastomer

TPU: thermoplastic polyurethane

TPV: thermoplastic vulcanisate

TTS: time-temperature superposition

UV: ultraviolet

VIS: visible light

WLF: Williams-Landel-Ferry

List of Figures

xxx

List of Tables

1. Introduction

1.1 Preface and Motivation

The first Additive Manufacturing (AM) technologies emerged in the 1980s, with their first application dedicated to the field of *rapid prototyping* (Klahn et al., 2015). Upcraft and Fletcher (2003) mention the American automotive industry as "the primary driver behind the early push to develop processes that could produce physical components quickly and without the need for tooling". The emergence of three-dimensional computer aided design systems helped boost this progress. Ligon et al. (2017) refer to the acceleration and cost reduction of product development as the initial economic motivation for the rise of AM technologies. In fact, when fast production is the goal, 3D printing becomes very useful, helping designers to create products and identify possible mistakes earlier, as well as ensuring the customer's desires are fulfilled and their specifications met.

AM technologies were initially available only for plastic materials. They produced parts with a low level of quality and finish in a slow and expensive printing process, being mostly used by large corporations in prototyping (Rayna and Striukova, 2016). Nowadays, the development of technologies as well as processing materials promote the insertion of AM in the *rapid manufacturing* sector. The *rapid tooling* of customized jigs, hardware and moulds with lower production times and costs than conventional manufacturing is another useful application.

Additive Manufacturing accepts a varied selection of materials, with polymers being the ones most commonly used. Among others, the range of employed polymers comprehends thermosets, thermoplastics, elastomers, hydrogels, polymer blends and biological systems (Izdebska-Podsiadły, 2022). Photopolymers are predominant in the market due to their regular use in prototyping and manufacturing applications. Although some progress has been achieved, the thermomechanical properties of 3D printed polymers are still limited. (Lukić et al., 2016; Ligon et al., 2017; Banjanin et al., 2022). This encourages a large amount of academic and industrial research on the optimisation of the mechanical performance of printed parts (Bakir et al., 2021).

A recent and very promising topic of interest is the 3D printing of elastic materials. This subject is in its initial stages of development (Zhou et al., 2020) and still relatively unexplored compared to stiff polymers. Elastomer components such as seals, membranes, bearings and hoses are widely used in complex machinery and equipment. They are of great significance and must fulfil multiple requirements. Typical requirements include low elastic modulus, high extensibility, resilience, damage and abrasion resistance, resistance

to chemicals and oils, and thermal stability over a wide temperature range. The hardness and tensile strength can be tailored by changing the conventional rubber composition with the addition of carbon black as a reinforcing filler, for example.

However, when in contact with heat, chemicals, radiation and weather conditions, elastomers can deteriorate (Smith, 1993). They are subjected to fatigue and ageing during operation, limiting their service life and often requiring replacements. Ageing during storage is another common phenomenon, which affects the storage of large quantities of elastic parts and increases its costs. Logistics can also be challenging, in particular for demands in remote locations.

By adopting AM in the elastomeric field, spare parts can be produced in shorter lead times while reducing warehousing costs. The replacement of damaged components can be carried out more promptly and whenever necessary, especially if they have been discontinued by original manufacturers. Local production can be significantly advantageous if elastomeric parts are required in places of difficult access. In the case of military operations, the presence of a 3D printer in the field can assist, for example, in the supply of O-ring seals, which can be easily lost or deteriorated under severe environment conditions.

Nevertheless, functional parts must ensure sufficient mechanical properties. Since traditional, vulcanised rubber is not suitable for the majority of the AM technologies, alternative materials with similar elastic properties are commonly applied. These include both already existing (e.g. thermoplastic elastomers) and newly developed materials (such as photocurable resins). The type of AM technology also influences the performance of the final part. Therefore, material knowledge and understanding is crucial for a comprehensive analysis of the mechanical behaviour of current 3D printed elastic materials and their feasibility for components in service, as well as for optimisations of printing processes. For the expansion of scientific knowledge on the subject, intensive research and testing are conducted in this work, providing an overview on the thermomechanical capabilities of selected 3D printed elastomers.

1.2 State of the Art

Additive Manufacturing is becoming an increasingly a hot topic in the literature. Research in metal AM is one of the dominant subjects, with an increasing rate of 55% per year in scientific papers. 3D printing of ceramics and clay is growing similarly, at a rate of about 45% per year (Banjanin et al., 2022). As for 3D printing of polymers, hydrogels or elastomers, statistics show an exponential increase in publications since 2014, which have been reported to be above 2,000 per year in 2018 and 2019 (Zhou et al., 2020). Review articles can be found comprising developed AM technologies, overviews of material behaviour and recent advances in the area (Ligon et al., 2017; Liravi and Toyserkani, 2018; Bagheri and Jin, 2019; Herzberger et al., 2019; Sheoran and Kumar, 2019; Zhou et al., 2020; Bakir et al., 2021; Pagac et al., 2021; Shaukat et al., 2022).

Among the technologies suitable for polymers, extrusion-based AM is widely used, particularly fused filament fabrication (FFF) due to its availability and lower costs (Shaukat

et al., 2022). This is reflected in the number of publications regarding FFF. The influence of printing parameters on the mechanical behaviour of the printed part is investigated frequently, mainly for stiff thermoplastic filaments. These parameters generally include the orientation angle of rasters (i.e. deposited lines), raster width, infill percentage and patterns, build orientation (flat, on-edge or vertical), layer height, printing temperature and printing speed. A large number of works are dedicated to specimens made of, for instance, polylactic acid (PLA) (Rajpurohit and Dave, 2018; Hannon et al., 2021; Morettini et al., 2022), polyethylene terephthalate-glycol (PETG) (Hannon et al., 2019), polyether-ether-ketone (PEEK) (Wu et al., 2015) and acrylonitrile butadiene styrene (ABS) (Wu et al., 2015; Mahmood et al., 2017). As a rule, rasters oriented at 0° and lower layer heights provide the best tensile results. A vertical building orientation is the most critical, since the perpendicular loading tends to separate the adjacent printed layers. Furthermore, higher printing speeds affect the layer bonding and thus contribute to a negative effect on the tensile strength (Farashi and Vafaee, 2022).

Examples of other investigations on FFF, which are usually valid for other types of filaments, comprise the resulting surface roughness (Ayrilmis, 2018), the optimisation of the mechanical properties of parts printed in an inert gas atmosphere (Lederle et al., 2016) and numerical modelling for extrusion failure prediction (Gilmer et al., 2018), and for assessment of the material flow deposition (Agassant et al., 2019). Finite element modelling is also reported for the analysis of mechanical properties (Bhandari and Lopez-Anido, 2018), quantification of the effect of microstructural imperfections (Nouri et al., 2016) and evaluation of damage under compressive loads (Guessasma, S. et al., 2016).

Adhesion in FFF prints is a key factor for better mechanical performance. The adhesion between layers was studied in publications by Fang et al. (2020), Coogan and Kazmer (2020) and Lepoivre et al., (2020). The first work also predicted material properties with finite element analysis; the latter two concentrated on measuring and modelling the thermal behaviour of the printed material strands to predict adhesion. All authors highlighted the importance of a sufficiently high printing temperature to promote an appropriate welding interface. Material bonding is a thermally driven process. Hence, cooling between rasters leads to partial bonding, according to Fitzharris et al. (2008). For this reason, the printing strategy, e.g. infill orientation, also affects the adhesion within the layer if there are long periods of time between two adjacent rasters. This was verified by Ai and Vogt (2022). In their work, infill paths at 90° had less cooling time between adjacent deposited lines than infill paths at 0°, which can lead to better intralayer welding, depending on print size. Crystallisation during bonding is another factor negatively affecting material adhesion (Collinson et al., 2022).

For other 3D printing technologies, such as those from vat photopolymerisation and material jetting processes, the final properties are closely related to the chemistry and processing of the printing material. Hence, results are not as easy to generalise. For this reason, publications in this regard are presented hereafter specifically for elastic materials.

In the field of AM with elastic polymers, most studies aim at fabricating actuators, robots, flexible electronics and sensing devices. Soft polymers are commonly used, which can be defined as polymers with a modulus in the range of that of soft biological materials, ranging from 10^3 to 10^9 Pa (Zhou et al., 2020). Research is often focused on biological applications.

Scaffold bioprinting and tissue engineering are common topics. 4D printing is also gaining attention, where parts can actively change their configurations over time in reaction to environmental stimuli. Printing materials include shape memory polymers, hydrogels, polyurethanes and silicones (Wallin et al., 2018; Izdebska-Podsiadły, 2022; Banjanin et al., 2022). Apart from biomedical studies, 3D printing of elastic polymers is explored with technologies that employ thermoplastic elastomers (TPEs) and ultraviolet (UV) curing resins (i.e. photopolymers) that possess elastomeric properties after being printed.

Wallin et al. (2018) conducted a review on positive and negative aspects of AM technologies and their application in the manufacturing of soft robotics. Herzberger et al. (2019) carried out an in-depth review on materials currently employed in AM for the printing of parts with elastomeric properties. The authors discussed the use of traditional polyurethanes for material jetting and material extrusion, and silicones for direct ink writing (DIW), vat photopolymerisation and material jetting. The use and development of photopolymers for vat photopolymerisation and material jetting technologies was also included. They analysed the challenges faced in the AM of elastomers, which are a combination of the printer and the polymer. Some examples include:

- the difficulty in printing complex geometries with FFF and its extrusion failure mechanisms;
- the potential for deformation or collapse of the printed part in DIW due to the low storage modulus of resulting networks of the printing material; and
- issues on the grinding for the production of powders used in powder bed fusion technologies due to the high toughness of some elastomers.

Herzberger et al. (2019) mentioned the inherent material properties as an important issue to be addressed. Nevertheless, the innovation of printer designs and polymer chemistry support the improvement of polymer processability and 3D printed part properties. Zhou et al. (2020) also discussed the limitations in the 3D printing of soft polymers. Besides the difficulties in powder production, the authors pointed out as challenges the low resolution and speed, and poor functionalities of the printed parts. In addition, material jetting is said to have rigorous requirements, which reduces the elastomeric options. Meanwhile, the printing requirements of vat photopolymerisation are less strict and allow the printing of "almost all soft photopolymers", but their variety in the polymer material catalogue is comparatively small.

Bakir et al. (2021) presented an overview of the knowledge on the mechanical behaviour of TPEs used in FFF. Additionally, the authors discussed the effects of printing parameters on the mechanical properties of prints, such as nozzle temperature, raster and build orientation, layer height and infill ratio. Leon-Calero et al. (2021) investigated the chemical composition, thermal behaviour and damping capacity in compression for a range of commercial TPUs (thermoplastic polyurethanes, which are a class of TPEs). The residual strain, softening and hysteresis of a thermoplastic styrenic elastomer under tensile cyclic loading was the focus of Tayeb et al. (2022). Other publications regarding printing of elastic thermoplastics in FFF machines address subjects such as: material friction properties for the fabrication of wheels (Farstad et al., 2017), effect of alternating infill angle and printing temperature on part quality (Xiao and Gao, 2017), use of pellet-based extrusion to eliminate buckling issues (Kumar et al., 2018), material characterisation and modelling of

viscoelastic/hyperelastic behaviour (Robinson et al., 2019; Płatek et al., 2020), comparison of the mechanical behaviour of FFF printed and injection moulded parts (Oelsch et al., 2021), and printing of magnetic elastomers (Dohmen et al., 2020) and of strain sensing elements (Georgopoulou et al., 2021).

Publications with respect to selective laser sintering (SLS) are considerably fewer than those regarding FFF. In general, SLS investigations deal with polyamide powders. Despite that, some of the recent works on powder bed fusion technologies have also been focusing on thermoplastic elastomers. The influence of powder size/shape of a TPU and its processability was analysed by Dadbakhsh et al. (2016). Kummert et al. (2018) measured the temperature distribution inside a SLS printed part. The processability of a powder blend of styrene-ethylene-butylene-styrene and polypropylene was studied by He et al. (2021). Additionally, the creeping and thermoresponsive shape-memory effects of a TPU were characterised in the work of Yuan et al. (2016).

Most works in the literature with 3D printing of thermoplastic materials with elastomeric properties deal with TPUs. They are a category of TPEs that can provide the elastic, non-linear behaviour similar to conventional elastomers. Furthermore, the lower the hardness of the printing TPU, the more this behaviour resembles that of rubber. Nevertheless, in the case of FFF, the softer the filament, the more difficult the printing process is (Farstad et al., 2017).

In the field of photopolymers, investigations with vat photopolymerisation technologies are primarily focused on the development of new elastic materials. In addition, they are directed towards materials for soft tissue engineering applications and biomedical devices. Sinh et al. (2016) documented the formulation of a UV curing polyurethane resin for stereolithography (SLA). The authors also highlighted the limited number of commercially available resins for SLA, whose networks are in their majority highly cross-linked and thus exhibit a stiff behaviour. The printability of photocurable resin formulations for digital light processing (DLP) printers was the topic in the works of Patel et al. (2017) and Thrasher et al. (2017). The latter produced specimens with maximum elongations at break of more than 450%. The first group of authors were able to achieve strains up to 1100%, which was reported as five times more than the elongation at break of the (few) commercially available photopolymers. The design of a self-healing elastomer resin and its use in the printing of a soft actuator, a structural composite and architected electronics in SLA were conducted by Yu et al. (2019).

In material jetting, particularly the PolyJet technology, Moore and Williams (2012) characterised fatigue properties of multi-material parts printed with TangoBlackPlus pristine photopolymer interfaced with VeroWhitePlus. The authors recommended strains below 20% for a long fatigue life (~10^6 cycles). Pristine Agilus30 and TangoPlus were the PolyJet printing materials studied by Abayazid and Ghajari (2020). In their work, the characterisation of the mechanical behaviour of the materials allowed the development of a visco-hyperelastic model for the prediction of their time-dependent response.

Among the publications with the softest and most stretchable polymers, silicone and silicone-based resins stand out as printing materials. The usual employed technologies consist of SLA or DLP, drop-on-demand (DOD) and material extrusion processes, e.g. DIW and liquid additive manufacturing (LAM). As there is a large interest in biological

applications, silicone is well suited due to its great elastic deformability, biocompatibility and translucency. Liravi and Toyserkani (2018) reviewed the challenges in developing AM systems that can operate with viscous thermosetting silicones, especially for biomedical applications, as well as the development of silicone customised for AM. Three key issues to be improved are the curing mechanism, the rheological properties along with printability and the mechanical performance, according to the authors.

Works without a specific aim at biomedicine are also available. As an example, Duoss et al. (2014) used silicone 3D printing to produce lattice structures with tailored compression and shear mechanical properties, namely negative stiffness, as a replacement alternative to foams. In the work of McCoul et al. (2017), thermally and UV-cured silicone elastomer materials were analysed. Thin patterned silicone membranes were printed, characterised and employed in dielectric elastomer actuators. Finite element investigations were also found in the literature. Liravi et al. (2017) modelled the flow of a highly viscous silicone in the nozzle of a material extrusion process. Thus, the dispensing profile and geometric parameters of the injected fluids were predicted. A hyperelastic model was developed and evaluated through finite element analysis by Putra et al. (2020) to predict the biaxial tensile behaviour of a silicone sheet printed in an extrusion-based AM process.

Several academic papers report investigations in custom-built printers or printing setups. In this context, the printing of silicone with sacrificial support structures made of carbohydrate glass (i.e. sugar) was carried out to create complex geometries (Hamidi and Tadesse, 2020). The development of a SLA printer capable of processing highly viscous resins was performed by Rodriguez et al. (2021). The authors also investigated the properties of a UV curing silicone formulated with reinforcements. Other studies include: the analysis of the rheological properties of an actuator printed in a 3D printer with an inline passive mixer with up to three silicone-based two-part composites (Miriyev et al., 2019), the assessment of printing parameters effects on the final stiffness of a medical grade silicone elastomer thermally cured by an infrared laser (Porter et al., 2019) and a calibration protocol for a fluid printhead, and the evaluation of the impact of silicone viscosity on geometry accuracy (Jaksa et al., 2022).

In extrusion-based silicone printing, Brusa da Costa Linn et al. (2022) focused on the 3D printing of heterogeneous magnetoactive layers in LAM by mixing iron particles in a silicone material prior to printing. Works of Plott et al. with moisture-cured silicone are some of the frequently cited in the literature. In Plott and Shih (2017), printing parameters were investigated to produce a thin-walled, solid part without voids between layers. The effect of infill raster orientation and adjacent line spacing on void formation and tensile strength within a layer was the topic of Plott et al. (2018a). In this study, the 0° raster printing strategy produced more voids inside the dumbbell specimens since the contoured part could not be completely filled with an axial deposition. Thus, the stress concentration under loading due to the voids led to lower strength and failure in the area of these voids. In Plott et al. (2018b), forces generated during the deposition process were measured and modelled. They consisted of tangential and normal forces arising from the silicone deposition and the nozzle tip as well as from the nozzle side and bottom surfaces dragging through the deposited silicone.

Most publications on elastic polymers deal with very specific subjects. New chemistry formulations and printer developments for 3D printing fluids, along with investigations of printing parameters in FFF stand out the literature. A small number of works explore the behaviour of commercially available materials. The behaviour under tensile loading is often analysed, although the dynamic properties in the high-frequency range are seldom assessed. An overview on the mechanical properties of multiple 3D printed elastomers in the market for the manufacturing of functional parts is lacking. With this in mind, it is essential to fill this gap and identify the capabilities of these materials in order to have an idea of which materials can be used to produce components for particular service applications.

1.3 Objectives and Structure

This thesis is the outcome of a four-year research in the field of 3D printing of elastic polymers. The main objective of the present work is to experimentally investigate the thermomechanical properties of a wide range of additively manufactured elastomeric materials processed by various technologies. The research evaluates the feasibility of 3D printing elastomers and creates a material database to assist in the selection of 3D printing materials for elastic components. In this way, it is possible to benefit from the production of spare parts for new components and for repair measures.

In order to achieve this goal, several steps are carried out, which are considered as specific objectives of this work. A comprehensive investigation on AM, its different technologies and rubber-like materials currently available in the market is initially conducted. Therefore, the advantages and disadvantages of the 3D printing processes can be analysed, as well as the constraints and adequacy for the fabrication of elastomeric parts. It is worth stating that throughout this thesis the term *flexible* refers exclusively to the ability of a material to bend, whereas *elastic* includes both flexibility and elasticity (i.e. the ability to bend combined with the ability to recover to the initial shape after stretching).

The printing of samples is also performed as a way to learn how the printing process works for some technologies. This is a significant step towards understanding the particularities of handling elastic materials in AM, including the evaluation of the pros and cons associated with these materials and printers. A material characterisation of several types of 3D printed elastomers is undertaken. The materials are submitted to thermomechanical testing with the purpose of identifying and assessing physical properties relevant to the operation of rubber components. Ultimately, a comparative analysis on the mechanical behaviour of the investigated materials is essential. Consequently, their suitability for technical applications can evaluated, and recommendations can be provided.

These objectives were reached throughout the thesis, whose structure is detailed as follows. Chapter 2 presents the basic concepts of continuum mechanics, including deformation gradient, strain and stress tensors as well as the balance principles and laws of thermodynamics. A literature review of polymers is carried out in Chapter 3, with a consequent focus on elastomers and their existing options. Chapter 4 addresses Additive Manufacturing. A detailed analysis on the characteristics, applications and limitations of AM is conducted, along with the main types of technology employing polymers. The

suitability of elastomers in 3D printing is subsequently discussed. Chapter 5 contains the methodology of the experimental investigations performed, describing the studied materials, the printing process and testing conditions. The mechanical characterisation was carried out through uniaxial tensile, cyclic and stress relaxation tests together with caloric and dynamic mechanical experiments.

Chapter 6 is dedicated to the comparative analysis of the tensile results, while the performances under cyclic loading are examined in Chapter 7. Chapter 8 deals with the assessment of the viscoelastic behaviour of 3D printed elastomers from stress relaxation tests. Thermal transitions are verified in Chapter 9 from differential scanning calorimetry testing, especially the glass transition temperature. The last series of tests, consisting of dynamic mechanical analyses, are evaluated in Chapter 10. They show the viscoelastic behaviour of the studied materials in the glass and rubbery states with respect to temperature as well as frequency. Chapter 11 addresses the overall discussion of the experimental results. Independent studies developed and published throughout the research with relevant findings are presented as well. Combined with the assessment of the thermomechanical behaviour of the investigated materials, an analysis on the suitability of the 3D printed elastomers is conducted. This thesis is finalised with conclusions collected from the experimental investigations, reported in Chapter 12. Finally, outlooks for future works are listed in Chapter 13.

2. Fundamentals of Continuum Mechanics

This chapter introduces the fundamentals of continuum mechanics for the description of a material body motion. According to Haupt (2002), continuum mechanics assumes that the matter is distributed in space in a continuous manner. As a result, processes and physical terms are represented by means of field functions, which are dependent on the coordinates of a specific material point. In this regard, the following figures present some concepts and thermomechanical measures pertinent to this work in a concise way. A more in-depth approach can be found in the literature, e.g. in the works of Haupt (2002), Holzapfel (2000), Betten (2001) and Dill (2007).

Using the notions of reference configuration (material, or Lagrangian description) and current configuration (spatial, or Eulerian description), the definition of the deformation gradient is initially demonstrated for the description of motion. Strain, rotation and stretch measures are shown thereafter with the concepts of strain tensors and associated time derivatives. Subsequently, stress tensors are introduced considering surface traction vectors. At last, balance principles of mass, linear momentum, angular momentum and energy are axiomatically presented, as well as the first and second laws of thermodynamics.

2.1 Kinematics

2.1.1 Deformation Gradient

The description in the continuum approach of the displacement and deformation (kinematics) of a continuum body $\mathcal{B}$ containing material points {P} considers the notion of configurations. Configuration is the region in space occupied by the body. It can be fixed (*reference configuration* Ω_0 of the initial, undeformed body, i.e. at time $t = t_0$) or instantaneous (*current configuration* Ω of the deformed body at a time $t > t_0$). The most convenient configuration is chosen according to the application, and Figure 2.1 illustrates the configuration concept.
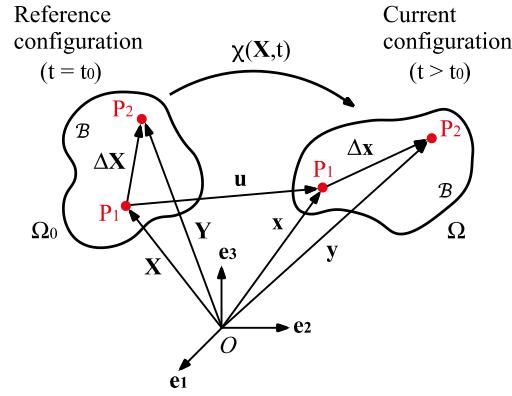
Figure 2.1: Motion of a continuum body considering reference and current configurations.

Considering a fixed origin $\mathcal{O}$ with orthonormal basis vectors $\{\boldsymbol{e}_1, \boldsymbol{e}_2, \boldsymbol{e}_3\}$, the material points P_1 and P_2 are identified with the position vectors $\mathbf{X}$ and $\mathbf{Y}$ in the reference configuration, respectively. As the body moves in space due to a loading process, points P_1 and P_2 assume respectively the position vectors $\mathbf{x}$ and $\mathbf{y}$ in the current configuration. The difference vector between material points P_2 and P_1 is given in the reference configuration as:

$$\Delta \mathbf{X} = \mathbf{Y} - \mathbf{X} \tag{2.1}$$

and in the current configuration as:

$$\Delta \mathbf{x} = \mathbf{y} - \mathbf{x} \tag{2.2}$$

The position vectors in both configurations can be linked by the body motion. This motion is represented by the bijective vector field $\boldsymbol{\chi}(\mathbf{X}, t)$. This vector field is uniquely invertible and has continuous derivatives with respect to position and time. It carries points in the reference configuration to points in the current configuration, that is:

$$\mathbf{x} = \boldsymbol{\chi}(\mathbf{X}, t), \quad \mathbf{X} = \boldsymbol{\chi}^{-1}(\mathbf{x}, t) \tag{2.3}$$

Often referred to as Lagrangian description, the characterisation of motion in the reference configuration considers the position vector $\mathbf{X}$ coordinates as well as time t as independent variables. When considering time and the coordinates of the position vector $\mathbf{x}$ (current configuration) as independent variables, the so-called Eulerian description is considered.

The displacement vector field relates position vector $\mathbf{X}$ to position vector $\mathbf{x}$. It is a function of the position vector and of time. In addition, it is generally used in solid mechanics for the description of motion and deformation of a continuum body. In the Lagrangian form, the displacement field is expressed as:

$$\mathcal{U}(\mathbf{X}, t) = \mathbf{x}(\mathbf{X}, t) - \mathbf{X} \tag{2.4}$$

and, in the Eulerian form, as:

$$\mathbf{u}(\mathbf{x}, t) = \mathbf{x} - \mathbf{X}(\mathbf{x}, t) \tag{2.5}$$

10

Both representations in Eqs. 2.4 and 2.5 are equivalent. They are related by means of the motion $\mathbf{x} = \chi(\mathbf{X}, t)$, assuming the same values, i.e.:

$$\mathcal{U}(\mathbf{X}, t) = \mathcal{U}(\chi^{-1}(\mathbf{x}, t), t) = \mathbf{u}(\mathbf{x}, t) \tag{2.6}$$

For the characterisation of the motion behaviour in the vicinity of a point, the deformation gradient $\mathbf{F}$ is subsequently defined. In this way, for two material points in direct vicinity, one can expand the body motion into a first-order Taylor series with a linear approximation, as:

$$\chi(\mathbf{Y}, t) = \chi(\mathbf{X}, t) + \frac{\partial \chi(\mathbf{X}, t)}{\partial \mathbf{X}} \cdot (\mathbf{Y} - \mathbf{X}) \tag{2.7}$$

Rearranging Eq. 2.7 and combining it with Eqs. 2.1 and 2.2, Eq. 2.8 is obtained:

$$\chi(\mathbf{Y}, t) - \chi(\mathbf{X}, t) = \frac{\partial \chi(\mathbf{X}, t)}{\partial \mathbf{X}} \cdot \Delta \mathbf{X}$$

$$\mathbf{y} - \mathbf{x} = \frac{\partial \chi(\mathbf{X}, t)}{\partial \mathbf{X}} \cdot \Delta \mathbf{X}$$

$$\Delta \mathbf{x} = \frac{\partial \chi(\mathbf{X}, t)}{\partial \mathbf{X}} \cdot \Delta \mathbf{X} \tag{2.8}$$

Considering infinitesimal difference vectors between the material points, Eq. 2.8 is rewritten in terms of the material $(d\mathbf{X})$ and spatial $(d\mathbf{x})$ line elements:

$$d\mathbf{x} = \frac{\partial \chi(\mathbf{X}, t)}{\partial \mathbf{X}} \cdot d\mathbf{X} \tag{2.9}$$

The deformation gradient is defined as the motion function derivative with respect to the position vector $\mathbf{X}$ (in the reference configuration), or as the material gradient (gradient from the reference configuration) of the position vector $\mathbf{x}$ (in the current configuration), as shown in Eq. 2.10. It is a second-order tensor. Considering Eq. 2.4, the deformation gradient can also be expressed by Eq. 2.11 in terms of the identity tensor $\mathbf{I}$ and the displacement field in Lagrangian form.

$$\mathbf{F} = \frac{\partial \chi(\mathbf{X}, t)}{\partial \mathbf{X}} = \frac{\partial \mathbf{x}}{\partial \mathbf{X}} = \text{Grad } \mathbf{x} \tag{2.10}$$

$$\mathbf{F} = \text{Grad} \left(\mathbf{X} + \mathcal{U}(\mathbf{X}, t) \right) = \mathbf{I} + \text{Grad } \mathcal{U} \tag{2.11}$$

Therefore, the mapping of line elements $d\mathbf{X}$ that connect two material points (in the reference configuration) into line elements $d\mathbf{x}$ (in the current configuration) can be performed by introducing the deformation gradient. Analogously, the mapping of line elements $d\mathbf{x}$ into line elements $d\mathbf{X}$ is done with the inverse of the deformation gradient, or the spatial gradient (gradient from the current configuration) of position vector $\mathbf{X}$:

$$\mathbf{F}^{-1}(\mathbf{x}, t) = \frac{\partial \mathbf{X}}{\partial \mathbf{x}} = \text{grad } \mathbf{X} = \mathbf{I} - \text{grad } \mathbf{u} \tag{2.12}$$

This implies that $\mathbf{F}$ is a non-singular tensor, i.e. its determinant is different from zero. The Jacobian determinant is thus expressed as $J = \det(\mathbf{F})$. The Jacobian represents the change in volume between the reference and current configurations at a time t. Considering the infinitesimal volume elements dV and dv in the reference and current configurations, respectively, and noting that those are positive, Eq. 2.13 is obtained:

$$dv = J(\mathbf{X}, t)\, dV \; ; \;\; J(\mathbf{X}, t) = \det(\mathbf{F}) > 0 \tag{2.13}$$

In the case of a motion with $J = 1$, the volume is kept constant (isochoric), and the material is incompressible when undergoing a deformation. If expressed as a dot product between the infinitesimal areas and the line elements, the infinitesimal volume elements can lead to:

$$dv = d\mathbf{a} \cdot d\mathbf{x} = J\, d\mathbf{A} \cdot d\mathbf{X} \tag{2.14}$$

Rewriting Eq. 2.14, the surface elements can be transformed between the two configurations according to:

$$
\begin{aligned}
d\mathbf{a} \cdot \mathbf{F}\, d\mathbf{X} &= J\, d\mathbf{A} \cdot d\mathbf{X} \\
(\mathbf{F}^{\mathrm{T}}\, d\mathbf{a} - J\, d\mathbf{A}) \cdot d\mathbf{X} &= 0 \\
d\mathbf{a} &= J\, \mathbf{F}^{-\mathrm{T}} \cdot d\mathbf{A}
\end{aligned}
\tag{2.15}
$$

2.1.2 Strain, Rotation and Stretch Measures

The deformation gradient is the fundamental kinematic tensor that characterizes changes in the body during motion, i.e. the rotations and distortions of infinitesimal line elements. The changes in length are expressed as strain tensors, which can be related to the reference or to the current configuration, and are presented in the following.

Strain tensors are defined considering the length $|d\mathbf{X}| = |\mathbf{Y} - \mathbf{X}|$ between two neighbouring points with position vectors $\mathbf{X}$ and $\mathbf{Y}$. As previously shown, these points are in the positions $\mathbf{x}$ and $\mathbf{y}$ in the current configuration as a result of motion. The stretched length between the points is thus $|d\mathbf{x}| = |\mathbf{y} - \mathbf{x}|$. Taking the square of this length, one obtains:

$$
\begin{aligned}
|\mathbf{y} - \mathbf{x}|^2 = |d\mathbf{x}|^2 = d\mathbf{x} \cdot d\mathbf{x} = (\mathbf{F} \cdot d\mathbf{X}) \cdot (\mathbf{F} \cdot d\mathbf{X}) &= d\mathbf{X} \cdot \mathbf{F}^{\mathrm{T}} \cdot \mathbf{F} \cdot d\mathbf{X} \tag{2.16} \\
&= d\mathbf{X} \cdot \mathbf{C} \cdot d\mathbf{X}
\end{aligned}
$$

$$\mathbf{C} = \mathbf{F}^{\mathrm{T}} \cdot \mathbf{F} \tag{2.17}$$

The deformation tensor $\mathbf{C}$ is called right Cauchy-Green tensor. It is a deformation measure in material coordinates (reference configuration), containing the deformation gradient on the right (and its transpose on the left). This tensor is symmetric and positive-definite at each point of position $\mathbf{X}$, that is:

$$\mathbf{C} = \mathbf{C}^{\mathrm{T}} \;\; \text{and} \;\; \mathbf{X} \cdot (\mathbf{C} \cdot \mathbf{X}) > 0, \forall\, \mathbf{X} \neq \mathbf{0} \tag{2.18}$$

The Piola deformation tensor is defined as the inverse of the right Cauchy-Green tensor, denoted by:

$$\mathbf{C}^{-1} = \mathbf{F}^{-1} \cdot \mathbf{F}^{-T} \tag{2.19}$$

A strain measure derived from the right Cauchy-Green tensor is the Green-Lagrange strain tensor $\mathbf{E}$, also in the reference configuration. It assumes the form below and describes a strain measure in the direction of a material line element $d\mathbf{X}$ at the position vector $\mathbf{X}$. Since $\mathbf{C}$ and the identity tensor $\mathbf{I}$ are both symmetric, so is $\mathbf{E}$:

$$\mathbf{E} = \frac{1}{2}\,(\mathbf{C} - \mathbf{I}) \tag{2.20}$$

For the particular case of $\mathbf{C} = \mathbf{I}$, Eq. 2.16 gives $d\mathbf{x} \cdot d\mathbf{x} = d\mathbf{X} \cdot d\mathbf{X}$. This indicates that the distance between the two neighbouring points is maintained during motion, characterising the rigid-body motion. If $\mathbf{C} \neq \mathbf{I}$, then the body is deformed, and $\mathbf{E} \neq \mathbf{0}$.

Analogously, when defining strain tensors considering the length $|d\mathbf{x}| = |\mathbf{y} - \mathbf{x}|$ between two neighbouring points of positions $\mathbf{x}$ and $\mathbf{y}$ in the current configuration and the square of its equivalent length $|d\mathbf{X}| = |\mathbf{Y} - \mathbf{X}|$ of the material line element, Eq. 2.21 is achieved:

$$|\mathbf{Y} - \mathbf{X}|^2 = |d\mathbf{X}|^2 = d\mathbf{X} \cdot d\mathbf{X} = (\mathbf{F}^{-1} \cdot d\mathbf{x}) \cdot (\mathbf{F}^{-1} \cdot d\mathbf{x}) = d\mathbf{x} \cdot \mathbf{F}^{-T} \cdot \mathbf{F}^{-1} \cdot d\mathbf{x}$$
$$|\mathbf{Y} - \mathbf{X}|^2 = d\mathbf{x} \cdot \mathbf{B}^{-1} \cdot d\mathbf{x} \tag{2.21}$$
$$\mathbf{B} = \mathbf{F} \cdot \mathbf{F}^T \tag{2.22}$$

The spatial deformation tensor $\mathbf{B}$ is named left Cauchy-Green tensor, as the deformation gradient is on the left. This strain measure is thus in terms of spatial coordinates (current configuration). Comparable with $\mathbf{C}$, $\mathbf{B}$ is also symmetric and positive-definite at each point of position $\mathbf{x}$.

At last, the strain measure $\mathbf{A}$, called Euler-Almansi strain tensor, is derived from the left Cauchy-Green tensor. This symmetric tensor in the current configuration describes a strain measure in the direction of a spatial line element $d\mathbf{x}$ at position vector $\mathbf{x}$:

$$\mathbf{A} = \frac{1}{2}\,(\mathbf{I} - \mathbf{B}^{-1}) \tag{2.23}$$

In order to transform between material and spatial quantities, the *push-forward* and *pull-back* operations are performed. These operations are based on multiplications by one description of the deformation gradient (i.e. $\mathbf{F}$, $\mathbf{F}^T$, $\mathbf{F}^{-1}$, $\mathbf{F}^{-T}$). The push-forward operation transforms a vector or tensor based on the reference configuration into the current configuration, while the pull-back operation transforms a vector or tensor based on the current configuration into the reference configuration. The strain tensor $\mathbf{E}$ can be transformed into the strain tensor $\mathbf{A}$ with the push-forward operation (Eq. 2.24) and $\mathbf{A}$ can be transformed into $\mathbf{E}$ with the pull-back operation (Eq. 2.25):

$$\mathbf{A} = \mathbf{F}^{-T} \cdot \mathbf{E} \cdot \mathbf{F}^{-1} \tag{2.24}$$
$$\mathbf{E} = \mathbf{F}^T \cdot \mathbf{A} \cdot \mathbf{F} \tag{2.25}$$

Considering Eqs. 2.11 and 2.12, both strain tensors can be expanded and also expressed as Eqs. 2.26 and 2.27, respectively:

$$\mathbf{E} = \frac{1}{2}\left(\text{Grad}\,\mathcal{U} + \text{Grad}^{\text{T}}\,\mathcal{U} + \text{Grad}^{\text{T}}\,\mathcal{U} \cdot \text{Grad}\,\mathcal{U}\right) \tag{2.26}$$

$$\mathbf{A} = \frac{1}{2}\left(\text{grad}\,\mathbf{u} + \text{grad}^{\text{T}}\,\mathbf{u} - \text{grad}^{\text{T}}\,\mathbf{u} \cdot \text{grad}\,\mathbf{u}\right) \tag{2.27}$$

In case of small displacement gradients (hence, small deformations), the nonlinear term in the right of Eq. 2.26 is neglected in comparison to the linear terms. Thus, the Green-Lagrange strain tensor (and similarly the Euler-Almansi strain) is simplified to the small-strain tensor presented in Eq. 2.28, whose components are the well-known engineering strains:

$$\boldsymbol{\varepsilon} = \frac{1}{2}\left(\text{Grad}\,\mathcal{U} + \text{Grad}^{\text{T}}\,\mathcal{U}\right) = \frac{1}{2}\left(\text{grad}\,\mathbf{u} + \text{grad}^{\text{T}}\,\mathbf{u}\right) \tag{2.28}$$

The line elements in the current and reference configurations can also be related by the stretch ratio λ. It is defined as the ratio between the lengths of the spatial and material line elements:

$$\lambda = \frac{|d\mathbf{x}|}{|d\mathbf{X}|} \tag{2.29}$$

If the stretch ratio is greater than 1 ($\lambda > 1$), the line element is said to be extended. If $\lambda = 1$, the line element is unstretched. If $\lambda < 1$, the line element is compressed.

Although the deformation gradient characterises the body changes due to motion, it accounts for both pure stretch and pure rotation. The motion, however, can be decomposed into these two local components. Figure 2.2 shows the polar decomposition of the deformation gradient.
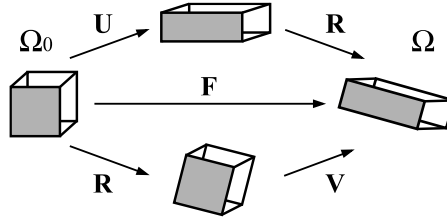
Figure 2.2: Polar decomposition of the deformation gradient.

In the polar decomposition, the motion is a combination of a deformation followed by a rotation ($\mathbf{U} \rightarrow \mathbf{R}$) or vice-versa ($\mathbf{R} \rightarrow \mathbf{V}$). Hence, the following applies:

$$\mathbf{F} = \mathbf{R} \cdot \mathbf{U} = \mathbf{V} \cdot \mathbf{R}; \quad \mathbf{R}^{\text{T}} \cdot \mathbf{R} = \mathbf{I}; \quad \mathbf{U} = \mathbf{U}^{\text{T}}; \quad \mathbf{V} = \mathbf{V}^{\text{T}} \tag{2.30}$$

Tensor $\mathbf{R}$ is the rotation tensor, measuring the local rotation. This tensor is unique and orthogonal ($\mathbf{R} \cdot \mathbf{R}^{\text{T}} = \mathbf{I}$). Tensors $\mathbf{U}$ and $\mathbf{V}$ are, respectively the right and left stretch tensors, which are positive-definite, symmetric and also unique. The first is defined with respect to the reference configuration while the latter, to the current configuration. Tensors $\mathbf{U}$ and $\mathbf{V}$ can be transformed into one another with forward and backward rotation, as shown in Eqs.

2.31 and 2.32. Furthermore, **U** and **V** can be used to express **C** and **B**, respectively. Eqs. 2.33 and 2.34 demonstrate that.

$$\mathbf{U} = \mathbf{R}^T \cdot \mathbf{F} = \mathbf{R}^T \cdot \mathbf{V} \cdot \mathbf{R} \tag{2.31}$$

$$\mathbf{V} = \mathbf{F} \cdot \mathbf{R}^T = \mathbf{R} \cdot \mathbf{U} \cdot \mathbf{R}^T \tag{2.32}$$

$$\mathbf{C} = \mathbf{F}^T \cdot \mathbf{F} = (\mathbf{R} \cdot \mathbf{U})^T \cdot \mathbf{R} \cdot \mathbf{U} = \mathbf{U} \cdot \mathbf{U} = \mathbf{U}^2 \tag{2.33}$$

$$\mathbf{B} = \mathbf{F} \cdot \mathbf{F}^T = \mathbf{V} \cdot \mathbf{R} \cdot (\mathbf{V} \cdot \mathbf{R})^T = \mathbf{V} \cdot \mathbf{V} = \mathbf{V}^2 \tag{2.34}$$

Another important concept is the rate of deformation. It depicts the rate at which the body changes regarding shape, position and orientation. For this, the material time derivative of the deformation gradient is defined. Considering the material velocity field $\boldsymbol{\mathcal{V}} = \dot{\boldsymbol{\mathcal{U}}} = \dot{\mathbf{x}}$ (derivative of position vector with respect to time), the material velocity gradient is achieved:

$$\dot{\mathbf{F}}(\mathbf{X}, t) = \frac{\partial}{\partial t}\left(\frac{\partial \boldsymbol{\chi}(\mathbf{X}, t)}{\partial \mathbf{X}}\right) = \frac{\partial}{\partial \mathbf{X}}\left(\frac{\partial \boldsymbol{\chi}(\mathbf{X}, t)}{\partial t}\right) = \frac{\partial \boldsymbol{\mathcal{V}}(\mathbf{X}, t)}{\partial \mathbf{X}} = \text{Grad } \boldsymbol{\mathcal{V}}(\mathbf{X}, t), \tag{2.35}$$

where $\boldsymbol{\mathcal{V}}$ is the material velocity. Likewise, the spatial velocity gradient **L** may be written as in Eq. 2.36, where **v** is the spatial velocity field. Furthermore, with the help of the chain rule, **L** can be expressed in terms of the material time derivative of the deformation gradient, as in Eq. 2.37, or $\dot{\mathbf{F}}$ in terms of **L** and **F** (Eq. 2.38).

$$\mathbf{L}(\mathbf{x}, t) = \text{grad } \mathbf{v}(\mathbf{x}, t) = \frac{\partial \mathbf{v}(\mathbf{x}, t)}{\partial \mathbf{x}} \tag{2.36}$$

$$\mathbf{L} = \frac{\partial \mathbf{v}(\mathbf{x}, t)}{\partial \mathbf{X}} \cdot \frac{\partial \mathbf{X}}{\partial \mathbf{x}} = \frac{\partial}{\partial \mathbf{X}}\left(\frac{\partial \mathbf{x}}{\partial t}\right) \cdot \frac{\partial \mathbf{X}}{\partial \mathbf{x}} = \frac{\partial}{\partial t}\left(\frac{\partial \mathbf{x}}{\partial \mathbf{X}}\right) \cdot \frac{\partial \mathbf{X}}{\partial \mathbf{x}} = \frac{\partial \mathbf{F}}{\partial t} \cdot \frac{\partial \mathbf{X}}{\partial \mathbf{x}} = \dot{\mathbf{F}} \cdot \mathbf{F}^{-1} \tag{2.37}$$

$$\dot{\mathbf{F}} = \mathbf{L} \cdot \mathbf{F} \tag{2.38}$$

The spatial velocity gradient can also describe the material time derivative of the spatial line element:

$$\dot{\overline{d\mathbf{x}}} = \frac{\partial}{\partial t}(\mathbf{F} \cdot d\mathbf{X}) = \dot{\mathbf{F}} \cdot d\mathbf{X} = \dot{\mathbf{F}} \cdot \mathbf{F}^{-1} \cdot d\mathbf{x} = \mathbf{L} \cdot d\mathbf{x} \tag{2.39}$$

The decomposition of the spatial velocity gradient into a symmetric and an antisymmetric part gives the rate of deformation tensor **D** and the spin tensor **W**. They are spatial fields; the first provides the rate of stretching and shearing of line elements, while the latter describes the rate of rotation of the body:

$$\mathbf{L} = \mathbf{D} + \mathbf{W} \tag{2.40}$$

$$\mathbf{D} = \frac{1}{2}(\mathbf{L} + \mathbf{L}^T) = \mathbf{D}^T \tag{2.41}$$

$$\mathbf{W} = \frac{1}{2}(\mathbf{L} - \mathbf{L}^T) = -\mathbf{W}^T \tag{2.42}$$

For the material time derivative of the Green-Lagrange strain tensor, Eqs. 2.17, 2.20, 2.38 and 2.41, with application of the product rule, give Eq. 2.43. This can be used to rewrite

the rate of deformation tensor as in Eq. 2.44, characterising the transformations between the strain rate tensors $\dot{\mathbf{E}}$ and $\mathbf{D}$. In addition, the (material) rate of the right Cauchy-Green tensor $\dot{\mathbf{C}}$ can be simply expressed as the double of $\dot{\mathbf{E}}$ (Eq. 2.45):

$$\dot{\mathbf{E}} = \frac{1}{2}\frac{\partial}{\partial t}(\mathbf{F}^{\mathrm{T}} \cdot \mathbf{F} - \mathbf{I}) = \mathbf{F}^{\mathrm{T}} \cdot \mathbf{D} \cdot \mathbf{F} \tag{2.43}$$

$$\mathbf{D} = \mathbf{F}^{-\mathrm{T}} \cdot \dot{\mathbf{E}} \cdot \mathbf{F}^{-1} \tag{2.44}$$

$$\dot{\mathbf{C}} = 2\dot{\mathbf{E}} \tag{2.45}$$

The material time derivative of the left Cauchy-Green strain tensor can also be expressed with respect to the spatial velocity gradient. In this case, Eq. 2.46 is achieved:

$$\dot{\mathbf{B}} = \frac{\partial}{\partial t}(\mathbf{F} \cdot \mathbf{F}^{\mathrm{T}}) = \mathbf{L} \cdot \mathbf{B} + \mathbf{B} \cdot \mathbf{L}^{\mathrm{T}} \tag{2.46}$$

The material time derivative of the Euler-Almansi strain tensor $\mathbf{A}$ requires several manipulations in its equation to reach the format in Eq. 2.47. With the help of the product rule, the tensor definitions in Eqs. 2.23, 2.37, 2.38 and 2.41, as well as the $\mathbf{I} = \mathbf{F}^{-1} \cdot \mathbf{F} = \mathbf{F}^{-\mathrm{T}} \cdot \mathbf{F}^{\mathrm{T}}$ identities, one obtains:

$$\dot{\mathbf{A}} = \frac{1}{2}\frac{\partial}{\partial t}(\mathbf{I} - \mathbf{F}^{-\mathrm{T}} \cdot \mathbf{F}^{-1}) = \mathbf{D} - \mathbf{L}^{\mathrm{T}} \cdot \mathbf{A} - \mathbf{A} \cdot \mathbf{L} \tag{2.47}$$

In the view of this, the material time derivative of all strain measures presented in this subsection were determined. The motion and deformations lead thus to interactions such as stress.

2.2 Stress Tensors

For the description of stress tensors, surface traction vectors are considered. These vectors may be related to the reference or current configuration. Furthermore, they are expressed as tensor fields that act on a normal vector ($\mathbf{N}$ in the reference configuration, or $\mathbf{n}$ in the current configuration) to a plane surface. Figure 2.3 illustrates these normal vectors on a deformable continuum body $\mathcal{B}$.
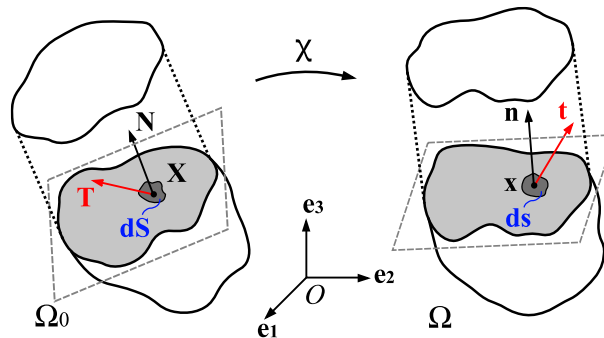
Figure 2.3: Traction vectors acting on infinitesimal surface elements.

Taking into account that arbitrary external forces (on the boundary surface) and internal forces (on the volume inside) act on the body, the traction at a particular point ($\mathbf{X}$, or $\mathbf{x}$) is the relation of the acting force over the surface area of its application. The plane of the surface element area is represented by dS and ds for the reference and current configurations, respectively, while the infinitesimal resultant acting force, by d$\mathbf{f}$. The outward normal vectors of dS and ds are correspondingly $\mathbf{N}$ and $\mathbf{n}$. For every surface element, Eqs. 2.48 and 2.49 apply, where $\mathbf{T}$ is named first Piola-Kirchhoff (or nominal) traction vector and $\mathbf{t}$ is the Cauchy (or true) traction vector:

$$d\mathbf{f} = \mathbf{t}\,ds = \mathbf{T}\,dS \tag{2.48}$$

$$\mathbf{t} = \mathbf{t}(\mathbf{x}, t, \mathbf{n}), \quad \mathbf{T} = \mathbf{T}(\mathbf{X}, t, \mathbf{N}) \tag{2.49}$$

Traction vectors $\mathbf{T}$ and $\mathbf{t}$ are also called surface tractions, or stress vectors. The second-order stress tensor is used to calculate the traction vector acting on an infinitesimal area considering its normal vector. From Eqs. 2.50 and 2.51, one finds the Cauchy's stress theorem:

$$\mathbf{T}(\mathbf{X}, t, \mathbf{N}) = \mathbf{P}(\mathbf{X}, t) \cdot \mathbf{N} \tag{2.50}$$

$$\mathbf{t}(\mathbf{x}, t, \mathbf{n}) = \boldsymbol{\sigma}(\mathbf{x}, t) \cdot \mathbf{n} \tag{2.51}$$

The tensor field $\mathbf{P}$ in the reference configuration is the first Piola-Kirchhoff (or nominal) stress tensor (PK1 stress), while $\boldsymbol{\sigma}$ is the symmetric, Cauchy (or true) stress tensor. The relation between $\boldsymbol{\sigma}$ and $\mathbf{P}$ is obtained from Eq. 2.48 combined with Eqs. 2.50, 2.51 and 2.15, with infinitesimal area elements d$\mathbf{A} = \mathbf{N}$ dS and d$\mathbf{a} = \mathbf{n}$ ds. It assumes the two forms:

$$\mathbf{P} = J\,\boldsymbol{\sigma} \cdot \mathbf{F}^{-T} \tag{2.52}$$

$$\boldsymbol{\sigma} = J^{-1}\,\mathbf{P} \cdot \mathbf{F}^{T} \tag{2.53}$$

As the Cauchy stress tensor is symmetric ($\boldsymbol{\sigma} = \boldsymbol{\sigma}^T$), from Eq. 2.52 it is implied that $\mathbf{P} \cdot \mathbf{F}^T = \mathbf{F} \cdot \mathbf{P}^T$. Since the deformation gradient is not symmetric, neither is $\mathbf{P}$. In addition, while $\boldsymbol{\sigma}$ is a spatial tensor field, $\mathbf{P}$ is not analogously purely Lagrangian. The PK1 stress is called a 2-point tensor, as it relates the force acting in the current configuration to the surface element in the reference configuration. Hence, the second Piola-Kirchhoff stress tensor (PK2 stress) $\mathbf{S}$ is defined by Eq. 2.54.

$$\mathbf{S} = J\,\mathbf{F}^{-1} \cdot \boldsymbol{\sigma} \cdot \mathbf{F}^{-T} \tag{2.54}$$

Although $\mathbf{S}$ does not have a physical interpretation, it is used as a measure of stress since it is symmetric, i.e. $\mathbf{S} = \mathbf{S}^T$, and a material tensor field (purely Lagrangian description). It represents the corresponding vector force d$\bar{\mathbf{f}}$ in the reference configuration divided by the corresponding area element in the reference configuration, which is associated with d$\mathbf{f}$ respecting Eq. 2.12. This gives Eq. 2.55, which using the definitions from Eqs. 2.48 and 2.50 leads to the relationships between PK1 and PK2 presented in Eq. 2.56:

$$d\bar{\mathbf{f}} = \mathbf{S} \cdot d\mathbf{A} = \mathbf{F}^{-1} \cdot d\mathbf{f} \tag{2.55}$$

$$\mathbf{S} = \mathbf{F}^{-1} \cdot \mathbf{P}, \quad \text{or} \quad \mathbf{P} = \mathbf{F} \cdot \mathbf{S} \tag{2.56}$$

Each Cauchy traction vector acting on surface elements with outward normal vectors in the directions $\mathbf{e}_1$, $\mathbf{e}_2$ and $\mathbf{e}_3$ of the orthonormal basis gives three components of the Cauchy stress tensor. One of them is in the normal vector direction, while the other two are in the plane of the surface element (see Figure 2.4).
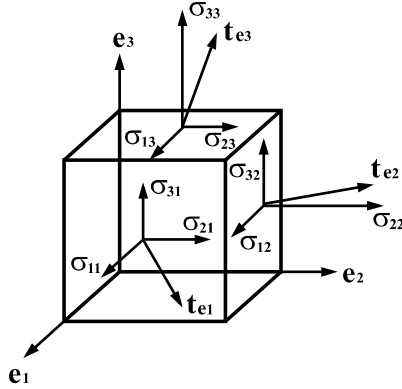
Figure 2.4: Components of traction vectors acting on the faces of an infinitesimal cube.

In this case, the following vectors and components are obtained:

$$\mathbf{t}_{\mathbf{e}_1} = \boldsymbol{\sigma} \cdot \mathbf{e}_1 = \sigma_{11}\, \mathbf{e}_1 + \sigma_{21}\, \mathbf{e}_2 + \sigma_{31}\, \mathbf{e}_3 \tag{2.57}$$

$$\mathbf{t}_{\mathbf{e}_2} = \boldsymbol{\sigma} \cdot \mathbf{e}_2 = \sigma_{12}\, \mathbf{e}_1 + \sigma_{22}\, \mathbf{e}_2 + \sigma_{32}\, \mathbf{e}_3 \tag{2.58}$$

$$\mathbf{t}_{\mathbf{e}_3} = \boldsymbol{\sigma} \cdot \mathbf{e}_3 = \sigma_{13}\, \mathbf{e}_1 + \sigma_{23}\, \mathbf{e}_2 + \sigma_{33}\, \mathbf{e}_3 \tag{2.59}$$

where:

$$[\boldsymbol{\sigma}] = \begin{bmatrix} \sigma_{11} & \sigma_{12} & \sigma_{13} \\ \sigma_{21} & \sigma_{22} & \sigma_{23} \\ \sigma_{31} & \sigma_{32} & \sigma_{33} \end{bmatrix} \tag{2.60}$$

Considering the symmetry of the Cauchy stress tensor, there are only six independent components, where $\sigma_{12} = \sigma_{21}$, $\sigma_{13} = \sigma_{31}$ and $\sigma_{23} = \sigma_{32}$. These components act tangentially to a surface element, receiving the name of shear stresses. The diagonal elements σ_{11}, σ_{22} and σ_{33} represent the normal stresses, as they act in the direction of the unit vector normal to a surface element. Positive normal stresses are called tensile stresses, while negative normal stresses are compressive stresses.

For the uniaxial tension state, $\sigma_{11} = \sigma > 0$ and all other components are zero (Eq. 2.61). The line elements change in length only, without changes in the angles between them. In other words, the components of position vector $d\mathbf{x}$ in the three coordinate axes are $x_i = \lambda_i X_i$. For incompressible materials such as rubber, the deformation gradient assumes the form in Eq. 2.62. Additionally, since there is only stretch and no rotation (i.e. $\mathbf{R} = \mathbf{I}$), from Eq. 2.30 the right stretch tensor $\mathbf{U}$ equals the deformation gradient:

$$[\boldsymbol{\sigma}] = \begin{bmatrix} \sigma & 0 & 0 \\ 0 & 0 & 0 \\ 0 & 0 & 0 \end{bmatrix} \tag{2.61}$$

$$[\mathbf{F}] = [\mathbf{U}] = \begin{bmatrix} \lambda & 0 & 0 \\ 0 & 1/\sqrt{\lambda} & 0 \\ 0 & 0 & 1/\sqrt{\lambda} \end{bmatrix} \tag{2.62}$$

2.3 Balance Principles and Laws of Thermodynamics

Following relevant concepts in kinematics for the description of the geometry of motion and deformation, the link between the sources of motion and the external influences is performed by the kinetics. In this context, there are basic balance equations, which correlate physical quantities in continuum mechanics. These principles must be satisfied for any particular material. They consist on the conservation of mass, the balance of linear momentum and the balance of angular momentum, the conservation of energy and the entropy inequality principle, which are axiomatically presented in this section.

A master balance is introduced since all balance equations have the same form. The global form of the master balance states that the material time derivative of a physical quantity $\psi(\mathbf{x}, t)$ in an arbitrary region Ω equals the sum of its outward normal flux $\phi(\mathbf{x}, t, \mathbf{n})$ over the boundary surface $\partial\Omega$ of the region, a volume-related source term $\Sigma(\mathbf{x}, t)$ and a production term $\widehat{\psi}(\mathbf{x}, t)$, both over the region volume (see Eq. 2.63):

$$\frac{d}{dt} \int_{\Omega} \psi(\mathbf{x}, t)\, dv = \int_{\partial\Omega} \phi(\mathbf{x}, t, \mathbf{n})\, ds + \int_{\Omega} \Sigma(\mathbf{x}, t)\, dv + \int_{\Omega} \widehat{\psi}(\mathbf{x}, t)\, dv \tag{2.63}$$

Applying Reynolds' transport theorem, the divergence theorem, material time derivative and after some mathematical reformulations, Eq. 2.64 is achieved. It is the local spatial form of the master balance for a material point. The total flux is taken as a scalar product with the normal vector $\mathbf{n}$, that is $\phi = \mathbf{\Phi} \cdot \mathbf{n}$, and $\mathbf{v}$ is the spatial velocity field:

$$\dot{\psi} + \psi\, \mathrm{div}\, \mathbf{v} = \mathrm{div}\, \mathbf{\Phi} + \Sigma + \widehat{\psi} \tag{2.64}$$

2.3.1 Conservation of Mass

The mass of a continuum body $\mathcal{B}$, which consists of a closed system, is a positive scalar measure and is invariant during motion. Consider a closed system (control mass) of a region Ω in space with a boundary surface $\partial\Omega$. In non-relativistic physics, the mass in Ω cannot be created nor destroyed. Hence, the mass is a conserved quantity, characterising the law of conservation of mass.

The material time derivative dm/dt is zero, and the infinitesimal mass element in the reference configuration equals the infinitesimal mass element in the current configuration. Taking the mass densities in a region Ω_0 in the reference configuration and in a region Ω in the current configuration as ρ_0 and ρ, respectively, one finds:

$$dm(\mathbf{X}) = dm(\mathbf{x}, t) > 0 \tag{2.65}$$

$$\rho_0(\mathbf{X}) \, dV = \rho(\mathbf{x}, t) \, dv > 0 \tag{2.66}$$

$$\dot{m} = \frac{dm}{dt} = \frac{d}{dt} \int_{\Omega_0} \rho_0 \, dV = \frac{d}{dt} \int_{\Omega} \rho \, dv = 0 \tag{2.67}$$

From the equations above, and Eqs. 2.13 and 2.3, the local continuity mass equation with respect to the reference configuration is obtained:

$$\int_{\Omega_0} \rho_0 \, dV - \int_{\Omega} \rho \, dv = \int_{\Omega_0} [\rho_0(\mathbf{X}) - \rho(\boldsymbol{\chi}(\mathbf{X}, t), t) \, J(\mathbf{X}, t)] \, dV = 0$$

$$\rho_0(\mathbf{X}) = \rho(\boldsymbol{\chi}(\mathbf{X}, t), t) \, J(\mathbf{X}, t) \,, \quad \forall \, \mathbf{X} \in \Omega_0 \tag{2.68}$$

Since the mass density in the reference configuration is independent of time, $J(\mathbf{X}, t) > 0$ and $\dot{J} = J \, \text{div} \, \mathbf{v}$, the following applies:

$$\frac{d\rho_0}{dt} = \frac{d}{dt}[J \, \rho] = J \, \dot{\rho} + \dot{J} \, \rho = J(\dot{\rho} + \rho \, \text{div} \, \mathbf{v}) = 0$$

$$\dot{\rho} + \rho \, \text{div} \, \mathbf{v} = 0 \tag{2.69}$$

For an incompressible material, the density is constant, leading to $\text{div} \, \mathbf{v} = 0$. Furthermore, comparing Eqs. 2.67 and 2.69 with the global and local spatial forms of the master balance, respectively, for the law of conservation of mass, the physical quantity $\psi(\mathbf{x}, t)$ is assumed as $\rho(\mathbf{x}, t)$, while the flux, source and production terms are null.

2.3.2 Balance of Linear Momentum

For a continuum body as a closed system, the linear momentum $\mathcal{L}(t)$ is defined as the volume integral over the mass density multiplied by the velocity field, as in Eq. 2.70. The linear momentum balance is an axiom expressed by the material time derivative of the linear momentum. The change in time of $\mathcal{L}(t)$, denoted by $\dot{\mathcal{L}}(t)$, is caused by (and equal to) the resultant force $\mathcal{F}(t)$ acting on the closed system (Eq. 2.71):

$$\mathcal{L}(t) = \int_{\Omega} \rho(\mathbf{x}, t) \, \mathbf{v}(\mathbf{x}, t) \, dv = \int_{\Omega_0} \rho_0(\mathbf{X}, t) \, \mathcal{V}(\mathbf{X}, t) \, dV \tag{2.70}$$

$$\dot{\mathcal{L}}(t) = \frac{d}{dt} \int_{\Omega} \rho(\mathbf{x}, t) \, \mathbf{v}(\mathbf{x}, t) \, dv = \frac{d}{dt} \int_{\Omega_0} \rho_0(\mathbf{X}, t) \, \mathcal{V}(\mathbf{X}, t) \, dV = \mathcal{F}(t) \tag{2.71}$$

The resultant force comprises the sum of all forces acting on surface elements (due to surface tractions) and on volume elements (due to body forces), as illustrated in Figure 2.5. In Eulerian description, $\mathcal{F}(t)$ is given by Eq. 2.72, where $\mathbf{b}(\mathbf{x}, t)$ is the body force vector in spatial coordinates. For simplification reasons, the resultant force in the Lagrangian

20

description is briefly presented in Eq. 2.73, with the body force vector $\bar{\mathbf{b}}(\mathbf{X}, t)$ in material coordinates assuming the relationship in Eq. 2.74.
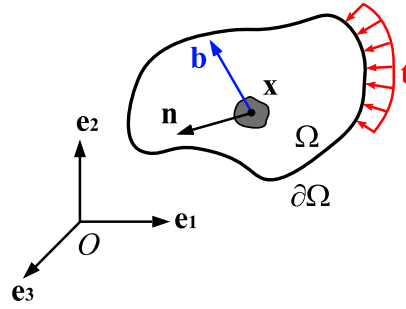
Figure 2.5: Forces acting on a continuum body in the current configuration.

$$\mathcal{F}(t) = \int_{\partial\Omega} \mathbf{t}(\mathbf{x}, t, \mathbf{n}) \, ds + \int_{\Omega} \mathbf{b}(\mathbf{x}, t) \, dv \tag{2.72}$$

$$\mathcal{F}(t) = \int_{\partial\Omega_0} \mathbf{T}(\mathbf{X}, t, \mathbf{N}) \, dS + \int_{\Omega_0} \bar{\mathbf{b}}(\mathbf{X}, t) \, dV \tag{2.73}$$

$$\bar{\mathbf{b}} = J \, \mathbf{b} \tag{2.74}$$

The linear momentum balance principle (as well as the angular momentum balance principle, presented in the next section) is satisfied if a spatial tensor field $\boldsymbol{\sigma}$ exists so that $\mathbf{t}(\mathbf{x}, t, \mathbf{n}) = \boldsymbol{\sigma}(\mathbf{x}, t) \cdot \mathbf{n}$, which corresponds to Eq. 2.51. After mathematical reformulations, one obtains:

$$\int_{\Omega} (\operatorname{div} \boldsymbol{\sigma} + \mathbf{b} - \rho \, \dot{\mathbf{v}}) \, dv = \mathbf{0} \tag{2.75}$$

$$\operatorname{div} \boldsymbol{\sigma} + \mathbf{b} = \rho \, \dot{\mathbf{v}} \tag{2.76}$$

Eqs. 2.75 and 2.76 are known as Cauchy's first equation of motion in the global and local forms, respectively. For static problems, the acceleration $\dot{\mathbf{v}}$ is zero, leading to Cauchy's equation of equilibrium:

$$\operatorname{div} \boldsymbol{\sigma} + \mathbf{b} = \mathbf{0} \tag{2.77}$$

Cauchy's first equation of motion (global and local forms) and equation of equilibrium can be expressed in terms of material coordinates, whose independent variables are $(\mathbf{X}, t)$, as Eqs. 2.78, 2.79 and 2.80, respectively. The relationships in Eqs. 2.13, 2.74 and 2.81 apply for the transformations between the reference and current configurations:

$$\int_{\Omega_0} \left(\operatorname{Div} \mathbf{P} + \bar{\mathbf{b}} - \rho_0 \, \dot{\boldsymbol{\mathcal{V}}} \right) dV = \mathbf{0} \tag{2.78}$$

$$\operatorname{Div} \mathbf{P} + \bar{\mathbf{b}} = \rho_0 \, \dot{\boldsymbol{\mathcal{V}}} \tag{2.79}$$

$$\text{Div } \mathbf{P} + \bar{\mathbf{b}} = \mathbf{0} \qquad (2.80)$$

$$\text{Div } \mathbf{P} = J \, \text{div } \boldsymbol{\sigma} \qquad (2.81)$$

From the master balance, the balance of linear momentum assumes the physical quantity $\psi(\mathbf{x}, t)$ as the impulse $\rho \mathbf{v}$. The flux term corresponds to the Cauchy stress field ($\boldsymbol{\Phi} = \boldsymbol{\sigma}$, or $\phi = \mathbf{t}$), the source term corresponds to the body forces ($\Sigma = \mathbf{b}$), and the production term is null.

2.3.3 Balance of Angular Momentum

For a closed system, the angular momentum $\mathcal{A}$ relative to a fixed point $\mathbf{x}_0$ is defined as the integral over volume of the cross product of position vector $\mathbf{r}$ with the multiplication of the mass density by the velocity field (Eq. 2.82). The position vector is expressed as the difference vector between the positon vector in the current configuration and the fixed point in question (Eq. 2.83).

$$\mathcal{A}(t) = \int_{\Omega} \mathbf{r} \times \rho(\mathbf{x}, t) \, \mathbf{v}(\mathbf{x}, t) \, dv = \int_{\Omega_0} \mathbf{r} \times \rho_0(\mathbf{X}, t) \, \mathcal{V}(\mathbf{X}, t) \, dV \qquad (2.82)$$

$$\mathbf{r}(\mathbf{x}) = \mathbf{x} - \mathbf{x}_0 = \boldsymbol{\chi}(\mathbf{X}, t) - \mathbf{x}_0 \qquad (2.83)$$

Analogous to the linear momentum, the axiomatic angular momentum balance is expressed by the material time derivative of the angular momentum, which is equal to the resultant moment $\mathcal{M}(t)$ acting on the closed system:

$$\dot{\mathcal{A}}(t) = \frac{d}{dt} \int_{\Omega} \mathbf{r} \times \rho(\mathbf{x}, t) \, \mathbf{v}(\mathbf{x}, t) \, dv = \frac{d}{dt} \int_{\Omega_0} \mathbf{r} \times \rho_0(\mathbf{X}, t) \, \mathcal{V}(\mathbf{X}, t) \, dV = \mathcal{M}(t) \qquad (2.84)$$

The resultant moment comprises the sum of all moments due to surface tractions and body forces. In Eulerian and Lagrangian descriptions, $\mathcal{M}(t)$ is given by Eqs. 2.85 and 2.86, respectively:

$$\mathcal{M}(t) = \int_{\partial\Omega} \mathbf{r} \times \mathbf{t}(\mathbf{x}, t, \mathbf{n}) \, ds + \int_{\Omega} \mathbf{r} \times \mathbf{b}(\mathbf{x}, t) \, dv \qquad (2.85)$$

$$\mathcal{M}(t) = \int_{\partial\Omega_0} \mathbf{r} \times \mathbf{T}(\mathbf{X}, t, \mathbf{N}) \, dS + \int_{\Omega_0} \mathbf{r} \times \bar{\mathbf{b}}(\mathbf{X}, t) \, dV \qquad (2.86)$$

The symmetry of the Cauchy stress tensor is a consequence of using Cauchy's stress theorem (Eq. 2.51) in Eq. 2.85. After mathematical reformulations, Eq. 2.88 is reached, where $\boldsymbol{\epsilon}$ is the third-order permutation tensor. Due to Cauchy's first equation of motion, the

integrand of the right-hand side of Eq. 2.88 should also be the null vector, leading to the equality of the components $\sigma_{ab} = \sigma_{ba}$. Hence, $\boldsymbol{\sigma} = \boldsymbol{\sigma}^{\mathrm{T}}$.

$$\int_{\partial\Omega} \boldsymbol{r} \times \boldsymbol{\sigma} \cdot \mathbf{n}\, \mathrm{ds} + \int_{\Omega} \boldsymbol{r} \times \mathbf{b}\, \mathrm{dv} = \int_{\Omega} \boldsymbol{r} \times \rho\, \dot{\mathbf{v}}\, \mathrm{dv} \tag{2.87}$$

$$\int_{\Omega} \boldsymbol{r} \times (\rho\, \dot{\mathbf{v}} - \mathbf{b} - \mathrm{div}\, \boldsymbol{\sigma})\, \mathrm{dv} = \int_{\Omega} \boldsymbol{\epsilon} : \boldsymbol{\sigma}^{\mathrm{T}}\, \mathrm{dv} \tag{2.88}$$

$$\boldsymbol{\epsilon} : \boldsymbol{\sigma}^{\mathrm{T}} = \mathbf{0} \implies \epsilon_{abc}\sigma_{cb} = 0 \implies \sigma_{ab} - \sigma_{ba} = 0 \tag{2.89}$$

By comparison with the master balance equation, the physical quantity $\psi = \boldsymbol{r} \times \rho\, \mathbf{v}$ is applied, along with the flux term $\boldsymbol{\Phi} = \boldsymbol{r} \times \boldsymbol{\sigma}$ (or in the form $\boldsymbol{\phi} = \boldsymbol{r} \times \mathbf{t}$) and the source term $\Sigma = \boldsymbol{r} \times \mathbf{b}$. Similarly to the linear momentum balance, the production term is equal to zero.

2.3.4 Balance of Energy

Considering both mechanical and thermal energy, the energy balance of a continuum body states that the rate of change of the total energy is equal to the rate of the external mechanical work $\mathcal{P}_{\mathrm{ext}}(t)$ done on the body in addition to the rate of the thermal work $\mathcal{Q}(t)$. The total energy is given by the sum of the kinetic energy $\mathcal{K}(t)$ and the internal energy $\mathcal{E}(t)$. Thus, the balance of energy is denoted by:

$$\frac{\mathrm{d}}{\mathrm{dt}} \mathcal{K}(t) + \frac{\mathrm{d}}{\mathrm{dt}} \mathcal{E}(t) = \mathcal{P}_{\mathrm{ext}}(t) + \mathcal{Q}(t) \tag{2.90}$$

The kinetic energy $\mathcal{K}(t)$ in spatial description is given by Eq. 2.91. It should be noted that in quasi-static problems, $\frac{\mathrm{d}}{\mathrm{dt}} \mathcal{K}(t) = 0$. The rate of the external mechanical work $\mathcal{P}_{\mathrm{ext}}(t)$, i.e. the power input on a region Ω, is a consequence of the surface tractions and body forces acting on the body, being expressed in spatial coordinates by Eq. 2.92.

$$\mathcal{K}(t) = \int_{\Omega} \frac{1}{2} \rho\, \mathbf{v}^2\, \mathrm{dv} = \int_{\Omega} \frac{1}{2} \rho\, \mathbf{v} \cdot \mathbf{v}\, \mathrm{dv} \tag{2.91}$$

$$\mathcal{P}_{\mathrm{ext}}(t) = \int_{\partial\Omega} \mathbf{t} \cdot \mathbf{v}\, \mathrm{ds} + \int_{\Omega} \mathbf{b} \cdot \mathbf{v}\, \mathrm{dv} \tag{2.92}$$

The internal energy $\mathcal{E}(t)$ of a body in a region is presented in the following, in spatial as well as material coordinates. The internal energy per unit reference volume $e(\mathbf{X}, t)$ is related to the internal energy per unit current volume $e_{\mathrm{c}}(\mathbf{X}, t)$ by the Jacobian determinant as a proportional factor:

$$\mathcal{E}(t) = \int_\Omega e_c(\mathbf{x}, t)\, dv = \int_{\Omega_0} e(\mathbf{X}, t)\, dV \tag{2.93}$$

$$e(\mathbf{X}, t) = J(\mathbf{X}, t)\, e_c(\mathbf{x}, t) \tag{2.94}$$

The rate of the thermal work $\mathcal{Q}(t)$ on a body in a region corresponds to the rate at which heat enters the region across its boundary surface (total heat flux) plus the rate at which heat is generated/destroyed in the region (total heat source). The scalar functions $[Q_N, q_n]$ are the heat fluxes (per unit time and unit volume) and $[R, r]$ are the heat sources (per unit time and unit volume) in the reference and current configurations, respectively. The following equations are valid:

$$\mathcal{Q}(t) = \int_{\partial\Omega} q_n\, ds + \int_\Omega r\, dv = \int_{\partial\Omega_0} Q_N\, dS + \int_{\Omega_0} R\, dV \tag{2.95}$$

$$\int_{\partial\Omega} q_n\, ds = \int_{\partial\Omega_0} Q_N\, dS \tag{2.96}$$

$$\int_\Omega r\, dv = \int_{\Omega_0} R\, dV \tag{2.97}$$

$$R = J\, r \tag{2.98}$$

With Stokes' heat flux theorem, the heat fluxes into the body are taken as linear functions of the outward unit normals to the surface elements (hence the negative signs). Functions $\mathbf{Q}(\mathbf{X}, t)$ and $\mathbf{q}(\mathbf{x}, t)$ are called Piola-Kirchhoff (nominal) and Cauchy (true) heat fluxes, respectively. They are related to one another according to Eq. 2.101:

$$q_n(\mathbf{x}, t, \mathbf{n}) = -\mathbf{q}(\mathbf{x}, t) \cdot \mathbf{n} \tag{2.99}$$

$$Q_n(\mathbf{X}, t, \mathbf{N}) = -\mathbf{Q}(\mathbf{X}, t) \cdot \mathbf{N} \tag{2.100}$$

$$\mathbf{Q} = J\, \mathbf{F}^{-T} \cdot \mathbf{q} \tag{2.101}$$

Rewriting the energy balance explicitly, the First Law of Thermodynamics is obtained. It is given in Eulerian and Lagrangian descriptions, respectively, by:

$$\frac{d}{dt} \int_\Omega \left(\frac{1}{2} \rho\, \mathbf{v}^2 + e_c \right) dv = \int_{\partial\Omega} (\mathbf{t} \cdot \mathbf{v} + q_n)\, ds + \int_\Omega (\mathbf{b} \cdot \mathbf{v} + r)\, dv \tag{2.102}$$

$$\frac{d}{dt} \int_{\Omega_0} \left(\frac{1}{2} \rho_0\, \boldsymbol{\mathcal{V}}^2 + e \right) dV = \int_{\partial\Omega_0} (\mathbf{T} \cdot \boldsymbol{\mathcal{V}} + Q_n)\, dS + \int_{\Omega_0} (\bar{\mathbf{b}} \cdot \boldsymbol{\mathcal{V}} + R)\, dV \tag{2.103}$$

According to the master balance, the energy balance assumes the physical quantity $\psi = \frac{1}{2} \rho\, \mathbf{v}^2 + e_c$, the flux term is $\phi = \mathbf{t} \cdot \mathbf{v} + q_n$, the source term is given by $\Sigma = \mathbf{b} \cdot \mathbf{v} + r$ and the production term is $\widehat{\psi} = 0$.

By developing Eqs. 2.102 and 2.103, with the help of algebraic operations of vectors and tensors, the divergence theorem and Cauchy's first equation of motion, the balance of energy can be obtained. The reduced global form of the balance of energy, which considers the balance of thermal energy, is commonly used. This form is in Eqs. 2.104 and 2.105 in material and spatial descriptions, respectively. Since the reference volume is independent of time, the derivative of the integral equals the integral of the derivative of the integrand, giving the material local form of this balance as in Eq. 2.106. The spatial local form of the balance of energy, after some mathematical reformulations, is expressed as in Eq. 2.107.

$$\frac{d}{dt} \int_{\Omega_0} e \, dV = \int_{\Omega_0} (\mathbf{P} : \dot{\mathbf{F}} - \text{Div} \, \mathbf{Q} + R) \, dV \tag{2.104}$$

$$\frac{d}{dt} \int_{\Omega} e_c \, dv = \int_{\Omega} (\boldsymbol{\sigma} : \mathbf{D} - \text{div} \, \mathbf{q} + r) \, dv \tag{2.105}$$

$$\dot{e} = \mathbf{P} : \dot{\mathbf{F}} - \text{Div} \, \mathbf{Q} + R \quad \text{or} \quad \dot{e} = \mathbf{S} : \dot{\mathbf{E}} - \text{Div} \, \mathbf{Q} + R \tag{2.106}$$

$$\dot{e}_c + e_c \, \text{div} \, \mathbf{v} = \boldsymbol{\sigma} : \mathbf{D} - \text{div} \, \mathbf{q} + r \tag{2.107}$$

2.3.5 Entropy Inequality Principle

Although the First Law of Thermodynamics governs the energy transfer within a thermodynamic process, the same cannot be said regarding the direction of this energy transfer. For this reason, the concept of entropy is introduced. Entropy is a physical property that measures the degree of molecular disorder, randomness or uncertainty of a system. The entropy $\mathcal{S}(t)$ of a continuum body occupying a region is given by:

$$\mathcal{S}(t) = \int_{\Omega} s_c(\mathbf{x}, t) \, dv = \int_{\Omega_0} s(\mathbf{X}, t) \, dV \tag{2.108}$$

where s and s_c are the entropy per unit volume in the reference and current configurations, respectively. They are related to one another by the Jacobian determinant according to:

$$s(\mathbf{X}, t) = J(\mathbf{X}, t) \, s_c(\mathbf{x}, t) \tag{2.109}$$

Entropy can also enter a region. The rate of the entropy input $\tilde{Q}(t)$ into the region is expressed by the equation below. Variables $\mathbf{H}(\mathbf{X}, t)$ and $\mathbf{h}(\mathbf{x}, t)$ are time-dependent vector fields, called Piola-Kirchhoff (nominal) and Cauchy (true) entropy fluxes per unit area in material and spatial descriptions, respectively. Their respective integrals hold a negative sign since the input is computed by considering the outward normal vector to the surface. The time-dependent scalar fields $\tilde{R}$ and $\tilde{r}$ are the material and spatial entropy sources per unit time and unit volume, respectively, whose integrals account for the total entropy source for the region volume.

$$\tilde{Q}(t) = -\int_{\partial\Omega} \mathbf{h}(\mathbf{x}, t) \cdot \mathbf{n} \, ds + \int_{\Omega} \tilde{r}(\mathbf{x}, t) \, dv$$

$$= -\int_{\partial\Omega_0} \mathbf{H}(\mathbf{X}, t) \cdot \mathbf{N} \, dS + \int_{\Omega_0} \tilde{R}(\mathbf{X}, t) \, dV \tag{2.110}$$

The Second Law of Thermodynamics states that the entropy of a system must not decrease for spontaneous processes, and is responsible for the direction of the associated energy transfer. Taking $\Gamma(t)$ as the total production of entropy per unit time, this is defined as the difference between the rate of entropy change of a body and the rate of entropy input into it. $\Gamma(t)$ should be non-negative, which expresses the second law of thermodynamics as:

$$\Gamma(t) = \dot{S}(t) - \tilde{Q}(t) \geq 0 \tag{2.111}$$

As it is an inequality rather than an equation, the second law of thermodynamics is also called Entropy Inequality Principle. In fact, it is not a balance principle, unlike mass or energy, since entropy is not conserved ($\Gamma(t) \geq 0$). For reversible thermodynamic processes, there is no production of entropy, hence $\Gamma(t) = 0$ (equilibrium thermodynamics). In non-equilibrium thermodynamics (irreversible processes), entropy is produced, then $\Gamma(t) > 0$. In global spatial form and taking $\hat{s}$ as the spatial production of entropy per unit volume, one finds the total production of entropy per unit time as:

$$\Gamma(t) = \int_{\Omega} \hat{s} \, dv = \frac{d}{dt} \int_{\Omega} s_c \, dv + \int_{\partial\Omega} \mathbf{h} \cdot \mathbf{n} \, ds - \int_{\Omega} \tilde{r} \, dv \geq 0 \tag{2.112}$$

Considering the equation above and comparing it to the master balance from Eq. 2.63, the second law of thermodynamics provides the function $\psi = s_c$, the flux term $\phi = -\mathbf{h} \cdot \mathbf{n}$, the source term $\Sigma = \tilde{r}$ and the production term $\widehat{\psi} = \hat{s}$.

By considering the absolute temperature Θ (in Kelvin units), the rate of entropy input variables can often be related to the heat flux and source variables as:

$$\mathbf{h} = \frac{\boldsymbol{q}}{\Theta} \ , \quad \boldsymbol{H} = \frac{\boldsymbol{Q}}{\Theta} \ , \quad \tilde{r} = \frac{r}{\Theta} \ , \quad \tilde{R} = \frac{R}{\Theta} \tag{2.113}$$

Rewriting the total production of entropy, one obtains the Clausius-Duhem Inequality in spatial and material descriptions, respectively. This inequality ensures the thermodynamic consistency of material models:

$$\Gamma(t) = \frac{d}{dt} \int_{\Omega} s_c \, dv + \int_{\partial\Omega} \frac{\boldsymbol{q}}{\Theta} \cdot \mathbf{n} \, ds - \int_{\Omega} \frac{r}{\Theta} \, dv \geq 0 \tag{2.114}$$

$$\Gamma(t) = \frac{d}{dt} \int_{\Omega_0} s \, dV + \int_{\partial\Omega_0} \frac{\boldsymbol{Q}}{\Theta} \cdot \mathbf{N} \, dS - \int_{\Omega_0} \frac{R}{\Theta} \, dV \geq 0 \tag{2.115}$$

After mathematical reformulations, the local form in the material description is written as in Eq. 2.116. Eliminating R with the help of Eq. 2.106, an alternative version is given by Eq. 2.117.

$$\dot{s} - \frac{R}{\Theta} + \frac{1}{\Theta} \operatorname{Div} \mathbf{Q} - \frac{1}{\Theta^2} \mathbf{Q} \cdot \operatorname{Grad} \Theta \geq 0 \tag{2.116}$$

$$\mathbf{P} : \dot{\mathbf{F}} - \dot{e} + \Theta \dot{s} - \frac{1}{\Theta} \mathbf{Q} \cdot \operatorname{Grad} \Theta \geq 0 \tag{2.117}$$

The last term on the left side of Eq. 2.117 (including the negative sign) represents the entropy production by heat conduction. This must be non-negative, as heat flows from warmer to colder regions. The absolute temperature is taken into account, i.e. $\Theta \geq 0$. Hence, the expression $\mathbf{Q} \cdot \operatorname{Grad} \Theta \leq 0$ is valid and affirms that the heat flows against a temperature gradient.

The second law of thermodynamics can also be expressed with the help of the Clausius-Planck Inequality. This inequality calls $\mathcal{D}_{\mathrm{int}}$ as the local production of entropy (or internal dissipation), given by Eq. 2.118. The local form of the balance of energy from Eq. 2.106 can be then written in terms of entropy rate and production, as shown in Eq. 2.119:

$$\mathcal{D}_{\mathrm{int}} = \mathbf{P} : \dot{\mathbf{F}} - \dot{e} + \Theta \dot{s} \geq 0 \tag{2.118}$$

$$\Theta \dot{s} = -\operatorname{Div} \mathbf{Q} + \mathcal{D}_{\mathrm{int}} + R \tag{2.119}$$

In material modelling, it is appropriate to work with a strain energy function, which combines internal energy and entropy. The Helmholtz free energy (or simply free energy; per unit volume) function Ψ is defined in the reference configuration as:

$$\Psi = e + \Theta s \tag{2.120}$$

Taking the material time derivative of the free energy $\dot{\Psi}$, the Clausius-Planck inequality can be rewritten as:

$$\mathcal{D}_{\mathrm{int}} = \mathbf{P} : \dot{\mathbf{F}} - \dot{\Psi} + s \dot{\Theta} \geq 0 \tag{2.121}$$

The free energy function is fundamental for material modelling. Constitutive equations, which are relations between thermodynamic or mechanical variables of a system, are mathematical models that describe the material behaviour by generally considering specific free energy functions. The free energy is expressed in terms of process (e.g. deformation gradient and temperature) and internal (e.g. computing viscosity or damage phenomena) variables.

For the modelling of the stress-strain behaviour of elastomers, for instance, several hyperelastic constitutive models have been developed. In the case of isotropic elastomers, the free energy is usually expressed in terms of the principal invariants II_i of the (right or left) Cauchy-Green strain tensor, or of the principal stretches λ_i of the characteristic polynomial equation of the deformation gradient (Bakir et al., 2021):

$$\Psi = \Psi(\mathrm{II}_1, \mathrm{II}_2, \mathrm{II}_3) = \Psi(\lambda_1, \lambda_2, \lambda_3) \tag{2.122}$$

$$II_1 = \text{tr}\,(\mathbf{C}) \tag{2.123}$$

$$II_2 = \frac{1}{2}\left(\text{tr}(\mathbf{C})^2 - \text{tr}(\mathbf{C}^2)\right) \tag{2.124}$$

$$II_3 = \det(\mathbf{C}) = (\det(\mathbf{F}))^2 \tag{2.125}$$

In the literature, one can find works with several constitutive models. The choice of the models is conditioned to the individual prediction accuracies to experimental data, as well as the assumptions of each model. Examples of hyperelastic constitutive models are the Neo-Hookean (Treloar, 1943a and 1943b), the Mooney-Rivlin (Mooney, 1940; Rivlin, 1948), the Valanis and Landel (Valanis and Landel, 1967) and the Ogden (Ogden and Hill, 1972) models. More recent models include the Van der Waals (Kilian, 1981; Kilian et al., 1986), the Yeoh (Yeoh, 1990) and the Arruda-Boyce (Arruda and Boyce, 1993) models. Since constitutive modelling is out of the scope of this thesis, although relevant for future works, these models are cited here without further discussions.

3. Fundamentals of Polymer Materials

Polymers are a class of materials characterised by a macromolecular structure. The macromolecules are composed of several monomeric units covalently bonded. Broadly found in everyday life, polymers can be either natural (e.g. silk, cellulose, natural rubber) or synthetic (e.g. nylon, polyvinyl chloride, silicone), as well as organic or inorganic. The monomers' chemical reaction to form long polymer chains, called polymerisation, produces a material with specific properties. Generally, polymers exhibit toughness, high strength-to-weight ratio, resistance to corrosion as well as electrical and thermal insulation (Brinson and Brinson, 2008; Askeland et al., 2011), among other useful properties, as a result of their molecular structure.

There are several classifications of polymers. Some consider their origin (natural or synthetic), others consider their structure (linear, branched chains or cross-linked), the polymerisation mechanism (addition or condensation) or the thermomechanical response (thermoplastics, thermosets or elastomers). The glass transition temperature, named Tg, is also an important parameter for the identification of the material state and its categorisation. Tg measures the ability of the molecules to move; the more difficult their movement, the higher the Tg. Glass transition is a second-order transition from glassy state to rubbery state, in which there are changes in some physical properties including elastic properties (Treloar, 1975; Roland, 2013). Considering the concept of Tg as well, the thermomechanical response classification is briefly reviewed in this chapter. A subsequent focus on elastomers is introduced, comprising silicone rubbers, thermoplastic elastomers and photopolymeric elastomers. The last subsection discusses the mechanical behaviour of elastic materials.

3.1 Thermoplastics

Thermoplastics are linear or branched structures with long, non-cross-linked molecular chains. Common examples include: polylactic acid (PLA), polycarbonate (PC), acrylonitrile butadiene styrene (ABS) and nylon. Upon heating, they soften and melt, while on cooling they reharden, in reversible processes as long as there is no thermal degradation. This behaviour particularly allows their use in processing techniques such as injection moulding and extrusion. Since intermolecular bonds are secondary, and not as strong as intramolecular ones, the increase in temperature weakens these secondary bonds. This promotes the relative movement of adjacent chains with the application of stress (Callister, 2000).

They can be either crystalline or amorphous, according to the presence of an orderly or a random arrangement of the molecules after cooling, respectively (Riande et al., 2000; Harper, 2002). Furthermore, crystalline polymers (or crystalline regions in a semi-crystalline polymer) have a sharp melting point; amorphous polymers do not. Taking into consideration the glass transition temperature (Tg), thermoplastics are used in a temperature range below Tg. The material has an energy-elastic behaviour, acting in a glass-like brittle mode (glassy state). Between Tg and the melting temperature, thermoplastics have a soft and rubber-like behaviour (rubbery state); for temperatures above melting, they behave as a viscous liquid (flow state). All thermoplastics are capable of existing in any of these three states with temperature changes Brinson and Brinson (2008).

3.2 Thermosets

Thermosetting materials, unlike thermoplastics, have a three-dimensional, cross-linked network, with covalent bonds between all molecules. For that reason, once chemically reacted and cross-linked by the process of curing, the material becomes solid and does not remelt upon heating. An increase in temperature will eventually lead to a degradation of the thermoset, characterising an irreversible process. Phenolic and epoxy resins are typical examples of thermosets.

The cross-linking density of polymer chains in thermosets is high, which considerably restricts chain motions. The material stiffness increases with increasing degrees of cross-linking (Riande et al., 2000). As the chemical bonds hinder a regular arrangement of the chains, thermosets are amorphous (Rösler et al., 2007). In addition, they typically exist only in the glassy state, as the Tg is above the decomposition temperature. Therefore, thermosetting materials are especially beneficial in applications that require dimensional and thermal stability (Brinson and Brinson, 2008).

3.3 Elastomers

Similar to thermosets, elastomers are chemically cross-linked polymers, although with substantially lower cross-linking density. The polymerisation process is called vulcanisation. The term vulcanisation is often used when dealing with the hardening of natural rubber with the addition of sulphur; nevertheless, it may consist of the curing of elastomers in general, whose definition will be used in this work. The orderly arrangement of the molecular chains is prevented by the cross-links. Consequently, regular elastomers are amorphous (Rösler et al., 2007), even though some of them may undergo crystallisation when maintained at low temperatures or by stretching (Treloar, 1975; Toki et al., 2000). Elastomers can be easily deformed to large elongations (up to five to ten times its unstretched length) when subjected to low stress due to the rearrangement of the long polymer chains. Furthermore, they have the ability to rapidly return to their original size

once the stress is released (Flory, 1953; Riande et al., 2000; Mark and Erman, 2007; Gent, 2013).

The operating temperature range of elastomers is above their glass transition. Hence, the material remains in the rubbery state. This allows the necessary internal mobility for the molecular rearrangements when deformation takes place, characterising the entropy-elastic behaviour. Thus, glass transition temperatures of elastomeric materials must be low. For instance, natural rubber has a Tg around -70°C in the unvulcanised state, and a few degrees higher in the vulcanised state (Treloar, 1975). Below Tg (glassy state), elastomers are brittle and exhibit an energy-elastic behaviour, determined by the lowest energy state of the polymer chains interaction forces. Figure 3.1 illustrates the behaviour of their elastic modulus over the temperature, as well as those of thermoplastics and thermosets.
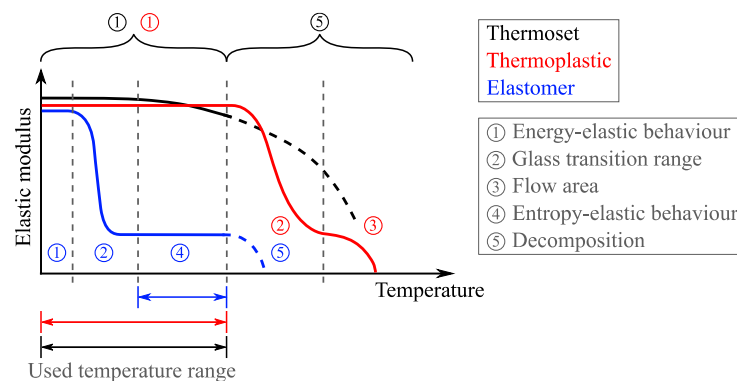
Figure 3.1: Evolution of elastic modulus of polymers over temperature.

The mechanical properties of elastomers can be improved by adding components to the mixture when preparing the material. Some of these include fillers for greater dimensional stability and stiffness (e.g. carbon black), plasticisers for better flowability of the unvulcanised elastomer mixture and for the distribution of the fillers, stabilisers for protection against oxidation and ozone, and vulcanisation components (e.g. sulphur, activators, catalysts). Elastomers can be formulated and/or modified for property optimisation according to the service application or set of performance requirements. Further discussion on this subject can be found in the work of Rodgers and Waddell (2013). Although undesirable in large quantities, small amounts of crystallinity may be beneficial. Crystallites can act as reinforcing agents, and thus substantially increase several failure properties such as toughness (Mark and Erman, 2007; Roland, 2013).

Among elastomers, there are natural and synthetic rubbers. Natural rubber (NR) is widely used in the automotive industry, particularly in tires, being generally vulcanised with sulphur as a cross-linking agent. This enables good resilience and high tensile strength, which is one of their greatest advantages. In addition, they exhibit a low compression set, resistance to wear and tear, and good electrical properties, with a Tg in the range of -70°C (Riande et al., 2000; Harper, 2002). Synthetic rubbers include styrene-butadiene rubber (SBR), acrylonitrile-butadiene rubber (NBR), butyl rubber, polybutadiene (BR), ethylene-propylene-diene monomer (EPDM), polychloroprene (neoprene) and silicone rubber (SiR), to mention a few. Table 3.1 summarises some characteristics associated to them.

It can be noted that there is a wide range of properties regarding the elastomeric material options. The applications limit the type of rubber to be used, as well as promoting the

development of improved or new materials to fulfil the operational requirements. Better performance and costs are some examples of driving factors. More recently, with the advent of Additive Manufacturing (AM), the working principle of the printing machines demands a material with a specific thermomechanical response (thermoset or thermoplastic) and a specific nature (e.g. filament, liquid, powder). The following subsections introduce the main elastomeric alternatives available for AM, while AM is presented in more detail in Chapter 4. Further discussions for polymers in general and rubber elasticity theory can be found in the works of Flory, (1953), Treloar (1975), Riande et al. (2000), Harper (2002), Mark and Erman (2007) and Gent (2013).

Table 3.1: Characteristics of conventional synthetic elastomers.

Elastomer	Characteristics
SBR	Most synthetic elastomer widely used [a]
	Greater hardness and toughness than NR [b]
	High tendency toward hysteresis in load-unload cycles [b]
NBR	Poor resilience at low temperatures [a]
	Resistance to oil absorption [a,c]
	No tendency to swell in contact with petroleum [b]
	Poor cold flex properties [c]
Butyl rubber	Low gas permeability [a,c]
	Low water absorption [c]
	Good heat, oxygen and ozone resistance [c]
BR	Highly resilient over a wide temperature range [a]
	Largest consumption of elastomers together with NR and SBR [c]
EPDM	Good resistance to ozone and oxidation [b,c]
	Moisture resistance [c]
Neoprene	Resistance to degradation superior to NR [a]
	Low flammability [a,b]
	Low oil absorption [a,c]
	High mechanical strength [b]
SiR	Highly resilient over a wide temperature range [a]
	Resistance to chemical degradation [a,b]
	Operating temperature range from -100°C to 300°C [a,b]
	Resistance to oxidation [b]
	Dielectric properties [b]
	High cost [b]
	Moderate mechanical strength at room temperature [b]

[a] Treloar, 1975; [b] Riande et al., 2000; [c] Rodgers and Waddell, 2013.

3.3.1 Silicone Rubbers

Silicones, also known as polysiloxanes, are a class of inorganic polymers, whose main chain is composed of a silicon-oxygen backbone linked to organic side groups (Treloar, 1975; Riande et al., 2000). Silicone properties can range from liquids to hard plastics depending on the side groups, the silicon-oxygen chain length and the degree of cross-linking. Silicones are especially used in medicine due to their biocompatibility and biodurability. Furthermore, silicones possess chemical stability and are unreactive (Hill, 2005; Hacker et al., 2019). Besides medical applications, silicones are used in sealants, coatings and adhesives. According to Noll (1968), silicones are divided from a

technological point of view into silicone oils, silicone resins and silicone rubbers. The latter is considered hereafter.

Some of the particular properties exhibited by silicone rubbers were already presented in Table 3.1. The thermal stability is a result of the strength of the silicon-oxygen bond, allowing them to be used in high-temperature applications (Mark et al., 2015). They are heat resistant up to 300°C (for a short time). Their flexibility is maintained at low temperatures in view of glass transition temperatures in the range of -120°C and stiffening (i.e. crystallisation) temperatures between -70°C and -50°C, depending on the material formulation. Consequently, silicone rubbers have a broad range of service temperatures (Noll, 1968). In addition, SiRs are hydrophobic due to the lack of polar groups in their structure, showing low moisture uptake (Hill, 2005), and present low surface tension (Hacker et al., 2019). Their resistance to oxygen, ozone and ultraviolet (UV) radiation, as well as their high permeability to gases and water vapour, are other characteristics of silicone rubbers, which can assume varying degrees of hardness (Butts et al., 2000). Regarding the tensile strength at room temperature, SiRs exhibit lower values than most organic elastomers (Noll, 1968).

Silicone rubbers are thermosets, i.e. the polymeric chains are chemically (and irreversibly) bonded. Two common types of SiRs are room temperature vulcanising silicones and liquid silicone rubbers (LSRs). The first consists of a one-component silicone that cures with atmospheric moisture, in which the vulcanisation rate depends on temperature and humidity. Hence, for low moisture environments, the curing process takes a longer time (in terms of days), which can be a major disadvantage. In contrast, LSR is a two-component system in which the components are mixed together and heated, while a catalyst present in the mixture starts the cross-linking process. They can show tensile strengths as high as 9.7 MPa and ultimate elongations of 500-775% (Butts et al., 2000; Harper, 2002). Benzoyl peroxide and platinum catalysts are commonly used (Hill, 2005), added to one of the components. The two components (Part A and Part B) are typically mixed in a ratio of 1:1 to 9:1 and both are composed minimally of polydimethylsiloxanes with vinyl groups. The use of fillers and additives contribute to the achievement of the final properties (Fink, 2019).

A recent technology developed by Wacker Chemie AG specifically for use in a 3D printing process involves the layer-by-layer deposition of droplets of high viscosity curable silicone by spatially controllable nozzles onto a substrate. The silicone is curable by spatially controllable electromagnetic radiation, induced either thermally or/and by UV (ultraviolet) or VIS (visible) light. Silicone is a one-component or multi-component system of moderate-to-high viscosity and contains platinum catalysts that are largely inert in the absence of light at room temperature. Further associated information can be found briefly in Fink (2019) and more extensively in the respective U.S. Patent No. 10,471,653 (Selbertinger et al., 2019).

3.3.2 Thermoplastic Elastomers

Thermoplastic elastomers (TPEs) have been in the market since the early 1960s and can be found in applications in the automobile industry (e.g. bearings, panelling, exterior bumpers), general industry (e.g. hoses, gears), healthcare and medical sector (e.g. angioplasty devices) as well as in sporting products (e.g. shoe soles, golf ball covers). Instead of the chemical cross-linking typical of conventional elastomers, TPE networks connect the polymer chains by means of physical cross-links. As a rule, these links are thermo-reversible. Therefore, TPEs can be processed as a standard thermoplastic when heated while exhibiting an elastic behaviour when cooled down, which is their greatest advantage over conventional vulcanised elastomers. However, this advantage may become a drawback, which limits the service temperature range and leads to poor chemical and temperature resistance, unlike the thermoset rubbers. Additionally, the TPEs available are limited in terms of low hardness, usually ranging above 50 Shore A (Riande et al., 2000; Grady et al., 2013; Drobny, 2014).

In order to be classified as a TPE, the polymer must meet the following three requirements (Grady et al., 2013):

- be stretched to moderate elongations and return to something close to its original shape upon the removal of stress;
- be processable as a melt at high temperatures; and
- show an absence of significant creep.

The unique behaviour of TPEs is a consequence of their structure. They consist of a biphasic structure: "soft" segments comprise the elastomeric matrix that are physically cross-linked by "hard" segments disperse within the matrix. The soft phase is responsible for the flexibility and elasticity; the hard phase, for the strength. Furthermore, the hard phase of several TPEs is crystalline (Roland, 2013), which is the driving force for the phase separation. The hard-to-soft segments ratio is one of the main factors that contribute to the wide range of material properties (Grady et al., 2013). The higher the hard segment content, the higher the hardness, tensile modulus and tear strength, for instance (Drobny, 2014). The higher the soft segment content, the more elastic the material becomes.

In terms of general properties of TPEs, they exhibit high tensile stress and elongation at break, i.e. high toughness. After stretching to high elongations and releasing the stress, permanent deformation (set) is usual. In addition, TPEs frequently display the Mullins effect, which may lead to undesired heat build-up in the material (Grady et al., 2013).

TPEs are generally copolymers that should operate in temperatures between the glass transition of the soft phase and the glass transition (when amorphous) or melting temperature, T_m, (when crystalline) of the hard phase (see Figure 3.2). Below the T_g of the soft phase, the TPE becomes brittle; the T_g or T_m of the hard phase dictates the softening point of the material, in which creep, permanent elongation and loss of mechanical properties are observed (Riande et al., 2000).
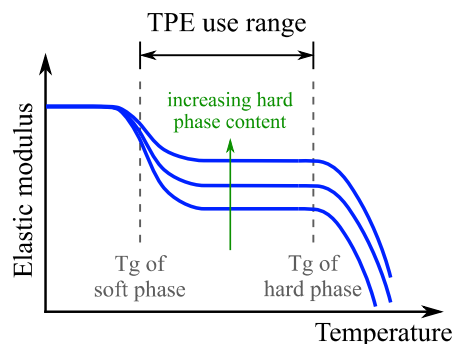
Figure 3.2: Evolution of elastic modulus of TPEs over temperature with increasing hard segment content.

According to the German Standard DIN EN ISO 18064:2022 (DIN, 2022), commercial TPEs are categorised as TPS (thermoplastic polystyrene elastomer), TPO (thermoplastic polyolefin elastomer), TPV (thermoplastic vulcanisate), TPC (thermoplastic copolyester), TPU (thermoplastic polyurethane), TPA (thermoplastic polyamide) and TPZ (unclassified thermoplastic elastomers that do not fall into the previous categories). The main characteristics of those categories, except for the latter, are summarised in Table 3.2.

TPSs were the first introduced in the market and are the most widely consumed TPEs. TPOs follow after in demand, and the TPVs are a modification of the TPOs. TPCs, TPUs and TPAs are considered TPEs for engineering. They were developed later, are more expensive but have better performance regarding to e.g. oil resistance, service temperature and flexibility at low temperatures (Riande et al., 2000; Grady et al., 2013).

Focusing on TPUs, some relevant aspects are noteworthy. Polyester-based TPUs are hydrophilic due to the ester components, which can be attacked by water. Nevertheless, the increase in the hardness of the TPU reduces the hydrophilic nature of the polymer due to a higher content of the hydrophobic hard segments. Furthermore, depending on the hard segment selection, the hard phase can be either crystalline (e.g. MDI) or amorphous (e.g. TDI) (Grady et al., 2013). According to Drobny (2014), most TPUs can be used at temperatures between -40°C and 80°C in the long term and up to 120°C in the short term, where the hard segment content is one of the contributing factors to a higher service temperature. The author also mentions the effect of thermal degradation starting to occur in ranges between 150°C and 200°C and taking place more measurably at 200°C to 250°C. Also stated by the author is discoloration (yellowing) and loss of mechanical properties of TPUs based on aromatic isocyanates on exposure to sunlight.

Table 3.2: Characteristics of thermoplastic elastomers.

TPE Type	Structure	Advantages | Disadvantages
TPS	SBS, SIS or SEBS (at least triblock) copolymers Soft phase: butadiene | isoprene | ethylene-butylene Hard phase: styrene	Low tolerance to moderately high service temperatures[a] Very good performance at low temperatures[a] Tendency to oxidation[a]
TPO	Blend of a crystalline oleofin (e.g. polypropylene) and a conventional rubber with little to no cross-linking (e.g. EPDM)	Broad range of hardness, modulus and tensile strength coverage[a] Lack of recovery capability[a] Low resilience (esp. at high temperatures)[a] Flexibility at low temperatures until nearly -50°C[a]
TPV	Blend of a thermoplastic and a conventional rubber (e.g. EPDM) with curing additives Small elastomeric phase is chemically cross-linked during mixing (dynamic vulcanisation) Isolated rubber phase	Elastic properties superior to those of TPOs[a] Better resistance to oils and solvents than TPOs[a] Higher performance and costs for polyester + silicone and polyamide + polyethylene acrylate blends[b]
TPC	Block polymer of alternating hard and soft segments Hard phase (crystalline): aromatic polyester Soft phase: polyether and/or polyester	Wide range of hardness coverage[a] Flexibility at low temperatures[a] Subject to hydrolysis above 60°C[a] Oil resistance[b] Stable to higher temperatures[b] Subject to oxidation[b]
TPU	Block polymer of alternating hard and soft segments Hard phase: aromatic rings with urethane groups Soft phase: ether, ester and/or carbonate linkages	Generally expensive[b] High performance applications[b] Subject to oxidation[b] Sensitivity to water/moisture[c] High tensile strength and elongation at break[c] Resistance to tear and abrasion[c]
TPA	Block polymer of alternating hard and soft segments Hard phase (crystalline): polyamide Soft phase: polyether and/or polyester	Flexibility at low temperatures down to -40°C[a] Low chemical permeability[b] Good properties at low temperatures[b] Subject to oxidation[b] Sensitivity to water/moisture[b]

[a] Riande et al. (2000); [b] Grady et al. (2013); [c] Drobny (2014)

3.3.3 Photopolymeric Elastomers

Photopolymers (often simply referred to as resins) are light-sensitive thermosetting polymer materials, commonly based on acrylics, polyamides, epoxies and polyisoprene, to mention a few. With the application of electromagnetic radiation, usually UV, VIS or IR (infrared), they undergo the process of curing. They are frequently commercialised in the liquid state. Peiffer (1997) mentions the first synthetic photopolymer materials being developed by Eastman Kodak Company (Rochester, USA), while Joseph et al. (2022) cite the discovery of photopolymers as a holographic recording material in the late 1960s.

Photopolymer components include monomers, oligomers and photoinitiators. The initiators convert the irradiated light energy into chemical energy, generating reactive species for the outset of the cross-linking. These polymerisation reactions occur by radical or cationic initiation (Pagac et al. (2021). The reactions can be temporally controlled, as turning the light source on and off respectively starts and stops the processes (Shaukat et al. (2022). According to the chemical and physical processes used, the light initiated reactions can be classified into five categories: photopolymerisation, photocrosslinking, photomolecular reactions, photodegradation and photo/thermal reactions (Peiffer, 1997). The chemistry involved is outside of the scope of this manuscript, and can be seen in depth in the works of Nakamura (2015), Bagheri and Jin (2019) and Shaukat et al. (2022).

Some of the most well-known applications of photopolymers are in the dental and medical sectors for restoration of teeth, prostheses and contact lenses, for instance. In imaging applications, one can find the production of UV or electro-beam curable printing inks, which offer faster printing speeds due to rapid curing. Liquid Crystal Displays and holographic materials and devices are examples of applications in optical engineering. Photopolymers are also used in the printing of plates for lithography and gravure purposes. Electronic micro devices are equally produced with photopolymers. Additionally, they can be applied in sealants, adhesives and coatings (Peiffer, 1997; Nakamura, 2015). On the downside, the applications of photopolymers normally are highly specialised. Furthermore, photopolymers may not particularly show the strength or durability of injection-moulded materials, being prone to creeping after long-term heavy loads (Fast Radius, 2020).

3D printing is currently the fastest growing market for photopolymers, where prototypes or final parts are fabricated by technologies such as stereolithography. Commercial AM resins are based on epoxides and acrylates (Izdebska-Podsiadły, 2022). Material development is driven by the limited range of available materials suitable for 3D printing and their inferior mechanical performance, as well as concerns regarding biocompatibility and general safety (Joseph et al., 2022). The specific requirements of the desired application assist in the selection of a suitable existing material or the development of a new one (Fast Radius, 2020).

Two types of classifications for photopolymer resins are available in the literature. The first combines the materials according to the curing method into three groups (Izdebska-Podsiadły, 2022):

- UV laser resin: polymerisation carried out by a UV laser;
- UV DLP resin: polymerisation carried out by a Digital Light Processing (DLP) projector; and
- Daylight resin: polymerisation carried out by light of wavelength of 460 nm.

The photopolymers display different mechanical and chemical properties after curing. Therefore, the second classification considers the type and application of the photopolymer and gathers them into the following resins: standard; structural (or industrial); flexible and elastic; durable and tough; ceramic and castable wax; biocompatible; and bioink (Pagac et al., 2021; Izdebska-Podsiadły, 2022).

The subsequent discussion is focused only on flexible and elastic resins, as they are the point of interest of this thesis. 3D printing companies are constantly developing and

offering new resins. In this scenario, flexible and elastic resins are not as numerous as stiff resins. In general, flexible resins are suitable for components designed to absorb compressive forces (Izdebska-Podsiadły, 2022). Additionally, the material catalogue for flexible resins, which are stiffer than elastomers, is typically more extensive than that of elastic resins.

Examples of this class of photopolymers comprise elastomeric polyurethane (EPU) and flexible polyurethane (FPU) resins. They were developed by Carbon® (Redwood City, USA), an American 3D printing company specialised in Vat Photopolymerisation. EPU is a group of highly elastic and flexible resins that behave elastically over a wide range of temperatures while keeping high flexibility. Applications include sports footwear, orthotic and prosthetic devices (Pagac et al., 2021). The EPU 40 material has a hardness of 68 Shore A, a glass transition temperature of 10°C, an ultimate stress of almost 8 MPa and 300% of elongation at break, according to Carbon®'s website. Its main advantages are high elasticity, tear resistance and energy damping capacities (Carbon, 2022a). FPU is a semi-rigid material exhibiting high resistance to impact, abrasion and fatigue. It is indicated for applications with repetitive stresses such as living hinges. However, its stress-strain curve shows some yielding, indicating greater plastic deformation, unlike conventional elastomers. For this resin, the value provided by Carbon® for ultimate stress is 25 MPa and for the elongation at break, 200% (Carbon, 2022b).

Other types of flexible and elastic resins can be found in the market. The flexible and elastic resin family produced by the American company Formlabs (Somerville, USA) consists of the Flexible 80A and Elastic 50A materials. The first has a hardness of 80 Shore A and is recommended for hard flexible prototypes, simulating rubber or TPU flexibility. It can withstand bending, flexing, and compressing, also considering repeated cycles. Flexible 80A has tensile strengths of 3.7 MPa and 8.9 MPa, and elongations at break of 100% and 120% for the resin without and with post-curing at 60°C for 10 min, respectively. Elastic 50A is the company's softest resin and has a 50 Shore A hardness. It is appropriate for prototyping parts commonly produced with silicone. This resin has the ability of bending, stretching, compressing and withstanding repeated cycles without tearing, as well as returning quickly to its original shape. The ultimate stress and elongation values for the resin without post-treatment are 1.61 MPa and 100%, while the ones for the post-cured resin (60°C for 20 min) are 3.23 MPa and 160% (Formlabs, 2022a). Other notable materials include the Agilus and Tango families from the American-Israeli company Stratasys® (Rehovot, Israel) (Stratasys, 2022a, 2022b), which are further discussed in Chapter 5.

Distinct values for the tensile behaviour are observed for photopolymeric elastomers. In fact, this is a consequence not only of the formulation of the material itself but also of the different manufacturing technologies employed from Carbon and Formlabs and their associated printing parameters. These are variables that interfere directly on the mechanical properties of the final products. In addition, photopolymeric elastomers do not show elongations as high as silicones and TPUs; nevertheless, material development in the area is intensive, and new material options appear every day.

3.4 Mechanical Behaviour of Elastomers

Whether thermosetting, thermoplastic or photopolymeric, elastomers exhibit particular material characteristics, some of which were already mentioned in the previous section (e.g. high elasticity, abrasion resistance and dampening properties). The material behaviour is dependent on several factors, such as polymer type, molecular weight and deformation history. temperature and rates (Harper, 2002). This section aims to briefly address the elasticity of elastomers in general and their stress-strain response. A discussion on viscoelasticity follows next, covering the notions of hysteresis, linear viscoelastic models and dynamic viscoelastic properties. Lastly, a review of the Mullins and Payne effects is provided.

3.4.1 Elasticity

Elasticity is defined as the ability of a material submitted to a deformation process to return to its original shape once the load is removed. Elastomers are elastic. All the more, they can be largely stretched, characterising their remarkable, hyperelastic behaviour. This is an effect of the entropic elasticity, typical of rubber-like materials. Entropic elastic materials have the property of null or small change in internal energy with deformation (Holzapfel, 2000). When the material is stretched, the randomly oriented, tangled polymeric chains become aligned in a specific direction. The degree of disorder of the system is decreased, i.e. its entropy decreases. After releasing the external load, the chains go back to the disordered state, increasing the system's entropy back again (Callister, 2000).

A typical stress-strain curve of an elastomer can be seen in Figure 3.3. The non-linear behaviour of the curve can be noted. In the low deformation region (up to approximately 1%), the stress is linear to the strain, i.e. the material has a Hookean behaviour. The high deformation region is marked by the entropic elasticity, underlining the non-linearity of the curve (Riande et al., 2000). For natural rubber without reinforcing fillers, Flory (1953) associates the sharp rise in slope to the strain-induced crystallisation. This induces the formation of a fibre-like oriented crystalline structure and, hence, the increase in the local stiffness. Riande et al. (2000) also attribute this increase to the extensibility of the network.
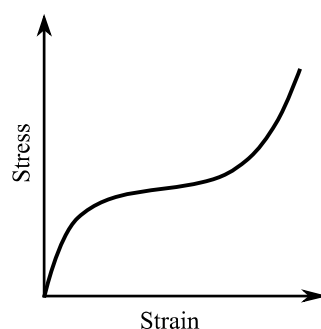
Figure 3.3: Typical stress-strain curve of an elastomer.

The non-linear course of the stress-strain curve of elastomers does not allow the assignment of a specific value to the Young's modulus outside of the low deformation region (Treloar, 1975). Below 1% strain, the Young's modulus, i.e. the stiffness of the material (given by the ratio of the applied stress to the generated strain), is defined by the tangent of the curve in this linear elastic region. Due to the easy extensibility of rubber, the elastic modulus is low. Compared to other polymers, elastomers display Young's moduli in the range of 0.1 to 100 MPa, while the stiffness of rigid polymers is 10^3-10^6 MPa (Shaukat et al., 2022).

3.4.2 Viscoelasticity

A typical characteristic of polymers is their process-dependent mechanical response, which is subjected to the testing conditions and the polymer type. This characteristic is called viscoelasticity, in which a material exhibits the combined behaviour of an elastic solid and a viscous fluid. The increase in the strain rate, for instance, makes the material appear stiffer, while its decrease leads to a softer behaviour (see Figure 3.4) (Harper, 2002). Regarding elastomers, they can preserve material integrity even in the case of high stresses or strains (Ngai et al., 2013). Their viscoelastic properties are crucial for applications such as tires, vibration and shock isolation and damping.
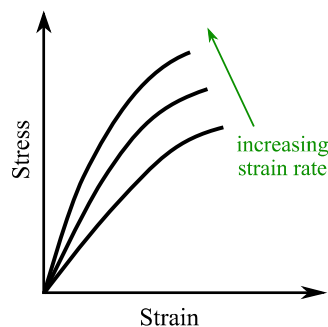
Figure 3.4: Influence of the strain rate on the stress-strain curve.

A viscoelastic material shows hysteresis. Viscoelastic hysteresis is defined as the non-recoverable energy in a cyclic loading of a material, where the lost energy occurs through heat transfer mechanisms. It is determined by the area between the loading and unloading curves forming the so-called hysteresis loop. Internal friction is the cause for viscoelastic hysteresis, in which there is a resistance to both extension and contraction. The type of elastomer influences the hysteresis loop; as an example, unreinforced natural rubber shows a smaller hysteresis than reinforced elastomers, which increases with the amount of reinforcing filler and the strain rate (Bauman, 2008). At the end of a loading-unloading cycle in the viscoelastic regime, the material returns to zero strain if a specific time is given afterwards. Otherwise, an extension of the specimen is seen as in Figure 3.5, which may also include a permanent set when the plastic regime is reached during loading.
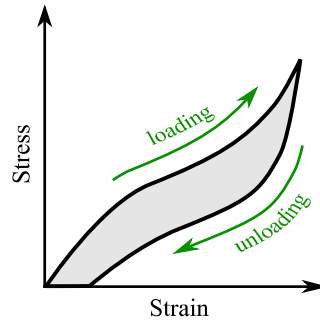
Figure 3.5: Hysteresis loop in cyclic loading.

The viscoelastic behaviour can be characterised through creep, stress relaxation or dynamic mechanical measurements. With time considered as the independent variable of strain and stress, one of the two is held constant while the other is measured as output. In creep, the material is under the action of a constant stress, and the strain gradually increases. Stress relaxation experiments keep the material at a constant strain, and a continuous decrease in the stress is observed, i.e. the material relaxes. Both of these phenomena are illustrated in Figure 3.6, representing the time-dependent return to a new equilibrium state after a disturbance (Holzapfel, 2000).
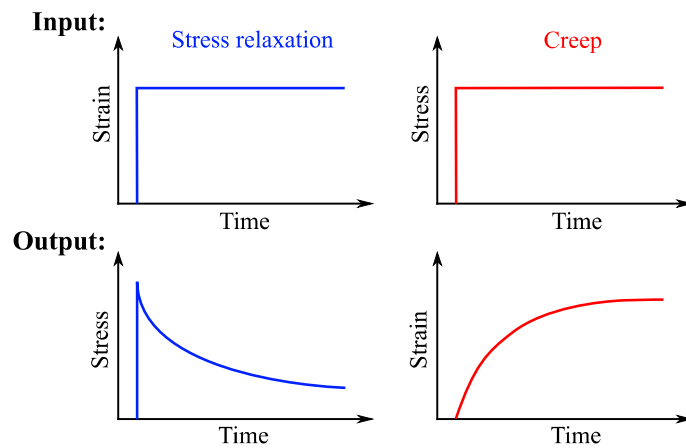
Figure 3.6: Input and output curves of stress relaxation and creep tests.

Dynamic mechanical tests evaluate the material response in the frequency domain. Sinusoidal strains (or stresses) at a specific frequency are applied to the specimen, leading to sinusoidal stress (or strain) results with a phase angle between the input and output curves (Figure 3.7). In order to remain in the linear viscoelastic regime, the strain and stress amplitudes need to be sufficiently small. If not, the material response may contain contributions at higher frequencies.
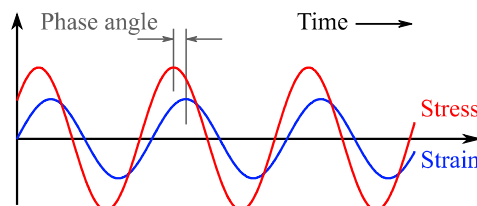
Figure 3.7: Sinusoidal input and output curves of dynamic mechanical tests.

The response in creep and stress relaxation is a consequence of the long-chain molecular structure of the material. The polymer molecules rotate and unwind to accommodate the load as the constant stress during creep gradually induces strain accumulation. In relaxation, the initial sudden strain does not allow the accommodation of the molecular structure. As time goes by, the molecules are able to rotate and unwind, loosening the molecular chain network and, hence, requiring less and less stress to keep the strain constant (Brinson and Brinson, 2008; Bauman, 2008). Both behaviours can be modelled by means of rheological models, which are presented below and subsequently focused on stress relaxation. The response in the frequency domain is provided subsequently. For further equation development, the reader may refer to the works of Ferry (1980), Holzapfel (2000), Rösler et al. (2007) and Bergström (2015).

Linear Viscoelasticity Models

Linear viscoelasticity is often employed to model the viscoelastic response of elastomeric materials. It is the simplest way to model this behaviour when small stresses and strains are applied, since the linear viscoelastic regime is predominant in such cases (Ngai et al., 2013; Bergström, 2015). In this context, the stress relaxation and creep behaviours can be described with elements that combine springs and dashpots. Thereby, Hooke's Law for a purely elastic material ($\sigma = E\varepsilon$) and Newton's Law for a purely viscous material ($\sigma = \eta\dot{\varepsilon}$) can be applied, where σ stands for stress, E for elastic modulus, ε for strain and η for viscosity.

For the qualitative representation of stress relaxation, a Maxwell element is sufficient, in which one spring and one dashpot are in series. Creep can be simply reproduced by using the spring and the dashpot in parallel, constituting a Kelvin-Voigt element. In order to represent more complex viscoelastic materials, exhibiting both relaxation and creep, the Generalised Maxwell model is applied. In this case, a spring is in parallel with an arbitrary number "n" of Maxwell elements. The three models are illustrated in Figure 3.8 with their respective constitutive equations. Another possibility for the representation of creep and stress relaxation is with a Generalised Kelvin-Voigt model. In this model, a spring is in series with an arbitrary number "n" of Kelvin-Voigt elements, which was omitted in this thesis.

Focusing on the stress relaxation behaviour, the time-dependent stress of a single Maxwell model is given by Eq. 3.1, where σ_0 is the maximum stress and τ is the characteristic relaxation time defined by the ratio of η to E:

$$\sigma(t) = \sigma_0 \exp\left(-\frac{t}{\tau}\right) \tag{3.1}$$

$$\tau = \frac{\eta}{E} \tag{3.2}$$
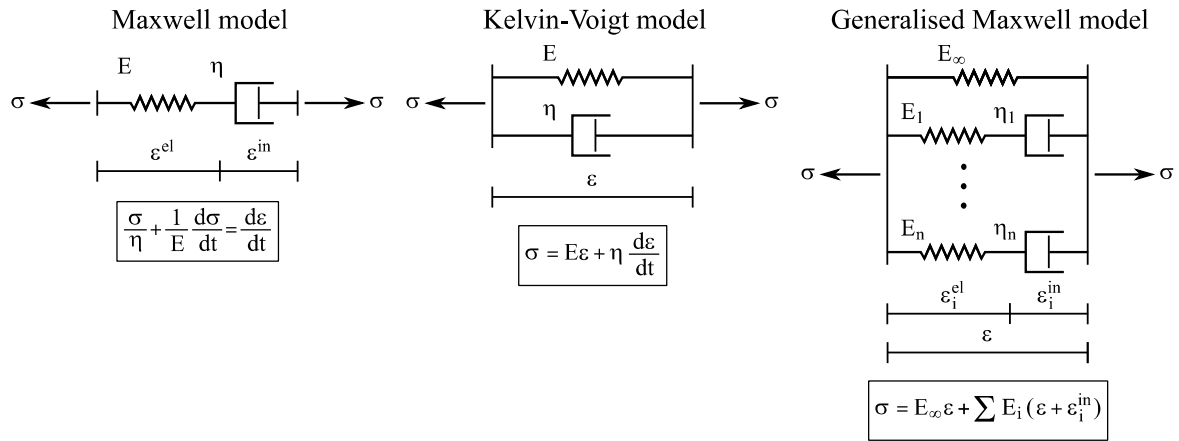
Figure 3.8: Representations of the Maxwell, Kelvin-Voigt and Generalised Maxwell models.

For the Generalised Maxwell model, the use of Eq. 3.1 for each Maxwell element leads to Eq. 3.3, which corresponds to a n-term Prony Series. The stress of the spring element is given by σ_∞, called equilibrium stress, which is the long-term stress of the fully relaxed material. For each Maxwell element there is a stress-like constant σ_i and a relaxation time τ_i. The summation in Eq. 3.3 is called non-equilibrium stress. In Figure 3.9, the stress and relaxation times are visualised.

$$\sigma(t) = \sigma_\infty + \sum_{i=1}^{n} \sigma_i \, \exp\left(-\frac{t}{\tau_i}\right) \tag{3.3}$$
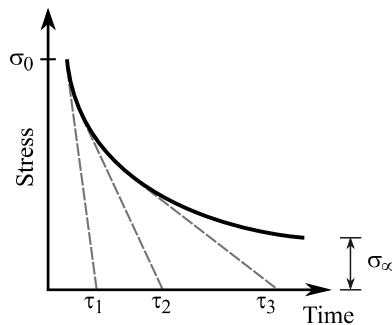
Figure 3.9: Stress relaxation curve for a Generalised Maxwell Model (n = 3).

Dynamic Mechanical Measurements

For a material in the linear viscoelastic regime, the application of a sinusoidal strain in the form of Eq. 3.4, with a strain amplitude ε_a and at a frequency $\omega = 2\pi f$ leads to a sinusoidal stress (Eq. 3.5) with an amplitude σ_a and an out-of-phase angle δ, as seen in Figure 3.7.

$$\varepsilon(t) = \varepsilon_a \sin(\omega t) \tag{3.4}$$

$$\sigma(t) = \sigma_a \sin(\omega t + \delta) \tag{3.5}$$

Eq. 3.5 can be rewritten with the help of trigonometry, leading to Eq. 3.6. The concepts of storage modulus (E′) and loss modulus (E″) are introduced as well. The storage modulus measures the energy stored and recovered per cycle and is defined as the stress in phase with the strain divided by the strain. The loss modulus is a measurement of the energy dissipated per deformation cycle; it is defined as the stress completely out of phase with the strain divided by the strain. The phase angle is a function of frequency, and so are the storage and the loss moduli. They are expressed by Eq. 3.7 and Eq. 3.8, respectively:

$$\sigma(t) = \varepsilon_a [E' \sin(\omega t) + E'' \cos(\omega t)] \tag{3.6}$$

$$E'(\omega) = \frac{\sigma_a}{\varepsilon_a} \cos \delta \tag{3.7}$$

$$E''(\omega) = \frac{\sigma_a}{\varepsilon_a} \sin \delta \tag{3.8}$$

According to Ferry (1980), it is generally convenient to write the sinusoidal strain and stress in complex notation (Eq. 3.9). As a result, the ratio of the complex stress σ^* to the complex strain ε^* is equal to the complex modulus E^*, whose real and imaginary components correspond to the storage and loss moduli, respectively (Eq. 3.10). The ratio between the output and input amplitudes is given by Eq. 3.11:

$$\varepsilon^* = \varepsilon_a \exp(i\omega t) \; ; \quad \sigma^* = \sigma_a \exp[i(\omega t + \delta)] \tag{3.9}$$

$$E^*(\omega) = \frac{\sigma^*}{\varepsilon^*} = E' + iE'' \tag{3.10}$$

$$|E^*| = \frac{\sigma_a}{\varepsilon_a} = \sqrt{E'^2 + E''^2} \tag{3.11}$$

Another important concept is the loss factor, $\tan \delta$. It corresponds to the ratio of the viscous to the elastic effects, i.e. the ratio of the dissipated energy to the stored energy per cyclic deformation (Eq. 3.12). In the case of a purely elastic solid, the phase angle is $\delta = 0°$, indicating no energy losses. For a purely viscous fluid, the phase angle is completely out of phase ($\delta = 90°$), and all energy is lost. Thus, a viscoelastic material shows $0° < \delta < 90°$, where the greater the angle, the greater its damping capacities. For that reason, the loss factor is of substantial practical interest (Ferry, 1980):

$$\tan \delta = \frac{E''}{E'} \tag{3.12}$$

It is worth mentioning that a dynamic mechanical measurement should be performed in the so-called Linear Viscoelastic Region (LVR). In this way, the viscoelastic parameters of the material are independent of the strain amplitude, and the stress-strain relationship is kept linear. In order to be in the LVR (Figure 3.10), the strain amplitude should assume a value below a critical strain to avoid changes in the microstructure of the material. The end of the LVR can be identified by the drop in the storage modulus in a strain sweep test. A drop of approximately 5% from the average of the plateau is a common practice to determine the critical strain (TA Instruments, 2021).
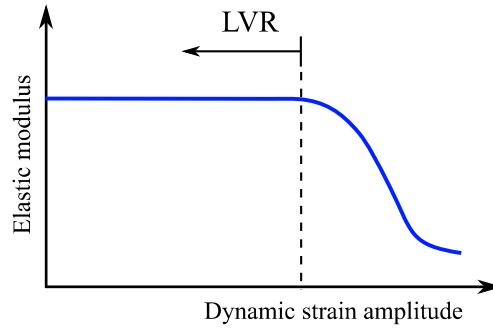
Figure 3.10: Linear Viscoelastic Region in the dynamic strain amplitude range.

Time-Temperature Superposition

The measurement of the dynamic mechanical properties is usually performed in a limited frequency range. This range can be extended by using the time-temperature superposition (TTS) principle, applicable for thermorheologically simple materials. In this case, the curves of the storage and loss moduli do not show a change in shape as the temperature is changed. Hence, the measurements can be performed in a narrower frequency range for several temperatures and the TTS is used. One of the temperatures is selected as reference (T_R), the corresponding curve is fixed and the others are horizontally shifted on a logarithmic frequency axis. The result is a "master curve" in an experimentally non-accessible, broader frequency range (Figure 3.11).
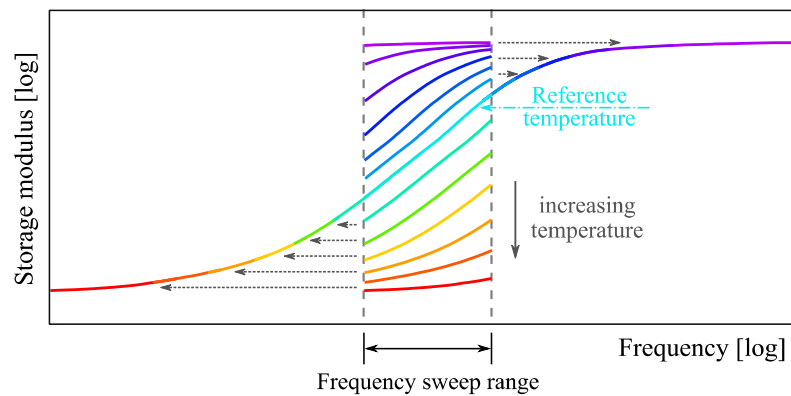
Figure 3.11: Time-temperature superposition principle.

The shift factor a_T is frequently given by the Williams-Landel-Ferry (WLF) equation (Williams et al., 1955), as shown in Eq. 3.13. Constants C_1 and C_2 are obtained experimentally. As stated by Bergström (2015), the superposition of time with temperature must be applied to all viscoelastic quantities, eg. E', E'' and $\tan \delta$, and the shift factor must be the same for the material to be thermorheologically simple.

$$\log_{10} a_T = -\frac{C_1(T - T_R)}{C_2 + (T - T_R)} \tag{3.13}$$

3.4.3 Mullins Effect

The Mullins effect is a typical phenomenon of rubber-like materials subjected to cyclic loadings with large strain amplitudes. This phenomenon was previously investigated by Mullins (1948; 1969) and is characterised by a stress softening after each loading cycle. The greatest stress softening occurs in the first cycle and is reduced as subsequent reloadings are performed, until a stationary hysteresis is reached (Dargazany and Itskov, 2013). The phenomenon appears in both filled and unfilled elastomers (more pronouncedly in rubbers with high filler contents) (Mullins, 1969; Machado et al., 2010), as well as in most TPEs (Grady et al., 2013; Tayeb et al., 2022). Figure 3.12 illustrates the Mullins effect.
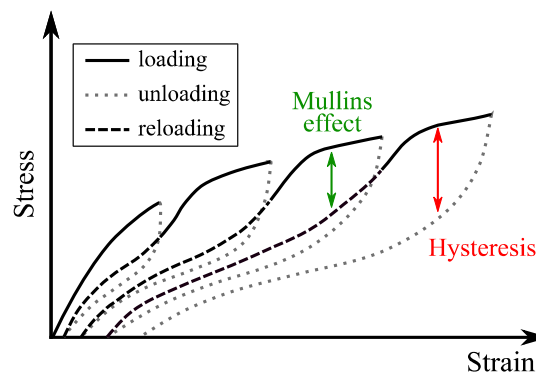
Figure 3.12: Mullins effect on a cyclic loading.

The Mullins effect is irreversible, without a universal explanation of its microscopic mechanisms. In the literature it is frequently considered as damage or change in the macromolecular network (Bauman, 2008; Holzapfel, 2000; Machado et al., 2010; Dargazany, 2013; Tayeb et al., 2022), considerations which are outside the scope of this work. The effect is independent of the loading rate, depending only on the strain level. The softening occurs whenever the stretching exceeds the prior maximum value of the loading history, following the primary curve until a new maximum is reached (Machado et al., 2010; Tayeb et al., 2022).

Quantifications of the Mullins effect in the works of Machado et al. (2010) and Tayeb et al. (2022) consider the ratio of the energy brought to the specimen by the second loading (W2L) to the energy brought to the specimen by the first loading (W1L). When a previous cycle at a lower maximum strain is performed, W1L must include the energy brought to the specimen if it has not been subjected to those cycles at lower strain. Thus, the actual energy brought to the specimen by the first loading curve at a higher maximum strain ($W1L_1$) is added to the energy between this first loading curve and its equivalent monotonous loading curve in the absence of previous cycles ($W1L_2$), as seen in Eq. 3.14 and Figure 3.13.

$$W1L = W1L_1 + W1L_2 \qquad (3.14)$$
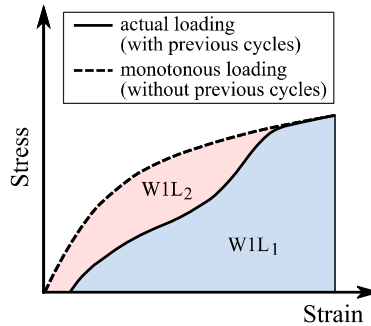
Figure 3.13: Quantification of the stored energy by the first cyclic loading.

3.4.4 Payne Effect

The Payne effect is characterised by a dependence of the complex modulus on the strain amplitude in a dynamic strain-controlled experiment. With an increasing amplitude under small strain oscillations, there is a rapid, non-linear decrease in the complex modulus that stabilises at large deformations. This effect is common to all filled elastomers, and increases with filler content (Figure 3.14). Payne (1962) also detected a region at very low strains in which the modulus remains constant with increasing strain. For elastomers without fillers or with inert fillers, the Payne effect is stated to be absent (Payne, 1962; Gauthier et al., 2004).
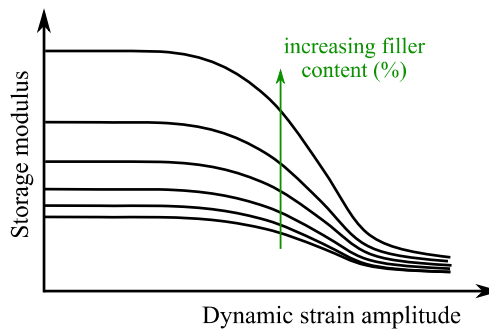
Figure 3.14: Payne effect in filled elastomers with increasing filler content.

According to Payne and Whittaker (1971), the Payne effect is associated to the secondary forces, i.e. van der Waals bonds, between the carbon black aggregates. The structure is continuously broken down under stress and reformed once the stress is removed. Hence, the Payne effect is a reversible phenomenon assigned to changes induced in the microstructure of the material by deformations. Since the DMA tests in this work were performed within the linear viscoelastic region (that corresponds to the left side of Figure 3.14), the Payne effect was not studied.

4. Additive Manufacturing

Additive Manufacturing (AM) needs a three-dimensional geometric model is needed for the production process of a part by. The model is either created with a computer-aided design (CAD) software or obtained by 3D scanning from a physical object. The conventional file format in AM is called STL (Standard Triangle Language), in which the surface geometry of a 3D object is represented by a mesh of triangles of various sizes. The model is then sliced into layers in a plane parallel to the building surface with the use of a specific software, often referred to as "slicer". Each AM technology has an appropriate slicer as well as corresponding parameters to be defined, generating a G-Code file with the printing instructions. In case of overhangs within the geometry, support structures may be added at this stage, depending on the AM technology. This completes the pre-processing stage. The reading of the G-Code file by the printer and the construction of each layer of the part is called processing. Once it is finished, the printed object is removed from the building surface. Depending on the technology, the geometry, the printing resolution and/or the final requirements, a post-processing stage may be necessary. This can be performed for the removal of supports or excess material, refinement of the surfaces, post-curing for mechanical properties improvement, or even for varnishing, coating or painting (Pagac et al., 2021).

In this context, this chapter presents the formal definition of AM, along with some general particularities of this manufacturing method. The application fields of AM are introduced thereafter, together with some of the main limitations and challenges faced by 3D printing. Subsequently, the AM technologies are classified, and those relevant to polymers are briefly discussed. Their positive and negative aspects are considered in addition to their singularities, e.g. post-processing requirements and resolution. The last section is dedicated to an overview of the 3D printing of elastomeric materials.

4.1 Definition and Particularities

Additive Manufacturing, commonly known as 3D Printing, has a variety of synonyms, among them: additive fabrication, additive processes, additive techniques, additive layer manufacturing, layer manufacturing and freeform fabrication. According to the American Society for Testing and Materials (ASTM, 2012), AM is defined as "a process of joining materials to make objects from 3D model data, usually layer upon layer", in which material is *added* to create the final shape of a desired geometry. This contrasts with conventional manufacturing methodologies e.g. Subtractive and Formative techniques. The first

comprises technologies like milling, drilling and turning, in which the objects are obtained by removing material from a solid bulk. In the latter, liquid material is injected or poured into a mould and allowed to cool down, such as in injection moulding, die casting, pressing and stamping processes.

Subtractive Manufacturing can be considered wasteful. It is also limited in terms of detail of geometry, with costs increasing significantly when using CNC (Computer Numerical Control) or a skilled machinist. It is, thus, advantageous in producing large volumes as well as simple parts. Formative Manufacturing allows the fabrication of geometries with a high level of quality and relatively low cost per part. However, one of the downsides of this technique is tooling, which is expensive and demands a longer time for its completion. Taking this into consideration, AM becomes an interesting option when a small-scale production of complex, custom-made small parts is desired.

According to Klahn et al. (2015), by breaking down the complex three-dimensional object into a series of two-dimensional steps, the layer manufacturing enables the complexity to no longer dominate manufacturing time and costs as in conventional processes. Furthermore, AM is a CAD driven process. Thus, it exempts the use of individual tooling, allowing the production of single parts and mass customisation economically when considering small lot sizes. Another advantage of additive processes is the reduction of waste by-products and a minimum need for post-processing (Janusziewicz et al., 2016; Bikas et al., 2016). There is also the reduced inventory to be considered; adopting 3D printing eliminates the need for physical storage and enables the creation of spare parts on-demand (Ford and Despeisse, 2016).

Time is, though, a relative advantage. Lead times can be considerably reduced to hours/days when producing a part by AM, since the steps comprise the creation of a digital model, the printing itself and post-processing techniques (if needed). Comparatively for Injection Moulding (IM), mould fabrication is a necessary step, which alone can take weeks to be performed. Nevertheless, the AM process is slow in its essence (Ligon et al., 2017). While IM parts are produced much faster – in a matter of minutes – once the mould is ready, AM is time-consuming due to its layered nature, as well as process limitations. Extrusion AM techniques, for instance, often have only one nozzle through which material is deposited, and techniques using thermosets must wait for the curing step. Consequently, the larger the lot size the more unfeasible the 3D printing becomes, at least for the technologies currently available. Hence, production speed is still a limitation for parts with larger dimensions. As the technology evolves, this limitation is reduced.

4.1.1 Applications

Currently, AM is adopted in the following categories: concept modelling, end-use parts, master patterns and direct tooling. The employed materials may vary and depend on the process used. They may be metals, ceramics, polymers or even composites, and their form can be liquid, filament/paste, powder or solid sheet. Despite the fact that several AM technologies do not allow common engineering materials to be processed with sufficient

mechanical properties, the improvement in the technologies as well as in the materials motivates the further exploration of AM for the manufacturing of functional components.

There is a great interest in the development of new materials with enhanced mechanical properties. Additionally, in cases where the mechanical performance is still an issue to be better addressed, rapid manufacturing is possible for applications that are not too demanding. Alternatively, printed parts can also be used in assembly or even in experimental testing where the part geometry is the focus, rather than the mechanical properties of the material (Upcraft and Fletcher, 2003).

The main fields of application for AM parts include industrial machines, motor vehicles, consumer products and electronics, aerospace, and the medical/dental sector, also with increasing importance in academic and government/military use. The US Army, for instance, started exploring this technology by producing spare parts like robot wheels, vehicle knobs and handles, and custom tools on demand (Rize Inc., 2019). Auxiliary tools have also been locally 3D printed at Audi, helping employees on the production lines in a quick way (Volkswagen AG, 2019).

The aerospace industry benefits from AM with weight reduction and design optimisation, besides the need to produce low-scale complex components. Examples include the production of pressure/temperature sensors, and complex laser sintered polymer parts in commercial and military aircraft (Mellor et al., 2014; Ligon et al., 2017). The medical sector particularly benefits from AM. CAD data can be generated by 3D medical imaging techniques, e.g. MRI (magnetic resonance imaging) and CAT (computed axial tomography) scanning for the 3D printing of a wide range of products, such as hearings aids, dental crowns, orthodontics, prosthetics, and implants (Ford and Despeisse, 2016). 3D bioprinting is also a growing subject, consisting of methods that use biological ingredients to build functional tissue and organs, and with the potential to revolutionise regenerative medicine in the near future (Noor et al., 2019).

AM is extended to other segments, in a smaller scale. In art and fashion, the manufacturing of designer and sport shoes (3D Printing Industry, 2019a; 2021a; 2022a) is recurrent. AM has also been applied to architecture for presentation of design models and more recently for housing (3D Printing Industry, 2022b). Jewellery, food industry, furniture, musical instruments and clothing are other application areas of AM (Mellor et al., 2014; Rayna and Striukova, 2016; Ligon et al., 2017).

4.1.2 Limitations and Challenges

AM is in constant expansion and has to be further explored and studied, whether in new technologies and materials or in process optimisation. Recent advances have been substantial, including a deeper understanding of the processes, research into new materials and development of better equipment (Klahn et al., 2015). Nevertheless, some issues remain and need to be addressed and improved if AM is to be established on the large-scale production sector. Ligon et al. (2017) listed the five most relevant aspects to deal with in order to achieve a better process performance and finished product. According to the

authors, build speed, mechanical properties, resolution, multi-material parts and biocompatibility are the main concerns.

As previously mentioned, AM is a slow technology compared to many conventional manufacturing processes. The economic feasibility comes into view when the whole lead time, from placing the order until getting the final product, is considered. AM is also more economically feasible when a small number of customised parts is involved. Build speed is still a limiting factor for mass production of simple objects, making way for studies on the optimisation of the printing process and the development of new technologies.

The mechanical properties of 3D printed parts continue to be a major challenge. These parts usually have inferior mechanical performance than conventionally manufactured ones, with a high level of anisotropy as a result from the layered fabrication process. Furthermore, the joint adjacent layers can be a source of weakness, with residual stresses and poor adhesion. Porosity is also a concern, which is inevitable in AM techniques such as powder bed fusion and material extrusion. Besides this, thermomechanical properties, long-term stability, creep and corrosion are topics of interest. Process parameters can greatly influence the final properties and the anisotropy of the material. For Bikas et al. (2016), control aspects of the process are the cause of the undesired effects. The authors point out the difficulties in optimisation on account of limited modelling approaches as well as the complexity of physical phenomena associated to AM processes, promoting it as an active field of investigation.

Spatial resolution is affected not only by the type of AM technology applied, but also by the processed material. Its influence on the quality and functionality of the final part shows its relevance in direct manufacturing. Upcraft and Fletcher (2003) named three components impacting on the roughness of the surface of the printed part. The first is the thickness of each layer, which is an inherent attribute producing the staircase effect combined with the built angle of the surface. The second is the end profile of each layer, which depends on the selected AM technology. The third is the material composition, which depends upon the material used and its form (e.g. powder) required by the AM technique. Additional post-processing steps such as coating, solvent treatment and sanding may be necessary to achieve the desired surface quality. Improvement in spatial resolution means a more effective manufacturing process and an increase in AM's competitiveness, providing geometries which are more faithful to CAD models and exempting post-processing techniques.

With respect to multi-material parts, resources like printing prototypes and models in multiple colours benefit the development stage in terms of aesthetics and demonstration. In manufacturing, a multi-material part excludes assembling as well. As hardships for multi-material processing, Ligon et al. (2017) indicate differences in reactivity, thermal and rheological behaviour, as well as incompatibilities of the materials themselves or of the different techniques used to process the component. Modifications in several existing AM technologies have been made. Nonetheless, contamination issues, slow transfers from one material to another and restrictions on material change only between rather than within layers are mentioned as limitations yet to be addressed.

Lastly, biocompatibility arises especially in medical applications. AM products, particularly those that are placed inside a person's body, must be biocompatible. That is the

case for dental restorations, implanted prosthetics and, from more recent research, organs. Further developments in this matter promote not only the expansion of AM use in the medical sector but also changes in the approach of personalised medicine.

4.2 3D Printing of Polymers

The number of Additive Manufacturing processes increases year after year. A wide variety of technologies is available at the moment. The differences from one to another lie in the way layers are deposited, in the operating principle and in the printing materials (Upcraft and Fletcher, 2003; Klahn et al., 2015). Bikas et al. (2016) underline that each technology has positive and negative aspects. The authors present as general considerations for choosing a specific technology: the speed of the machine, the cost of the printed part, the cost and range of feed materials and the colour capabilities. The printing resolution and size, along with the performance of the printed materials are other elements to consider (Shaukat et al., 2022).

AM processes are categorised by the ASTM into seven groups. The criterion is based on the layer deposition mechanism, classifying the processes in (ASTM, 2012):

- **binder jetting**: a liquid bonding agent is selectively deposited to join powder materials;
- **direct energy deposition**: focused thermal energy is used to fuse materials by melting as they are being deposited;
- **material extrusion**: material is selectively dispensed through a nozzle or orifice;
- **material jetting**: droplets of build material are selectively deposited;
- **powder bed fusion**: thermal energy selectively fuses regions of a powder bed;
- **sheet lamination**: sheets of material are bonded to form an object;
- **vat photopolymerisation**: a liquid photopolymer in a vat is selectively cured by light-activated polymerization.

With a focus on the additive manufacturing of polymers, direct energy deposition is not addressed in this thesis, as it is a typical process for metals. The remaining categories are subsequently presented along with the main technologies available for each.

4.2.1 Binder Jetting

Binder jetting processes commonly use sand or metal but polymers and ceramics are also available. The representative technology of this category receives the same name: *Binder Jetting*, having other synonyms such as 3D Powder Binding Technology and Three-Dimensional Printing, or simply 3DP. This can be quite confusing, since the term 3D Printing is frequently used when referring to AM in the industry and in the literature (as well as in this work). At the same time, 3D printing is commonly understood by the public domain as the technology of filament printers (to be later introduced).

Binder Jetting

This technology creates a geometry by selectively deposing droplets (a liquid bonding agent) through a moving print head in a powder material bed. The droplets bind the powder particles, creating each layer at a time. An initial layer of powder is required on the build platform. After printing one layer, the powder bed is lowered and a new layer of powder is distributed over the previous layer. The process is repeated until all layers are printed (Figure 4.1). The geometry is left in the powder in order to cure and gain strength, and is later cleaned with compressed air to remove unbound powder. No heat or light is needed in the process. Support structures are not required as the part is supported by the loose powder in the bed, saving material and reducing post-processing.
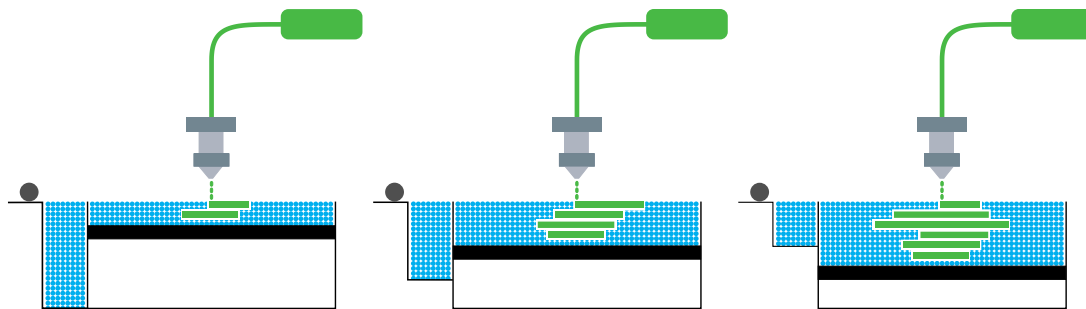
Figure 4.1: Binder Jetting process.

Among the advantages of this technology are the shorter build times and the use of cheaper raw materials. Furthermore, not requiring supports allows the creation of complex geometries (Upcraft and Fletcher, 2003). Printing in multiple materials and colours is possible as well. Ligon et al. (2017) include in the benefits the occurrence of the process at low temperatures and the slightly lower costs in purchase and maintenance compared to SLS (to be later presented). Nevertheless, the authors cite as negative points the limited strength of the parts and the rough surfaces, which frequently do not meet the demands for applications as tooling and rapid manufacturing. Time-consuming post-processing techniques are necessary to give the final product better surface finish and mechanical properties. Another fact stated by the authors is the unsuitability of some binders for most office environments, in particular the chlorinated organic solvents.

4.2.2 Material Extrusion

In material extrusion processes, the printing material is pushed through a movable nozzle. After one layer is completed, the extrusion head moves up or the build platform moves down in preparation for the next layer. Three technologies of this type are *Fused Filament Fabrication*, *3D Dispensing* and the more recent *Liquid Additive Manufacturing*. They are presented below.

Fused Filament Fabrication (FFF)

FFF is also known as Fused Deposition Modelling (FDM), a term trademarked by the company Stratasys (Stratasys, 2022a). It is the most commonly available and cheapest AM technology. FFF has spread across domestic environments and hobby activities. For this reason, FFF is popularly known as 3D printing, although the term may refer to other AM technologies. Applications include low-cost rapid prototyping, moulds and end-use parts.

For FFF, the printer nozzle is heated to a desired temperature while the material in filament form is fed through to it and pushed by a motor, melting the material in the process. Other types of printers make use of the material in pellet form. The deposition occurs under constant pressure and in a continuous stream. Once deposited, the material cools down and solidifies to form the geometry. FFF machines usually have two nozzles, one for the part material and one for the support material (Figure 4.2). Depending on the geometry, supports may be required, especially in case of overhanging parts. Besides balance of the printed part, supports are also important in terms of printability and heat dissipation (Jiang et al., 2018).
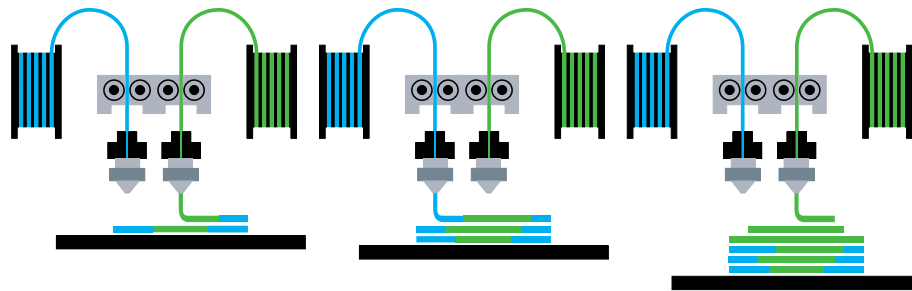
Figure 4.2: FFF process.

The benefits this technology provides were the main reason for its dissemination. The machines and materials are the least expensive among the AM technologies. In addition, they are simple, clean and office-friendly. A great variety of non-toxic, odourless and coloured thermoplastics is available as well (Bikas et al., 2016). Besides, the process can be easily scaled to any size and create stable-over-time geometries.

Nevertheless, accuracy is impaired by the rough surfaces of the printed parts, and details are limited by the size of the nozzle. The surface finish is reduced due to the tendency of the layers to be clearly visible. Furthermore, the support structures must be removed. As a consequence, post-processing may be required to improve surface quality. Moreover, it is a high temperature process that delivers parts with highly anisotropic mechanical properties. The strength of the print is limited due to layer adhesion, being lower in the vertical direction even in cases of an infill rate of 100% (Klahn et al., 2015; Bikas et al., 2016; Ligon et al., 2017). Many factors should be controlled in order to print an adequate geometry. Kotlinski (2014) states that the mechanical properties are subject to process parameters such as bead width (i.e. width of a deposited line of material), air gap, build temperature and filament orientation inside the cross section. Finally, there is also the matter of printing time: the thinner the layers, the higher the quality, but the more time consuming the printing. Since the material is deposited by one nozzle at a time, the printing of large mass parts is slow.

3D Dispensing

Synonyms for the 3D Dispensing process include *3D Plotting* and *3D Micro Extrusion*. In this technology, the nozzle is similar to a syringe, depositing the layers at a constant rate under a specific pressure (Figure 4.3). The extrusion is performed by means of pneumatic pressure, avoiding the need for piezoelectric or thermal print heads (Nathan-Walleser et al., 2014).
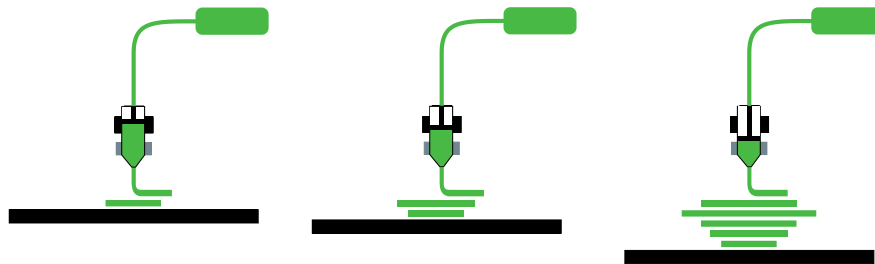
Figure 4.3: 3D Dispensing process.

Among the processing materials, we can find thermoplastics, thermosets, ceramics, liquid rubbers, silicones, hydrogels and biomaterials. The broad range of materials is an interesting advantage of 3D Dispensing. The solidification occurs by other phenomena, including reversible and irreversible crosslinking, whilst FFF works with polymer crystallisation and chain entanglement (Landers et al., 2002; Ligon et al., 2017). In addition, it can operate with melts of different viscosities by adjusting the pressure and the nozzle's inner diameter (Nathan-Walleser et al., 2014). Given that parts can be printed without heat, thermally sensitive biologically active components and living cells can also be applied, promoting 3D Dispensing to be the base of 3D bioplotting (Landers and Mülhaupt, 2000; Bose et al., 2013).

However, this technology also provides parts with rough surfaces, which impairs accuracy. Furthermore, difficulties in extruding strands of material in the micrometre domain leads to a limited spatial resolution. Additionally, as the strand diameter is reduced, the process becomes slower (Landers et al., 2002; Ligon et al., 2017). Bose et al. (2013) also mention the need for heating or post-processing for some materials, restricting 3D Dispensing to be incorporated into the biomolecule field.

Liquid Additive Manufacturing (LAM)

The first prototypes of this technology were presented to the public in November 2016 at the Formnext exhibition (Frankfurt) by the company innovatiQ (Feldkirchen, Germany; formerly German RepRap). Two years later, the company introduced in the market its first LAM 3D printer production, currently represented by the LiQ320 version (3DR Holdings, 2018). LAM is based on the extrusion of a thermosetting liquid or high-viscosity material onto a build plate. The printing material consists of a two-part component. The components are mixed together in a 1:1 ratio in a screw-like manner right before the deposition at room temperature. After the deposition, the curing process takes place thermally by means of a halogen lamp with a power of 2 kW that passes over the geometry between the extrusion

of two consecutive layers (or only at the end) in a certain speed and height, as desired by the operator (Figure 4.4).
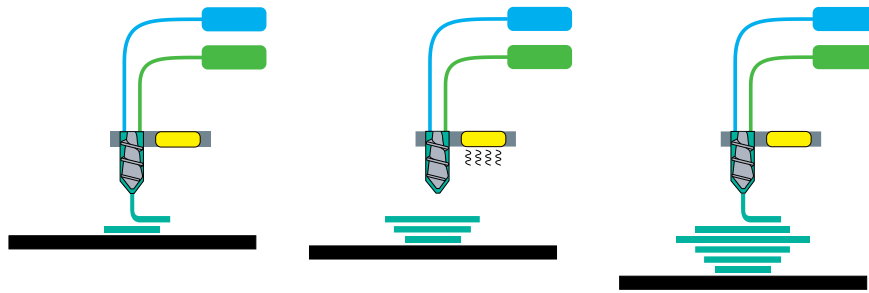
Figure 4.4: LAM process.

The vulcanisation process of LAM enables the full cross-linking at the molecular level between the individual layers. In LAM, the layers are effectively bonded rather than welded together (as in FFF). A liquid silicone rubber (LSR) of hardness 50 Shore A is mainly used, although other silicone hardness grades and materials such as polyurethane are also possible. The application of the material can be accurately controlled due to the volumetric extrusion. Furthermore, printing times are reduced since fewer tools are required and the object is fully cured at the end of the printing, exempting post-processing steps. The manufacturers also state that LAM printed parts exhibit similar material properties to injection moulding, being isotropic (innovatiQ, 2022). Another great advantage of LAM is the use of real silicones. They provide a superior lifetime compared to UV-cured elastomers, as the latter age with exposure to sunlight, for instance. Moreover, silicones can provide outstanding elasticity and recovery, as well as chemical, temperature, ageing and wear resistance, which are typical characteristics of this class of materials.

The production of functional prototypes and small-scale manufacturing of complex parts with LAM is the recommendation from 3D Activation (2022). The technology is more suitable for highly viscous materials to avoid the intense spreading of the material on the build platform after deposition. The use of low-viscosity fluids is restricted and requires an extensive knowledge of the material involved in order to adapt the printing settings. The extrusion itself is slow, as it is performed by a single nozzle up to 0.8 mm in diameter and does not allow print speeds as high as the ones for FFF. The printing of support structures is not possible either. The printing strategy and parameters can, however, be adjusted to enable the extrusion of overhangs.

4.2.3 Material Jetting

Material jetting (or simply inkjet printing) also prints geometries by nozzle deposition. In contrast to others, this process makes use of multiple thin nozzles to jet droplets, in spray mode. It works similarly to a two-dimensional inkjet printer as each layer is printed. The material is jetted either continuously or only when needed. Processing materials include photopolymer resins and wax casting materials. Their viscous nature is a critical factor to enable the formation of the drops (Izdebska-Podsiadły, 2022). Once a layer is printed, it is allowed to cool and harden or cured by UV light. The platform lowers one layer in height

and the next layer is printed. Support material is required and must be removed in a post-processing stage. The main technologies include *PolyJet*, *MultiJet Printing*, *Aerosol Jet* and *Drop-On-Demand*.

PolyJet and MultiJet Printing (MJP)

PolyJet and MJP are similar processes, being also referred to as *Multi Jet Modelling* (MJM). They work like a standard 2D inkjet printer, building multiple layers upon each other instead of a single one. The print head contains several nozzles, which deposit droplets of wax or photopolymers that are then exposed to UV light for curing (Figure 4.5). For this reason, no post-curing is required.
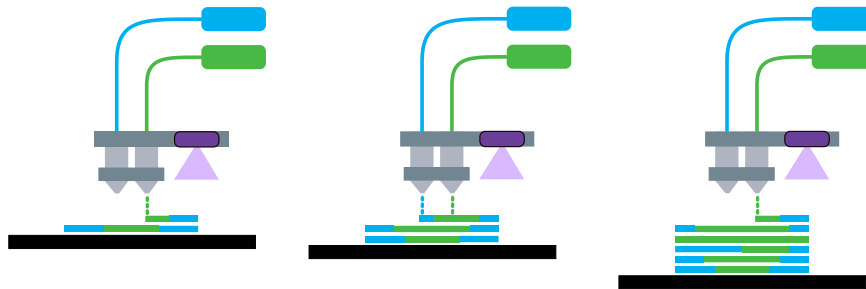
Figure 4.5: PolyJet process.

The differences between the technologies remain mainly on branding and post-processing. PolyJet is a proprietary technology by the company Stratasys (Stratasys, 2022c) while MJP is a term used by the company 3D Systems (Rock Hill, USA) (3D Systems, 2022a). The PolyJet support material is water soluble, and is removed by subjecting printed geometries to a water jet system under high-pressure conditions. MJP uses a meltable or dissolvable support material, in a hands-free process.

A good aspect of these technologies is the printing of multiple materials and colours. Furthermore, the line-wise deposition mode allows the fabrication of multiple objects with no impact on build speed, characterising a fast process (Upcraft and Fletcher, 2003; Ligon et al., 2017). They also provide high accuracy for the parts, presenting a smooth and detailed surface. Moreover, the process is office-friendly. The dense support structure required is a negative point since it is printed over the whole build volume (and not only in areas with severe overhangs, as in e.g. FFF). Therefore, more material is used, making it a less economical AM process. Besides, post-processing becomes a necessary and time-consuming stage. Finally, the operating materials are limited and must have a low viscosity to allow the formation of the droplets (Ligon et al., 2017).

Drop-On-Demand (DOD)

In the DOD approach, the print head equipped with several nozzles selectively deposits the droplets of material on a build plate and cures it by exposure to light (as in Figure 4.5). That is, the material is sprayed only when necessary. The process is carried out one layer at a time until the full geometry is obtained. Similarly to PolyJet and MJP, multi-material printing is enabled due to the nature of the process.

While in continuous inkjet printing the ink is continually ejected through a piezoelectric crystal vibrating at a constant frequency, DOD controls each nozzle individually under pressure applied by a valve. DOD usually has lower printing rates than continuous inkjet and the nozzles can clog more easily due to non-continuous use. Nevertheless, it provides better resolution and precision (Liu et al., 2017; Pitayachaval et al., 2018). Additionally, DOD is less wasteful, as it uses only the amount of ink to print the part (Afsana et al., 2018). Applications of this technology include the printing of multi-material microstructures such as electronic circuits, chips and semiconductors (Jiao et al., 2018).

Aerosol Jet

This more recent material jetting technology was developed by the Optomec® company (Albuquerque, USA) (Optomec, 2020). In the Aerosol Jet technology, a dense aerosol is transferred by an inert gas stream to the deposition head, within which this stream is focused and accelerated through a nozzle (Figure 4.6). Subsequent printing steps build additional layers to provide the final part.
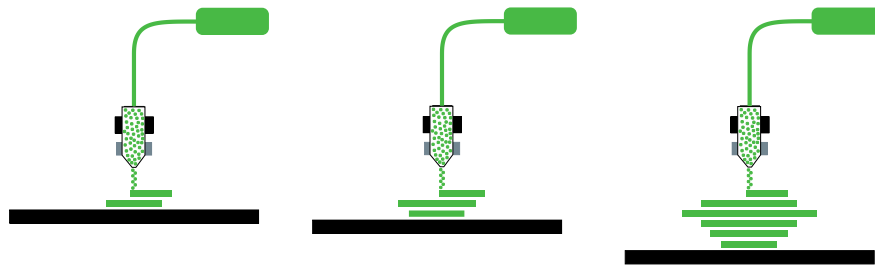
Figure 4.6: Aerosol Jet process.

Ligon et al. (2017) state that Aerosol Jet can be upscaled by combining multiple nozzles and increasing the lateral mobility and the size of the building platform. They also point out that the stream is continuous throughout the process, and a shutter controls and prevents the stream from hitting the substrate. It is a low temperature process that provides parts with a high resolution. The limitation remains on the required low viscosity of the ink, although it is not as strict as for inkjet printing.

Optomec® (2020) affirms that the printed features can show a resolution as high as 10µm, which is higher than that of inkjet printing. Furthermore, a wide variety of plastics, ceramics and metals is available, including metal nanoparticle inks, thermosetting polymers and photopolymers. The company also mentions the possibility of post-treatment methods to enhance material functionality, e.g. traditional oven sintering, UV curing and laser sintering. The main application consists of electronics, including resistors, capacitors, antennas, sensors and thin film transistors.

4.2.4 Powder Bed Fusion

Powder bed fusion creates parts by using a thermal energy source (e.g. laser or electron beam) to selectively melt and fuse powder particles together. A powder bed receives the thermal energy on the top surface, sintering the powder corresponding to a layer. The bed is lowered one layer in height and new powder is spread by a roller or a blade, preparing the printing surface for the sintering of the next layer. The process can use any kind of powder-based materials, being more common for thermoplastic polymers and metals. For polymers, the representative technology is *Selective Laser Sintering*. Another technology that often falls into this category is *Multi Jet Fusion*, which is a combination of binder jetting and powder bed fusion. Both are presented below.

Selective Laser Sintering (SLS)

For the SLS technology, the powder bed is heated to a temperature just below the polymer's softening point. A laser is targeted at points defined by a 3D CAD model, tracing the cross section of the layer and sintering the powdered material (Figure 4.7). The print chamber is warmed up to minimise shrinkage effects and reduce processing time. The printing parameters that influence the material properties are build orientation, powder bed temperature and energy density of the laser beam (Kotlinski, 2014). A certain percentage of the powder can be reused in subsequent printing processes. However, the higher amount of reused powder, the lower the quality of the printed part will be. As the whole area of the chamber must be filled with powder, the printing of a larger part or several small parts is more favourable when using SLS.
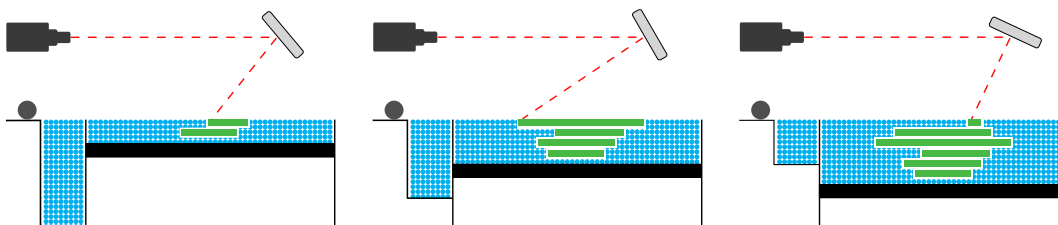
Figure 4.7: SLS process.

A great advantage of this technology is that no additional support is required. The unsintered powder itself works as a support for the geometry. Furthermore, printed parts show good mechanical properties, being strong enough to be subjected to mechanical loads. Moreover, among the processing materials there are thermoplastic elastomers (Ligon et al., 2017). In addition, no post curing is needed (Upcraft and Fletcher, 2003). Kotlinski (2014) also highlights the anisotropy of SLS parts as being the least critical among the polymer AM processes.

Despite the benefits, the printed parts present grainy surfaces as a consequence of the sintered powder, exhibiting rough surface finish. Powder particle size has an influence on the finish quality as well, besides the percentage of reused powder. Shrinkage is also a relevant aspect to consider since parts can warp significantly. Furthermore, the machines are expensive and take a long time to heat up and cool down the bed chamber, making it a

slow process (Upcraft and Fletcher, 2003; Bikas et al., 2016; Ligon et al., 2017). Moreover, the geometries may be somewhat limited; when printing hollow parts, unsintered powder cannot be removed from the inside. For such cases, small holes must ensure powder removal. Finally, because the process deals with fine powder, it is not an office-friendly technology. The fabrication and, most importantly, the part removal and cleaning can be quite messy and dangerous, demanding safety devices.

Multi Jet Fusion (MJF)

MJF is a technology developed and introduced in the market in 2016 by the company HP (Palo Alto, USA). It is equipped with an inkjet printing head that applies binder fluids to the surface of a bed filled with thermoplastic powder. In contrast to the Binder Jetting process, MJF sprays two fluids across the full build area: a fusing agent and a detailing agent. The first is sprayed where the powder is intended to solidify together. The second is applied around the edges to modify the fusing and mark the separation with the finished object. This allows the creation of smooth and finely detailed surfaces. The reaction between the agents and the material is initiated by the exposition to an infrared energy source, whose heat promotes the selective fusion of the particles to form the part. The applications of the agents and of the fusing energy take place in the same continuous pass (HP, 2022; Dassault Systèmes, 2022). The platform goes down a distance equivalent to one-layer height, and the process is repeated until the full geometry is printed (Figure 4.8). Due to the combined nature of the process, MJF can be associated with either powder bed fusion or binder jetting categories. The former case is more common, referring to the melting of powder particles. The main difference between MJF and SLS is in the heat source (infrared acting on the fusing agent in MJF *vs* laser in SLS).
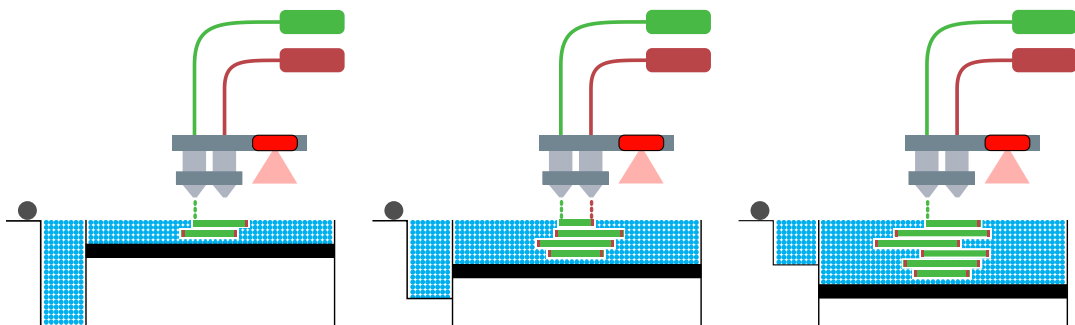
Figure 4.8: Multi Jet Fusion process.

The current material options for MJF comprise nylon (PA 11, PA12), TPU (hardness of about 90 Shore A) and a type of polypropylene (enabled by the German company BASF). These options are limited and, so far, only marketed by HP. Nevertheless, HP has announced an open platform project for the development of new materials in collaboration with partners, offering the prospect of a larger variety of materials in the future (Dassault Systèmes, 2022; Protiq, 2022). HP claims a fast production of functional parts at a low cost per part, with precision and dimensional accuracy. The quality is ensured by the proper fusion of the material and the smoothness and sharp definition of the edges. Additionally, the company states that the process has an accurate temperature control across the entire material, which is fundamental for the full control over the mechanical properties,

dimensional accuracy and repeatability (HP, 2022). According to Protiq (2022), the build speed of MJF is one of the highest among the available 3D printing processes. This advancement is crucial, since machine time is still one of the main drivers of production costs.

Other benefits of MJF include: no need for support structures due to the unfused powder; quality and functionality superior to Fused Filament Fabrication and Stereolithography; mechanical properties and surface finishes comparable to Selective Laser Sintering, although more cost-effective due to more efficient use of an infrared energy source instead of laser and the better excess powder recycling rates; low porosity; and isotropic mechanical properties since the agents fully penetrate the prints, leading to a homogeneous fusion of the individual layers. One of the drawbacks of MJF is a rougher surface finish compared to parts produced by stereolithography and material jetting technologies. In addition, the 3D printers are high-priced, with most models costing in the mid-six figures. There is also the time-consuming post-processing in order to remove the excess, unfused powder from the final prints, not to mention the possibility of damage to fine details during the bead blasting process (Dassault Systèmes, 2022; Protiq, 2022).

4.2.5 Sheet Lamination

In Sheet Lamination, any material in sheet form is possible, mainly paper, polymer and metals. The process works by cutting thin-layered materials into appropriately shaped layers by means of lasers or sharp blades. The layer is coated with a heat-sensitive adhesive on its bottom surface. The layer is pressed down onto the previous layer by a heated compactor, which activates the adhesive and glues it to the substrate (Bikas et al., 2016). The process is also known by one of its representative technologies, called *Laminated Object Manufacturing*.

Laminated Object Manufacturing (LOM)

LOM is reported by Ligon et al. (2017) as a hybrid process, since it combines additive manufacturing with subtractive processing. The process is as follows: a sheet with adhesive coating on its lower surface is placed on a platform; a heated roller passes over it, activating the adhesive and bonding the sheet to the previous layer; the required shape is cut by a laser or a knife from the sheet; the platform is lowered in one layer of thickness, and the next sheet is added, repeating the process (Figure 4.9). Once finished, the excess material is broken away to achieve the final geometry.
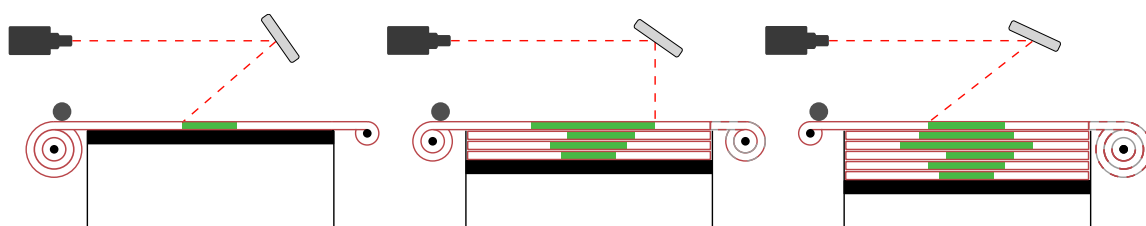
Figure 4.9: LOM process.

This technology is frequently used to make wooden patterns for sand casting. Paper is the most common material, but thermoplastic polymers, ceramics and composites are also applicable. As the excess material outside the model contour remains during the process, there is no need for support structures (Jiang et al., 2018). Furthermore, LOM is considered one of the cheapest rapid prototyping technologies, providing large parts in a quick and relatively inexpensive way (Upcraft and Fletcher, 2003). It can also act as a compact desktop printer (Ligon et al., 2017).

Nevertheless, it is a low resolution process that may require post-processing if improved surface quality and dimensional accuracy are desired. In addition, the breaking out of parts while removing the excess material can be an arduous task, in particular for hollow structures (Upcraft and Fletcher, 2003; Ligon et al., 2017). The high anisotropy of the process – the worst among the AM technologies for polymers – is also a major issue (Kotlinski, 2014).

4.2.6 Vat Photopolymerisation

Vat Photopolymerisation works with liquid photopolymer resins, which are contained in a vat and are selectively cured by a light-activated polymerisation (ASTM, 2012). The platform moves the printing object upwards or downwards (depending on the technology) after the curing of one layer to allow the printing of the next. The light should pass through the material sufficiently to guarantee good adherence between layers and part resolution (Monzón et al., 2017). Support structures are mandatory, as the operating material is a liquid and cannot provide support by itself. The main technologies include *Stereolithography*, *Digital Light Processing*, *Multiphoton Polymerisation* and the most recent *Digital Light Synthesis*. They differ from one another in terms of the curing principle (Pagac et al., 2021).

Stereolithography (SLA)

According to ASTM (2012), SLA is defined as a process that produces parts from photopolymer materials in a liquid state with the use of one or more lasers to "selectively cure to a predetermined thickness and harden the material into shape layer upon layer". It was one of the first 3D printing technologies, developed by 3D Systems corporation's founder (3D Systems, 2022a), and the first one to be commercialised (Mellor et al., 2014). SLA is still significantly applied today, mainly for functional prototyping, jewellery prototyping and casting, as well as model making (Formlabs, 2022b). It is also frequently used in master fabrication for silicone moulds, and it is capable of delivering complex parts with a surface finish in similar quality to many conventionally machined components (Upcraft and Fletcher, 2003).

For the printing process, there are two types of machines, depending on the exposure to the laser: one receives the laser beam from the top (Figure 4.10), and the other traces the laser across the bottom surface (Figure 4.11). In both types, a vat contains a liquid photopolymer resin, and the building platform moves until it is just below the liquid surface. UV radiation

is directed by mirrors in form of a laser beam, tracing on the resin surface the cross section of one layer of the part, curing the material. Once the layer is fully scanned, the platform moves one layer down and, for some machines, a blade sweeps the surface ensuring flatness (exposure from the top). Alternatively, the platform moves up, the recoater blade sweeps the surface of the liquid and the platform moves down again to a thickness of one layer higher than before (exposure from the bottom). Then the next layer is scanned and cured. The process is repeated until the full geometry is obtained. The printed part is removed from the vat and the excess liquid is cleaned. Post-curing in an ultraviolet oven completes the process.
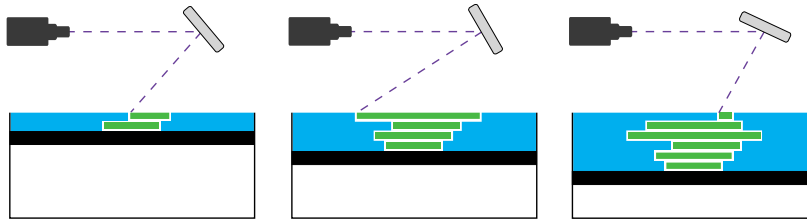
Figure 4.10: SLA process (exposure from the top).
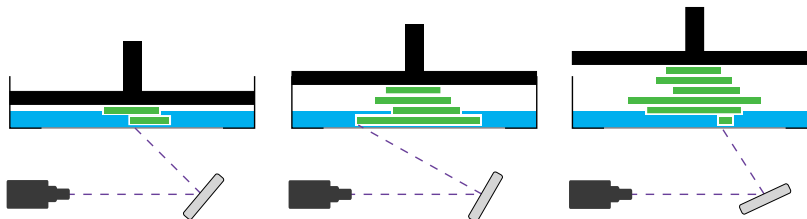
Figure 4.11: SLA process (exposure from the bottom).

Supports are imperative for printability, preventing the printing from flowing away, as well as for part balance, supporting overhanging parts, helping the structure to resist lateral pressure from the resin-filled blade and to prevent deflection from gravity (Jiang et al., 2018; Formlabs, 2022b). SLA parts can be smooth and detailed, presenting high surface quality and accuracy. The possibility of manufacturing master patterns for injection moulding or metal casting accelerates these conventional processes. In addition, SLA operates close to room temperature since it uses light instead of heat in curing, dismissing thermal expansion and contraction effects. Particularly for the exposure from the bottom machines, the initial vat volume is lower and the build volume can exceed the volume of the tank, since the part is printed coming out of the vat (Upcraft and Fletcher, 2003; Ligon et al., 2017; Formlabs, 2022b).

A disadvantage of SLA is its often-high costs, both in terms of machine and materials. The post-processing stage involving support removal and the requirement of post-curing to finish the polymerisation and ensure the mechanical properties are also downsides. Due to the sticky nature of photopolymers, they should be handled with care (Upcraft and Fletcher, 2003), not being the most recommended process for an office environment.

SLA printing is not the fastest process. The laser-scanning takes place point-by-point. However, the most time-consuming step consists on the deposition of new layer of material, besides post-processing. The mechanical properties are still limited, but constant improvements are carried out (Ligon et al., 2017). As well as for SLS, SLA is limited for

hollow geometries, being necessary to add holes to remove the resin from the inside. The sensitivity of photopolymers to long-term UV exposure should also be noted; this can be crucial when dealing with elastomers, which harden in prolonged periods of ultraviolet light exposure and have their lives reduced. Use of more flexible materials can also be limited especially for the exposure to the bottom machines. The reason is associated with the peel forces when separating the print from the tank surface, requiring the use of larger supports (Formlabs, 2022b).

Digital Light Processing (DLP)

DLP technology is very similar to SLA. Both contain a vat filled with a liquid photopolymer resin that is cured layer-by-layer. The primary difference lies on the type of light source in the curing step. Instead of scanning the cross section of the layer at each point with a laser, DLP flashes a single image of the layer by a digital light processor – sending multiple flashes in the case of larger parts (Figure 4.12). The projector consists of a digital screen where the image is composed by square pixels.
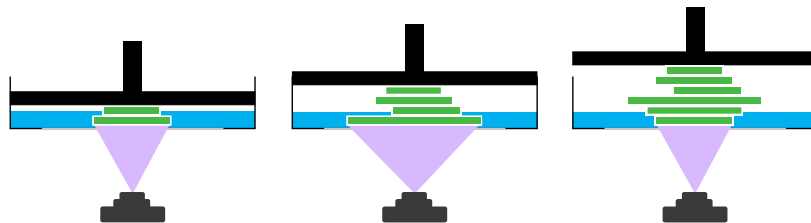
Figure 4.12: DLP process.

Since the whole layer is exposed all at once, print times can be faster than for SLA (Pagac et al., 2021). However, there are no changes in build time if the entire available illumination field has been exposed or just a part of it. In addition, DLP is less affected by curing inhibition by oxygen compared to SLA as the layer of resin in the polymerisation process is kept on the bottom of the vat, without direct contact with air (Ligon et al., 2017).

DLP is more appropriate for small complex parts that do not fill the total build volume of the printer. In contrast to SLA printers, whose build volume is independent of print resolution, DLP printers are limited by pixel size. This hinders the production of small details in a large part (or several parts in the full build volume), since the amount of pixels is fixed (Formlabs, 2022c). Thus, the number of pixels defines the resolution of the print. As a consequence, DLP is suitable for small accurate parts with applications in sectors where there is a demand for micro-parts with small features and complex shapes. Examples comprise micro-fluidic components such as valves and pumps, and electromechanical structures such as capacitors (Monzón et al., 2017).

Multiphoton Polymerisation (MPP)

Also called *Multiphoton Absorption Polymerization*, *Two-Photon Polymerization* and *Direct Laser Writing*, among other names, this technology allows the 3D printing of nanoscale structures. The printing process occurs by means of a laser that scans through

the volume of a photosensitive material. The photopolymerisation is locally induced by the absorption of photons, solidifying the material according to the 3D model. Once a layer is finished, the laser focal plane moves to the next layer (Figure 4.13). Ligon et al. (2017) state that MPP is not a proper layer-by-layer technique, since the focal point of the laser is free to move in any direction within the volume of the resin. The light source is provided by Near-Infrared light (NIR).
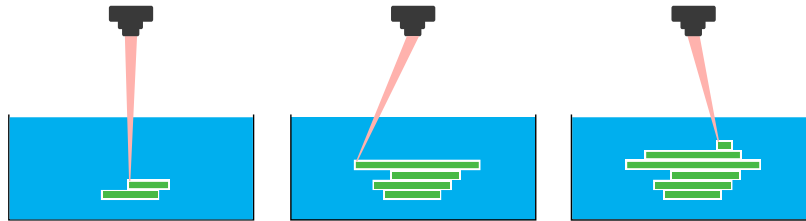
Figure 4.13: MPP process.

Among the advantages of this process, we point out its very high resolution, which can reach 0.1 µm. It has the highest precision among AM processes, offering 3D printing of nano- and micro-structures. The build speed is low, and the materials may be limited. Nevertheless, a fair range of applicable materials has been extensively developed, such as photopolymers, photoresists and hybrid materials. Applications include optical and biomedical micro-devices and microelectromechanical systems devices (Maruo and Fourkas, 2008; Ligon et al., 2017).

Digital Light Synthesis (DLS)

Presented to the public in 2015, DLS is a technology based on SLA in which parts are produced in a continuous process instead of the typical layer-to-layer approach of other AM technologies. It is a process trademarked by the Carbon corporation (Carbon, 2022c), which was previously referred to as *Continuous Liquid Interface Production (CLIP)*. ETEC corporation (EnvisionTec, 2021) has a similar trademarked technology called *Continuous Digital Light Manufacturing (CDLM)*, and both can be sometimes mentioned as *continuous Digital Light Processing (cDLP)*.

In DLS, oxygen inhibition on polymerisation is used to enable continuous fabrication. An uninterrupted sequence of UV images is projected with LEDs on the bottom of a vat containing liquid (Pagac et al., 2021). The system has an oxygen permeable, UV transparent projection window. This creates a controlled thin area of uncured photopolymer (dead zone) between the window and the cured part above it. As a consequence, the part is continuously printed and removed from the vat. Therefore, the UV exposure and the print movement become not anymore individual but concomitant steps (Figure 4.14). In addition, the constant removal of the cured geometry creates suction forces that keep renewing the reactive liquid in the vat. This excludes the recoating step to flatten the surface before printing a new layer, as it occurs for SLA machines (Tumbleston et al., 2015).
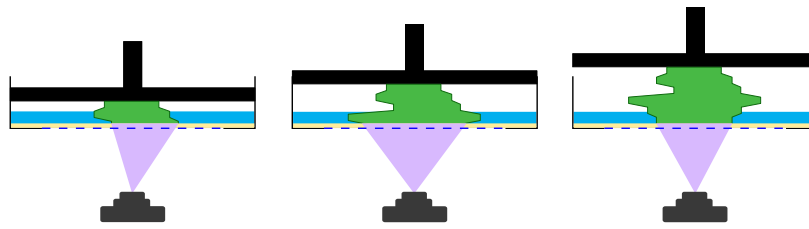
Figure 4.14: DLS process (oxygen permeable window in dashed blue; dead zone in yellow).

The particularities of this process enable it to have a considerably higher build speed compared to other Vat Photopolymerisation techniques. This leads AM into the way of viable mass manufacturing. Print speed, on the other hand, is ruled by the resin cure rates and viscosity (Tumbleston et al., 2015), limiting the printing materials to low-viscosity resins (Ligon et al., 2017). Due to its continuous nature, DLS produces layerless parts, reducing the staircasing effect without impacts on the overall printing time. In addition, it is said to provide geometries with isotropic mechanical properties. This is because the lack of chemical cohesion between the layers and of deformation of the print resulting from peeling forces of the separation step do not apply. For this reason, large overhangs can be printed without additional support, unlike other AM technologies (Janusziewicz et al., 2016). However, the printed parts are not ready to use once the process is finished. They must be placed inside an oven to improve the mechanical properties by heat (Carbon, 2022c).

4.3 Elastomers in the 3D Printing Scenario

As discussed in the previous section, the operating principle of each AM technology dictates the type of material to be used as well as its form. The required material is either a thermoplastic or a thermoset (thermally or UV-cured), in liquid, powder, pellet or filament form. The selected technology also affects the final quality of the part. Concerning the 3D printing of soft polymers, the use of traditional, vulcanised rubber is not suitable for most technologies since the vulcanisation process cannot be easily transferred to AM. As seen in Section 4.2, an exception is LAM, which operates with traditional LSR. The majority of the processes demand thermoplastics or UV-curable resins. Consequently, the rubber-like options for 3D printing comprise already existing as well as newly developed materials with improved properties, such as thermoplastic elastomers, silicones and elastic photopolymers.

Some of the current AM technologies are capable of processing elastic materials, and more and more soft materials appear every day. Table 4.1 summarises the material feasibility for several 3D printing technologies, including the appropriate elastic option. The table also provides some commercially available elastomeric materials for these technologies.

For elastomeric materials in general, the printing of complex geometries is more arduous compared to stiff materials. The support structures cannot be easily removed in the case of breakaway due to the elastic nature of the material. In the case of printing support structures with other materials, this may be unfeasible on account of material compatibility.

Table 4.1: Commercially available materials for AM technologies of elastomers.

Technology	Material requirement	Elastomeric options and manufacturers
MJF (HP)	Thermoplastic powder (*TPEs*)	Estane 3D TPU M95A (Lubrizol, USA) Ultrasint TPU01 (BASF, Germany)
FFF	Thermoplastic filament or pellets (*TPEs*)	Filaflex family 60A-95A (Recreus, Spain) TPU 95A (Ultimaker, Netherlands) Third-party companies*
LAM (innovatiQ)	High-viscosity thermosetting liquid (*LSR*)	Silastic 3D 3335 LSR (Dow Corning, USA)
Material Jetting	Low-viscosity photopolymer (liquid) (*elastic photopolymer*)	AR-G1L/H (Keyence, Japan) Tango family, Agilus, Elastico (Stratasys, Israel-USA) VisiJet family (3D Systems, USA)
SLS	Thermoplastic powder (*TPE*)	Duraform family (3D Systems, USA)
Vat photopolymerisation	(Liquid) photopolymer (*elastic photopolymer*)	EPU family, SIL 30 (Carbon, USA) Elastic 50A (Formlabs, USA) Elastomeric 8195 Gray (Loctite, Germany)

*See Bakir et al. (2021) for more TPE options.

Alternative materials (TPEs and elastic photopolymers) typically have an inferior mechanical behaviour (Lukić et al., 2016; Ligon et al., 2017) in terms of operational performance and lifespan compared to conventional materials. The combination of large allowable deformations with a total and instantaneous recovery after releasing the stress, along with long-term stability, is not always fully achieved. TPEs, for instance, display a significant permanent set, while photopolymers in general are subjected to further hardening under exposure to light. Nevertheless, there is a continuous development in material science, which is changing the everyday scenario; materials are improved, and new ones with enhanced mechanical properties are created.

Among the available TPEs, TPUs are widely used in 3D printing. Although the different types of TPEs exhibit flexibility (i.e. ease of bending), TPU also shows good elasticity (i.e. ease of stretching) and better recovery, which is not a rule for all thermoplastic elastomeric materials. Some restrictions on 3D printing with TPUs are particularly related to FFF. Printing with TPU filaments is already known to the 3D printing community as a challenging task. The main issue is the under-extrusion, in other words, the extrusion of less material than intended. The extrusion control is hindered by the buckling of the filament due to its low stiffness (Gilmer et al., 2018). The lower the hardness, the more difficult the extrusion control becomes. As a consequence, the use of TPUs with hardness below 70 Shore A requires an intensive knowledge on the material and adjustments on the 3D printer. In fact, this is the lowest hardness commonly used for TPUs in FFF, even though a filament of hardness of 60 Shore A has been recently introduced in the market by the company Recreus (Elda, Spain). Furthermore, the use of a Direct extruder over a Bowden extruder is preferred. The first extruder type is mounted directly on the print head. The second is mounted away from the print head, requiring a longer section of filament being compressed and, hence, more chance of buckling. Pellet-based systems are an alternative to eliminate buckling during printing of elastic materials.

Moisture is another issue when dealing with TPUs, especially in FFF. As they are hygroscopic, TPUs easily absorb moisture from the air if not properly stored during printing and when the filament is not in use. The usual printing temperatures above 100°C lead to steam formation at the hot end, inducing bubbles and voids in the material flow. The result is a part with a lower quality due to bubbles trapped inside and induced cracks. The filament diameter may also change depending on the absorption levels, which impairs the extrusion process even more, and sometimes leads to the interruption of the print job (Herzberger et al., 2019). These extrusion failure issues were addressed and documented in Bruère et al. (2022a) and Bruère et al. (2022b). In Loos et al. (2021), the moisture absorption of some 3D printing elastomers was investigated and published.

For vat photopolymerisation techniques, in addition to the constraints of 3D printers, the photopolymers are typically limited by design strategies and material chemistries (Shaukat et al., 2022). In particular, the 3D printing with elastomeric resins demands a denser support structure to handle the peeling forces. Furthermore, the longer the post-curing processes, the higher the hardness of the final part, which should be soft.

It can be affirmed that each AM technology has its own particular printing conditions and post-processing procedures. The quality and the mechanical performance of the final prints are affected not only by the material but also by the process deviations and the choice of the printing parameters. As the author had direct experience with the printing of samples by means of FFF and LAM, those are further explored.

The printing of silicone parts with LAM has the benefit of using traditional silicone. However, besides the drawbacks presented in Section 4.2.2, the process is very susceptible to the appearance of bubbles. They can be caused by the choice of printing parameters and strategy, which did not extrude enough material to fill the voids, or even did not allow sufficient time for the silicone to spread through the geometry and fill those voids before curing. They can also be caused by inadequate operation of the pressurised system. If the machine is constantly turned off and on (and so the pressure), it conditions the silicone cartridges to air inside the flow. At the same time, bubbles in the first layer can be a result of a distance greater than appropriate from the nozzle to the building plate. The dominant parameters in LAM are presented below, which should be adapted for each geometry:

- Layer height:
  It is the height of each layer deposition. For a 0.4 mm nozzle, for instance, the layer height should be in the range 0.39-0.41 mm;
- Flow:
  It stands for the correction factor in the amount of material extruded, also called extrusion multiplier. The higher the flow, the lower the chances of bubbles but also the higher the chances of the object exceeding dimensional tolerances;
- Line width:
  It is the width of each deposited silicone thread. Combined with the layer height and the flow, it controls the volume of extrusion and, hence, improves the printing; and
- Retraction settings:
  These parameters are adapted in order to avoid stringing as well as the lack or excess of material at the end of a path.

For FFF, some key parameters that influence the mechanical properties of TPU-printed parts are listed and discussed by Bakir et al. (2021). The fusion of lines within the same layer and between layers as well as the air gaps inherent in the process have an impact on the mechanical behaviour of the printed geometry. The printing parameters suggested by filament manufacturers are often insufficient. Information on the matter and troubleshooting are acquired via online exchanges with the 3D printing community and experience. For elastic filaments, the following parameters have a substantial effect on print quality and should be adjusted as follows:

- Higher nozzle temperatures:
  It directly influences the flow dynamics during extrusion. Too low nozzle temperatures do not melt the material sufficiently, leading to nozzle clogging and incomplete fusion between the layers. Too high nozzle temperatures may cause warping and material degradation. The temperature for TPU filaments should be preferably in the upper range, as a way to compensate the under-extrusion issues;
- Increased flow:
  Similar to the nozzle temperature, a higher flow helps in correcting the under-extrusion typical of FFF with elastic filaments;
- Low retraction:
  Retraction corresponds to the filament being pulled back in order to prevent dripping and stringing of material during the displacements of the print head. As the extrusion control is already hindered, retraction should be minimal (or even deactivated). Faster print head movements in the X–Y plane can compensate the low retraction settings without inducing too much stringing into the printing; and
- Lower printing speeds:
  Slower printing allows more time for the material to be extruded and to successfully bond to the previous layer. The print speeds for elastic filaments are the lowest in FFF.

The raster orientation, the layer height and the line width are also noteworthy, as for any type of filament. The first parameter represents the trajectory of the thread deposition within a layer, frequently referred to as the infill direction path. Common raster orientations are 0°, 90°, 45° and -45°, relative to the loading direction. The second parameter is directly associated to the printing resolution, as well as the printing time. The lower the layer height, the smoother the surfaces and the longer the printing time. The third parameter affects especially the first layer, and is related to part strength and print quality. A higher line width improves the adhesion of the first layer and increases the strength of the print; a lower line width delivers geometries that are more precise.

The wide range of AM elastomeric material options and printing parameters lead to a wide variety of resulting mechanical properties. Furthermore, both technologies and materials for soft polymers in particular are still somewhat immature. The offer of materials in the market is still small compared to stiff polymers. Moreover, the catalogue for elastomeric solutions is more oriented to flexible rather than elastic materials, and the softer the elastomer, the fewer options there are. Additionally, they are primarily appropriate for prototyping and component design, not (yet) for the manufacturing of functional parts. Research in the area has been increasing, although it is still modest compared to rigid polymers and metals.

70

5. Materials and Methods

Several materials from the technologies presented in Chapter 4 were selected and characterised by means of thermal and mechanical testing. This chapter describes the methods for the tests performed, including the materials investigated, the preparation of the samples and the setup of the experiments. Remarks on the printing processes practiced and the obtained samples are reported. The material characterisation was conducted with the help of tensile, cyclic and relaxation tests as well as Differential Scanning Calorimetry (DSC) and Dynamic Mechanical Analysis (DMA) tests. Each of the following chapters deals with one specific type of test, presenting the results and comparatively discussing pertinent properties.

5.1 Materials

The aim was to investigate at least one type of each major group of elastomers from Chapter 3, that is, at least one silicone polymer, one TPE and one elastic photopolymer. With this in mind, the AM technologies were chosen and the appropriate materials were selected based on the availability of machines and materials at the Institute of Mechanics (UniBw Munich, Germany) and at the partner research institute WIWeB (Erding, Germany). In case of unavailability, samples were acquired from printing services in the market. The investigated materials can be seen in Table 5.1, where the first column indicates the material terminology used in this work. Information about the technology and the 3D printers used is also provided.

Recreus 70A and *Recreus 82A* are specified as thermoplastic polyether-polyurethane elastomers with additives. These TPU elastic filaments can be highly stretched to more than 600% of their original size. The numbers in their names stand for the Shore A hardness of the filaments. They exhibit great bed adhesion without the need of heating the build platform. Furthermore, the manufacturer states that the filaments are odourless and resistant to solvents, acetone and fuel. Another category of TPE was investigated, and the material selected was *Arnitel*. This filament is a bio-based thermoplastic copolyester (TPC) filament. According to the manufacturer, it has high UV and chemical resistance as well as high energy return. Moreover, it is considered to be suitable for soft, flexible applications, e.g. shoe in-soles and midsoles, protective sport equipment, gaskets and tubes.

Table 5.1: Specifications and printing information for the investigated materials.

Material	Technical name	Company	Technology	3D printer
Arnitel	Arnitel® ID2045	DSM (NL)	FFF	innovatiQ x500
Recreus 70A	Filaflex 70A	Recreus (ES)	FFF	innovatiQ x500
Recreus 82A	Filaflex 82A	Recreus (ES)	FFF	innovatiQ x500
Duraform	DuraForm® TPU Elastomer	3D Systems (USA)	SLS	sPro 60 HD-HS
Estane	ESTANE®0, 3D TPU M95A	Lubrizol (USA)	MJF	HP Jet Fusion 4200 Series
Wacker	ACEO® Silicone GP	Wacker Chemie AG (DE)	DOD	ACEO® Technology
Silastic	SILASTIC™ 3D 3335 LSR	Dow Corning (USA)	LAM	innovatiQ L320
Tango 30 | 40 | 50 | 60 | 70	TangoBlackPlus and VeroClear	Stratasys (IL-USA)	PolyJet	Objet500 Connex
Agilus	Agilus30 Black and Vero	Stratasys (IL-USA)	PolyJet	Not informed
Keyence H | L	AR-G1H | AR-G1L	Keyence (JP)	MJM	Agilista-3000

Duraform and *Estane* are thermoplastic polyurethanes, originally in powder form. According to the manufacturer, Duraform exhibits rubber-like flexibility. It is recommended for functional prototypes of gaskets, seals and hoses, and for the prototyping and production of footwear components. Estane is a polyether thermoplastic polyurethane reported as appropriate for both prototyping and manufacturing. In addition, it shows high energy rebound and good abrasion resistance.

Wacker is the term designed for the UV-cured silicone used in Wacker's trademark Aceo® 3D printing technology. Although information on the material and the technology have been difficult to obtain, it is known to be a DOD-based process with water-soluble support material. It uses inorganic synthetic rubber, whose platinum catalyst is activated by UV light. This technology was presented in Section 3.3.1. The printed silicone undergoes vacuum post-curing at 200°C for 4 hours to improve the mechanical properties and remove the volatiles. The end product is said to show UV resistance, sterilisability and thermal stability. ACEO was a printing service provider for silicone prototypes and small series goods. Although being an innovative technology with revolutionary potential, the service was unfortunately discontinued in December 2021. Experts indicate poor marketing and continuous coverage by industry-specialised media, especially on a global scale, as a major cause for the lack of success (3D Printing Media Network, 2021).

Silastic is a conventional two-component (1:1 mix ratio) viscous LSR. The material is platinum catalysed and thermally cured, with a hardness of 50 Shore A. This LSR was developed by Dow Corning (Midland, USA) specifically for the LAM technology. It is recommended for fast prototyping, and small-scale manufacturing of complex parts and applications where typical LSRs are employed. Silastic offers the performance benefits of standard silicone rubbers while allowing the processing advantages of 3D printing. Thermal ageing begins to take place only above 100°C if the material is kept in this condition for a few weeks. If exposed for a short time, its temperature resistance is of 200°C. Resistance to UV and ozone are also typical of Silastic.

The Tango materials consist of photopolymers that are a combination of the components TangoBlackPlus and VeroClear. The higher the content of the first component, the softer the material is. *Tango 30* corresponds to a printing with a 100% TangoBlackPlus, i.e. no VeroClear is present in the mixture. The terminologies (*Tango 30*, *Tango 40*, *Tango 50*, *Tango 60* and *Tango 70*) are associated with the hardness Shore A grades resulting from the mixture of the two base components. All samples are black in colour. For Tango 30, a transparent sample was also obtained, referred to as *Tango 30 (t)*. For the samples made from the *Agilus* material, only a hardness of 50 Shore A was investigated. As for Tango, the material is a combination of Agilus30 Black (originally with a hardness of 30-35 Shore A) and Vero (a stiff thermoset acrylic resin).

Keyence H and *Keyence L* are elastic, silicone-based photopolymers with the same chemistry. The silicone content is what gives the different hardness grades and elastic capabilities. The first is heat resistant to 150°C, while the second is more flexible and withstands temperatures up to 200°C. The materials are specially developed for the technology itself (closed source); the type of material is chosen in the slicing software and no printing parameters need to be manually set. The printing makes use of a water soluble support material and does not need post-curing stages.

A chemical characterisation using Infrared Spectroscopy for Recreus 70A, Silastic, Tango 70 and Tango 50 was published in Loos et al. (2021). The Recreus 70A and 82A TPU filaments showed the same composition, being identified as polyether polyurethanes, as specified by the manufacturer. The higher soft-to-hard segment ratio of Recreus 70A is responsible for the softer nature of the filament (as explained in Section 3.3.2). Silastic was confirmed as a silicone, with the Si-O-Si backbone. The Tango photopolymers were identified as polyurethane acrylates. As the chemistry is not the focus of this work, no further investigations were conducted. The material properties obtained from the manufacturers are shown in Table 5.2.

Table 5.2: Material properties for the investigated samples.

Material	Tensile Strength (MPa)	Elongation at break (%)	Tensile testing standard	Shore hardness (A)
Arnitel[1]	8.0 (0°/90°) 7.6 (45°/-45°)	350 390	ISO 527-1/-2	85
Recreus 70A[2]	32.0	900	DIN 53504-S2	70
Recreus 82A[3]	45.0	650	DIN 53504-S2	82
Duraform[4]	2.1	200	ASTM D412	59
Estane[5]	17.0	400	DIN-53504 / ISO-37	93 ± 3
Wacker[6]	7.0	250	ISO 37 Type 1	50
Silastic[7]	9.5	480	ASTM D412	50
Tango 30[8]	0.8-1.5	170-220	ASTM D412	26-28
Tango 40[9]	1.3-1.8	110-130	ASTM D412	35-40
Tango 50[9]	1.9-3.0	95-110	ASTM D412	45-50
Tango 60[9]	2.5-4.0	75-85	ASTM D412	57-63
Tango 70[9]	3.5-5.0	65-80	ASTM D412	68-72
Agilus[9]	3.0-4.0	120-170	ASTM D412	50-55
Keyence H[10]	2.0-2.5	160	ASTM D412	65
Keyence L[10]	0.5-0.8	160	ASTM D412	35

[1]Colorfabb (2022); [2]Recreus (2022a); [3]Recreus (2022b); [4]3D Systems (2022b); [5]Lubrizol (2022); [6]Wacker (2019); [7]Dow (2022); [8]Stratasys (2022b); [9]Stratasys (2017); [10]Keyence (2020).

In total, four TPUs, one TPC, two silicone types and eight photopolymers were analysed. Keyence L, the two silicones, Agilus and the Tango grades 30 to 50 are *Medium Soft* (hardness of 25-55 in the Shore A scale). The Recreus filaments, Arnitel, Duraform and Keyence H are *Medium Hard* (hardness of 55A-85A). Estane is the only *Hard* material (hardness of 85A-100A).

Throughout the research, the Institute of Mechanics was equipped with LAM and FFF 3D printers, which were personally operated by the author herself. Although the institute owned a DLP 3D printer as well, it was not possible, due to the timeframe of the research, to handle printing on a third machine.

For other vat photopolymerisation techniques, there were no materials + technologies available, as there are specific materials that can only be printed in specific technologies (closed source). In addition, a proper printing service was not found. In fact, several AM processes had elastomeric options in their material catalogue but either there was no printing service or the material was not available for the service. No response was received after the attempt to reach Formlabs. The company Carbon was contacted, but demanded a non-disclosure agreement and is based in the USA. For Binder Jetting, Aerosol Jet and LOM, no suitable elastomer offers were found at the time. Since 3D Dispensing is mainly targeted at biological applications and MPP is dedicated to nano-scale printing, these technologies were not explored.

Duraform, Estane, Wacker and Agilus are among the acquired samples from printing services. It is worth mentioning that other elastic materials appeared in the market while the research was being conducted, but were not investigated. Examples include a Recreus filament with a hardness of 60 Shore A and the resins Elastico and TissueMatrix from Stratasys.

5.2 Sample Printing and Preparation

For all thermomechanical tests, except DSC, the S3A dumbbell geometry from the Standard DIN 53504 (DIN, 2017) was used. The specimens from Wacker, Duraform, Estane and Agilus were acquired from printing services. Keyence H, Keyence L and Tango specimens were provided by the institute WIWeB. Recreus 70A, Recreus 82A, Arnitel (FFF) and Silastic (LAM) specimens were printed by the author. Due to the material and for cost saving reasons, Wacker and Duraform were obtained directly as S3A dumbbells. Recreus 70A, Recreus 82A, Arnitel and Silastic were printed as square plates of 60x60x2 mm³ while Agilus, Estane, Keyence H, Keyence L, and the Tango grades were printed as square plates of 120x120x2 mm³. All printings were obtained with 100% infill. The dumbbells were then punched from the plates. Particularly for the FFF and LAM specimens, this allowed printings with a fully unidirectional infill without contour lines. The staircase effect within the same layer was avoided (Figure 5.1) and a smooth transition in the cross section was ensured. Furthermore, gaps in the infill were also avoided. These gaps appear especially for the infill at 0° relative to the tensile direction if the specimen is printed with contours, and are stress concentration points (Figure 5.2), as addressed by Plott et al. (2018a).

74
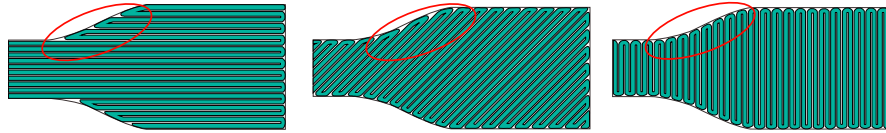
Figure 5.1: Staircase effect in a layer due to the absence of outlines for 0°, 45° and 90° infill angles (from left to right).
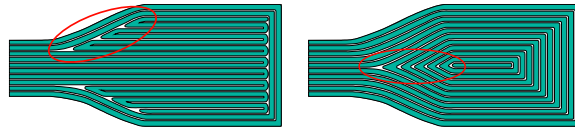
Figure 5.2: Infill gaps on specimen with outlines for rectilinear and concentric filling (from left to right).

The line deposition in material extrusion (e.g. FFF, LAM) processes is widely called raster in the 3D printing field. For the Arnitel specimens, the plates were printed with horizontal and diagonal raster orientations. The dumbbells with unidirectional infill angles at 0°, 45° or 90° were punched and submitted to tensile tests. The investigations with Arnitel were limited to this stage (as discussed later in Chapter 6). The effect of the infill angle on Recreus 70A and 82A was studied and documented in publications of the author (Bruère et al., 2022b; 2023). It was concluded that there is no influence of the infill orientation on the tensile properties for the lower strain range ($\varepsilon < 100\%$). For the higher strain range, the infill at 90° is the critical condition and, therefore, analysed in this work.

The plates for the FFF materials were manufactured on an x500 3D printer from innovatiQ, equipped with a 0.4 mm nozzle and a Direct Drive extruder. The appropriate filament diameter for the machine is 1.75 mm. As recommended for the printing of elastic filaments, the retraction settings were minimised. Nevertheless, they were not relevant in this case. The printing of plates without contour lines led to a continuous material flow throughout each layer, eliminating under-extrusion effects due to retraction. In addition, the spool was confined in a storage box to prevent moisture absorption during printing. More details on humidity control are provided in Section 5.3.

Combined with low printing speeds, the under-extrusion was minimised. The drying of the filaments prior to printing was performed when signs of moisture were detected. In these cases, the filaments were dried at 50°C for at least 4 hours in a Nabertherm TR60 convection oven (450 × 380 × 350 mm). Recreus 70A and 82A showed a good bed adhesion; only skirts, i.e. outlines surrounding the part without touching it and ensuring a fine flow at the beginning, were applied. On the other hand, Arnitel was subjected to warping, which led to the use of brims (i.e. outlines touching the part) associated with glue on the print bed to avoid this effect.

The plates from Silastic were printed one at a time in just over four hours on a L320 3D printer from innovatiQ (a former version of the current LiQ320) with a 0.4 mm nozzle. Similarly, only skirts were applied to the geometry. Considering the volumetric extrusion, the flow was considerably increased in order to squeeze the lines together and avoid the appearance of bubbles. Although this led to exceeding the dimensional tolerances of the plate, it was not critical since the specimens were then punched. The single dimension of

interest was the height of 2 mm. Therefore, only four layers of 0.4 mm height each were printed; the high flow compensated the lack of a fifth layer and the desired total height was achieved. After the finishing of each layer, there was a waiting time of 5 minutes before the lamp for the thermal curing passed over the geometry. This enabled the silicone to flow and settle in the layer, further reducing the chances of gaps. Two additional lamp movements at the end of the print job were necessary to complete the curing process. The Silastic plates were visibly clear and uniform, with a very slight undulation on the top layer, with strong indications of the isotropy mentioned by the L320 printer manufacturers. For this reason, the specimen punching direction was not worthy of analysis. An alteration in the microscale is, however, not discarded, and is an interesting topic for future studies. For consistency in the results, all specimens were punched with an "infill angle of 0°".

Both the x500 and the L320 models use the slicing software Simplify3D. The printing parameters were studied and adapted following the recommendations presented in Section 4.3. Temperature optimisation was also performed for the Recreus filaments (see Appendix A). The final printing parameters can be seen in Table 5.3 (printing G-Code settings available in Appendix B.1). The layer height for the L320 printer is limited to the range between 0.39-0.41 mm, while the printing speed for the 0.4 mm nozzle should be between 5 and 10 mm/s for a successful print job.

Table 5.3: Printing parameters for the FFF and LAM processes.

Parameters	Arnitel	Recreus 70A	Recreus 82A	Silastic
Printing temperature (°C)	230	240	230	-
Bed temperature (°C)	45	30	30	-
Printing speed (mm/s)	10	10	10	6.7
Layer height (mm)	0.2*	0.2	0.2*	0.4
Line width (mm)	0.48*	0.48*	0.48*	0.41
Flow (%)	120	135	135	145
Infill angles (°)	0 | 45	0	0	0

*First layer with 130% increase.

For the requested specimens, details on the printing parameters were not readily available. For some 3D printers, e.g. Agilista from Keyence and Connex from Stratasys, the selection of the material in the closed-source machine software defines the already optimised printing parameters, the so-called "digital materials" mode. For the Connex 3D printer, the only choice available is the mixing ratio for the different Tango hardness grades. To provide an insight, the layer height resolutions of the other 3D printers are shown in Table 5.4. No information on the ACEO technology could be found. Figure 5.3 illustrates the Connex and Agilista printers.

Table 5.4: Typical layer heights for the employed 3D printers.

3D Printer	sPro 60 (SLS)	HP Jet Fusion 4200 (MJF)	Objet500 Connex (PolyJet)	Agilista-3000 (MJM)
Resolution (µm)	80-150	80	16-30	15

Figure 5.3: Objet500 Connex (left) and Agilista-3000 (right) 3D printer series
[courtesy of WIWeB].

5.3 Remarks on Printing and Final Samples

Additional comments regarding the printing process in the filament and silicone printers are presented. Common issues and solutions until the achievement of the final printing parameters are described. Furthermore, observations on the requested samples are provided.

5.3.1 Printing with FFF and LAM

Since moisture is a relevant issue for hygroscopic materials such as TPUs, a solution was sought to keep the humidity levels in the filament as steady as possible during printing and to preserve print quality. At first, a commercially available storage box, called PolyBox, was used. It contained silica inside and ensured humidity below 15%. The tube coming out of the PolyBox was directly connected to the tube (on the left side) of the printer. In spite of that, there was an inconsistency in the flow for the Recreus 70A and 82A materials due to under-extrusion, even with the Direct extruder. As reported in Bruère et al. (2022a), there was friction of the filament inside the PolyBox and printer tubes towards the nozzle, although the filament was kept as loose as possible to reduce this effect (Figure 5.4, left).

The final solution for these two materials was a custom-made storage box containing the filament length necessary for only one printed plate coming out of a hole. In this way, the spool was spared from the exposure to moisture in the course of the print job. There was no silica inside this box as in PolyBox. Nonetheless, the printing of one plate took approximately four hours, during which the exposure to air was prevented. An improvement of this solution by adding moisture control with silica is under consideration. The material came out of the box directly into the print head, without tube connections and avoiding its related friction. A very light pull of the filament by the extruder was enough to take the required amount out of the box, also assisted by gravity. Although a short length

of filament was exposed to air during printing, this exposure was brief. In addition, the filament was in large, loose loops supported by a black shaft free to roll (Figure 5.4, right).
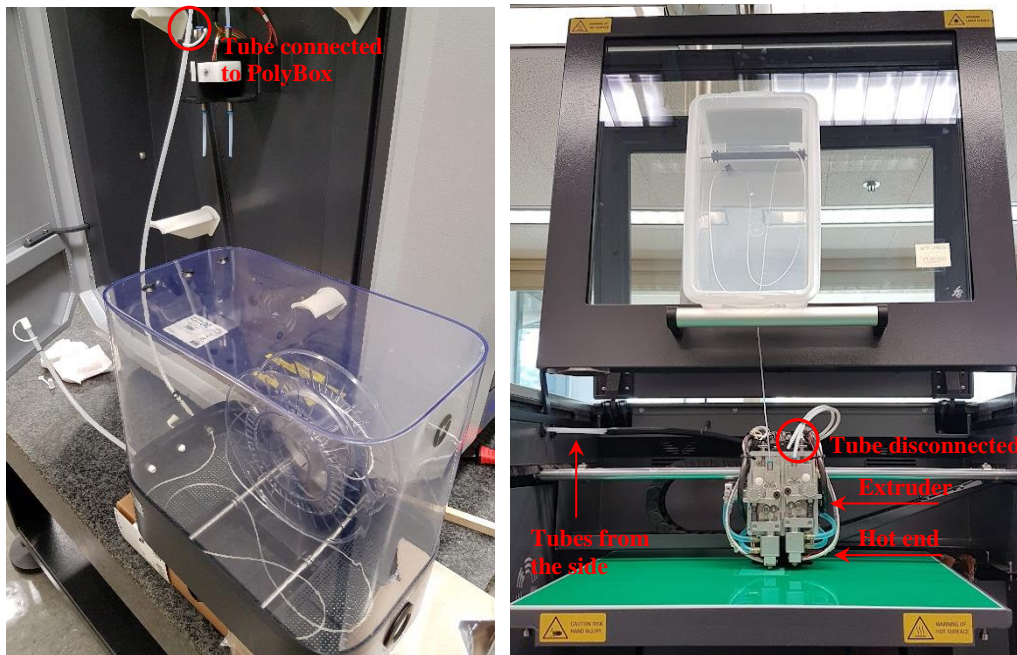
Figure 5.4: Humidity and under-extrusion solutions for FFF:
PolyBox connected to the tubes (left), and custom-made storage box with filament inserted directly in the print head (right).

When dealing with elastic materials in FFF, one should bear in mind that under-extrusion is nearly inevitable. For stiff filaments, the indentation generated by the extruder movement deforms the filament plastically, which aids the extrusion process. However, the extruder teeth do not easily deform the elastic filament, but rather compress it. This compromises the motor grip on the filament. If the gear teeth are already slightly worn or there is leftover material between them from extruding other filaments, the grip is worsened. In this way, the elastic filament is at risk of slipping on contact with the extruder and not being properly pushed towards the hot nozzle. This incident took place during printing on the innovatiQ x500 and hindered the repeatability of plate printing. Furthermore, the softer the filament, the more challenging it was to print in FFF and the more under-extrusion issues occurred.

Dimensional changes in the filament may also appear as a result of moisture absorption and lead to under-extrusion. In addition to the bubbles induced in the flow, the nozzle can become clogged as the filament diameter increases. For this reason, the nozzle was frequently cleaned with the so-called *hot pull* and *cold pull* (often before each plate print) apart from the drying processes.

Regarding printing silicone parts in the innovatiQ L320 printer (Figure 5.5), a few points are worth addressing. At first, the LAM machine seemed easier to use than the FFF printer. There were fewer variables involved in the process. The repeatability was also considerably higher. Starting from the factory printing parameters, which are set to Silastic, some parameters were adjusted to succeed in the print job. The main parameters to be adapted for the desired geometry were the layer height, the flow and the line width, as commented in Chapter 4. However, this process was proven to be more arduous than expected.
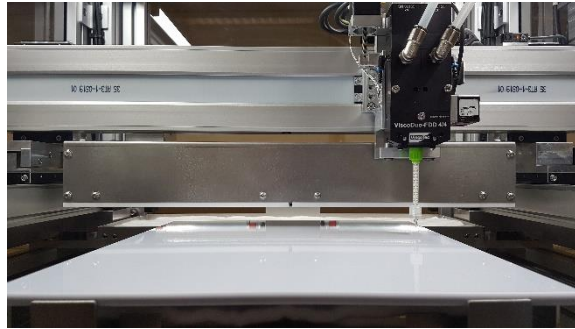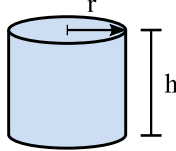
Figure 5.5: L320 3D printer series.

The concept of volumetric extrusion should be understood for a more conscious adjustment. Recalling the definition of *flow* presented in Section 4.3, this printing parameter corrects the extrusion to match the desired amount of material to be deposited. Hence, the volume of a cylinder is multiplied by a correction factor given by the extrusion multiplier, i.e. flow. This volume considers the effective amount of silicone coming out of the nozzle (Figure 5.6). For instance, the presence of bubbles was reduced by decreasing the line width so that the deposition lines were closer together and the air was squeezed out of the sample. If the amount of material was sufficient in the first case, the flow needed to be increased to compensate the lower amount with the new line with, as long as the final volume was maintained. The final printing parameters were obtained by trial-and-error based on these calculations.

$$\text{Volume}_{\text{cylinder}} = \pi\, r^2 h$$

$$\text{Volume}_{\text{extrusion}} = \pi \left(\frac{\text{line width}}{2}\right)^2 (\text{layer height}) \, (\text{flow})$$

Figure 5.6: Basic calculation for the volumetric extrusion in LAM.

According to the manufacturer, the parts printed in the L320 machine show the same properties as those produced by injection moulding. This was not verified by the author. Furthermore, the 3D printer is theoretically able to print silicone materials in a broader range, and not only the current Silastic LSR of 50 Shore A hardness. Polyurethane is an alternative, and its use in the L320 printer has been demonstrated in trade fairs. An important aspect is the high viscosity. In this context, knowing the material is crucial for the mastering of the parameters leading to successful prints. When changing the printing material, the viscous properties and thus the deposition behaviour are also different. These must be intimately known to the user in order to be able to adjust the printing parameters for this material.

With LAM printing, the under-extrusion issues related to the pushing of a filament common in FFF were eliminated since the printing material was a highly viscous fluid. The liquid material also offered great adhesion. The use of actual liquid silicone rubber is a major advantage, resulting in a part with the benefits of a real feel of rubber, thermal stability, heat resistance and many others. In addition, the infill raster angle does not influence the

mechanical behaviour of the print due to the liquid nature of the silicone, which settles between the deposited lines.

On the other hand, some issues are associated with this technology. Besides electricity, a pressurised system at 4 bar is required for the operation of the machine. Furthermore, the layer height is limited to 0.39-0.41 mm, and the final part height to its multiples. No support structures can be printed, although by changing the printing strategy some overhangs are possible. The user should be aware of the silicone shrinking in about 3% after cooling and consider the necessary dimensional changes in the 3D model to achieve the desired size of the final part. As the samples were obtained from printed plates, shrinkage did not play a role in this work.

A continuous use of the L320 is recommended. Otherwise, the silicone inside the mixer and nozzle hardens completely in about a week without extruding (and eventually having to discard them and replace them with new components). Failed prints were also obtained after the machine had not been used for some time (Figure 5.7). In contact with technical support, no other causes could be identified. A solution found for this matter was to extrude some amount of silicone every day, or every other day, to replace the old silicone hardening inside the extrusion head with a freshly mixed one. In this way, the printer is kept running regularly while preserving the mixer and nozzle. A FFF printer works in a simpler way. It only needs to be plugged in, can be used more sporadically and, depending on its size, can be moved around.

Figure 5.7: Failed reproduction of a previously successful print after some time without operating the L320 printer.

As for FFF, the printing strategy in LAM can lead to gaps in the geometry (as seen in Figure 5.2), which will turn into air bubbles with the deposition of the next layer. The difference is that by adjusting the printing parameters as previously mentioned, the air bubbles can be reduced and even avoided (see Figure 5.8), while FFF printed parts continuously have some degree of porosity. An alternative used to minimise bubbles was to allow some time for the silicone in a printed layer to settle before curing it, hence a waiting time of 5 min was introduced before the lamp movement. These resources, however, took some time to be learned and to understand how the silicone printer works. Similarly to FFF, the deposition of the silicone was slow.
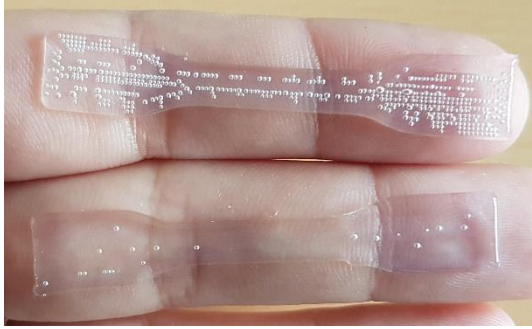
Figure 5.8: Example of reduction of bubbles by adjusting printing parameter.

5.3.2 Characteristics of the Requested Samples

In general, the photopolymers presented a strong and particular smell. The other elastomeric materials were odourless. The intensity of the smell was the greatest shortly after printing and receiving the samples. It decreased slowly over time, especially after the materials were in contact with the atmosphere. In conversation with employees at Keyence and Stratasys, it was found that their photopolymers do have this odour and that it has to do with their chemistry, although not further clarified which substances cause it. In addition, the PolyJet photopolymers had a considerably sticky surface, which made it difficult to handle the samples and place them in the testing machines. Their tackiness was justified by leftover support material that was not fully removed in the post-processing stage. However, the tackiness was never fully gone.

Few elastomeric materials for AM were available in the material catalogues, and even fewer in printing services. This applied to all 3D printing technologies surveyed. The offer of stiff materials was much larger. Furthermore, elastic photopolymers were constantly reported to be limited to prototyping purposes. The Stratasys staff claimed that they are not intended for functional parts, but rather for aesthetic models. They will deteriorate over time, especially with regular exposure to UV radiation. Signs of deterioration were said to comprise cracking, crumbling and deterioration in corners/crevices or areas of the print where more pressure is applied. A lower bounce back behaviour compared to conventional rubber was also reported by Stratasys. Moreover, they seemed more fragile than the other materials, particularly the softer the Tango grade was.

Among all samples, only Wacker had a smooth, tactile surface similar to Silastic. No odour was detected for the DOD printed silicone. The Estane samples were initially found to be quite stiff, although capable of bending to some degree. They could not be easily pressed by fingers like the other samples. They were, however, the hardest of all. Additionally, Duraform was soft and its specimens showed some compressibility to the touch. Nonetheless, the TPU powder did not seem properly fused, evidencing a crumbling quality. Microscopic images of the surface topography of the printed and requested samples can be seen in Appendix B.2. The porous nature due to the powder-based technologies was particularly noticeable in Duraform and Estane, while the LSRs and the PolyJet photopolymers showed the lowest surface roughness.

5.4 Testing and Setup

For the uniaxial mechanical testing (tensile, cyclic and relaxation tests), a ZwickRoell universal testing machine was used at room temperature (23°C), with a force sensor of 500 N (Xforce HP from ZwickRoell, accuracy of 1 N) and an initial gauge length of 15 mm. Since this work was aimed at a comparative analysis, each set of tests was carried out for all materials with the same displacement rates. The specimens were held by a pair of pincer clamps with a rough surface for better grip. However, these clamps were damaging the softest PolyJet materials, namely Agilus, Tango 30, Tango 40 and Tango 50. Round, polished clamps already available in the laboratory were also ineffective, tearing the specimens with the gripping pressure. Therefore, a pair of flat, polished clamps was manufactured (Figure 5.9, right). Since the PolyJet materials exhibited considerable tackiness, there were no grip issues regarding slipping, although the aligned positioning of the samples in the clamps was more challenging than for the remaining materials.

Figure 5.9: Pincer grip and the three types of clamping surface attempts (successful in green, unsuccessful in red).

The stresses from the uniaxial mechanical experiments are presented in terms of nominal stress, that is, the PK1 stress in the reference configuration (defined in Chapter 2, Eq. 2.52). For the uniaxial tension state of an incompressible material ($J = 1$), from Eqs. 2.61 and 2.62, the PK1 stress tensor **P** can be written as in Eq. 5.1. Applying the uniaxial loading conditions to Eqs. 2.54, 2.17 and 2.20, the PK2 stress tensor (**S**) and the right Cauchy-Green (**C**) and Green-Lagrange (**E**) material strain tensors assume the form of Eqs. 5.2, 5.3 and 5.4, respectively:

$$[\mathbf{P}] = \begin{bmatrix} \sigma/\lambda & 0 & 0 \\ 0 & 0 & 0 \\ 0 & 0 & 0 \end{bmatrix} \tag{5.1}$$

$$[\mathbf{S}] = \begin{bmatrix} \sigma/\lambda^2 & 0 & 0 \\ 0 & 0 & 0 \\ 0 & 0 & 0 \end{bmatrix} \tag{5.2}$$

$$[\mathbf{C}] = \begin{bmatrix} \lambda^2 & 0 & 0 \\ 0 & 1/\lambda & 0 \\ 0 & 0 & 1/\lambda \end{bmatrix} \tag{5.3}$$

$$[\mathbf{E}] = \frac{1}{2} \begin{bmatrix} \lambda^2 - 1 & 0 & 0 \\ 0 & 1/\lambda - 1 & 0 \\ 0 & 0 & 1/\lambda - 1 \end{bmatrix} \tag{5.4}$$

Sections 5.4.1, 5.4.2 and 5.4.3 present the specific features of the tensile, cyclic and relaxation tests, respectively. Section 5.4.4 describes the experimental setup for the DSC measurements, while the machine and testing parameters for the DMA are in Section 5.4.5. The plotting and data analysis were conducted using the graphing software OriginLab, version 2020b. Table 5.5 shows a summary of the tests performed for each material.

Table 5.5: Thermal and mechanical testing per material.

Material	Tensile	Cyclic	Relaxation	DSC	DMA
Arnitel	X				
Recreus 70A	X	X	X	X	X
Recreus 82A	X	X	X	X	X
Duraform	X	X	X	X	X
Estane	X	X	X	X	X
Wacker	X	X	X	X	X
Silastic	X	X	X	X	X
Tango 30	X	X	X	X	X
Tango 30 (t)	X	X			
Tango 40	X	X	X	X	X
Tango 50	X	X	X	X	X
Tango 60	X	X	X	X	X
Tango 70	X	X	X	X	X
Agilus	X	X	X	X	X
Keyence H	X	X	X	X	X
Keyence L	X	X	X	X	X

5.4.1 Uniaxial Tensile Testing

The uniaxial tensile experiments were performed according to the Standard DIN 53504-S3A (DIN, 2017), also taking in consideration the information provided at the beginning of Section 5.4. The quasi-static behaviour was evaluated for 5 specimens per sample, for a total of 90 experiments (excluding preliminary and printing optimisation tests). A displacement rate of 15mm/min was applied throughout the test, corresponding to a nominal strain rate of 1.67%/s.

5.4.2 Uniaxial Cyclic Testing

The cyclic tests were similarly performed with a displacement rate of 15mm/min. Five strain levels were defined without waiting times between loading and unloading: 10%, 20%, 30%, 40% and 50%. Each strain level consisted of 10 loading-unloading cycles. To verify the repeatability of the results, 3 specimens per sample were tested (a total of 45, excluding preliminary tests). One of the representative curves for each material is presented and analysed in Chapter 7.

5.4.3 Uniaxial Stress Relaxation Testing

Deformations were applied to the specimens with a displacement rate of 200 mm/min (strain rate of 22.2%/s). The stress relaxation took place during a hold time of 12 hours. For each sample, 3 specimens were investigated. One of the representative curves for each material is presented and analysed in Chapter 8. In a first analysis, different strains were applied for each sample to verify their capabilities. For the PolyJet materials, there were damages to the specimens for similar strain levels as the other materials. Hence, all the Tango grades and Agilus specimens were submitted to lower strains of 15% for a comparison among them. Since Tango 30 and Tango 30 (t) had very similar behaviours, the latter was omitted in this and in subsequent investigations. Due to the low stresses in the PolyJet photopolymers, a smaller force sensor of 10 N (KD24s from ME Messsysteme, accuracy of 0.01 N) was used for these materials in a custom-made tensile testing machine. In a second analysis, the specimens were kept at a strain of 30% throughout the test. All materials except Agilus and the Tango grades 50, 40 and 30 withstood this strain. The other materials were tested in the ZwickRoell machine. Since the custom-made tensile machine was calibrated to the ZwickRoell equipment, a comparison of the results from both machines was possible.

The experimental data of each sample was fitted to a model using the Python programming language. Thereby, the viscoelastic parameters were analysed and the equilibrium stress reached at the end of the stress relaxation was predicted. A generalised Maxwell model of linear viscoelasticity was considered. Eq. 3.3 (recalled here) was rewritten to remove the equilibrium stress σ_∞, which is unknown, from the time-dependent stress expression with the help of Eq. 6.5. In this way, $\sigma(t)$ was given as a function of the parameters of the Maxwell elements and the (experimental) maximum stress σ_0 for the fitting. Optimisation runs were performed in Eq. 6.6 with the *scipy.signal.savgol_filter* function, which uses the non-linear least squares method. The stress-like constants, the relaxation times and, consequently, the equilibrium stress (from Eq. 6.5) of each sample were determined.

$$\sigma(t) = \sigma_\infty + \sum_{i=1}^{n} \sigma_i \, \exp\left(-\frac{t}{\tau_i}\right) \tag{3.3}$$

$$\sigma_\infty = \sigma(t = 0) - \sum_{i=1}^{n} \sigma_i \, \exp\left(-\frac{0}{\tau_i}\right) = \sigma_0 - \sum_{i=1}^{n} \sigma_i \tag{5.5}$$

$$\sigma(t) = \sigma_0 - \sum_{i=1}^{n} \sigma_i \left[1 - \exp\left(-\frac{t}{\tau_i}\right)\right] \tag{5.6}$$

5.4.4 Differential Scanning Calorimetry

A heat flux DSC 204 F1 Phoenix machine (enthalpy accuracy $< 1\%$) from Netzsch (Selb, Germany) was used for the caloric experiments. The two open aluminium crucibles consisted of an empty reference pan and a pan with the sample. One specimen per sample

of 6-10 mg was subjected to a specific temperature program. The amount of heat per unit time applied to the sample pan compared to the reference pan was then measured by the machine. The reproducibility of the results was verified, although not included in this work. For temperature programs with minimum temperatures above -90°C, the cooling process was carried out with gaseous nitrogen (GN2); for lower temperatures, liquid nitrogen (LN2) was applied. Nitrogen was equally used as purge gas. The three investigations conducted are described below.

Recreus Filament Drying

DSC experiments simulating the drying process of the Recreus filaments were performed. The specimens were cut from the filament spool. The temperature program consisted of 3 heating-cooling cycles at a rate of 10°C/min from 20°C to 50°C and 5-min isotherms at each temperature boundary. The second isotherm at 50°C is an exception, with a duration of 4 hours corresponding to the drying time (see Figure 5.10). The first heating scan (in Segment 1) has the purpose of "erasing" the material memory from the manufacturing process, while the third heating (after drying, in Segment 3) aims to verify changes in the measured mass specific enthalpy rate compared to the second heating (before drying, in Segment 2).
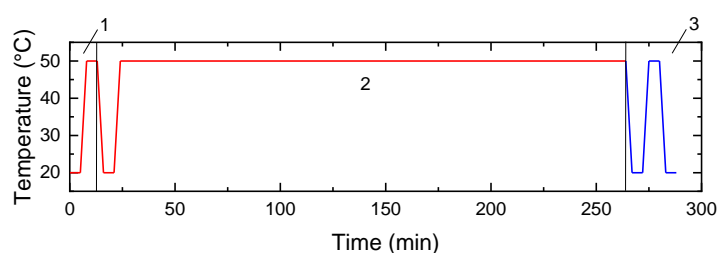
Figure 5.10: Temperature program for filament drying simulation.

Investigations on Recreus Filaments at Multiple Cooling Rates

As the Recreus 70A and 82A filaments were printed at a maximum of 250°C (see Appendix A), DSC tests were performed from -90°C up to this temperature. The specimens were cut from the filament spool. The main goal was to evaluate the effect of the cooling rate on the results and enable a preliminary analysis of the filaments' morphologies. Thus, cooling rates of 20°, 15°, 10° and 5°C/min were applied to the temperature programs. All heating rates were of 10°C/min. The glass transition temperature was also detected in these investigations. For its determination, the midpoint temperature corresponding to half of the step height was considered, since this method is recommended even in cases of unsteady baselines (Ehrenstein et al., 2004).

Figure 5.11 illustrates the temperature evolution over time. Segment 1 represents the erasing of the filament's memory, with an incomplete heating scan followed by a complete cooling-heating cycle. Segment 2 contains the first valid curve for the analysis. The cooling rate of both segments 1 and 2 was of 20°C/min. Segment 3 contains cooling at 15°C/min and subsequent heating. The same applies for segments 4 and 5, with respective cooling

rates of 10°C/min and 5°C/min. Segment 6 is cooling back to room temperature at the end of the experiment. Isothermal intervals of 5 min were implemented at each boundary temperature.
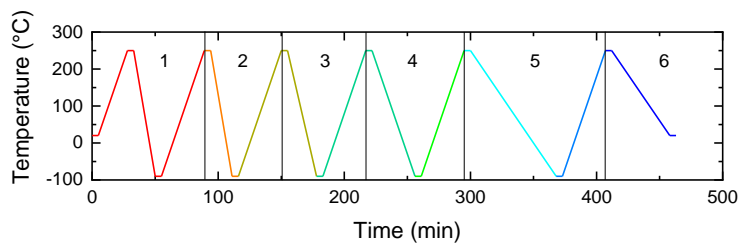
Figure 5.11: Temperature program for the investigations at multiple cooling rates of 20 °C/min (Seg. 1-2), 15°C/min (Seg. 3), 10 °C/min (Seg. 4) and 5 °C/min (Seg. 5-6).

Determination of Glass Transition and Specific Heat Capacity

For this round of experiments, the temperature program consisted of 3 heating-cooling cycles at a rate of 10°C/min and 5-min isotherms at each temperature boundary. In Figure 5.12, the temperature program for the Tango samples can be seen as an example. The curves resulting from Segment 2 were primarily analysed after erasing the material's thermal and mechanical history (in Seg. 1). The heating scans from Segment 3 were used for validation purposes. The Recreus specimens were cut from the filament spool while the specimens of the other materials were cut out of the printed parts.
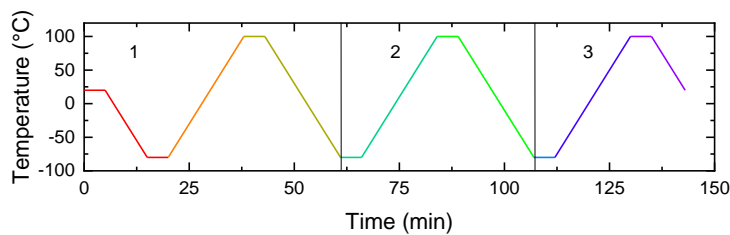
Figure 5.12: Temperature program for the determination of glass transition and specific heat capacity for the Tango samples.

Table 5.6 presents the testing conditions regarding the temperature limits and the refrigeration system for each sample. Samples tested above -80°C were cooled with gaseous nitrogen (GN2), while below that level liquid nitrogen (LN2) was used. The temperature control of the DSC machine was more affected at very low temperature values. Hence, the isotherms at -150°C and -170°C for the LSR and Keyence samples were removed while still ensuring a sufficient margin for an appropriate detection of the Tg.

Focusing on the identification of the glass transition and shorter testing duration, Duraform and Estane were tested at temperatures below their theoretical melting points. The reduced maximum temperatures of the Recreus and the LSR samples had the same goal. The glass transition temperature was obtained by the midpoint method. A linear baseline was used for the calculation of the heat of fusion.

Table 5.6: Testing conditions of each sample for the determination of glass transition and specific heat capacity.

Sample	Temperatures (°C)		Cooling	Sample	Temperatures (°C)		Cooling
	Min.	Max.			Min.	Max.	
Recreus 70A	-100	80	LN2	Tango 40	-80	100	GN2
Recreus 82A	-100	80	LN2	Tango 50	-80	100	GN2
Duraform	-100	120	LN2	Tango 60	-80	100	GN2
Estane	-120	120	LN2	Tango 70	-80	100	GN2
Wacker	-150	50	LN2	Agilus	-100	100	LN2
Silastic	-150	50	LN2	Keyence H	-170	100	LN2
Tango 30	-80	100	GN2	Keyence L	-170	100	LN2

For the determination of the isobaric specific heat capacity, c_p, the Three-Run Method was applied. The amount of energy per unit mass required to raise the temperature of the samples by one degree Celsius was obtained by means of three separate experiments, where:

1. in the first run, the sample pan remained empty for the baseline correction (*baseline*);
2. in the second run, the sample pan contained an amount of sapphire similar to that of the sample (*sapphire*). This standard reference run was used for the sensitivity calibration, as sapphire has a theoretically known c_p; and
3. in the third run, the actual sample was placed in the sample pan (*sample*).

All three experiments were conducted with the same reference and sample crucibles, under the same temperature program and conditions. The specific heat capacity, i.e. the ratio of the enthalpy rate to the temperature rate, was calculated based on Eq. 5.7 and the sensitivity, according to Eq. 5.8. The curves for this thermodynamic property were determined directly within the Netzsch Proteus thermal analysis software from the second heating curves (Seg. 2).

$$c_p(t) = \frac{\text{DSC signal (sample)} - \text{DSC signal (baseline)}}{\text{sample mass} * \text{heat rate} * \text{sensitivity}} \tag{5.7}$$

$$\text{Sensitivity} = \frac{\text{DSC signal (sapphire)} - \text{DSC signal (baseline)}}{\text{sapphire mass} * \text{heat rate} * c_p(\text{sapphire})} \tag{5.8}$$

5.4.5 Dynamic Mechanical Analysis

The DMA experiments were performed on a DMA Gabo Eplexor® machine from Netzsch. The cooling system was by means of gaseous nitrogen, with compressed dried air as purge gas. A sinusoidal, strain-controlled tensile load was applied to the specimens with an initial length of 15 mm. For all materials, the temperature increments were of 5°C with the recommended "step to temperature" setting, which controls the target temperature as quickly as possible to save nitrogen consumption particularly at low start temperatures. A soak time of 3-5 min at the start temperature and at the beginning of a new isotherm was used.

One specimen per sample was tested with specific input parameters. Due to the thermoviscoelastic nature of the materials, the dynamic testing was quite challenging. The significant change in the stiffness from extremely low to (at least) ambient temperatures hindered the application of a single strain amplitude throughout the experiments. Whereas at low temperatures the force sensor limits were easily reached, the stresses at temperatures above the glass transition were considerably small. This became even more difficult when combined with a broad frequency range. Although more frequency decades assist in a suitable time-temperature superposition (TTS), most materials did not allow it. Therefore, the maximum frequency for each sample was adjusted in a way that the temperature-frequency (T-f) sweep was mainly achievable. The same applied for the definition of the dynamic loading conditions. In order to avoid machine resonance, the general maximum frequency employed was of 70 Hz.

The TPUs, Tango and Agilus samples were able to be submitted to a temperature-frequency (T-f) sweep from a specified maximum frequency value decreasing until 1 Hz. That is, the specimen was oscillated in a range of frequencies from the highest to the lowest value at each isotherm. The maximum frequency for Recreus 70A, Recreus 82A and Estane was 70 Hz, while for Duraform, Agilus and the Tango grades it was 50 Hz. Five steps per frequency decade were used.

Due to apparatus limitations regarding temperature control, it was difficult to test the LSRs and Keyence samples at temperatures below -120°C, hence below glass transition. Exceptionally for Silastic, the machine was able to achieve -130°C but failed to stabilise the temperature at this level in subsequent tests. In addition, these materials were neither able to withstand a T-f sweep nor a full temperature sweep. The specification of a single amplitude for the whole temperature range without material damage was not possible. Consequently, a two-part temperature sweep at 1 Hz was performed for each one, named *cold* and *hot* temperature sweeps. The first was limited to the lower temperature range and the second to the higher temperature range. Since it was not possible to verify the Tg, the aim of these tests was to analyse the orders of magnitude of the storage and loss moduli.

In all investigations, the load was removed between measurement points. This means that both static and dynamic loads are removed, the contact force is controlled and the length of the specimen is updated before each measurement point. This allows the machine to consider the changes to the specimen length during testing. Table 5.7 presents the temperatures for the cold (c) and hot (h) temperature sweeps with the LSRs and the Keyence samples. Table 5.8 shows the temperature ranges and maximum frequency for the TPUs and the PolyJet photopolymers.

Table 5.7: DMA temperatures of the "cold" (c) and "hot" (h) temperature sweeps.

Sample	Temperatures (°C)		Sample	Temperatures (°C)	
	Min.	Max.		Min.	Max.
Wacker (c)	-120	-40	Keyence H (c)	-120	-50
Wacker (h)	-40	50	Keyence H (h)	-50	80
Silastic (c)	-130	-40	Keyence L (c)	-120	-50
Silastic (h)	-40	50	Keyence L (h)	-50	80

Table 5.8: DMA temperatures and maximum frequency of the T-f sweeps.

Sample	Temperatures (°C)		Max. frequency (Hz)
	Min.	Max.	
Recreus 70A	-100	80	70
Recreus 82A	-100	80	70
Duraform	-70	60	50
Estane	-80	80	70
Tango 30	-50	60	50
Tango 40	-50	60	50
Tango 50	-50	60	50
Tango 60	-50	60	50
Tango 70	-50	60	50
Agilus	-40	70	50

Strain amplitude tests were performed to find an appropriate dynamic strain amplitude within the linear viscoelastic region (LVR). Hence, Payne effects were disregarded. The storage modulus was measured as a function of the amplitude at a fixed frequency (Ehrenstein et al., 2004). The two most critical conditions were analysed: maximum temperature with minimum frequency (the softest condition) and minimum temperature with maximum frequency (the stiffest condition). When necessary, the static strain was adjusted to prevent reaching the force sensor limits as well as damaging the sample. The appropriate dynamic strains were taken below a 5% drop in the storage modulus from the LVR plateau (recall Figures 3.10 and 3.14). Overall, static strains of 2-3% and dynamic strain amplitudes of 0.15-0.8% were used. Figure 5.13 illustrates the dynamic strain amplitude tests for Recreus 70A, where an amplitude of 0.35 % met the 5% drop requirement for both critical conditions. In Appendix C, the strain amplitude test plots can be seen and all testing parameters are detailed, including contact forces and force sensors.
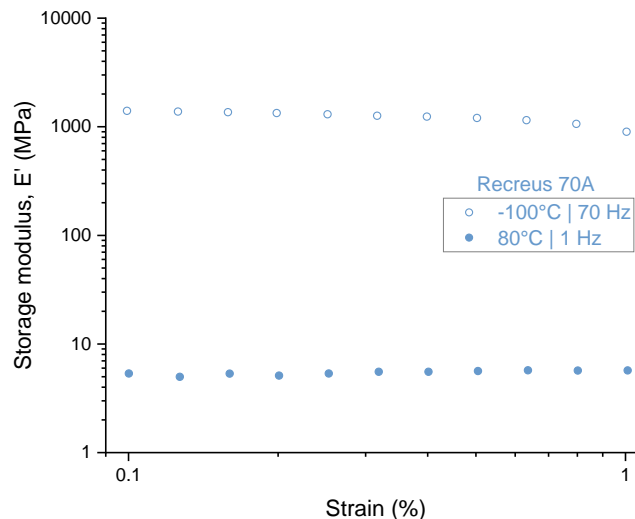
Figure 5.13: Dynamic strain amplitude tests for Recreus 70A.

The glass transition temperature was identified for the TPUs and PolyJet photopolymers. Three methods are commonly cited: the storage modulus step, the loss modulus peak and the loss factor peak. The peak at the loss modulus, E", was the method chosen in this thesis, as peaks are easier to evaluate. This method is also recommended by testing standards and

gives similar results to DSC experiments (Ehrenstein et al., 2004; Menczel and Prime, 2009). The master curves and calculations of respective TTS parameters were obtained through the machine's software Eplexor9®. A reference temperature of 20°C was applied for all T-f sweeps.

6. Uniaxial Tensile Testing

The strengths of the studied samples were primarily obtained from the tensile test results. This data set contributed to a first comparative analysis of the mechanical behaviour of the 3D printed materials, especially in the high deformation range. The permanent set was one characteristic observed for some samples. The following sections present and discuss the ultimate stress and stretchability of the selected materials, the permanent set recorded and the calculated toughness, as well as an analysis of all samples at the strain level of 80%.

6.1 Ultimate Strength

The ultimate strength of the materials is assessed in parts. First, the results of the TPC Arnitel samples with different infill orientations are presented. The TPUs are grouped and discussed together. The liquid silicone rubbers Wacker and Silastic follow thereafter. Finally, the photopolymers are analysed collectively.

6.1.1 Arnitel

A non-linear stress-strain behaviour was observed for most of the investigated 3D printed elastomers. Exceptions included the FFF printed Arnitel samples, regardless of the infill angle. As seen in Figure 6.1, the samples with the three infill angles suggest the existence of a yield point. Soft rubbers present instead a smooth curve course without an apparent transition between elastic and possibly inelastic behaviour. In fact, the filament itself was very flexible, i.e. easy to bend. However, it was not stretched as easily as Recreus 82A, which had a similar hardness. The indentation marks left on the filament by the extruder were an evidence of the expected plasticity of the material after testing (Figure 6.2). These marks are typically seen in stiff filaments, which are deformed in the extrusion process due to the pressure imposed by the extruder gears. This was not observed in the TPU filaments, though. For these reasons, neither printing optimisations nor further testing were performed for this filament.
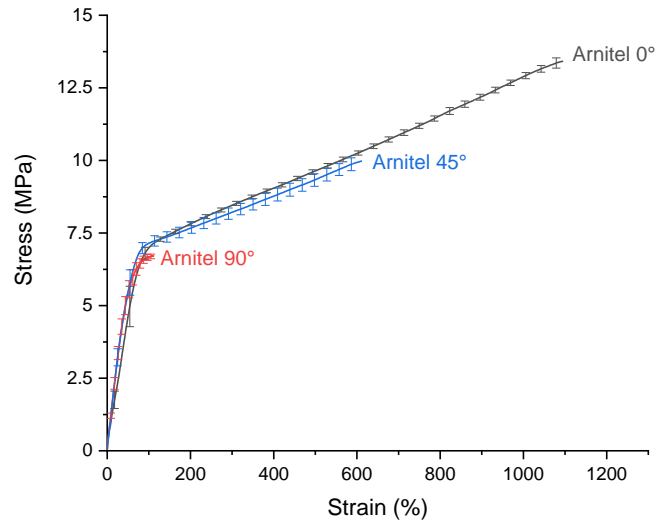
Figure 6.1: Tensile stress-strain curves for Arnitel at infill angles at 0°, 45° and 90°.

Figure 6.2: Indentation marks in the Arnitel filament from the extrusion process.

Due to the lack of printing optimisation to improve part adhesion, the most critical condition (90°) showed a premature, brittle failure in comparison to the others. On the other hand, the 0° orientation presents the highest tensile strength and elongation. This is largely associated with the raster deposition in the loading direction. In other words, the deposited strands of filament are the main factor bearing the load. For other infill orientations, the load capacity is particularly defined by the efficiency of the intra-layer adhesion, i.e. how well the rasters within the same layer are bonded together. During the uniaxial tensile loading, the deposition lines at 90° tend to separate (Figure 6.3), while the strands at an angle between 0° and 90° are also distorted towards the loading direction. For the 0° infill angle, the influence of the intra-layer adhesion is not as determinant for the tensile strength as it is for 45° and 90°, since the rasters are already in the direction of the tensile load. This topic was investigated and reported in Bruère et al. (2022b) for a TPU. In accordance with results in this publication, the shapes of the curves for the three infill orientations of Arnitel are similar. In addition, in the lower strain range ($\varepsilon < 100\%$) the infill angle does not play a significant role in the mechanical behaviour.
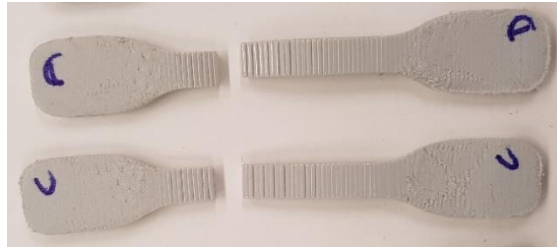
Figure 6.3: Line separation as the main failure cause for the Arnitel 90° specimens.

The ultimate stress and elongation at break for Arnitel can be seen in Table 6.1. The tensile strengths for the 45° and 90° samples are respectively 25.6% and 50% away from the stress at failure for 0°. No effective comparison can be made with the material properties provided by the manufacturer, as the testing standard and the infill orientations are dissimilar. However, it can be noted that the tensile strengths are in similar orders of magnitude (except for the 0° sample at the order of 10^1). The elongations at break for Arnitel 0° and Arnitel 45° are considerably larger than those of the alternating infill angles of the manufacturer. Arnitel 90° achieves a much lower maximum strain, although still above 100%. A final remark is made regarding plastic deformation, which was particularly significant for Arnitel 0° and Arnitel 45° were. These are presented and discussed together with the permanent set for all samples in Section 6.2. For a comprehensive analysis of plasticity, loading-unloading tests are required and recommended in future studies.

Table 6.1: Ultimate tensile stresses for Arnitel at infill angles of 0°, 45° and 90°.

Sample	Tensile Strength (MPa)	Elongation at break (%)
Arnitel 0°	13.42 ± 0.29	1,095
Arnitel 45°	9.98 ± 0.32	612
Arnitel 90°	6.71 ± 0.06	113

6.1.2 Thermoplastic Polyurethanes

The stress-strain curves for the four investigated TPUs are plotted in Figure 6.4. Recreus 70A and 82A were printed in FFF, Duraform was obtained from SLS and Estane was provided from MJF. Unlike Arnitel, the Recreus filaments did not show indentation marks from the extrusion process. In addition, they clearly exhibited both flexibility (ease to bend) and stretchability (recovery to initial size) in the unprocessed stage. This is reflected in the shape of the curves of the printed samples, which follow the typical non-linear behaviour of elastomers. Duraform also showed an elastic nature before testing. Its non-linear evolution of the stress-strain relationship is not as pronounced as for the Recreus samples. Estane is the hardest of the materials (hardness of 95 Shore A), exhibiting significantly greater stiffness.
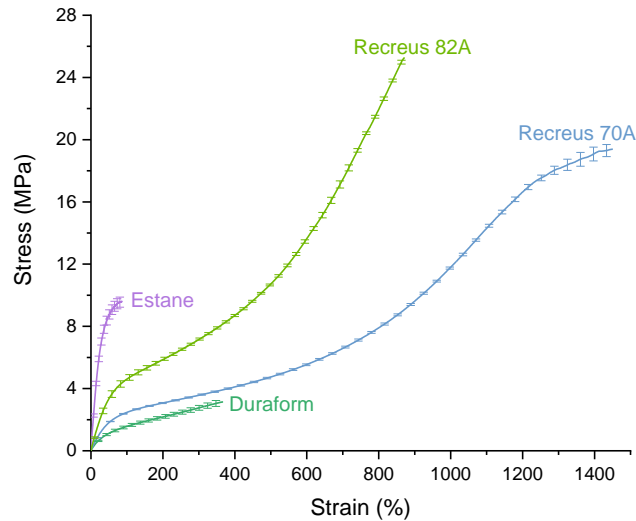
Figure 6.4: Tensile stress-strain curves for the TPU samples.

As already mentioned in Chapter 5, a distinctive fact observed was the crumbling texture of the Duraform specimens (Figure 6.5, left). Although no printing information for this requested sample was provided, this texture suggests poor sintering of the material. As a consequence, the powder particles do not efficiently bond together. This was also noticed during the tensile testing (Figure 6.5, right), in addition to the tearing throughout the cross section. Tearing was likewise detected on the outer surface of the punched Estane specimens (Figure 6.6), eventually leading to failure. Contrary to Duraform, the requested Estane plates had a great bonding of the particles on the external faces and no crumbling was seen. The uniformity on the lateral faces of the cross section, visible as a result of the punching, suggests an efficient material bonding. The Recreus samples showed no tearing or crumbling.
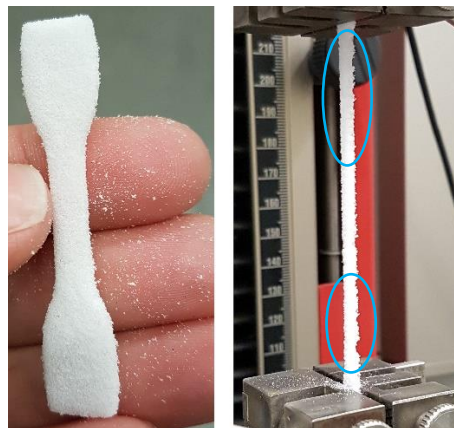
Figure 6.5: Duraform specimen with crumbling texture (left) and tearing during testing (right).

Figure 6.6: Estane specimen with tearing on the outer surface.

Duraform and Estane presented the lowest tensile strengths, as quantified in Table 6.2. The ultimate stress achieved by Duraform was low. Nevertheless, it was slightly higher than the value from its technical datasheet. Its elongation at break was superior in view of the higher stress level. Despite that fact, the technical information and the experiments are in agreement; at 200% strain, the Duraform sample reached a stress of ~2.1 MPa, as supplied by the manufacturer.

Table 6.2: Ultimate tensile stresses for the TPU samples.

Sample	Tensile Strength (MPa)	Elongation at break (%)
Recreus 70A	19.39 ± 0.35	1,451
Recreus 82A	25.29 ± 0.13	872
Duraform	3.15 ± 0.24	369
Estane	9.60 ± 0.34	88

The Estane sample displayed exceptionally lower values compared to the technical data. The tensile strength is over 40% below the 17 MPa listed in Table 5.2, while the elongation at break did not even reach 100% in strain. There is a strong probability that the inferior performance of Estane is due to the punching of the samples. Indeed, the MJF technology sprays a detailing agent for the smoothness of the edges of a part. By punching the S3A dumbbell geometry, the surfaces are distinct from those of a directly 3D printed dumbbell. Some S3A specimens from Estane were acquired and tested as well, reaching 13.18 ± 0.90 MPa of tensile strength at 303% strain. The error to the technical data failure stress reduces to 22.5%, while the elongation at break is tripled and 24% away from the 400% strain limit of the manufacturer. However, Figure 6.7 shows that the courses of the curves for both punched and printed samples are similar. The punched specimens were chosen for uniformity assessment purposes, as there were not enough individual dumbbell specimens for all the testing presented in this work. Furthermore, the remaining experiments were not carried out beyond 50% in strain, being in the available stress-strain range of the punched Estane sample.
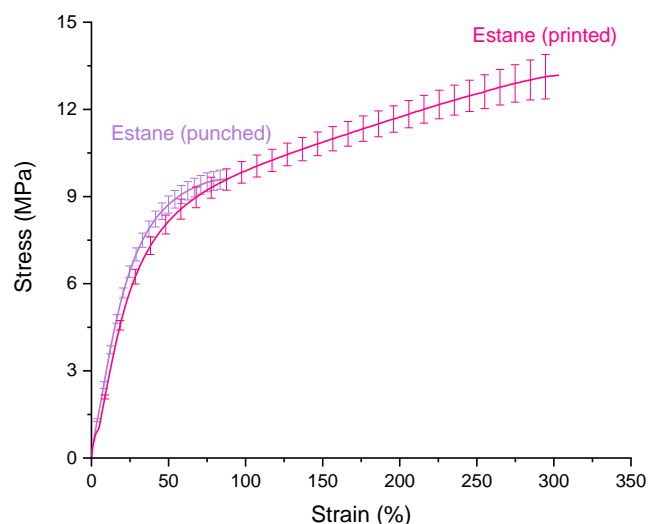
Figure 6.7: Tensile stress-strain curves for punched and printed Estane samples.

Although they were printed with the critical raster infill angle at 90°, the Recreus filaments were able to achieve significant levels of ultimate stress and strain. This is intrinsically connected to the printing optimisations previously performed, which was not the case for Arnitel 90°. The tensile strengths were found to be respectively 39.4% and 43.5% lower than those of the technical datasheets for Recreus 70A and 82A. The elongations at break achieved higher values, deviating in 61.2% and 34.1% respectively. The technical datasheets do not provide the printing parameters (in particular the infill angles), to which the differences in the results are attributed. In addition, the stiffer response of the harder Recreus 82A sample compared to Recreus 70A is the validation of the influence of the higher hard-to-soft segment ratio in this TPU.

Overall, the stiffness of the TPUs increase with their hardness for the samples printed with the MJF, FFF and SLS technologies. The Recreus samples exhibited high tensile strength and elongation at break typical of TPUs. The MJF and SLS samples are the ones with the lowest tensile strength and elongations at break. This can be a consequence of the material selection and/or the printing parameters of the technology. The powder nature of the unprocessed materials should also not be disregarded, especially in the case of ineffective bonding. In FFF, even in under-extrusion conditions, the part integrity can be favoured by a proper selection of printing parameters. In Bruère et al. (2022b), this is demonstrated by the use of alternating instead of unidirectional infill orientation.

6.1.3 Liquid Silicone Rubbers

The investigated LSRs, of hardness 50 Shore A, showed a similar non-linear stress-strain behaviour, as observed in Figure 6.8. Since both are stated as 100% pure silicone by the manufacturers, their great elastic capabilities could be noticed even before testing. Furthermore, they were able to reach elongations over 400% and moderate mechanical strengths in the 10^0 order of magnitude, characteristic of silicone rubbers (as seen in Chapter 3). Their complete recovery to the initial length was instant and is comparatively discussed in Section 6.2.
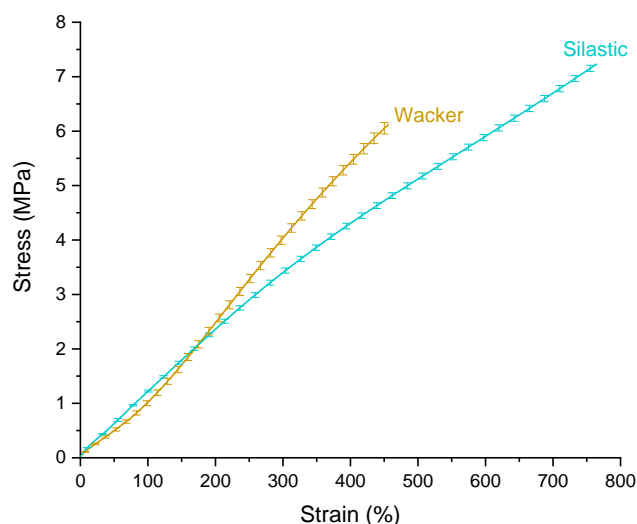
Figure 6.8: Tensile stress-strain curves for the LSR samples.

The stiffness levels of Wacker and Silastic are alike up to their intersection point at 173% in strain. Below this, the maximum distance between the two curves occurs at around 88% in strain, in which Wacker's stress values are approximately 20% lower than those of Silastic. Table 6.3 displays the ultimate values from the tensile testing of the LSRs. Regarding the manufacturer's technical information, both tested samples withstood lower stresses at higher elongations at break. The results are not directly comparable, since the testing standards are distinct. However, it can be noted that the tensile strengths are close in values (12.5% and 23.8% lower than those of the technical datasheets for Wacker and Silastic, respectively). In contrast, the ultimate strains are 1.5-2 times greater, although this did not interfere in the recovery of the samples. At its point of failure, Wacker reached a stress which was 28.2% higher than that of Silastic. This indicates a moderate divergence in the performance of these LSRs in the higher strain range (> 450%).

Table 6.3: Ultimate tensile stresses for Wacker and Silastic.

Sample	Tensile Strength (MPa)	Elongation at break (%)
Wacker	6.12 ± 0.10	457
Silastic	7.24 ± 0.06	766

6.1.4 Photopolymers

The photopolymer samples exhibited the typical elastomeric non-linear behaviour in the stress-strain curves. For the harder Tango 70 and Tango 60 samples, the non-linearity was not as pronounced as for the other Tango grades (Figure 6.9). The course of the stress-strain relationship of the Tango 30 and (the transparent) Tango 30 (t) samples were equivalent. The maximum divergence of Tango 30 (t) values at failure from Tango 30 was of 7% (relative to Tango 30). It can be concluded that the different colorations of the Tango 30 and of Tango 30 (t) samples have no significant influence on the mechanical stress-strain behaviour.
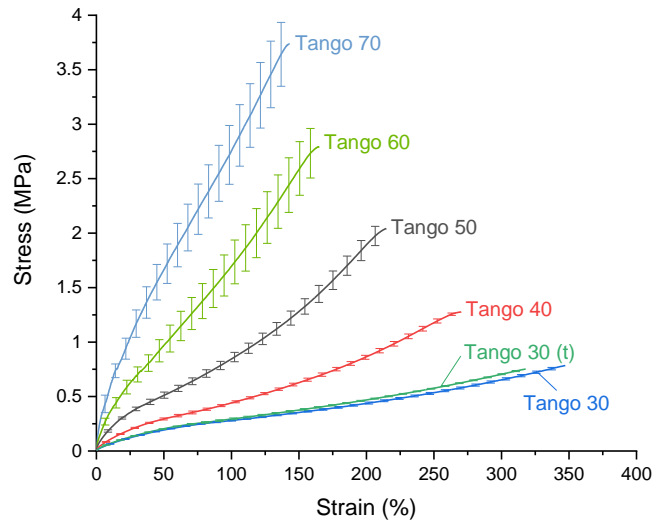
Figure 6.9: Tensile stress-strain curves for the Tango samples.

Analogous to Tango 70 and Tango 60, the Keyence materials presented a less pronounced non-linearity, which did not show an inflection point in their curves (Figure 6.10). The behaviours of Keyence H and L were similar; the magnitudes of their stress response were a result of the lower/greater elastic composition in their chemistry. Agilus delivered a stress-strain relationship comparable to the softer Tango samples, between the curves of Tango 40 and Tango 50. All photopolymer specimens showed an essentially elastic material behaviour. However, their recovery at the end of the tensile test was not instant as for the LSRs, for example. Furthermore, they contained tears along their entire length, as observed in Figure 6.11 for specimens of Tango 70 and Keyence L.
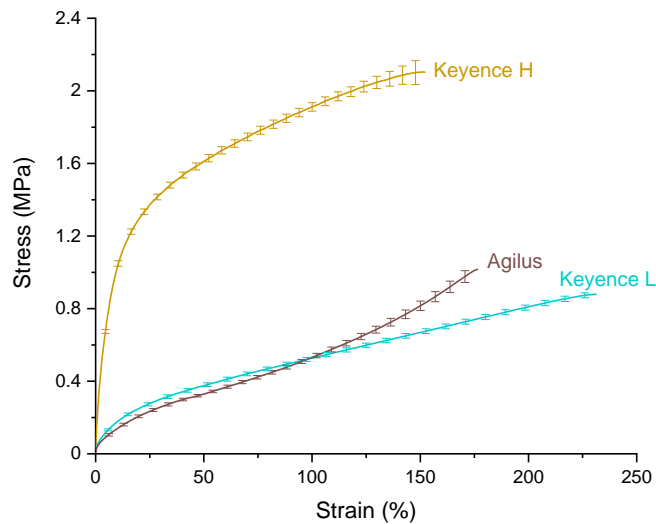
Figure 6.10: Tensile stress-strain curves for the Keyence and Agilus samples.
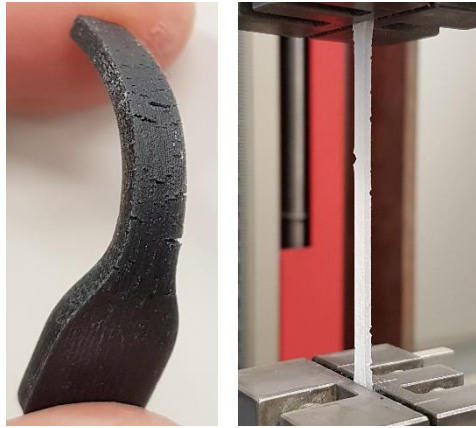
Figure 6.11: Tearing throughout the cross sections of Tango 70 (left) and Keyence L (right) specimens.

The tensile strengths and respective elongations at break of the photopolymers are listed in Table 6.4. In spite of the different testing standards, the Tango samples were able to withstand stresses close to those provided in the technical information from the manufacturers. However, the ultimate strains were much greater (about 1.5-2 times) than those from the technical datasheet. The opposite occurred for Agilus: the elongation at break was similar to the theoretical value, while the tensile strength was 3 times lower. In the case of Keyence L, the sample failed at a slightly higher stress, although at a quite greater strain. In contrast, Keyence H performed correspondingly to the technical data.

Table 6.4: Ultimate tensile stresses for the Tango samples.

Sample	Tensile Strength (MPa)	Elongation at break (%)
Tango 30	0.78 ± 0.01	347
Tango 30 (t)	0.75 ± 0.01	317
Tango 40	1.28 ± 0.02	270
Tango 50	2.04 ± 0.06	215
Tango 60	2.79 ± 0.18	165
Tango 70	3.74 ± 0.25	143
Agilus	1.02 ± 0.03	177
Keyence H	2.10 ± 0.08	152
Keyence L	0.88 ± 0.01	231

An interesting observation is the increase in the stiffness at failure of the Tango samples, i.e. the ratio between the tensile strength and the elongation at break. With the help of the fitting feature from the Origin software, it was found that the final stiffness increases with the sample hardness following a polynomial of order 4 (Figure 6.12). The fitting equation was $7.97 * 10^{-4} + 1.67 * 10^{-3}x - 6.55 * 10^{-4}x^2 + 4.88 * 10^{-4}x^3 - 4.44 * 10^{-5}x^4$, for a R-Squared of 1. Finally, it is noteworthy that all photopolymers showed the lowest tensile strength among the 3D printed elastomers investigated.
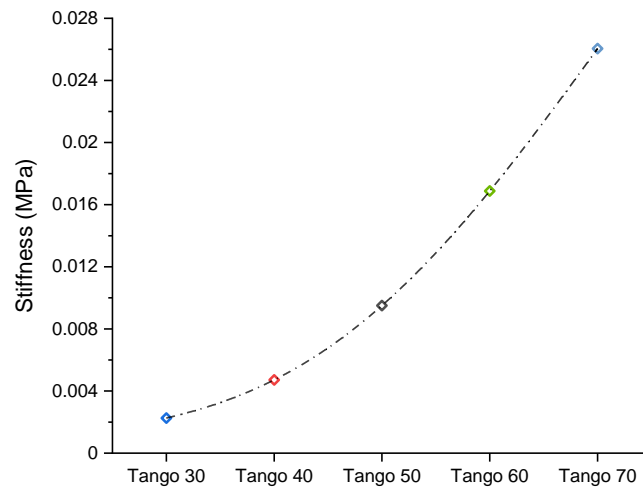
Figure 6.12: Evolution of the stiffness at failure (tensile strength over elongation at break) for the Tango samples.

6.2 Permanent Set and Toughness

The inability of the specimens to return to their original size once the load is removed was observed for several materials. The permanent set of the TPEs were the most noticeable. As mentioned in Chapter 3, thermoplastic elastomers do not have a recovery capacity as great as that of conventional rubber. A residual deformation was expected after the tensile testing of these materials due to the high elongations reached, and it was indeed detected. Table 6.5 displays the permanent set recorded for each sample.

Table 6.5: Permanent set of the samples after some recovery time.

Sample	Permanent set (%)	Sample	Permanent set (%)
Arnitel 0°	143.0	Tango 30	0.0
Arnitel 90°	5.0	Tango 30 (t)	0.0
Arnitel 45°	92.0	Tango 40	0.0
Recreus 70A	42.0	Tango 50	0.0
Recreus 82A	31.0	Tango 60	0.0
Duraform	23.5	Tango 70	0.0
Estane	3.0	Agilus	0.0
Wacker	0.0	Keyence H	3.4
Silastic	0.0	Keyence L	2.0

The LSR samples, i.e. Wacker and Silastic, presented 100% recovery to their original size, which occurred instantly once the test was finished (Figure 6.13). Even though there may be some chemistry modification to suit their corresponding 3D printing technologies, Wacker and Silastic offered elastic reversibility with outstanding extensibility, which is the typical behaviour of traditional elastomers. Arnitel 0° showed the highest plasticity, as observed in Figure 6.14 (left). The plastic deformation for Arnitel 45° was substantial as well. Arnitel 90° had a reduced permanent set. However, this is a result of the poor intra-

layer adhesion of the specimens (as seen in Figure 6.3, the lines detached in several points of the cross section). Thus, although being classified as a *thermoplastic elastomer*, this TPC is not the most suitable for applications requiring high elasticity.
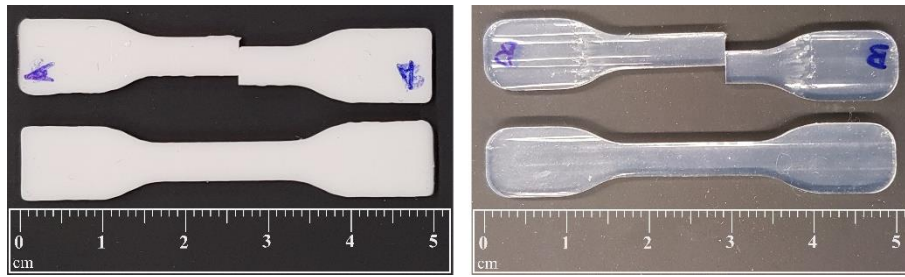
Figure 6.13: Wacker (left) and Silastic (right) specimens before (on the bottom) and after (on the top) the tensile test.
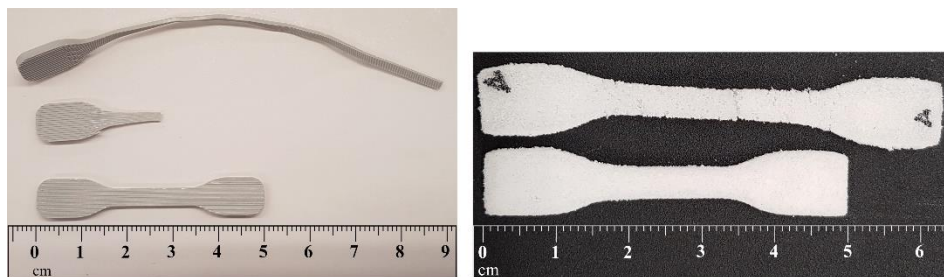
Figure 6.14: Arnitel 0° (left) and Duraform (right) specimens before (on the bottom) and after (on the top) the tensile test.

The moderate permanent set values for the Recreus 70A and Recreus 82A materials are a consequence of the printing optimisation presented in Appendix A, which improved intra-layer adhesion. In this way, these TPUs were able to resist to higher stresses and elongations, also allowing the development of more plastic deformation. This is the reason behind the discrepancies to Arnitel 90°, printed with the same infill orientation. Despite not being explored in this work, preliminary tests and tests from previous publications with Recreus 70A and 82A specimens at a 0° infill angle consistently showed a permanent set below 60%. As discussed in Section 6.1.6, for a 0° infill angle, the strength of the lines is considerably more determinant for the tensile failure than the intra-layer adhesion. Since the printing optimisations presented in Appendix A were focused on enhancing the bonding of the lines within the same layer, it can be inferred that there would be no significant changes in the tensile behaviour of the 0° specimens as there was for the 90° specimens. Therefore, the permanent set from preliminary and published tests are comparable to the results in this work. Taking this into account, it can be noticed that the TPU filaments exhibited a greater recovery capacity than the TPC filament investigated.

The other TPUs also presented a permanent set. Duraform (Figure 6.14, right) showed it to a greater extent. Indeed, its stress-strain curve was able to develop its course and achieve high strains, following the typical shape of elastomers. This did not take place in the same way for Estane. The MJF (punched) sample did not reach elongations as high as the other TPUs, as discussed in Section 6.1.2. Hence its low permanent set of 3%. For purposes of comparison, the directly printed dumbbell specimens from Estane displayed an average of

15% of plastic deformation (omitted from Table 6.5). This value was the lowest among the TPUs from this work but similarly in the 10^1 order of magnitude.

In the majority, the photopolymers did not show permanent set. Nevertheless, it should be noted that the recovery for the Tango, Agilus and Keyence samples was not instant, as opposed to the LSRs. In fact, the specimens required some time (a matter of minutes) for the return of the resulting deformation after the tensile test. Keyence H and Keyence L specimens had a respective deformation of 15% and 7% directly after failure. They eventually reduced to 3.4% and 2%, respectively, as listed in Table 6.5. Agilus specimens, for instance, needed 1-5 minutes to return to their original size. Additionally, the softer the material, the faster the recovery with time. Figure 6.15 displays the different specimen sizes immediately after failure for Tango 70 and Tango 30. Among the Tango 30 specimens, a maximum deformation of 1% was noticed directly after the test.
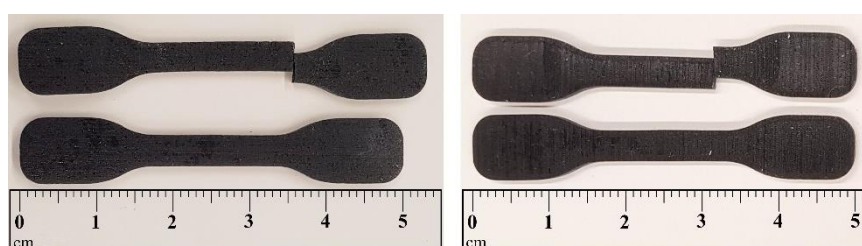
Figure 6.15: Tango 70 (left) and Tango 30 (right) specimens before (on the bottom) and immediately after (on the top) the tensile test.

The transition from elastic to viscoelastic or plastic behaviour (if present) in rubbers is not evident, as previously mentioned. Consequently, the resilience of the samples, i.e. the ability to absorb energy when elastically deformed, could not be determined for all materials. On the other hand, for the samples with a permanent set, the fracture toughness (i.e. the measure of the ability to absorb energy up to failure) was determined. For the samples without plasticity, resilience and toughness are equivalent. In both cases, the respective areas under the tensile curves were calculated in the Origin software. Table 6.6 displays the energy absorption of each material.

Table 6.6: Energy absorbed by the samples in ascending order.

Sample	Resilience (MJ/m³)	Sample	Toughness (MJ/m³)
Agilus	90.1	Keyence L	128.8
Tango 30 (t)	127.6	Keyence H	255.7
Tango 30	141.2	Arnitel 90°	553.5
Tango 40	167.2	Estane	636.3
Tango 50	210.4	Duraform	743.0
Tango 60	243.9	Arnitel 45°	4,854.2
Tango 70	303.0	Recreus 82A	9,646.3
Wacker	1,353.9	Arnitel 0°	10,659.8
Silastic	3,028.3	Recreus 70A	12,820.8

It is clear that the Agilus and Tango photopolymers resulted in the lowest resilience values, as a consequence of the low tensile strengths and elongations at break. The LSRs were substantially more resilient due to their high elasticity at moderate stresses. The Wacker sample absorbed 4.5 times more energy than Tango 70, while Silastic absorbed almost 10 times more energy than the stiffer Tango sample.

Similarly, the Keyence photopolymers had the lowest toughness values. The Recreus samples and Arnitel 0° were the toughest materials, as a result of the high tensile strength and elongation at break typical of TPEs. In spite of having the lowest ultimate strains, Estane and Arnitel 90° absorbed about 2-2.5 times more energy than Keyence H, since they withstood greater stresses until failure. The modest toughness of Duraform in comparison to Arnitel 0° and 45° as well as the Recreus samples resulted mostly from the lowest tensile strength among the TPUs. Provided with this information, the designing of functional components can be accomplished more efficiently for their resistance without a catastrophic failure.

6.3 Mechanical behaviour up to 80% Strain

This section aims to compare all samples at a same strain. The value 80% was chosen, as Estane achieved the lowest elongation at break, of 88%. This strain was also below the apparent yield point of the Arnitel samples. The following figures present the stress-strain relationship of the investigated TPEs. The similarity of the curve behaviour of the Arnitel samples with different infill orientations is evident (Figure 6.16). A slight divergence of the Arnitel 0° curve, as well as its higher standard deviation, are due to the accommodation of the pincer clamps for some specimens. The shapes of the tensile curves of the different TPUs are alike (Figure 6.17). The stresses achieved are a consequence of the increasing hardness, from Duraform (59 Shore A) to Estane (95 Shore A). Despite being from different AM technologies and likely having variations in the chemical composition, Estane, Recreus 82A, Recreus 70A and Duraform exhibited comparable tensile behaviours.
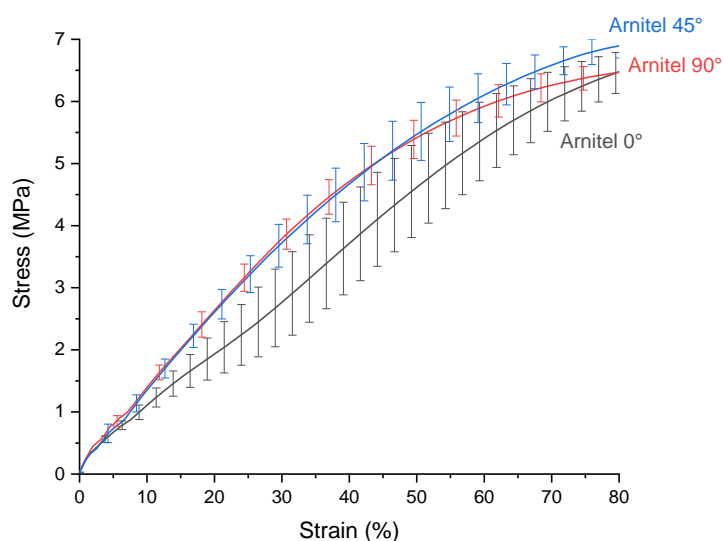
Figure 6.16: Tensile stress-strain curves for the Arnitel samples up to 80% strain.
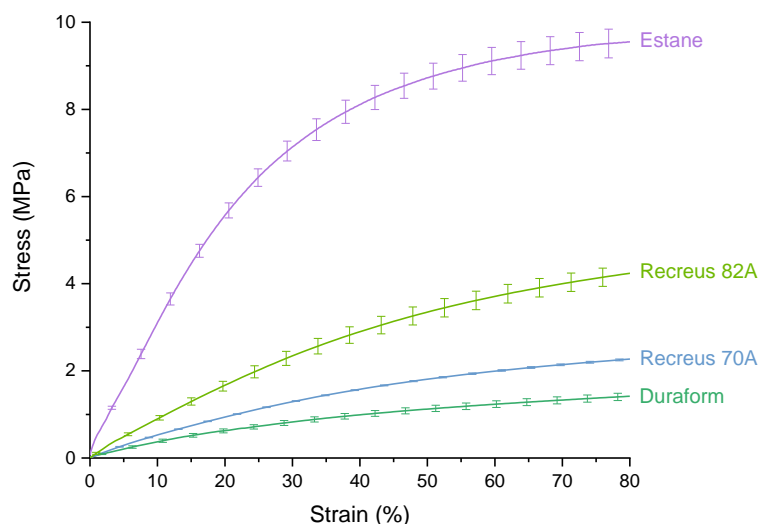
Figure 6.17: Tensile stress-strain curves for the TPU samples up to 80% strain.

For the LSRs, which have the same hardness of 50 Shore A, there was a noticeable variation in the stress values at the same strain (Figure 6.18). However, this correlates to the distance between the curves below their intersection point at 173% strain (see Figure 6.8 in Section 6.1.3). The Tango photopolymers showed the same tendency as in the full tensile curves (Figure 6.19). Their stresses at a deformation of 80% followed a polynomial of order 4. It is also possible to see the great similarity of the Tango 30 and (the transparent) Tango 30 (t) curves in the lower strain range. The same can be said for Keyence L and Agilus (Figure 6.20). They behaved analogously, both in shape and in values. With the increase in the strain beyond that, the curves intersected and started to diverge, as previously seen in Figure 6.10.
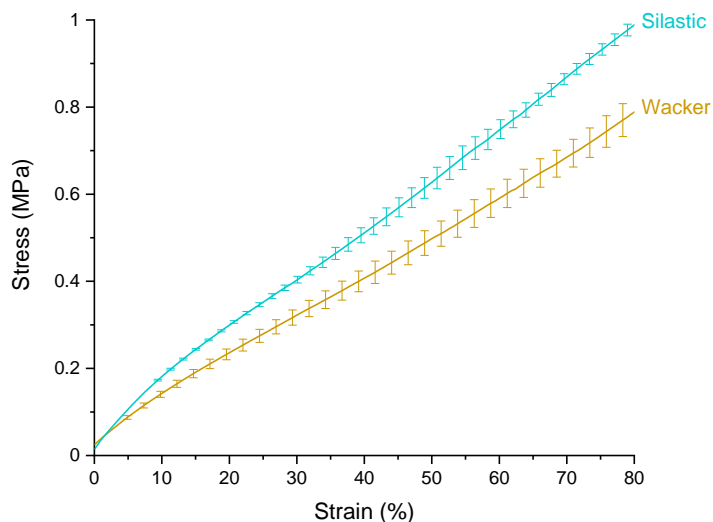
Figure 6.18: Tensile stress-strain curves for the LSR samples up to 80% strain.
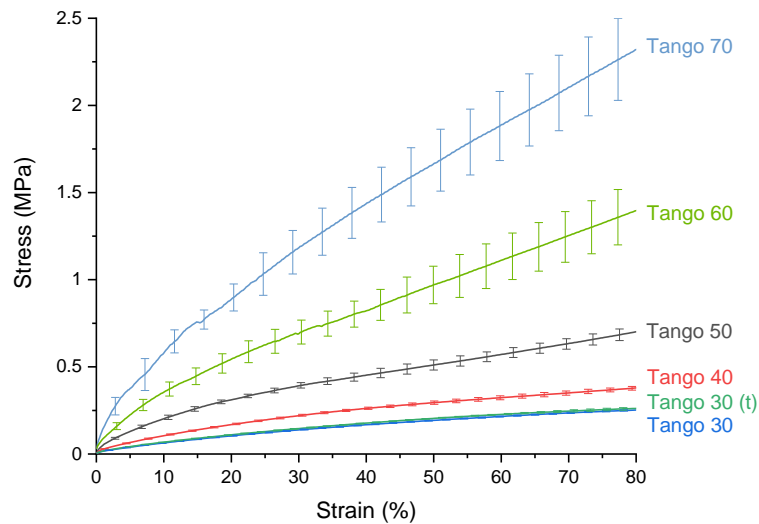
Figure 6.19: Tensile stress-strain curves for the Tango samples up to 80% strain.
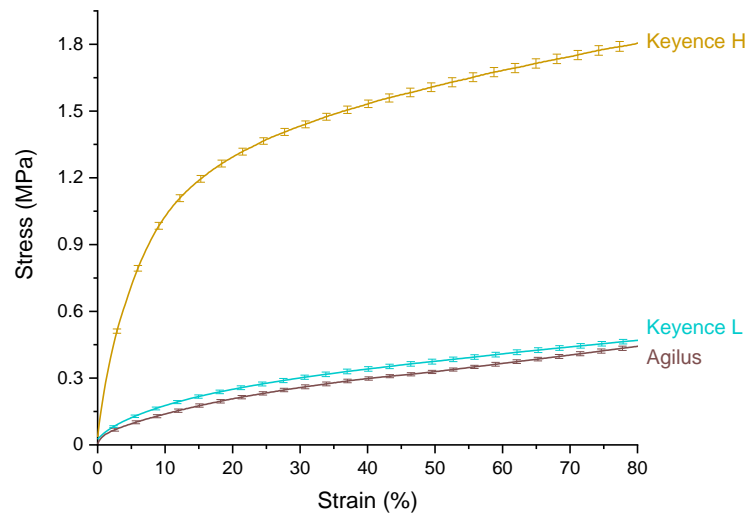
Figure 6.20: Tensile stress-strain curves for the Keyence and Agilus samples up to 80% strain.

Table 6.7 shows the tensile stresses at 80% strain for all samples in ascending order. Except for Keyence L, the stresses increased with material hardness. For the materials with the same hardness of 50 Shore A, it can be seen that Agilus achieved considerably lower values than Tango 50 (Figure 6.21). The stress of Agilus was in fact 37% lower than that of the other PolyJet photopolymer. Although from different types of material and AM technologies, Tango 50 and Wacker obtained close values, with a difference of 11%. Finally, Wacker led to a 20% lower stress than Silastic. However, if the higher strain range is considered, it can be concluded from the tensile strengths that the performance of Agilus and Tango 50 is significantly lower than the one observed for the LSRs.

Table 6.7: Stresses at 80% strain for each sample in ascending order.

Sample	Stress (MPa)	Sample	Stress (MPa)
Tango 30	0.252 ± 0.004	Duraform	1.417 ± 0.084
Tango 30 (t)	0.261 ± 0.007	Keyence H	1.805 ± 0.022
Tango 40	0.379 ± 0.010	Recreus 70A	2.268 ± 0.023
Agilus	0.443 ± 0.010	Tango 70	2.321 ± 0.240
Keyence L	0.470 ± 0.010	Recreus 82A	4.233 ± 0.208
Tango 50	0.702 ± 0.034	Arnitel 0°	6.458 ± 0.330
Wacker	0.790 ± 0.038	Arnitel 90°	6.469 ± 0.155
Silastic	0.988 ± 0.014	Arnitel 45°	6.898 ± 0.197
Tango 60	1.396 ± 0.163	Estane	9.549 ± 0.328
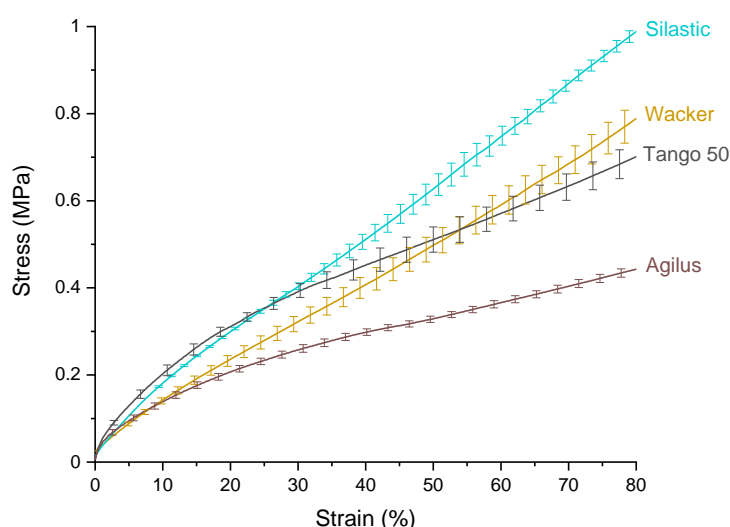
Figure 6.21: Stress-strain curves for the samples of hardness 50 Shore A up to 80% strain.

The materials with a hardness of 70 Shore A, namely Recreus 70A and Tango 70, were able to reach quite close values. Recreus 70A was only 2% below Tango 70. Their stress-strain relationship in this lower deformation range was also very similar up to about 80% strain. Nevertheless, from then on, the behaviour of the curves started to diverge. The result is discrepant and led to tensile strengths of 3.7 MPa for the photopolymer and 19.4 MPa for the TPU, presented in Section 6.1. Being the stiffest and the least elastic materials, Arnitel and Estane obtained the highest stresses at 80% strain.

6.4 Final Remarks

All samples achieved high elongations at break. Except for Estane and Arnitel 90°, which showed signs of a premature failure, the photopolymers were the materials with the lowest ultimate strains. The distinction goes to the silicones and the TPUs. Furthermore, the secant moduli at failure (tensile strength over elongation at break) of the investigated materials was low, ranging from 0.226 MPa to 10.947 MPa (as expected for rubbers). At the same

time, pure elasticity was not observed for all samples. As stated in Section 6.2, the TPUs presented a permanent set, which is likely to happen due to the high deformations imposed. The TPC samples, in particular Arnitel 0° and Arnitel 45°, displayed excessive plasticity.

The photopolymers in general showed the weakest tensile strengths. They also led to the lowest toughness/resilience values. It has to be mentioned that the used PolyJet technology from Stratasys deposits the base components of the combined material (in this case, the TangoBlackPlus and the VeroClear materials for the several Tango samples) through different nozzles. Hence, only a slight mixture of the materials occurs after the deposition, and there are countless material interfaces inside the printed parts. From a macroscopic point of view, this should not interfere in the mechanical behaviour. However, the same cannot be said at the microscopic level, in which cases the mechanical properties differ more significantly. The LSRs had moderate mechanical strength, as usual. The TPUs were the strongest materials, although at the expense of residual deformation. The total recovery for almost all photopolymeric samples required a waiting time, whereas the LSRs returned immediately to their original size. In the design of components, these characteristics should be taken into account when selecting the 3D printing material.

7. Uniaxial Cyclic Testing

The viscoelastic behaviour of the 3D printed samples was analysed and compared through the cyclic tests. For this purpose, the hysteresis ratio was computed from the last loading-unloading cycle of each strain level tested. The stress softening, i.e. Mullins effect, was identified for all samples and computed as well. Both phenomena are assessed and discussed in the following sections.

7.1 Cyclic Curves

Figures 7.1 to 7.4 show the stress-strain relationships resulting from strain-controlled experiments for each material investigated. The more pronounced stress softening of Estane compared to the other TPU samples can be particularly noticed; the same can be said for Keyence H in contrast to Keyence L and Agilus. For these materials, the loading-unloading loop needed more cycles to stabilise. By the last cycle, stabilisation was more apparent. For Keyence H, for instance, the maximum stress decreased by only 1% from the 9th to the 10th cycle. Additionally, a permanent set of 2% was observed for Estane and Keyence H. The other samples exhibited complete recovery to the original size. This is particularly aligned with the definition of a thermoplastic elastomer: when submitted to moderate elongations, TPEs return to something close to their original size upon the removal of the stress (see Chapter 3).
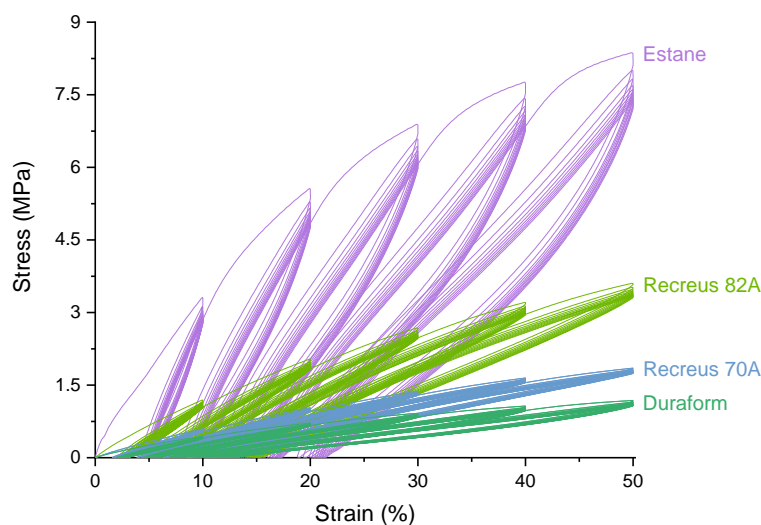
Figure 7.1: Cyclic stress-strain curves for the TPU samples.
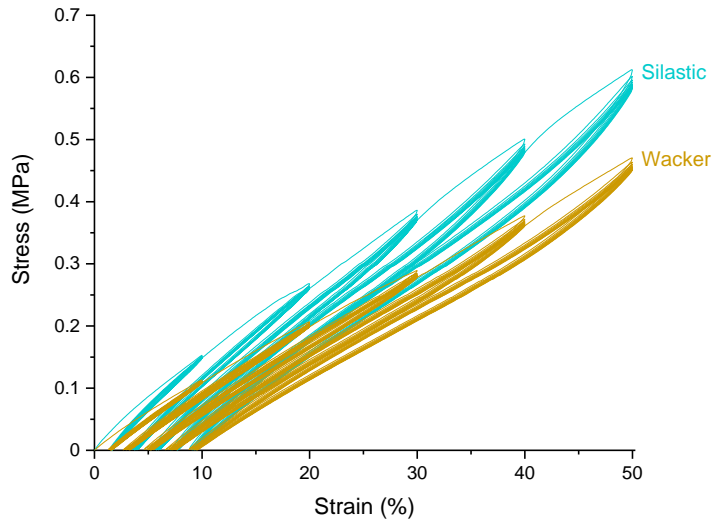
Figure 7.2: Cyclic stress-strain curves for the LSR samples.
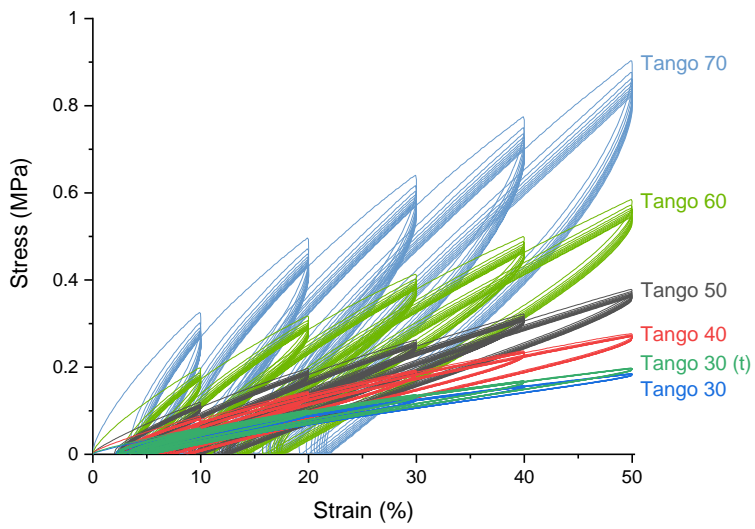
Figure 7.3: Cyclic stress-strain curves for the Tango samples.
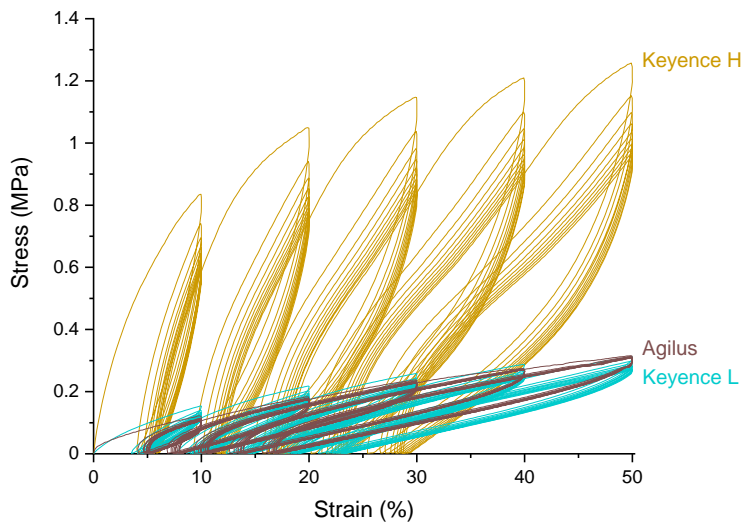
Figure 7.4: Cyclic stress-strain curves for the Keyence and Agilus samples.

The silicones presented low stress softening and reached a stationary hysteresis after a few loading-unloading cycles. This behaviour was also exhibited by the softer Tango samples, namely Tango 40, Tango 30 and Tango 30 (t). It is worth mentioning that after unloading the specimens there seemed to be a residual deformation. In fact, this was a consequence of no waiting time for the recovery of the specimen after unloading, as mentioned in Chapter 3. Regarding hysteresis, the results visually indicate low energy dissipation for the LSRs and the softest Tango material. Some quantitative analyses are discussed hereafter.

7.2 Hysteresis

The areas under the 10th loading and unloading curves (W10L and W10U, respectively) were obtained for the strain levels at 10%, 20%, 30%, 40% and 50%. Following Tayeb et al. (2022), the hysteresis ratio was calculated as the ratio of the energy difference between these curves over the energy of the loading curve. In this way, the stretch level was taken into account. In other words, the hysteresis ratio was taken as:

$$\text{histeresis ratio} = \frac{\text{W10L} - \text{W10U}}{\text{W10L}} \qquad (7.1)$$

The hysteresis ratio of the different materials under cyclic loadings is quantitatively expressed in Figure 7.5. The closest the value is to 1, the more hysteresis the material showed. It is noteworthy that Wacker and Silastic provided the lowest hysteresis ratios for all strain levels of the cyclic loading. The maximum energy dissipated was of 6% and 7% at 50% strain for Wacker and Silastic, respectively. With a great amount of the energy necessary for the deformations applied returning upon unloading, the silicone samples were highly resilient. In contrast, the photopolymers displayed the highest energy dissipation. Agilus, Tango 70 and Keyence H were among the samples with superior hysteresis ratios in all strain levels. In addition, for the cyclic loading at 10% strain, all photopolymers had hysteresis ratios above those shown by the TPUs, which were above the LSRs.
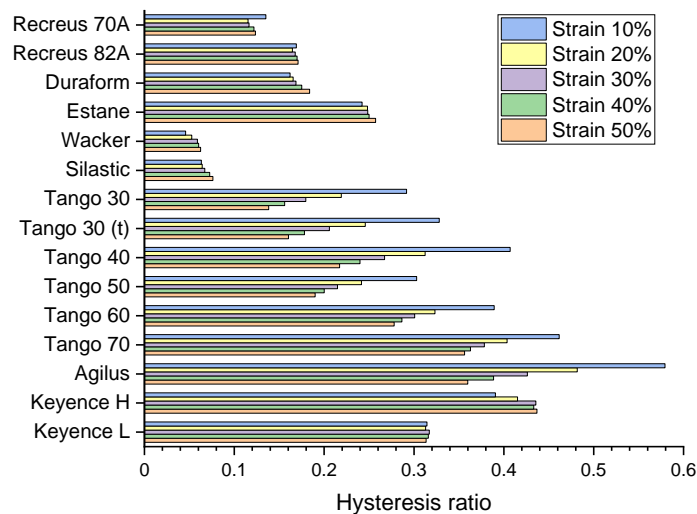
Figure 7.5: Hysteresis ratio relative to the energy brought to the sample by the 10th loading.

The PolyJet materials revealed a pronounced hysteresis ratio decrease with the strain increase, indicating the progressive reduction of internal friction in the specimens. This tendency was not observed for the remaining photopolymers, specifically the Keyence materials. Keyence H showed a slight increase in the energy dissipation in the first strain levels, with a difference of about 10% between the maximum and minimum hysteresis ratios. The dissipated energy of Keyence occurred in a relatively constant manner at the five stages. The variation of its hysteresis ratio values was below 2%.

Recreus 82A behaved similarly to Keyence L, with a difference in the extreme hysteresis intensities of less than 4%. The first strain level led to the highest hysteresis, as for Recreus 70A. However, the softest TPU filament sample had a maximum variation of 15%. This can be partially explained by the proportionally lower energy recovered at the 10th unloading cycle relative to the energy demanded at the 10th loading cycle (i.e. lower W10U/W10L) at the 10% strain level. Additionally, the values dealt with in the first level of deformation are low, which can lead to more pronounced changes in the results even for small deviations on the obtained loading and unloading energies. Duraform and Estane showed an ascending hysteresis ratio, although not greater than 12% for the first and 6% for the second material. Also with monotonic values, Wacker and Silastic increased in 27% and 17%, respectively, from the cyclic loading at 10% strain to that at 50% strain.

Comparing the samples with a hardness of 70 Shore A, it was noticed that Tango 70 presented hysteresis ratios 2.9-3.5 times higher than Recreus 70A. The damping capabilities of this photopolymer are significantly higher in contrast with the TPU sample. Similarly, for the samples of a hardness of 50 Shore A, Tango 50 and Agilus are capable of dissipating more energy under cyclic loadings (see Figure 7.6). Indeed, the high resilience of the silicones Wacker and Silastic had already been observed. The most hysteretic LSR i.e. Silastic, is still 2.5 to 4.8 times away from Tango 50, which displayed half the hysteresis of Agilus.
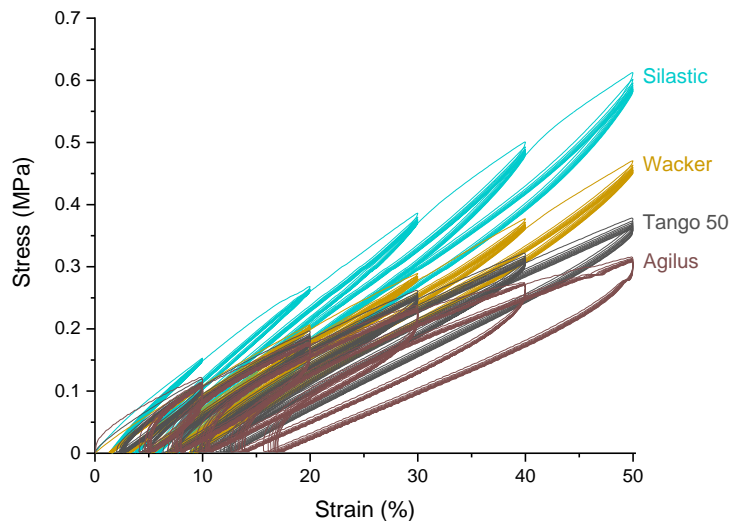
Figure 7.6: Cyclic stress-strain curves for the samples of hardness 50 Shore A.

7.3 Mullins Effect

As reported in Section 3.4.3, the Mullins effect was quantified using the ratio of the energies W2L/W1L i.e. the area under the 2nd loading curve over the area under the 1st loading curve at each strain level. This ratio is named in this work as *Energy ratio*. As described in Section 3.4.3 (recall Eq. 3.14 and Figure 3.13), the required deformation energy that was not included due to previous cycles at a lower strain ($W1L_2$) should be taken into account for a proper computation of the Mullins effect. Hence, a monotonic curve was fitted to each sample in order to calculate the actual amount of energy required by the first loading curve of the 20% to 50% strain cycles i.e. $W1L = W1L_1 + W1L_2$. A polynomial fitting of order 4 was suitable for all samples, except for Agilus, which was best fitted to a polynomial of order 5. Figure 7.7 illustrates the identification of the areas for $W1L_1$ and $W1L_2$ in the first loading of the 50% strain level.
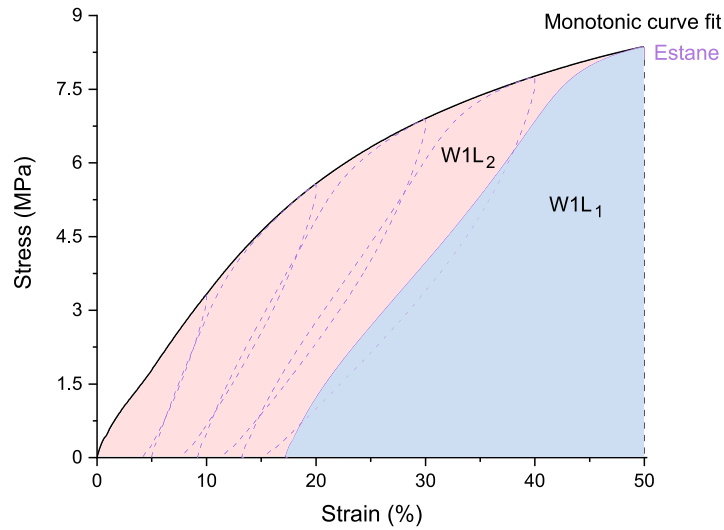
Figure 7.7: Monotonic curve fit for Estane (solid, black), with the 1st loading-unloading curves of strain levels 10% to 40% (dashed, purple) and 1st loading curve of the 50% strain level (solid, purple).

All materials exhibited the Mullins effect to some degree in all strain levels. The Energy ratios per sample can be seen in Figure 7.8. The closest this ratio is to 1, the less stress softening was verified for the sample. The closest to 0, the more pronounced the Mullins effect is. Therefore, the amount of Mullins effect presented is taken as given in Eq. 7.2. The higher the Energy ratio, the lower the Mullins effect.

$$\text{Mullins effect} = 1 - \text{Energy ratio}$$
$$\text{Mullins effect} = 1 - \frac{\text{W2L}}{\text{W1L}} \tag{7.2}$$
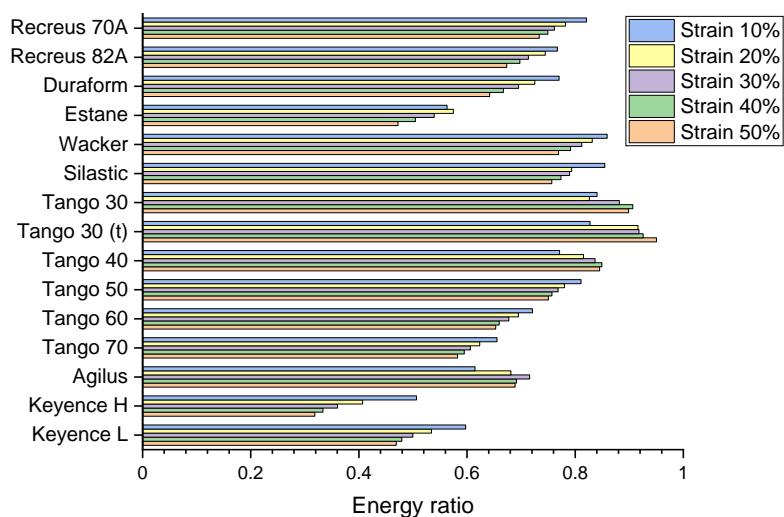
Figure 7.8: Energy ratio brought to the samples between the 2nd and the 1st loading.

In general, the TPUs exhibited a decreasing Energy ratio as the strain levels increased i.e. an increasing Mullins effect. From the 10% to the 20% strain levels, the Energy ratio of Estane in fact increased; nevertheless, the increase is of only 2%. This increase is minor, considering that the difference between the extreme Energy ratio values of the MJF sample was of 18%. This difference was of 12% for Recreus 70A, 14% for Recreus 82A and 20% for Duraform. An increasing Mullins effect was also observed for Wacker and Silastic. While the first had a maximum variation of 11.5% between the Energy ratios at 10% strain and 50% strain, for the second this variation was of 13%. Keyence H and Keyence showed the same tendency. The photopolymers were the samples with the greatest rise in Mullins effect from the 10% to the 50% strain level. Keyence L varied its Energy ratio by 27% whereas for Keyence H the variation reached 59%.

The behaviour was not uniform for the Tango samples. The Energy ratio of the harder PolyJet materials, namely Tango 50, Tango 60 and Tango 70, also presented a decrease. The variations between the extreme values were of 8%, 10.5% and 12.5%, respectively. This suggests a lower propensity for an increase in the Mullins effect for greater strain levels as hardness reduces. However, Tango 40, Tango 30 and Tango 30 (t) showed the opposite. The greater the strain level, the greater the Energy ratio and thus the lesser the cyclic stress softening. This behaviour was not monotonic for Tango 40 and Tango 30. The Energy ratio for Tango 30 decreased by less than 2% between the 10% and the 20% strain levels, and less than 3% from 40% to 50% strain. The last drop for Tango 40 was of 0.5%. Since these decreases were small, they can be attributed to computing deviations. In addition, the difference between the extreme values of the Energy ratio were found to be 14%, 13% and 9% for Tango 40, Tango 30 (t) and Tango 30, respectively.

Agilus had a more particular behaviour. Up to 30% strain, the stress of the 1st loading cycle was softening less and less. Then the Energy ratio reduced (and the Mullins effect rose) in 3.4% at 40% strain and in less than 0.4% at 50% strain. As well as for the softer PolyJet materials, the reduction related to the final strain levels can be a result of computing deviations, especially considering the maximum variation of 14% in the Energy ratios. A stabilisation of the stress softening for loadings at strain levels above 30% should also not be excluded. In order to verify this, conducting further tests at higher strains is required.

7.4 Final Remarks

From the uniaxial cyclic tests, it was possible to notice the high energy dissipation capabilities of the photopolymers, especially the stiffer they were. The discrepancy of the hysteresis ratio of these materials to the behaviour of the silicone samples was evident, leaving them at the two extreme positions. The TPUs were found to have an intermediate performance. Therefore, when dealing with vibration absorption applications, this information is valuable for the most appropriate 3D printed material selection.

Furthermore, it can be stated that for all PolyJet photopolymers (i.e. the different Tango grades and Agilus), the Mullins effect varied little in comparison to the Keyence photopolymers. When working with Keyence H and Keyence L, one should be aware of the more progressive "damage" suffered by these materials, especially if they are submitted to larger cyclic strains. Another interesting remark is that Tango 30 and Tango 30 (t) together with the LSRs were among the samples with a low-to-moderate Mullins effect at all strain levels investigated. Moreover, Estane was the TPU with the highest stress softening in all cyclic stages. No relation between the intensity of the phenomenon and the material hardness could be confirmed.

The relevance of investigating the Mullins effect in 3D printed elastomers lies in their history-dependent behaviour in technical products, as well as in future constitutive modelling approaches. The phenomenon must be considered in order to ensure the constant properties and performance of the elastomers under long-term operations. Consequently, a more reliable behaviour prediction can be conducted with the help of numerical simulations. Lastly, it should be pointed out that the type of cyclic test may have influenced the results.

8. Uniaxial Stress Relaxation Testing

The stress relaxation tests enabled the characterisation of the viscoelastic behaviour of the studied materials. Thus, the experimental data provided the basis for the parameter identification of the generalised Maxwell viscoelastic model. The following sections are dedicated to the analysis of the stress relaxation tests for distinct strain conditions. The first section presents preliminary results for the TPUs, the silicones and the Keyence photopolymers. In the second section, the Tango and Agilus materials tested at 15% strain are examined. A comparative analysis of the stress relaxation of the samples stretched at 30% strain is conducted in the third section. Lastly, pertinent final remarks are provided.

8.1 Preliminary Assessments

For the first stress relaxation tests, appropriate strain values were chosen based on the tensile tests previously performed. The reference was the region near the end of the initial "linear" behaviour of the tensile curves. Some preliminary stress relaxation tests showed damage to the specimens or excessive plastic deformation at the end of the experiment. Hence, the strain values were reduced to avoid those effects. Due to their high stretchability and recovery, the silicones were tested at 70% strain. A strain of 50% was applied to Recreus 70A, Recreus 82A and Keyence L. Duraform and Keyence H were tested at 40% strain in view of the crumbling structure of the first and the stiffer behaviour of the second. The higher stiffness and distancing from the typical non-linear behaviour of elastomers in tensile loading of Estane led to the application of a constant strain of 30% to the specimens. A minor permanent set was observed for the Recreus (1%) and Keyence materials (2%). Duraform, Estane, Wacker and Silastic recovered to their original length after testing.

The experimentally observed stress relaxations, as well as the fitted curves from the viscoelasticity models, are shown in Figures 8.1 to 8.3 in a semi-logarithmic scale. The quality of the fits can be noticed. This resulted from several optimisation runs for each sample with varied Maxwell element numbers. The plots exhibit the "best solution". The criteria taken into account for the determination of the best fit were:

- at least one (when possible) and up to two (Johlitz et al., 2010) relaxation times per time decade for a proper representation of the relaxation behaviour;
- the absence of very small Maxwell stress-like constants (σ_i from Eq. 3.3.), whose contributions are minor;

- the "best" R-Squared values (especially if the changes were only at the 4th-5th decimal place for an additional Maxwell element); and
- the visual aspect of the fitting along the entire curve.
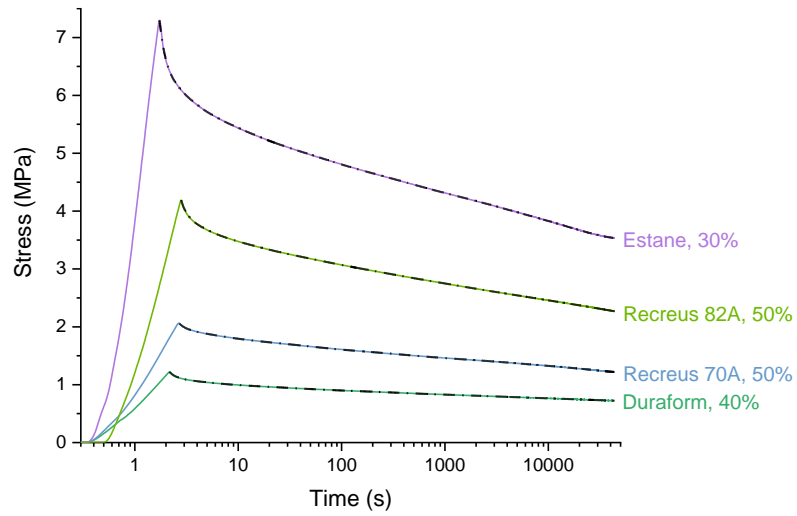
Figure 8.1: Stress relaxation data (solid) and fitting (dash-dot) curves for the TPU samples at different strains.
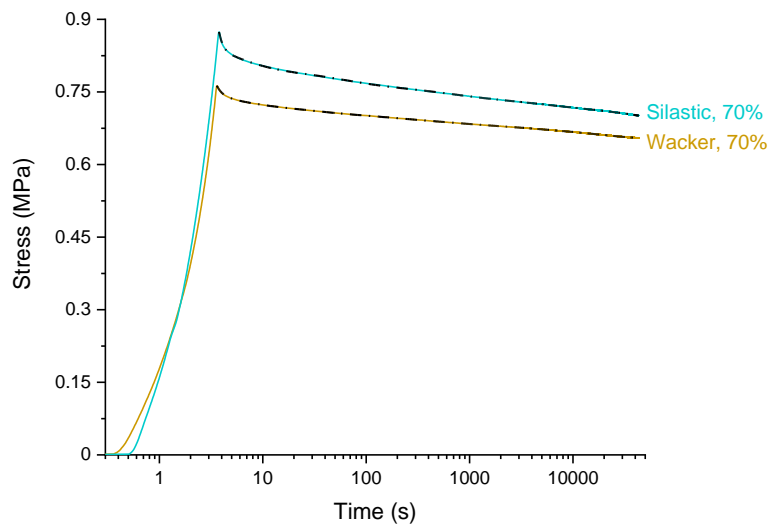
Figure 8.2: Stress relaxation data (solid) and fitting (dash-dot) curves for the LSR samples at different strains.
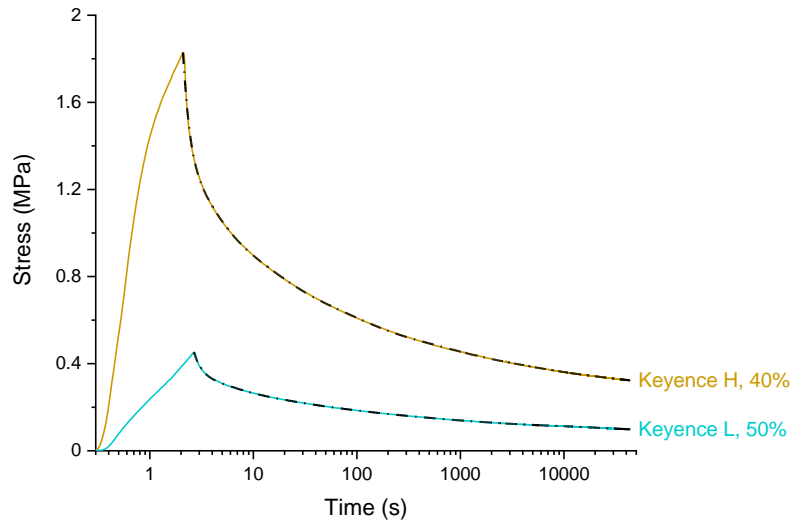
Figure 8.3: Stress relaxation data (solid) and fitting (dash-dot) curves for the Keyence samples at different strains.

The R-Squared values and the obtained viscoelastic parameters of the Maxwell elements are found in Appendix D.1 for each material. Table 8.1 below shows relevant figures from both the experimental data and the fitting values. For all samples, it is verified that the equilibrium stress was not achieved after the 12 hours of stress relaxation. Nevertheless, the last stress recorded, i.e. $\sigma(t = 12h)$ was close to the identified equilibrium stress (σ_∞), with a maximum deviation of 5%. In addition, a minimum of 6 Maxwell elements were generally required for an appropriate fitting.

Table 8.1: Experimental and fitting values from preliminary tests.

Sample	σ_0 (MPa)	$\sigma(t = 12h)$ (MPa)	Stress drop, exp. (%)	Maxwell Elements	σ_∞ (MPa)	$\sigma(12h)$ to σ_∞ deviation (%)
Recreus 70A	2.06	1.22	40.88	6	1.18	3.13
Recreus 82A	4.19	2.27	45.81	8	2.17	4.49
Duraform	1.22	0.72	40.68	6	0.71	1.47
Estane	7.30	3.54	51.53	7	3.49	1.19
Wacker	0.76	0.65	14.17	6	0.65	0.42
Silastic	0.87	0.70	19.74	6	0.68	2.52
Keyence H	1.83	0.32	82.31	7	0.31	3.23
Keyence L	0.45	0.10	78.13	7	0.09	4.65

As noticed qualitatively in Figure 8.3 and quantitatively in Table 8.1, Keyence H experimentally presented the most pronounced stress drop the among all tested materials: more than 82%. Keyence L had the same tendency, with a stress drop of around 78% from the maximum to the last recorded stress. This denotes the high stress relaxation behaviour of the Keyence photopolymers. In contrast, the lowest stress relaxations were recorded for the Wacker and Silastic silicones (below 20%), even considering their higher imposed strain. The TPUs were in an intermediate position, showing a decrease in stress of around 40-50%. No concrete comparative statements can be made since the loading conditions were diverse. Therefore, Section 8.3 is dedicated to this.

119

8.2 PolyJet Photopolymers at 15% Strain

The Agilus and Tango materials were tested starting from strains of 50%. Nevertheless, either the stresses exhibited an acute drop after a few hours of testing indicating damage, or the specimens broke in the process. The softest and most fragile material (i.e. Tango 30) was taken as a reference, and several tests were performed for decreasing strain values, which are not presented in this work. A strain of 15% was found to be suitable for the stress relaxation experiments. Hence, this value was applied for all other PolyJet photopolymers. None of the materials displayed permanent set after testing.

Since the experimental data from this section showed some noise in the force measurements, the signal obtained was processed subsequently. Thus, the functions *scipy.signal.savgol_filter* and *scipy.signal.savgol_coeffs* were used in the Python programming language for data smoothing, which applies a Savitzky-Golay filter to an array. Figure 8.4 illustrates the data processing for the Tango 50 sample.
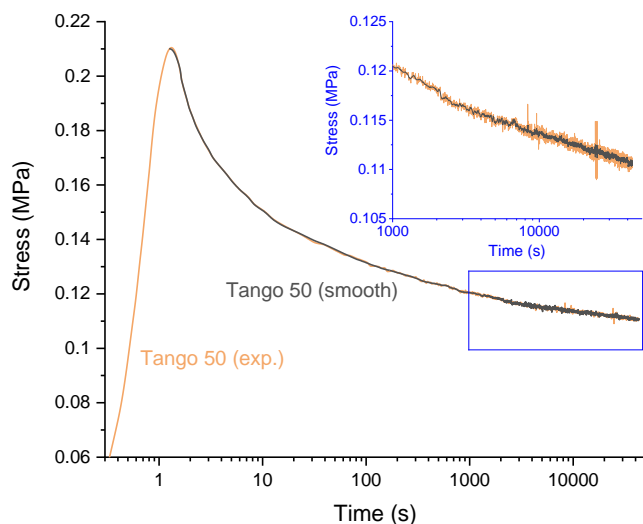
Figure 8.4: Smoothing (smooth) from the experimental data (exp.) for the Tango 50 sample.

Once all signals were processed, the curve fittings took place. Figure 8.5 gathers the experimental and fitted curves for the different Tango grades and Agilus materials. The criteria described in Section 8.1 for an optimal fitting were considered. The identified parameters of the Maxwell elements and the R-Squared values are in Appendix D.2. In addition, experimental and fitting information is shown in Table 8.2.
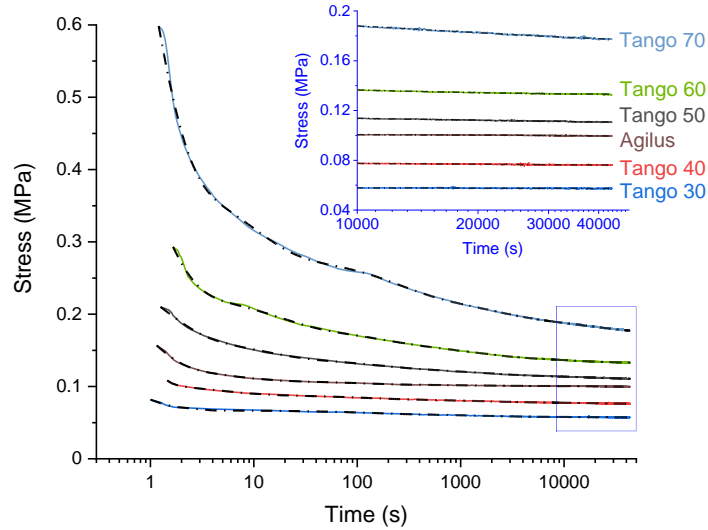
Figure 8.5: Stress relaxation data (solid) and fitting (dash-dot) curves for the Tango and Agilus samples at 15% strain.

Table 8.2: Experimental and fitting values from PolyJet photopolymers at 15% strain.

Sample	σ_0 (MPa)	$\sigma(t = 12h)$ (MPa)	Stress drop, exp. (%)	Maxwell Elements	σ_∞ (MPa)	$\sigma(12h)$ to σ_∞ deviation (%)
Tango 30	0.08	0.06	29.62	4	0.06	0.60
Tango 40	0.11	0.08	29.11	5	0.08	1.33
Tango 50	0.21	0.11	47.36	5	0.11	0.52
Tango 60	0.29	0.13	54.45	5	0.13	0.98
Tango 70	0.60	0.18	70.37	5	0.18	1.22
Agilus	0.16	0.10	36.74	5	0.09	9.04

A total of 5 Maxwell elements was suitable for the curve fitting of all PolyJet photopolymers, except Tango 30. Although also not reaching equilibrium within the test duration, the deviations from the last recorded values to the identified equilibrium stresses for the Tango samples were small. The largest deviation was circa 1.3% for Tango 40. The same cannot be said for Agilus, which deviated by more than 9%. This implies a much longer time required for its full relaxation compared to the Tango materials.

The experimental stress decays of Tango 30 and Tango 40 were similar, with the first being slightly larger than the latter. Considering the complete stress drop until reaching equilibrium in Table 8.3, called *Stress drop, eq.* and taken as $(\sigma_0 - \sigma_\infty)/\sigma_0$, this scenario was reversed. For the Tango 50, 60 and 70 materials, the stress drop listed in Table 8.2 increased with the material hardness. Nevertheless, no relationship could be established between the stress drop and the different hardness grades of the Tango samples. The pronounced decrease in stress on Tango 70 was remarkable, exceeding 70%. With a similar hardness to Tango 50, Agilus presented a slightly lower stress reduction. Taking the *Stress drop, eq.*, this dissimilarity reduced. Tango 50 relaxed by ~ 48% of the maximum stress, while it was of 42% for Agilus, consisting of a variation below 12% relative to Tango 50. This shows the distinct stress relaxation behaviour of similar materials printed with the same AM technology, but from different families and thus different chemistries.

Table 8.3: Total stress decrease until equilibrium from PolyJet photopolymers at 15% strain.

Sample	Stress drop, eq. (%)
Tango 30	30.04
Tango 40	30.04
Tango 50	47.64
Tango 60	54.90
Tango 70	70.72
Agilus	41.99

8.3 Stress Relaxation at 30% Strain

For a comparative analysis of the diverse materials, almost all samples were submitted to the same constant strain of 30%. This value was chosen as it was the minimum strain applied in Section 8.1. Among the PolyJet photopolymers, only Tango 60 and Tango 70 withstood this loading. The softer Tango specimens broke during testing. An unusual and more pronounced stress decay in the last hours of the experiment were noted for Agilus, whose damage was visually confirmed by the tearing throughout the cross section. Once more, Keyence H and Keyence L showed a permanent set of 2% and 1%, respectively, after unloading. The other tested materials fully recovered at the end of the tests.

Following the "best fit" criteria from Section 8.1, the curve fittings and the parameter identification of the viscoelastic models were performed. The fittings are shown in Figures 8.6 to 8.8, while the stress-like constants and relaxation times of the Maxwell elements with their respective R-Squared values can be found in Appendix D.3. Similar to Section 8.2, noise in the stress response of the Tango 70 and Tango 60 samples led to the smoothing of their test curves. The data processing took place in the same way as previously reported.
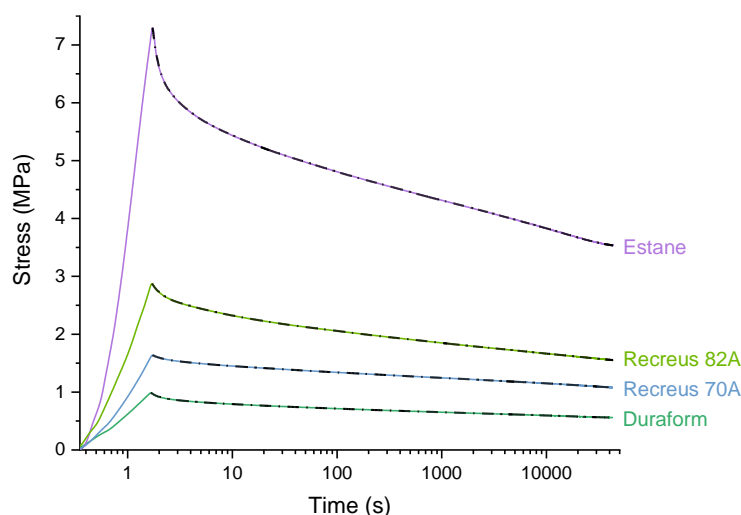
Figure 8.6: Stress relaxation data (solid) and fitting (dash-dot) curves for the TPU samples at 30% strain.
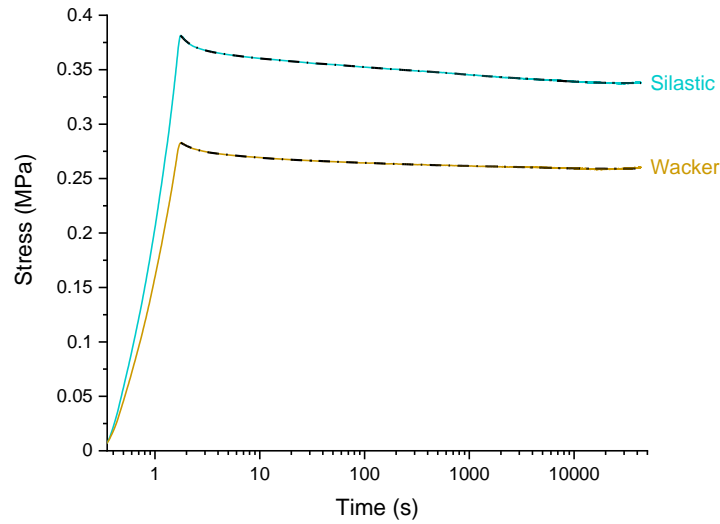
Figure 8.7: Stress relaxation data (solid) and fitting (dash-dot) curves for the LSR samples at 30% strain.
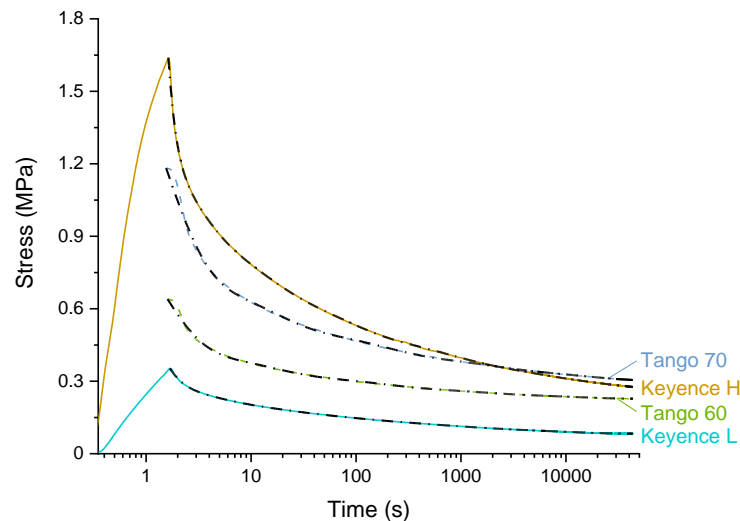
Figure 8.8: Stress relaxation data (solid) and fitting (dash-dot) curves for the photopolymer samples at 30% strain.

Table 8.4 contains relevant experimental and fitting data. The softest samples exhibited the lowest deviations between the last recorded stress values and the identified equilibrium stresses. That is, Keyence L and the Wacker and Silastic silicones, with harnesses of 35 and 50 Shore A, respectively. In fact, almost all samples relaxed to near equilibrium, with deviations of less than 3%. The exception was the TPU Recreus 70A, which was even further away from equilibrium after 12 hours of relaxation at 30% deformation than previously at 50% strain. This indicates a longer relaxation time required for this sample at a lower imposed deformation. The extrusion performance inherent to the printing process, i.e. the presence of a greater or lesser degree of under-extrusion typical of elastic filaments, could justify the dissimilarities between these deviations for the two Recreus materials. Conversely, by reducing the applied strain from 50% to 30% for Keyence L, so did the deviations of $\sigma(12h)$ to σ_∞, implying a faster stress relaxation at lower strain levels.

Table 8.4: Experimental and fitting values from stress relaxation at 30% strain.

Sample	σ_0 (MPa)	$\sigma(t = 12h)$ (MPa)	Stress drop, exp. (%)	Maxwell Elements	σ_∞ (MPa)	$\sigma(12h)$ to σ_∞ deviation (%)
Recreus 70A	1.64	1.08	34.14	7	1.01	7.13
Recreus 82A	2.87	1.55	45.97	7	1.51	2.96
Duraform	0.99	0.56	43.29	7	0.55	1.03
Estane	7.30	3.54	51.53	7	3.49	1.19
Wacker	0.28	0.26	7.94	5	0.26	0.51
Silastic	0.38	0.34	11.33	6	0.34	0.14
Tango 60	0.64	0.23	64.34	5	0.23	0.61
Tango 70	1.18	0.30	74.20	5	0.30	0.74
Keyence H	1.64	0.28	83.17	7	0.27	2.79
Keyence L	0.35	0.08	76.51	7	0.08	0.27

The silicones continuously displayed the lowest stress relaxation during testing, not exceeding a reduction of 12% of the maximum stress. The TPUs were next, with a stress decrease in the range of 34% to 52%. The greatest stress relaxation was observed for the photopolymers, which lost from 64% to even more than 83% in the process. The total stress decrease from the maximum to the equilibrium stress, i.e. *Stress drop, eq.*, is shown in Table 8.5 in ascending order.

Table 8.5: Total stress decrease until equilibrium for each sample in ascending order from stress relaxation at 30% strain.

Sample	Stress drop, eq. (%)	Type
Wacker	8.41	LSR
Silastic	11.45	LSR
Recreus 70A	38.52	TPU
Duraform	43.87	TPU
Recreus 82A	47.52	TPU
Estane	52.10	TPU
Tango 60	64.56	Photopolymer
Tango 70	74.37	Photopolymer
Keyence L	76.58	Photopolymer
Keyence H	83.63	Photopolymer

From the comparative analysis at 30% strain, the most pronounced stress drop among the silicone samples, i.e. Silastic, was at least 3 times lower than the stress decrease of the next material in ascending order, i.e. Recreus 70A. This fact was observed throughout the 12 hours of experiments and until equilibrium. The photopolymer samples were distinctly the materials with the greatest loss in stress. Among them, the Keyence samples were first in rank. In particular, Keyence L and Keyence H exhibited stress decays in the same range in the results from Section 8.1 (50% and 40% strain, respectively) and Section 8.3 (30% strain).

8.4 Final Remarks

From the analyses presented, it was evident that the silicone materials Wacker and Silastic were those with the lowest stress relaxations. This took place even for an imposed strain higher than for the other materials (70% for the silicones, as opposed to the varied strains of 15%, 30%, 40% or 50% for the TPUs and the photopolymers). Inversely, Keyence H and Keyence L exhibited the most pronounced stress decays. This fact was verified in the preliminary results from Section 8.1 (at strains of 40% and 50% for the harder and the softer Keyence samples, respectively), as well as in the stress relaxation experiments at 30% strain from Section 8.3. Similarly, the stiffest Tango materials, namely Tango 60 and Tango 70, also showed a stress relaxation superior to the TPUs, whether at 15% strain or 30% strain.

For applications that require a constant loading in terms of strain e.g. sealings, one should be aware of these facts when selecting 3D printing materials for the manufacturing of elastomeric parts. For photopolymers, a pronounced stress relaxation is to be expected. Further and more in-depth studies are definitely worth conducting for a more thorough investigation of the behaviour of 3D printed elastomers under the action of a constant deformation, considering different loading requirements, temperature changes and more material options.

126

9. Differential Scanning Calorimetry

The thermal transitions in the studied 3D printed elastomers were analysed by means of DSC experiments. The determination of the glass transition temperature was the focal point of this investigation. The evaluation of the specific heat capacity was also conducted. In this chapter, the first section focusses on studying the drying conditions of the TPU filaments. Subsequently, DSC runs performed at various cooling rates were assessed for a better understanding of the thermal behaviour of the Recreus samples. The last section is dedicated to the identification of the glass transition and specific heat capacity for all samples using the Three-Run-Method.

9.1 Recreus Filament Drying

Since TPUs are hygroscopic, the Recreus filaments were submitted to drying processes before printing if signs of moisture were detected. It is desirable for TPU filaments to have a moisture content level below 0.15% (Recreus, 2021) for good printability. No specific drying recommendations were available, but common practices in the 3D printing community include drying TPE filaments at 50°-60°C for at least 4 hours. Hence, a DSC experiment was carried out to study the impact of the drying process at 50°C for a duration of 4 hours.

The specific enthalpy rate represented by "DSC Signal" over the temperature is shown in Figure 9.1. Endothermic enthalpy changes are directed upwards. It can be noted that neither of the filaments presented changes in the course of the curves before and after drying. Neither enthalpy variations from first-order transitions (i.e. endothermic or exothermic events) nor baseline curve shifts from second-order transitions (e.g. glass transition) were observed. Furthermore, the samples did not visually show any kind of colour change after the test as an indication of possible degradation. In addition, the cooling curves (omitted here) were in conformity with each other and corresponding to a 180° rotation of the heating curves. The results infer that the filament drying procedure is appropriate taking into account the preservation of the material properties.

However, the performance of future studies is recommended for the evaluation of longer drying periods. Since the drying temperature is low, the removal of the moisture from the TPU filament takes some time. Furthermore, the higher the moisture content, the longer the drying should be in order to be effective. A short period of time such as 4 hours may not be sufficient for a possible ageing of the material during drying, which could potentially

change the filament's properties in prolonged times. Drying optimisation is also a relevant topic for further investigations for an efficient drying procedure.
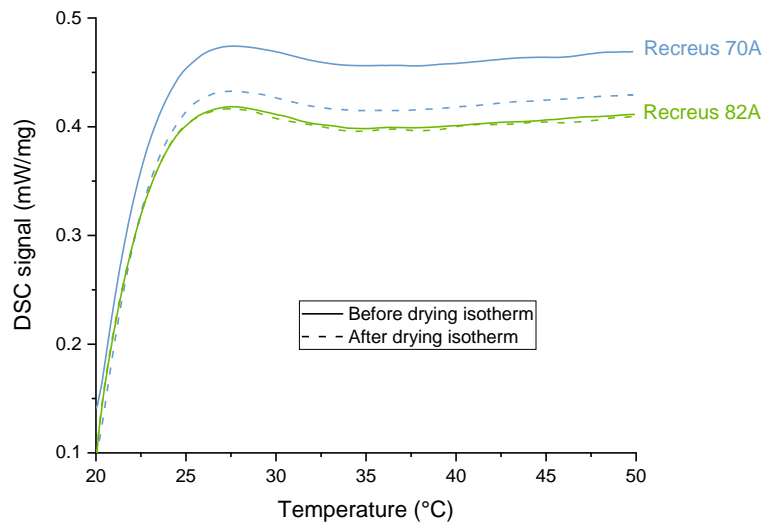
Figure 9.1: DSC results from the investigation on the drying of the Recreus filaments.

9.2 Investigations on Recreus Filaments at Multiple Cooling Rates

Since the focus of this chapter lies on the material characteristics of the filaments, the DSC results up to the first complete cooling-heating cycle (erasing the material's memory) are omitted in this section. Recalling Figure 5.11, this means that the DSC signals from Segment 1 are not displayed; only from Segment 2 onwards the curves are shown. The cooling scan from Segment 2 is also included due to the varying cooling rates analysed in this section. The DSC curves for Recreus 70A and Recreus 82A are shown in Figures 9.2 and 9.3, respectively, where the endothermic enthalpy changes are directed upwards.

For both TPU filaments, there was a pronounced glass transition at negative temperatures. The glass transition temperature Tg is usually below room temperature for typical rubbers. It can be noted that Recreus 70A behaved almost similarly to an amorphous thermoplastic. The change in the cooling rates did not produce any significant changes in the course of the curves, which were quite in agreement. A particular thermal event at around 20°C was observed for both TPU filaments. Figure 9.4 displays the heating curves after cooling at 10°C/min (Segment 4 from the temperature program) magnified in this region.

128
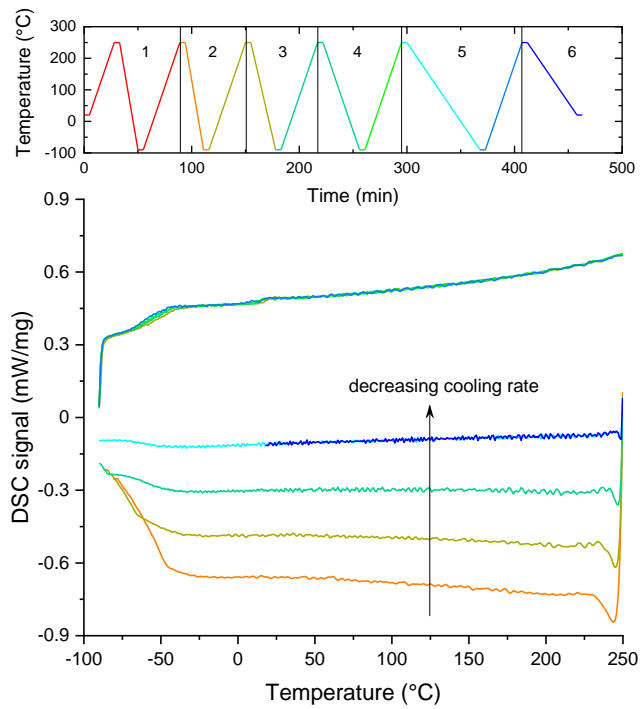
Figure 9.2: DSC results from Recreus 70A for the investigations at multiple cooling rates of 20 °C/min (Seg. 2), 15°C/min (Seg. 3), 10 °C/min (Seg. 4) and 5 °C/min (Seg. 5-6).
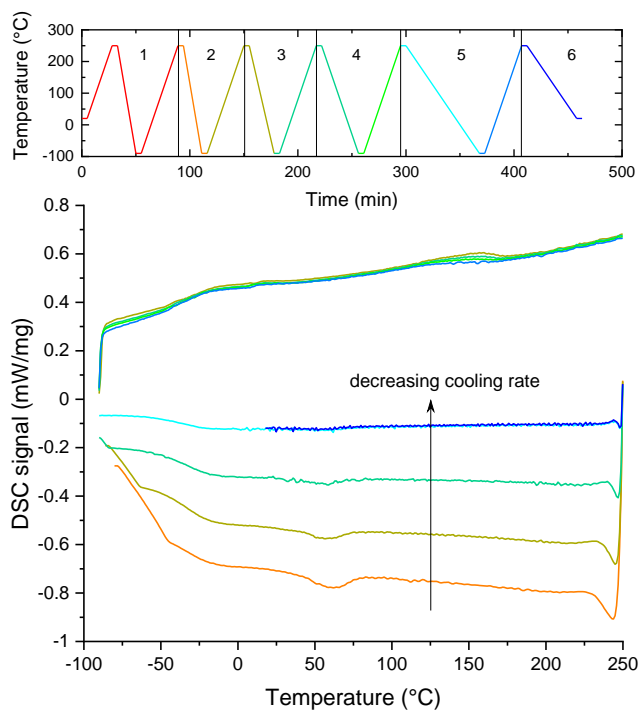
Figure 9.3: DSC results from Recreus 82A for the investigations at multiple cooling rates of 20 °C/min (Seg. 2), 15°C/min (Seg. 3), 10 °C/min (Seg. 4) and 5 °C/min (Seg. 5-6).
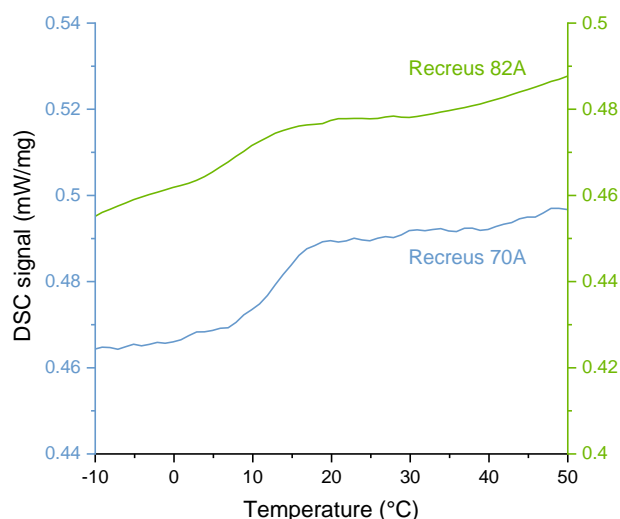
Figure 9.4: Thermal event at circa 20°C on heating curves after cooling at 10°C/min (Seg. 4).

At first, this event appeared to be a small, second glass transition. After further analysis, that was attributed to a smooth, extended melting peak, as identified by León-Calero et al. (2021). No other peaks in cooling or heating were detected for Recreus 70A, denoting its low crystallisation degree. On the other hand, Recreus 82A showed more evident endothermic peaks at around 155°C. The melting peaks indicate the disordering of existing crystallites from the hard segment content. This is reasonable, as most TPEs have a crystalline hard phase (Roland, 2013). Furthermore, Recreus 82A has lower elastic capabilities than Recreus 70A due to the higher hard-to-soft segment ratio (Léon-Calero et al., 2021), having thus more crystallinity. The crystallinity degree was not investigated. Nevertheless, the results suggest a highly amorphous content for Recreus 70A and Recreus 82A, since their theoretical melting points at 195°-220°C (Recreus, 2022a) and 220°-240°C (Recreus, 2022b), respectively, were not recorded in the DSC experiments.

The presence of a single melting peak at around 20°C during heating (see Figure 9.1) implies only one morphology from the crystallisation of the softer TPU Recreus 70A. Recreus 82A, on the other hand, probably has two crystal morphologies. This is assumed to be due to the two melting peaks identified at circa 20°C and 155°C, with the predominance of the crystal structure that melts at higher temperatures. In addition, both the fusion and the crystallisation heat of the stiffer TPU decreased with the cooling rate. In fact, the area of the peaks in the cooling curve at 5°C/min and the following heating curve from Segment 5 seemed to have disappeared. This contradicts the tendency of increasing crystallinity with decreasing cooling rate, as the polymer has more time to crystallise before molecular motions become slower. Frequently stated in the literature, faster cooling processes reduce the amount of polymer that crystallises from the molten state (i.e. during cooling), while peaks of recrystallisation (i.e. crystallisation upon reheating) rise (Wellen et al., 2015; Hu et al., 2022). The decreased crystallisation tendency of Recreus 82A may be a result of chemical changes occurring after several cooling-heating cycles, as reported by Mittermeier and Lion (2020) for repeated DSC segments with polyethylene terephthalate. For further clarification, individual tests with the different cooling rates are suggested in future studies.

130

The single endothermic step from the glass transition in Figures 9.2 and 9.3 infers the presence of two miscible amorphous contents, one from the soft segments and one from the hard segments. The glass transition temperatures for both Recreus 70A and Recreus 82A decreased with the cooling rate. The values identified by the midpoint method from the heating curves after cooling at the different rates are shown in Table 9.1 below. The glass transition temperature of Recreus 82A was higher compared to Recreus 70A. This demonstrates the lower mobility of the polymer chains of the stiffer filament (Menczel and Prime, 2009).

Table 9.1: Glass transition temperatures from the investigations at multiple cooling rates.

Material	Heating curve after cooling at:			
	20°C/min (Seg. 2)	15°C/min (Seg. 3)	10°C/min (Seg. 4)	5°C/min (Seg. 5)
Recreus 70A	-40	-44	-51	-53
Recreus 82A	-26	-26	-29	-33

The measured DSC signals of both filaments (recall Figures 9.2 and 9.3) showed some difficulty in controlling the temperature change in cooling towards -90°C. Hence the sudden increase of the signals can be seen on the left side of the graphs. Furthermore, the lower the cooling rate, the better the temperature control. For the cooling at 5°C/min, the target temperatures were easily achieved. This reveals the limitations of the gaseous nitrogen for refrigeration at such low temperatures. Therefore, liquid nitrogen was applied for the materials from Section 9.3 for testing below -80°C. From the experiments, the subsequent heating scans with isotherms of 5 minutes led to little variation in the curves. Moreover, the temperature of a 5% weight loss for these Recreus filaments is reported in the literature as approximately. 290°C, with a temperature stability up to 250°C (León-Calero, M. et al., 2021). Hence, it can be concluded that printing up to 250°C in FFF machines appears to be a safe procedure.

9.3 Determination of Glass Transition and Specific Heat Capacity

This section presents and analyses the results from the DSC runs for all samples with the same heating/cooling rates using the Three-Run-Method. First, the glass transition temperatures are identified and discussed. In a second subsection, the specific heat capacities are identified.

9.3.1 Glass Transition

The results of the third set of DSC experiments are presented in the following figures. Endothermic enthalpy changes are directed upwards. Both the second and the third heating scans are plotted, assisting in the analysis of the thermal events and their repeatability. Figure 9.5 presents the DSC curves for the TPU samples. Since the maximum testing temperature of the Recreus samples was lower than in Section 9.2, no major endothermic

peak was observed for Recreus 82A. The small peaks at circa 20°C were again recorded for the Recreus filaments in a range of temperatures but without an absolute maximum. Additionally, their curves are in agreement with those from the previous investigation. The results of the four materials also correspond to literature values of the Tg of polyurethane elastomers between -60°C and -40°C (Drobny, 2014). Duraform and Estane showed endothermic peaks, representing the melting of the crystalline region of these samples. For all TPUs, a large glass transition at negative temperatures was detected, which is related to their amorphous content. Finally, the third consecutive heating scans were also in compliance with the second heating scans.
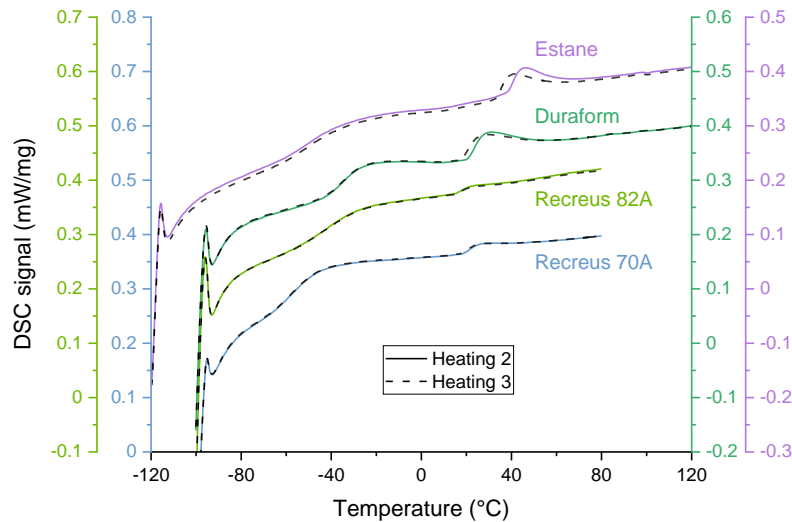
Figure 9.5: DSC results from the Tg investigation for the TPU samples.

The LSRs samples exhibited their characteristic glass transition at very low temperatures, as seen in Figure 9.6. The jump in the baseline at around -110°C was similar for Wacker and Silastic. A significant melting peak was also observed for both samples at -45°C. The LSRs contain a notable crystalline phase, hardening on cooling below -84°C, which was the crystallisation temperature detected in the cooling curves (but omitted here). The results are in accordance with the glass transition and melting temperatures of polysiloxanes in the literature of approximately -120°C and -40°C, respectively (Mark and Erman, 2007). Furthermore, the third heating scan was in line with the second heating scan, demonstrating the reversibility of the thermal events. Although being processed in different 3D printing technologies, i.e. Silastic in LAM and Wacker in DOD, their thermal behaviours from the DSC measurements were nearly the same.
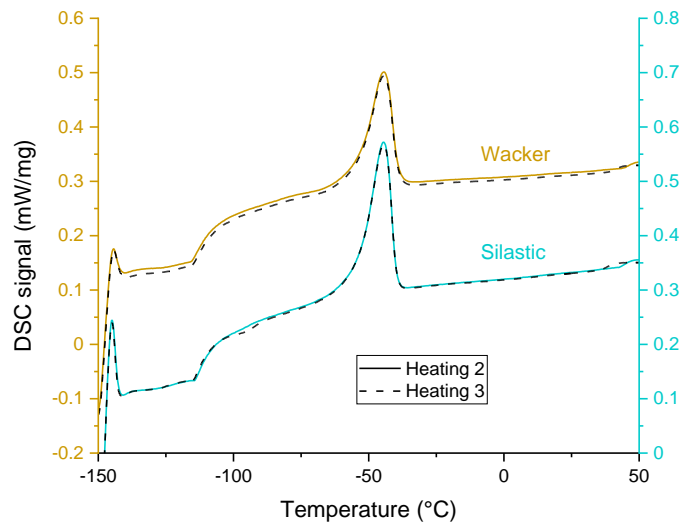
Figure 9.6: DSC results from the Tg investigation for the LSR samples.

For the Tango photopolymers (Figure 9.7), the curve shapes were similar to those of the Recreus materials. A large glass transition was identified, however, close to 0°C. This limits the lower temperature range in which a part printed with the Tango materials can operate. A slight melting peak appeared in temperatures between 31°C and 46°C. Hence, a small crystalline content is likely found in the Tango samples. No other endothermic peaks were recorded. In addition, the second and third heating scans were similar.
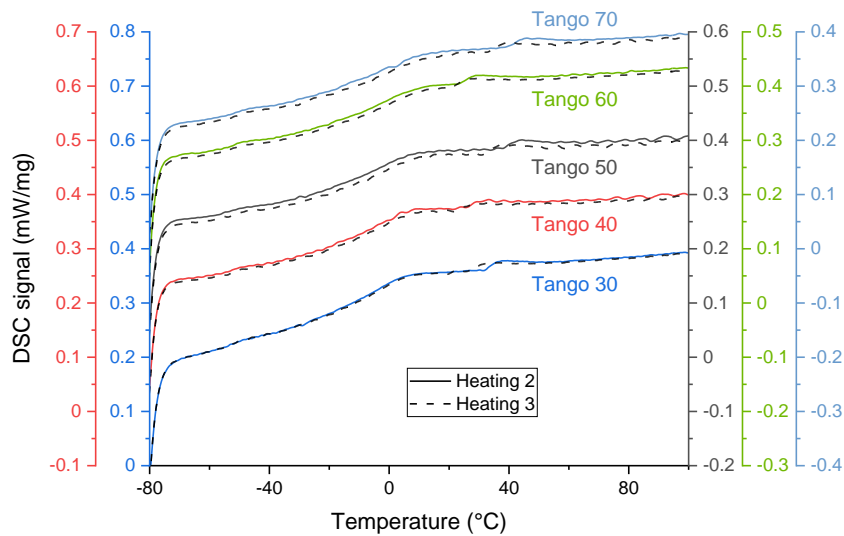
Figure 9.7: DSC results from the Tg investigation for the Tango samples.

It can be noted from Figure 9.8 that, unlike the other PolyJet photopolymers, an evident melting peak was present for Agilus. This sample showed an endothermic peak of 2.5 J/g at 40°C. In addition, the endothermic peak in the third heating scan was shifted by about 6°C to lower temperatures. This may suggest an alteration in its structure. Further studies are required to better assess the structure and morphology of the 3D printed Agilus material, since this work concentrated on a general analysis of the transition of the glassy to the rubbery state.
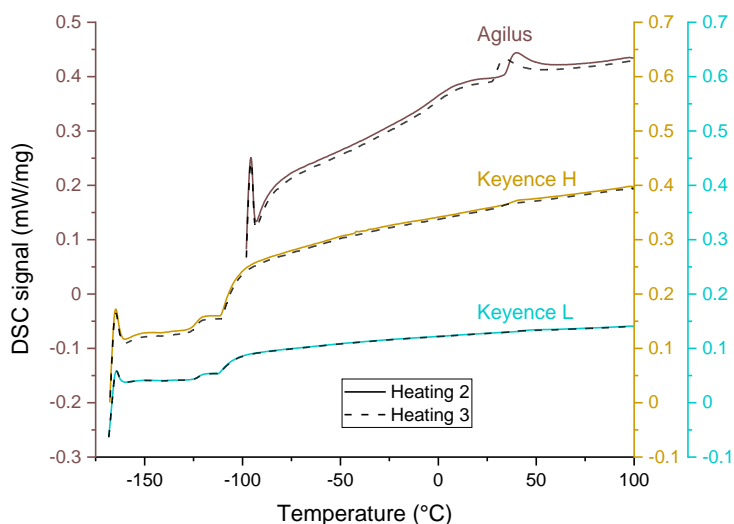
Figure 9.8: DSC results from the Tg investigation for the Keyence and Agilus samples.

The DS signals of the Keyence samples plotted in Figure 9.8 had a more distinct thermal behaviour compared to the PolyJet photopolymers. The very low glass transition temperatures around -110°C are due to their silicone content. Barely noticeable endothermic peaks were verified near 40°C. Once again, this indicates a small crystalline content. For the photopolymers Keyence H and Keyence L, the subsequent heating scans were in good agreement. There were apparently peaks at the onset of the glass transition, but no crystallisation exotherms in the cooling scans. Experiments performed at cooling rates of 5°C/min and 20°C/min (but not shown here) revealed that these peaks were reduced with the cooling rate. Future in-depth investigations may provide more clarity in this regard.

Relevant figures retrieved from the DSC results and discussed here are listed in Table 9.2 for each sample. The glass transition temperature taken as the midpoint temperature of the baseline step, the identified peak temperature (Tm) of the endothermic events and its respective heat of fusion, ΔH_f, are detailed below.

Table 9.2: Glass transition temperature, endothermic peak temperature and heat of fusion from the Tg investigation.

Sample	Tg (°C)	Tm (°C)	ΔH_f (J/g)	Sample	Tg (°C)	Tm (°C)	ΔH_f (J/g)
Recreus 70A	-49	18-45	1.03	Tango 40	-1	33	0.47
Recreus 82A	-40	15-50	0.80	Tango 50	-3	44	0.52
Duraform	-33	32	4.00	Tango 60	-5	31	0.47
Estane	-41	45	2.21	Tango 70	-3	46	0.57
Wacker	-112	-45	13.54	Agilus	-1	40	2.50
Silastic	-110	-45	16.91	Keyence H	-108	34-50	0.18
Tango 30	-2	40	1.09	Keyence L	-109	42-53	0.05

In comparison with the results of the heating scans after cooling at 10°C/min from Section 9.2, Recreus 82A showed a lower glass transition temperature. An assumption for the higher mobility of the Recreus 82A molecules in this section is the temperature program used. In Section 9.2, the material was submitted to a higher temperature from the start, leading to the melting of the crystals within the structure. With the cooling scan, crystallisation took place, which restricted chain mobility. Since no significant melting

occurred in the DSC tests with Recreus 82A in the current section, the resulting mobility of the molecules was higher, and the glass transition temperature was lower. On the other hand, Recreus 70A did not reveal a substantial melting peak in the previous investigation, which led to the conclusion of the lower crystallinity of the softer TPU filament. There was no effective crystallization due to its highly amorphous nature. Hence, both temperature programs from Sections 9.2 and 9.3 yielded similar results for the glass transition of Recreus 70A.

All PolyJet photopolymers exhibited similar values for the Tg. The negative glass transition temperatures of the Keyence materials were in accordance to those of the LSRs since they all have silicone in their composition. In fact, the DSC signals from Keyence H and Keyence L were quite similar to those from Wacker and Silastic (except for the absence of a melting peak). At last, it is worth mentioning that for all materials apart from the Tango grades there was a "start-up hook" on the left side. This was a consequence of the refrigeration system of the machine, which used liquid nitrogen in these experiments.

9.3.2 Specific Heat Capacity

The specific heat capacity curves were calculated for all samples and are plotted in Figures 9.9 to 9.12. As the specific heat capacity is proportional to the DSC signal, the endothermic peaks were equally reflected in the curve. As expected, c_p was positive since it is the amount of energy per unit mass needed to raise the temperature of a system by one degree. The endothermic peaks and the step changes due to the glass transitions (except for Keyence L due to the graphic scale) can also be seen.
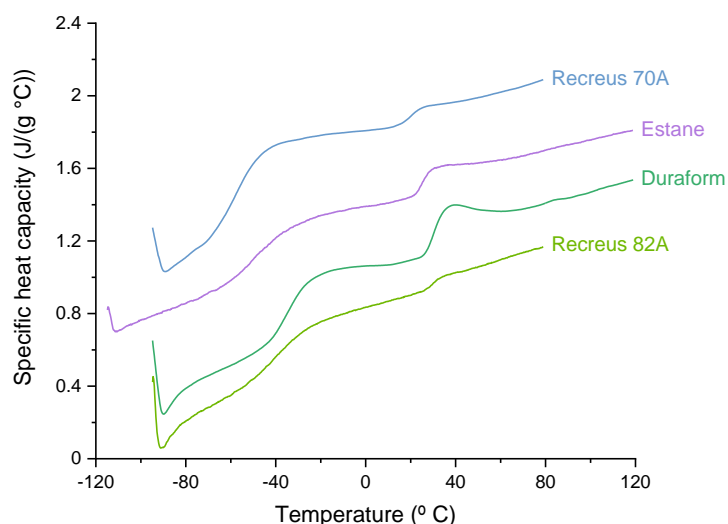
Figure 9.9: Specific heat capacity for the TPU samples.
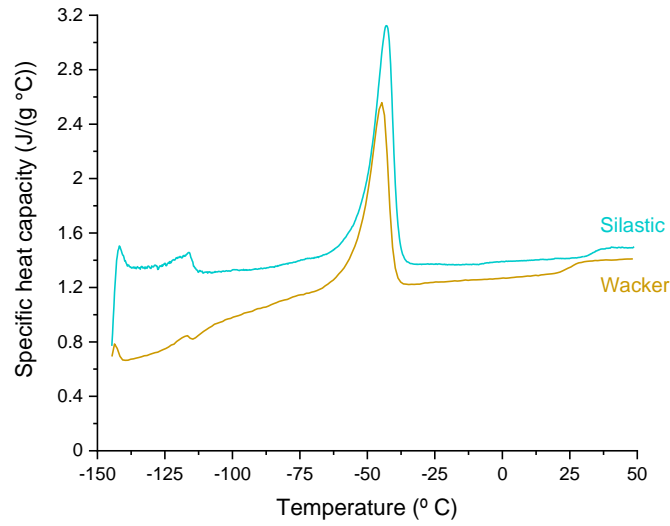
Figure 9.10: Specific heat capacity for the LSR samples.
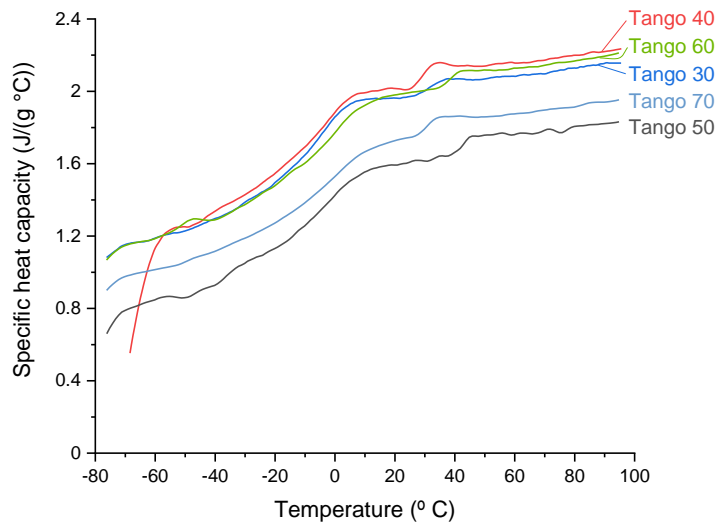
Figure 9.11: Specific heat capacity for the Tango samples.
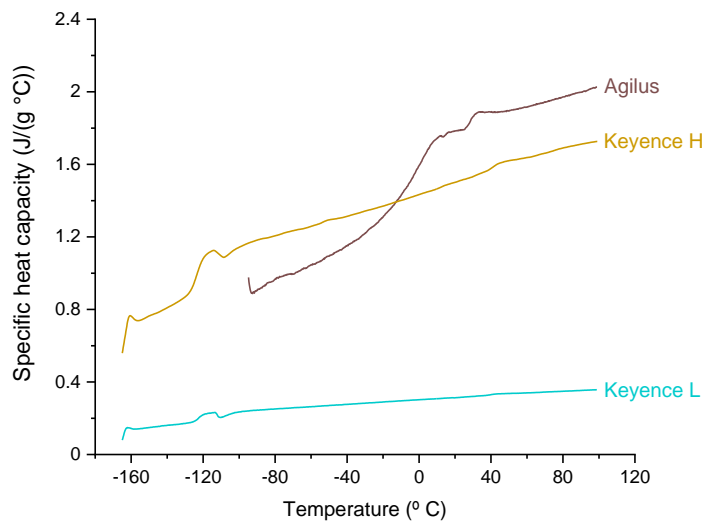
Figure 9.12: Specific heat capacity for the Keyence and Agilus samples.

136

Although not as perceptible in the DSC signals, the c_p curves for the TPUs seem to have a slight step in the temperature range of 20°C to 60°C, where the melting peaks are. The same can be said for Agilus for temperatures between 25°C and 45°C. This could indicate a second glass transition or it may be a reflection of a broad fusion range. Similarly, for both silicone samples a glass transition seems to arise at the end of the testing temperature range. Further investigations are required encompassing various heating/cooling rates and a higher testing temperature (in particular for the LSRs). In this way, the possible presence of a second Tg for these materials can be verified.

It can be noted that the increase in the specific heat capacity with the temperature does not assume a linear form for all materials in the shared temperature range. This is due to the endothermic events between 20°C and 50°C. For this reason, fittings were performed in the Origin software to obtain linear piecewise equations. In some cases, no linear fitting was possible because of the proximity to the glass transition or the oscillations of the signal. The description of the trendlines and their valid temperature ranges can be found in Appendix E.

9.4 Final Remarks

From the DSC analyses, the similarities between the caloric behaviour of the LSRs and the Keyence photopolymers, particularly Keyence H with comparable heat flow values, were observed. In spite of the lack of an evident melting peak, as for Wacker and Silastic, Keyence H and Keyence L displayed a large temperature range in the rubbery state. This information is very pertinent concerning operating temperatures. The LSRs and the Keyence samples are processed in different AM technologies and showed very distinct mechanical behaviours (as verified in the previous chapters). Nevertheless, the silicone content in all four materials was the major factor for their analogous thermal response. This demonstrates the key role of the chemical formulation rather than the material type.

Despite also being photopolymers, the PolyJet samples did not behave similarly. They were the ones with the highest glass transition temperatures. The glass transition of the Agilus and Tango materials were placed in negative temperatures very close to 0°C. Therefore, their operational temperature in the lower range is more limited.

Along with the glass transition temperature, the specific heat capacity is an essential property for calculations that involve thermal processes. The identification of the c_p presented here for several 3D printed elastomers constitutes a relevant database for future works. These include the development of constitutive models for the investigation of the material behaviour (Bergström, 2015), particularly for numerical modelling purposes. Finally, it should be pointed out that the results from this chapter are closely associated with the algorithms of the thermal analysis software used, and that analysis on a software with different algorithms may provide different results (Ehrenstein et al., 2004).

10. Dynamic Mechanical Analysis

The aim of the DMA tests was the characterisation of the viscoelastic behaviour of the investigated materials by measuring their mechanical properties as a function of frequency and temperature. The evolution of the storage modulus, loss modulus and loss factor with temperature was analysed. For most of the samples, the glass transition was identified and a master curve of the viscoelastic parameters over a broader frequency range was obtained with the time-temperature superposition procedure. In the following sections, the DMA results of the T-f sweeps of the TPUs and the PolyJet materials are initially assessed. The second section deals with the temperature sweeps of the LSRs and the Keyence photopolymers. Finally, the master curves resulting from the temperature-frequency sweeps are presented and discussed.

10.1 Temperature-Frequency Sweeps

The viscoelastic properties of the TPUs, the Agilus and the Tango materials were measured using temperature-frequency sweeps. As an example, Figure 10.1 shows the evolution of the storage and loss moduli along with the loss factor over the temperature for Recreus 82A. The curves for the minimum and maximum frequencies as well as for an intermediate frequency are displayed.
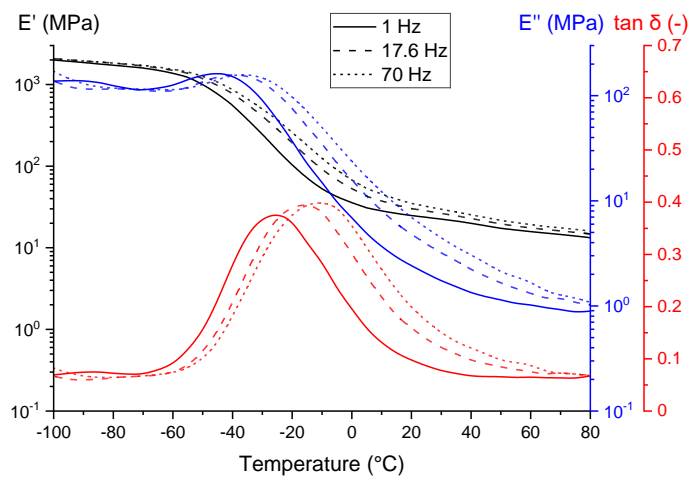
Figure 10.1: Storage modulus (E'), loss modulus (E") and loss factor (tan δ) of Recreus 82A as a function of temperature for different frequencies.

As expected, there was a shift to higher temperatures with increasing frequency as a result of the rise in stiffness for faster oscillations (Ehrenstein et al., 2004; Menczel and Prime, 2009), which occurred for all samples. The glass transition was identified in the temperature range containing the steep drop in E′ and the peaks of E″ and tan δ. As mentioned, the peak in the loss modulus was considered for the determination of Tg.

Due to the frequency dependence of the glass transition temperature, a frequency of 1 Hz is traditionally adopted as a convention for measuring Tg (Menczel and Prime, 2009). This was also the convention used in this chapter. The viscoelastic properties of the TPUs are seen in Figures 10.2 to 10.4. Being rubber-like materials at ambient temperature, the stiffness changed in 2-3 orders of magnitude to values in the 10^0-10^1 decade. This consisted of a 97% to 99% drop in storage modulus for all four thermoplastic polyurethanes. As the TPUs were tested below their softening and melting points, no steps related to these events were recorded in E′.
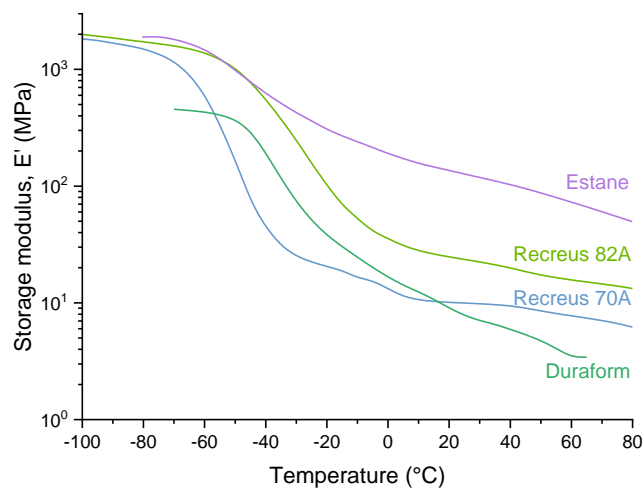
Figure 10.2: Storage modulus at 1 Hz as a function of temperature for the TPUs.
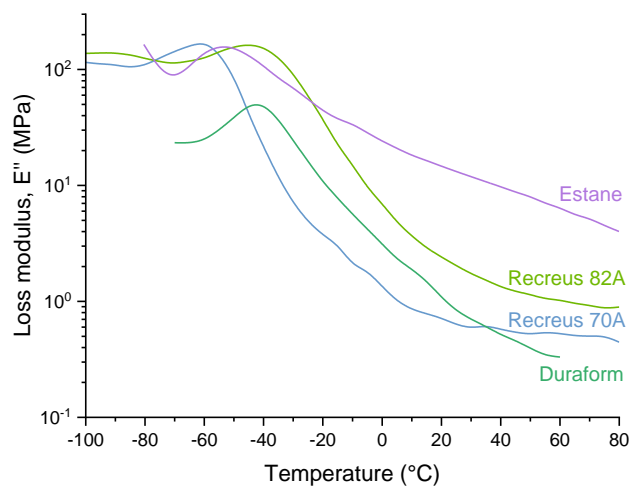
Figure 10.3: Loss modulus at 1 Hz as a function of temperature for the TPUs.
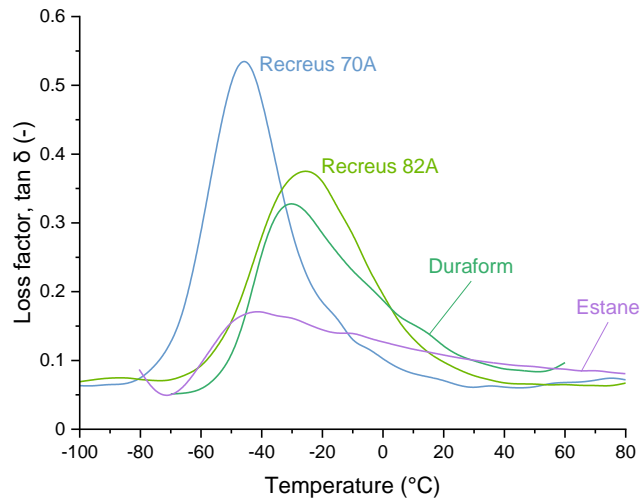
Figure 10.4: Loss factor at 1 Hz as a function of temperature for the TPUs.

The more pronounced change in the storage modulus for Recreus 70A compared to Recreus 82A demonstrates the higher soft segment content in the softer filament. Furthermore, the evolution of the loss factor over the temperature shows the damping capabilities of Recreus 70A in the glass transition region. At ambient temperature (20°C to 25°C), this material has the lowest tendency to dissipate energy among the TPUs, as already verified in the cyclic tests from Chapter 7.

The viscoelastic parameters for the PolyJet photopolymers are displayed in Figures 10.5 to 10.7. The stiffness decreased by 3-4 orders of magnitude during the experiments, corresponding to reductions of 99.92% to 99.98% in the storage modulus. As observed in previous mechanical testing, these materials exhibited the lowest stiffness among all samples investigated, with storage moduli between 0.36 MPa and 1.70 MPa at 60°C. Similarly to the Recreus materials, the softest Tango sample had the most pronounced change in the storage modulus. As the soft segment content decreased in the Tango materials with the progressive addition of the VeroClear component (see Section 5.1), E' was reduced more smoothly and to a greater degree.
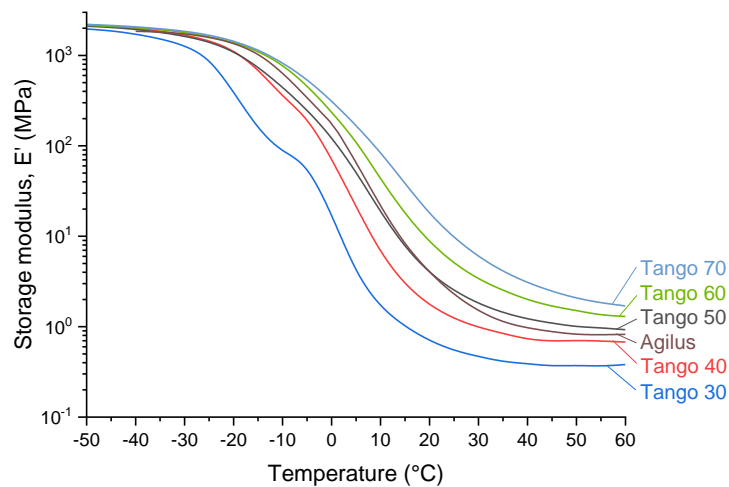
Figure 10.5: Storage modulus at 1 Hz as a function of temperature for the PolyJet photopolymers.
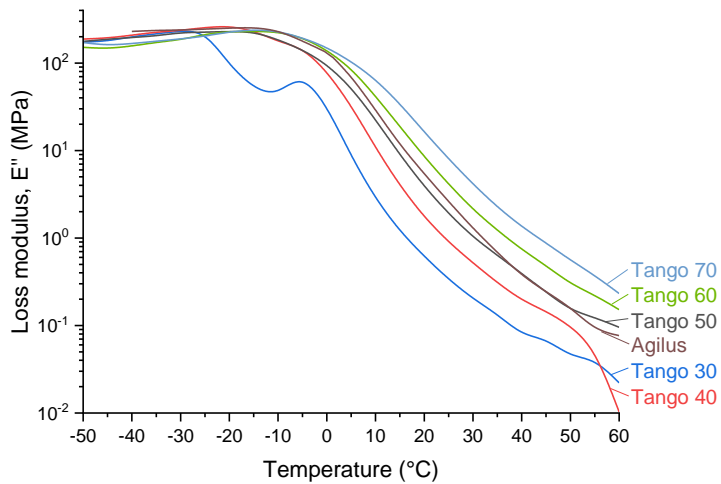
Figure 10.6: Loss modulus at 1 Hz as a function of temperature for the PolyJet photopolymers.
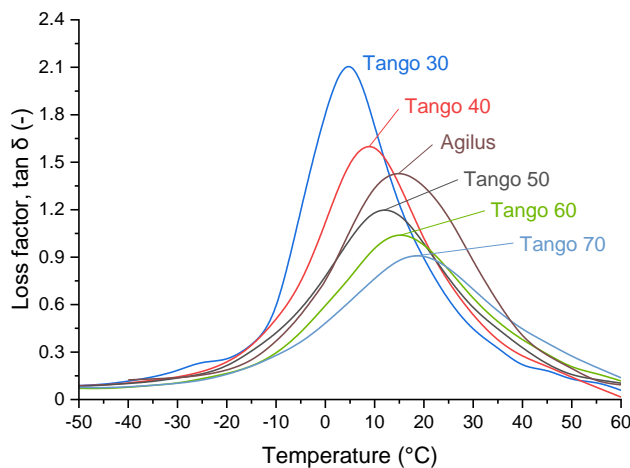
Figure 10.7: Loss factor at 1 Hz as a function of temperature for the PolyJet photopolymers.

The change in the composition of the Tango photopolymers was also verified in the decreasing height of the $\tan \delta$ peak with increasing hard segment content. The relative height of the peaks can be used to quantify the component proportions (Ehrenstein et al., 2004). For instance, the height of Tango 70's peak relative to Tango 30 was 0.41, indicating a proportion of approximately 40/60 of TangoBlackPlus/VeroClear. Nevertheless, at temperatures above the glass transition there was a significant reduction in the damping of the softer Tango material. In this temperature range, the tendency shown previously in the cyclic testing in Chapter 7 repeated itself: the harder the Tango sample, the higher the damping. Additionally, the samples of equivalent hardness grades Tango 50 and Agilus presented similar behaviours. Agilus, however, indicated a higher damping capacity.

The loss factor peaks at higher temperatures and the broader glass transition region of the PolyJet photopolymers compared to the TPUs is noteworthy. According to Menczel and Prime (2009), crosslinked thermosets and crystalline polymers show a broad glass transition, which is rather narrow for most amorphous polymers. The occurrence of the

142

peaks of tan δ in positive temperatures is another fact observed. This limits the minimum service temperature of a part printed with these materials.

An interesting fact is the presence of a local maximum at -5°C in Tango 30's loss modulus. In fact, there was also a change in the slope and a second drop in the storage modulus around this temperature. This response was found in all of the frequencies tested in the T-f sweep and corresponds to a softening point. A second peak in the loss factor of Tango 30 was not seen. However, the area of the peak was wide, and it is likely that this event was concealed. The same behaviour was almost imperceptible in Tango 40, while it was not detected for the harder Tango materials. It is supposed that, by adding the VeroClear component to the mix with the TangoBlackPlus component, this softening point tends to disappear due to changes in the material chemistry. Another possibility that cannot be disregarded is errors in the measurement caused by the very soft nature of these two grades of Tango, especially Tango 30.

Table 10.1 gathers the identified glass transition temperatures with the respective E″ peak values, the storage modulus in the glassy and rubbery states, and the magnitude and location of the loss factor peaks. It can be noted that the results from the DMA and the DSC (Table 9.2) tests were in good agreement. As these are different measurement processes, a variation in Tg was expected. Nonetheless, the glass transition temperatures identified in the caloric experiments were all within the temperature range given by the intervals between the peaks of E″ and tan δ. Contrary to the DSC analysis, the melting peaks of the materials at temperatures between 30°C and 50°C were not detected. One assumption is that these peaks were too small compared to the impact of the glass transition and did not cause a significant enough change in the storage and loss moduli for their detection by the sensor used. Further investigations are required for a more accurate statement in this regard.

Table 10.1: Glass transition temperatures and relevant figures of the viscoelastic parameters of the TPUs and PolyJet photopolymers.

Sample	Tg (°C)	E″ at peak (MPa)	E′ (MPa)		tan δ at peak	
			Max.	Min.	Value (-)	Temperature (°C)
Recreus 70A	-61	174.39	1,824.51	6.20	0.55	-46
Recreus 82A	-45	164.56	2,000.19	13.29	0.38	-25
Duraform	-42	50.44	455.58	3.42	0.33	-30
Estane	-53	158.57	1,914.15	49.65	0.17	-41
Tango 30	-29	232.59	1,965.46	0.36	2.27	5
Tango 40	-21	264.83	2,160.95	0.68	1.66	9
Tango 50	-19	230.07	2,103.25	0.93	1.22	12
Tango 60	-16	230.59	2,154.15	1.30	1.07	15
Tango 70	-15	240.85	2,201.86	1.70	0.92	19
Agilus	-17	255.55	1,847.98	0.81	1.46	15

The service temperature is defined by the plateau region of the E′ vs. T plots (Grady et al., 2013), while Tg indicates the thermal operating limits. Thus, from the temperature sweeps at 1 Hz, it can be affirmed that the TPUs can be used at lower temperatures than the PolyJet photopolymers. The former revealed glass transition temperatures between -61°C and -42°C while for the latter, they were between -29°C and -15°C. In addition, the storage

modulus stabilised after the glass transition drop in temperatures around 20°-30°C for the PolyJet and Recreus materials. The minimum operating temperature can also be expressed by the temperature at the loss factor peak. In this case, the TPUs could generally be used in applications as low as -25°C. Agilus and the different Tango grades would only be applicable in positive temperatures and, depending on the Tango hardness, only above room temperature.

10.2 Temperature Sweeps at 1 Hz

The DMA measurements of the LSRs and the silicone-based materials from Keyence are shown in Figures 10.8 and 10.9. Recalling Section 5.4.5, it was not possible to perform a continuous measurement with the same strain amplitude for these materials.
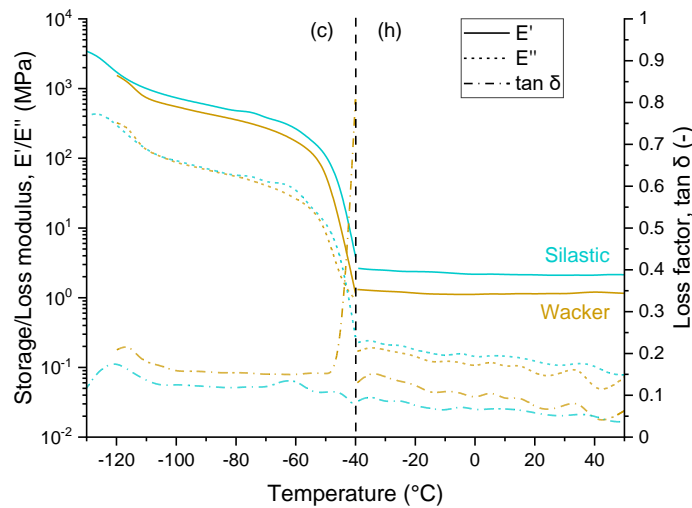
Figure 10.8: Storage modulus, loss modulus and loss factor at 1 Hz as a function of temperature for the cold (c) and hot (h) temperature sweeps of the LSRs.
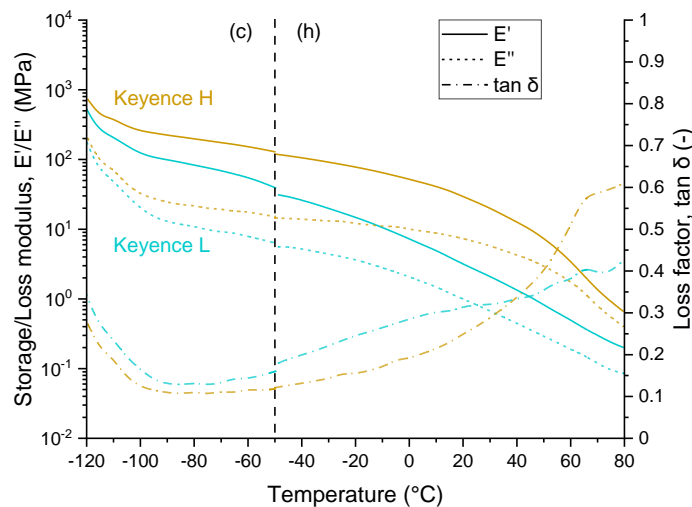
Figure 10.9: Storage modulus, loss modulus and loss factor at 1 Hz as a function of temperature for the cold (c) and hot (h) temperature sweeps of the Keyence samples.

144

Despite the inability to test at temperatures below -120°C to assess the entire glass transition range, it was possible to see the end of the storage modulus drop due to Tg down to approximately -100°C for all four samples. While for Keyence H and Keyence L all three viscoelastic functions were decreasing since the beginning of the experiments, the Wacker and Silastic loss factors exhibited local maxima at -116°C and at -121°C, respectively, which hint at the presence of the glass transition in this range.

In addition, the Wacker and Silastic curves had a strong decrease in both the storage and loss moduli starting from around -50°C. This is in accordance with the DSC results, which demonstrated melting of the crystalline phase of the LSRs at about -45°C. Wacker, in particular, showed a strong increase in $\tan \delta$ at the end of the cold temperature sweep, characteristic of the melting of crystalline domains. The intensity of this increase is a reflection of the fact that its loss modulus was nearing a plateau while the storage modulus kept decreasing abruptly.

Contrary to Wacker, both the storage and loss moduli of Silastic were still dropping at a similar rate, not giving rise to the same $\tan \delta$ response at the end of the cold sweep. The loss factor of Wacker did not evidence high values at the start of the hot sweep equally. The crystallisation temperature of the LSRs was identified as -84°C in the DSC runs. Since the initial cooling of the hot sweep was only down to -40°C, no crystallisation occurred before the DMA measurements and, hence, no corresponding increase in $\tan \delta$ was present. After the softening of the silicones at about -50°C, their storage and loss moduli remained relatively constant.

Unlike the LSRs, Keyence H and Keyence L revealed a smooth, continuous decrease in E′ throughout the temperature sweeps. There was no evidence of a plateau in the higher temperature range. In fact, up to the end temperature the storage modulus decreased more strongly in 2-3 orders of magnitude. A tendency towards a local maximum in $\tan \delta$ can also be noticed close to 80°C. The loss modulus kept decreasing with the storage modulus, indicating a melting/softening. The DSC results from Chapter 9 recorded a slight melting of these materials at around 40°C. This corresponds in particular to a second drop in E′ of Keyence H. Therefore, the caloric and the dynamic mechanical findings are in line.

The maximum and minimum values recorded for the storage and loss moduli are listed in Table 10.2, along with the magnitude and location of the local maxima of the loss factor. It can be noted that at very low temperatures the LSR samples had a storage modulus of the order of 10^3, while E′ was of order 10^2 for the Keyence materials. Their greatest drop occurred during the cold sweep (c) for the LSRs and during the hot sweep (h) for Keyence H and Keyence L. For the four samples, the storage modulus at the end of the hot temperature sweep was the minimum value measured, which was higher for the silicones. Nevertheless, the loss factors of Wacker and Silastic were below the values of the two Keyence materials, demonstrating the lower damping capabilities of the LSRs compared to the silicone-based photopolymers.

Table 10.2: Relevant figures of the viscoelastic parameters of the LSRs and the Keyence photopolymers.

Sample	E′ (MPa)		E″ (MPa)		tan δ at local maximum	
	Max.	Min.	Max.	Min.	Value (-)	Temperature (°C)
Wacker (c)	1,548.29	1.15	323.17	0.93	0.22	-116
Wacker (h)	1.31	1.11	0.20	0.05	-	-
Silastic (c)	3,531.46	3.87	472.73	0.27	0.18	-121
Silastic (h)	2.64	2.10	0.25	0.08	-	-
Keyence H (c)	741.54	128.54	203.74	15.19	0.27	-120
Keyence H (h)	120.16	0.66	14.50	0.40	0.61	80
Keyence L (c)	630.81	38.85	227.11	6.24	0.36	-120
Keyence L (h)	31.11	0.20	5.59	0.08	0.43	80

10.3 Time-Temperature Superposition

For the construction of the master curves from the T-f sweeps, the validity of the TTS was verified with Wicket plots, also known as Cole-Cole plots. In this case, the storage modulus is plotted against the loss factor (or the loss modulus) to verify if the material is thermorheologically simple (i.e. has a single relaxation time). The plot should produce a smooth curve in the form of an arc or a "croquette wicket". Additionally, in the plot of the shift factor $\log_{10} a_T$ over the temperature, a straight line should be observed through the data (Menard, 2008). If these conditions are met, the TTS principle is applicable. Consequently, the frequency sweeps for the different isotherms can be shifted horizontally according to the WLF equation by the empirically calculated shift factor (see Eq. 3.13).

In Appendix F, the Wicket plots in logarithmic scale and the shift factor plots for the TPUs and the PolyJet photopolymers can be seen. All samples exhibited the expected behaviour of the shift factors. Almost all Wicket plots yielded the required curve shape. For the TPUs, there were slight distortions mainly in the lower values of the storage modulus (corresponding to higher temperatures). Figure 10.10 illustrates the case of Duraform. The measured points on the left side of the graph diverged from a smooth curve, as the material was tested through its melting temperature of 32°C, identified in DSC tests.

For the photopolymer Tango 30, however, there was a strong distortion in the Wicket plot for negative temperatures in the range of -25°C to 0°C, as seen in Figure 10.11. This is a strong evidence that the time-temperature superposition cannot be applied. Indeed, the master curves of the softest Tango sample showed a non-physical behaviour corresponding to these temperatures.
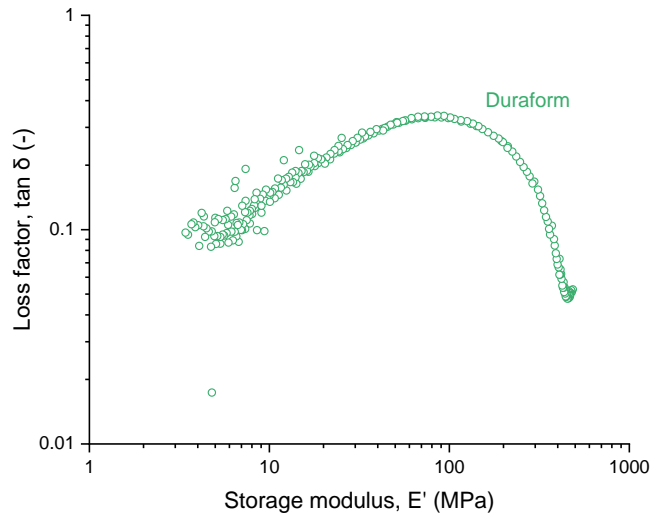
Figure 10.10: Wicket plot for Duraform with distortion on the left side.
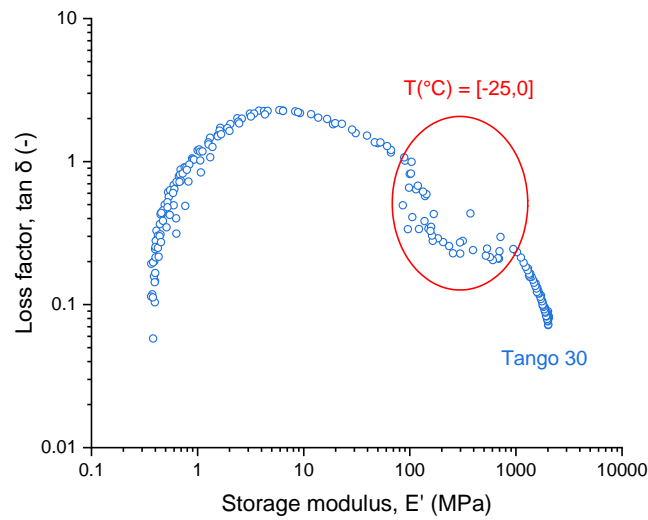
Figure 10.11: Wicket plot for Tango 30 with great distortion between -25°C and 0°C.

The time-temperature superpositions performed with 20°C as reference temperature enabled the prediction of the material behaviour over a broader frequency range from 10^{-4} to 10^{16} Hz. Figures 10.12 to 10.17 present the master curves for the TPUs, the Tango grades and Agilus, including the failed case of Tango 30. The identified shifting parameters C_1 and C_2 of the WLF equation are listed in Appendix F.
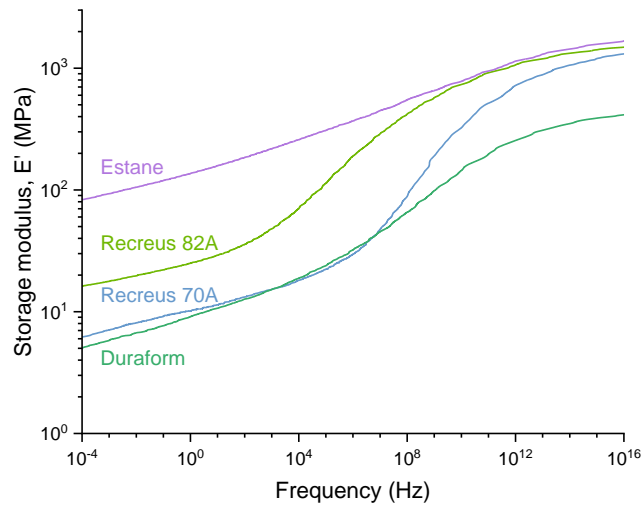
Figure 10.12: Master curves of the storage modulus for the TPUs.
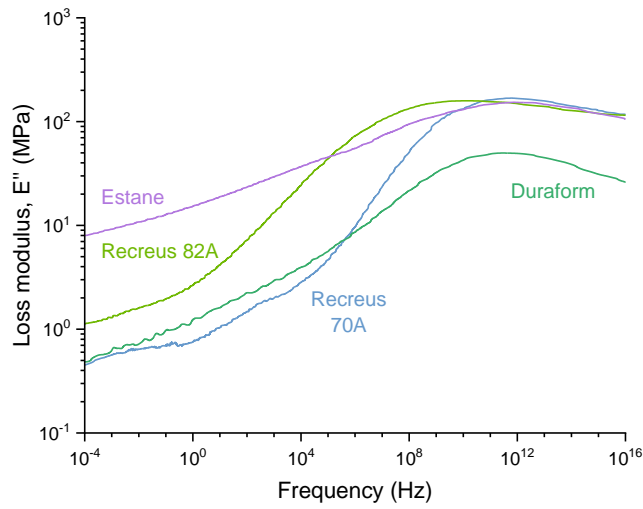
Figure 10.13: Master curves of the loss modulus for the TPUs.
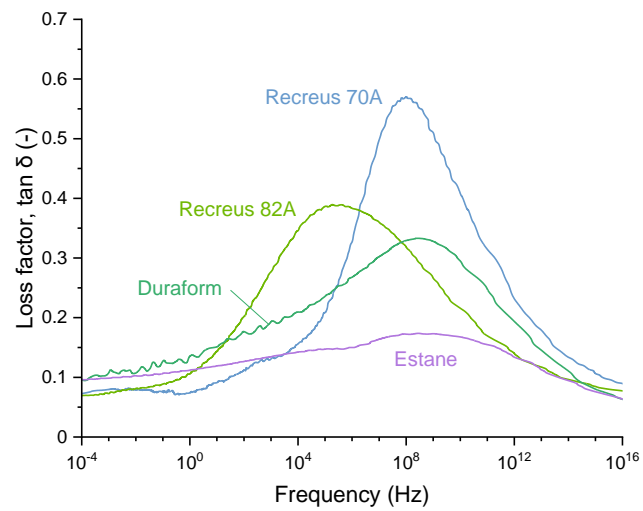
Figure 10.14: Master curves of the loss factor for the TPUs.
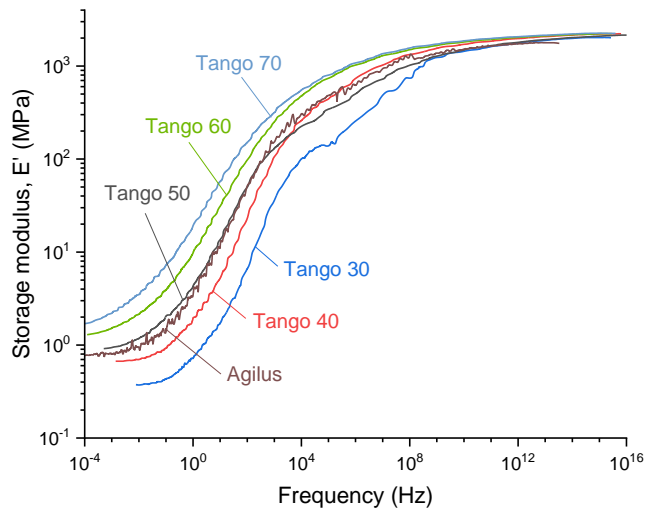
Figure 10.15: Master curves of the storage modulus for the PolyJet photopolymers.
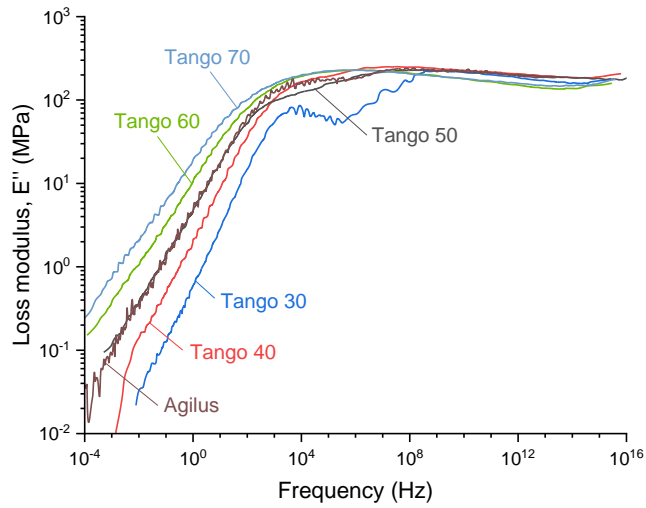
Figure 10.16: Master curves of the loss modulus for the PolyJet photopolymers.
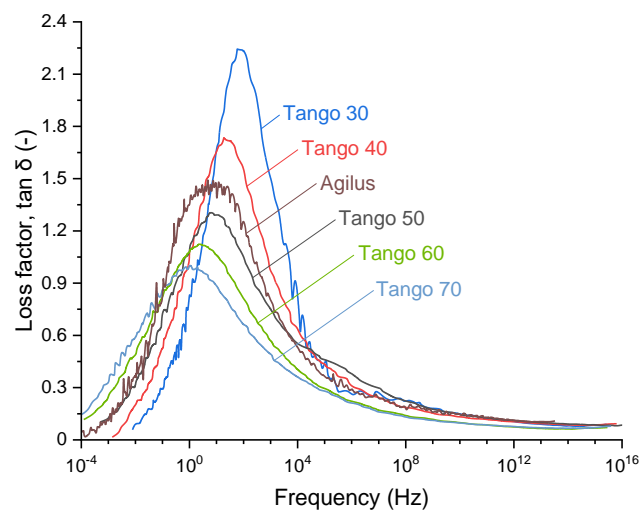
Figure 10.17: Master curves of the loss factor for the PolyJet photopolymers.

149

An adequate TTS has a proper data overlap. This was achieved for the TPUs and most of the Tango materials. Small oscillations were especially observed in the loss modulus and loss factor of Duraform in the lower frequency range. This corresponded to the shifting of the higher temperature range tested, where the Wicket curve was not as smooth. The same can be said, to a lesser extent, about Recreus 70A. As mentioned, the failure of the superposition of Tango 30 was confirmed by the large oscillation of its loss modulus in the frequency range 10^4 Hz to 10^9 Hz. Unexpectedly, Agilus presented an intense fluctuation in the master curves of E', E'' and $\tan\delta$, raising questions about the applicability of the superposition. This suggests either some care in interpreting its results or even an unsuitability of its TTS.

The predicted values for the storage and loss moduli, as well as the loss factor at the frequency limits of 10^{16} and 10^{-4} Hz, are listed in Table 10.3. It can be observed that in the stiffer state, i.e. at maximum frequency, all Tango materials showed similar E' values. The relative deviations were about 10% from each other. Likewise, Recreus 70A and Recreus 82A displayed analogous storage moduli at 10^{16} Hz, while they diverged considerably towards 10^{-4} Hz. This is due to the softer nature of Recreus 70A in the rubbery state, which manifests itself at low frequencies. According to Grady et al. (2013) and Drobny (2014), softer TPUs, which contain more soft segments in their structure, show higher loss factor peaks and greater storage modulus drops at room temperature. This was indeed verified for Recreus 70A and Recreus 82A. Compared to the TPUs, the PolyJet photopolymers were stiffer at high frequencies but also softer at low frequencies. In addition, at both frequency extremes the loss factors were small.

Table 10.3: Master curve viscoelastic parameters at $f_{max} = 10^{16}$ Hz and $f_{min} = 10^{-4}$ Hz for the TPUs and the PolyJet photopolymers.

Sample	E' at: (MPa)		E'' at: (MPa)		$\tan\delta$ at: (-)	
	f_{max}	f_{min}	f_{max}	f_{min}	f_{max}	f_{min}
Recreus 70A	1,308.16	6.28	118.75	0.46	0.09	0.07
Recreus 82A	1,492.04	16.27	114.79	1.13	0.08	0.07
Duraform	415.35	5.01	26.03	0.49	0.06	0.10
Estane	1,674.64	83.77	105.23	8.05	0.06	0.10
Tango 30*	2,016.96	0.38	181.09	0.02	0.09	0.06
Tango 40	2,225.32	0.67	206.65	0.01	0.09	0.02
Tango 50	2,151.24	0.91	185.25	0.09	0.09	0.10
Tango 60	2,231.65	1.29	159.21	0.15	0.07	0.12
Tango 70	2,244.68	1.74	176.07	0.29	0.08	0.17
Agilus	1,753.39	0.78	190.64	0.03	0.11	0.04

*failed TTS

The peak values of the loss factor and their corresponding frequencies are in Table 10.4. The maximum damping capacity was registered for the PolyJet materials. These peaks appeared at low frequencies, from 1 Hz to 20 Hz (for the successful time-temperature superpositions). The softer the Tango photopolymer, the higher the $\tan\delta$ peak frequency was. In fact, the loss factor peak of Tango 40 was more than 3 times greater than that of Recreus 70A (which was the highest among the TPUs). The loss factors of Recreus 82A,

Recreus 70A, Duraform and Estane only exceeded those of the photopolymers from 10^4 Hz, 10^6 Hz, 10^7 Hz and 10^9 Hz onwards, respectively. Taking into account a frequency of ~ 0.08 Hz, which was used in the cyclic testing with strains up to 10%, Recreus 70A showed the lowest damping capacity. The damping increased with the remaining TPUs, followed by the Tango photopolymers. The Tango material with the most damping was the stiffest, i.e. Tango 70. The results were in accordance with the cyclic tests.

Table 10.4: Loss factor peak data from the master curves for the TPUs and the PolyJet photopolymers.

Sample	Peak value (-)	Frequency at peak (Hz)	Sample	Peak value (-)	Frequency at peak (Hz)
Recreus 70A	5.72E-01	1.05E+08	Tango 40	1.74E+00	1.89E+01
Recreus 82A	3.90E-01	1.85E+05	Tango 50	1.31E+00	5.26E+00
Duraform	3.33E-01	2.47E+08	Tango 60	1.13E+00	2.21E+00
Estane	1.74E-01	3.34E+08	Tango 70	1.01E+00	1.00E+00
Tango 30*	2.25E+00	5.85E+01	Agilus	1.54E+00	4.86E+00

*failed TTS

10.4 Final Remarks

The investigations discussed in this chapter demonstrated the high loss factors of the PolyJet photopolymers. When used in the peak frequencies, the softer Tango grades were able to absorb more energy from the system. Furthermore, from the master curves at 20°C, it was observed that the greatest energy absorption of the Tango materials and Agilus occurred at common frequencies of 10^{-1}-10^4 Hz.

In the T-f sweeps, Recreus 70A presented a decrease in E′ greater than Recreus 82A and a higher maximum $\tan\delta$ as a consequence of its softer nature. Nevertheless, among all samples, the greatest decrease in stiffness was registered for the PolyJet photopolymers. Of all temperature sweeps at 1 Hz shown in Sections 10.1 and 10.2, the lowest change in stiffness was observed for the LSRs and the Keyence photopolymers. They were followed by the TPUs and subsequently, by Agilus and the Tango grades.

The service temperatures for the studied materials were varied. Considering the evolution of the viscoelastic functions at 1 Hz over the temperature, it was found that TPUs could be used at lower temperatures compared to the PolyJet photopolymers. The LSRs were the samples with the lowest thermal operating limit, with a quite constant storage modulus above the softening temperature at around -40°C. Due to the broad range of the glass transition and the several variables to be considered in determining it, no precise statement on the minimum service temperature can be made. A further study on the material of interest, with the operating conditions should be performed for definite results.

11. Further Discussion and Overall Analysis

This chapter aims to gather the knowledge generated with the thermomechanical and caloric experiments performed and enhance it beyond the measurement and analysis of the material properties. Initially, independent investigations are described, which assisted in the understanding of the 3D printing process with elastic materials, as well as in the evaluation of material properties. Subsequently, complementary remarks are presented, including correspondence with the available literature. Thereafter, the thermomechanical and caloric behaviour of the samples assessed in Chapters 6 to 10 are collectively analysed. From this analysis, the suitability of the 3D printed elastomers in technical applications is discussed and recommendations are provided.

11.1 Additional Studies

Besides the experimental investigations explored in this work, other aspects on 3D printed elastomers were analysed and published in the literature. In Loos et al. (2021), the materials Recreus 70A, Silastic Tango 50 and Tango 70 were chemically characterised via IR spectroscopy. The TPU filament was identified as a polyether polyurethane, whereas silicone-specific bands, e.g. the Si-O-Si backbone, were verified for Silastic. Tango 50 and Tango 70 showed urethane and acrylate contents. In absorption tests with toluene, Silastic and Recreus 70A swelled considerably up to 135% of their original size. The swelling of the Tango materials was so pronounced that they broke after a few hours of testing. Furthermore, water uptake tests revealed the hygroscopic nature of the TPU and the photopolymers, while Silastic had very little water absorption. The tensile strength of the hydrophilic materials was affected, where Tango 70 was the most impaired, with a 50% reduction in the ultimate stress.

The influence of moisture was also a topic studied in Bruère et al. (2022a). Extrusion failure issues on printing elastic filaments with FFF machines were addressed in this paper. The material extrusion was particularly affected by the type of extruder as well as by moisture inside the filament prior to printing. A discussion on the feeding system along with microscopic and mechanical analyses regarding moisture were conducted. The (remote) Bowden extruder imposed a long length of filament being compressed, which increased the tendency to buckling and compromised the reproducibility. The direct drive extruder was found to be best suited for printing with elastic materials. In addition, the tensile behaviour of parts printed with moist filament was negatively influenced, particularly in the higher strain range.

An example of the advantageous use of AM in the prototyping field was investigated in Goularte et al. (2023). The mechanical behaviour of 3D printed elastomers was characterised and implemented in a commercial finite element analysis software for the design optimisation of aircraft door seals. Tensile tests on Silastic, Wacker, Keyence H and Keyence L were performed for the application of a hyperelastic material model. The model parameters were identified by means of a numerical optimisation algorithm to enable the design optimisation step, which was carried out with genetic algorithms. Whereas the numerical analysis reduces the time for determining the optimal geometric parameters, AM allows the faster on-site fabrication of components in the development stage, which usually takes 6-12 months in conventional manufacturing.

The AM technologies were synthesised in Bruère et al. (2022b) as well as their applicability and material options for elastomeric parts. Typical attributes of printing in the FFF technology with elastic materials were also discussed. Furthermore, investigations on the infill raster angle and the printing temperature of Recreus 82A samples printed with contour lines were conducted. Key findings demonstrated the influence of infill orientation on the stress-strain response limited to the higher strain range, while an alternating infill angle helped prevent a premature failure even at weaker line adhesion due to insufficient printing temperature. The influence of infill orientation on the mechanical behaviour was also a topic in Bruère et al. (2023). The documented results showed the role of alternating and fully unidirectional infill angles on the tensile strength, in addition to the impact of contour lines on the geometry. Different alternating angles provided equivalent stress-strain results, and favourably affected the integrity of the print. Without perimeters, the lines of the samples filled unidirectionally at an angle of 90° to the tensile direction detached more easily during loading, leading to considerably lower stresses than the 0° and 45° infill angles. With the addition of contour lines, the tensile strength of the sample filled at 90° was comparable to that of the 0° infill. A stress relaxation analysis was performed as well, revealing a similar viscoelastic behaviour of samples with raster angles at 0° and 90°.

The mentioned publications are listed in Appendix G. The title and authorship of the works are outlined. Each publication is f by its abstract and its Digital Object Identifier.

11.2 Thermomechanical Behaviour and Material Suitability

The use of the word *flexible* as a synonym for *elastic* in the advertising of commercial materials, especially filaments for the FFF technology, is common. The term *flexible* generally covers materials that are easily bent but do not necessarily have a good recovery to their initial shape after stretching. They are therefore often categorised together with polyamides, for instance. Caution should be exercised when looking for options in material catalogues in which high elasticity is desired.

Furthermore, several types of TPEs do not exhibit a fully rubber-like behaviour. This was the case for the samples printed with the Arnitel TPC filament. Their uniaxial tensile results revealed a distinct yield point at about 100% strain. The 90° Arnitel sample showed a permanent set since it broke shortly after the yield point. The samples with 45° and 0° infill orientations failed well past that point, which was reflected in their residual deformation.

Although they achieved elongations as high as the Recreus filaments, their permanent sets were considerably larger. Hence, not all TPEs can be an alternative to conventional rubber in their full deformation range. Nonetheless, if stresses below their elastic limit are considered, they may be useful. Further studies in this regard are suggested in order to define the applicability limits of 3D printed TPEs like Arnitel as rubber substitutes.

Polymer chemistry plays an important role, affecting both the material properties and the surface of the final part. The material provided by Wacker, for instance, is a UV-cured silicone. It had the smoothness typical of silicones; however, it did not show the tackiness or the typical smell of the photopolymers. Hence, polymer chemistry would be an interesting topic in future works. Unfortunately, the ACEO® printing service offered by Wacker was discontinued at the end of 2021. Nevertheless, the findings of the Wacker samples are significant, as it shows that a silicone from another formulation (UV-initiated curing instead of thermal curing) and another process (DOD) provided results comparable to conventional LSR used in LAM.

A remark should be made regarding 3D printed parts. Especially in material extrusion processes, a large number of parameters is provided to the printing instructions, i.e. the G-Code. This leads to a broad variation in the final part quality regarding not only geometry accuracy but also mechanical behaviour. All specimens of this work were printed with a 100% infill, as specified in Chapter 5. If lower infill percentages are considered, for instance, it is possible to obtain more flexible or compressible specimens. In Figure 11.1, two cylinders printed with Silastic were submitted to the same compressive load of 50 N. The cylinder on the left had a 25% infill percentage, whereas the one on the right was 50% filled. The lower the infill percentage, the more deformable the cylinder was. This visually exemplifies the combination of both the nature of the material and the printing parameters in controlling the final performance of the part. Hence, even if (at the moment) FFF is not capable of processing filaments softer than 60-70 Shore A hardness and LAM mainly uses a silicone of hardness 50 Shore A, it is possible to manufacture a part with more flexible characteristics by optimising the printing parameters. It should also be noted that a lower infill percentage reduces printing time and manufacturing costs in material extrusion technologies but in contrast compromises the strength of the component (Bakir et al., 2021).
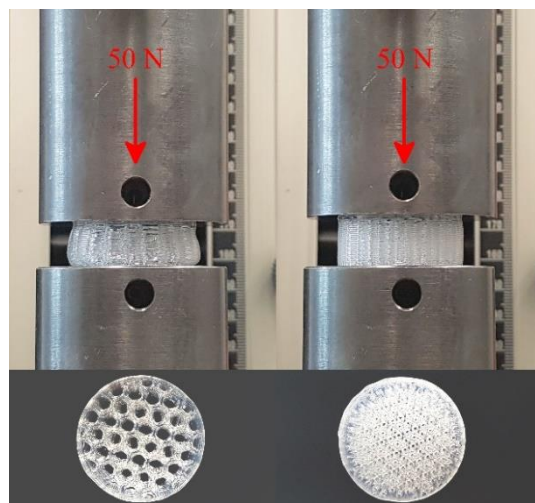
Figure 11.1: Compressive load of 50 N on cylinders printed with Silastic with 25% (left) and 50% (right) infill percentages.

Two publications dealing with similar materials to those studied in this research were found in the literature. Among the investigations by Leon-Calero et al. (2021), the Tg was determined for Recreus 70A and Recreus 82A through DSC experiments. Although the testing conditions were different, the glass transition temperatures were in a similar range as those determined in Chapter 9. Furthermore, thermogravimetric analyses reported in their work revealed temperatures relative to a 5% weight loss of circa 290°C for both filaments, as discussed in Chapter 9. Their aim was to determine the maximum temperature used during manufacturing while preserving the integrity of the material. According to the authors' results, Recreus 70A and Recreus 82A were stable up to 250°C, with degradation occurring at higher temperatures. However, it should be emphasised that this temperature threshold is indeed restricted to the manufacturing process. Regarding the service temperature, Recreus 70A and Recreus 82A should be employed below their softening temperature, specified by the manufacturers at 90°C (Recreus, 2022a) and 105°C (Recreus, 2022b), respectively. The onset of the softening of Recreus 70A, for instance, could be slightly observed at the highest testing temperatures of the DMA experiments shown in Figure 10.2, where the storage modulus started to decrease somewhat more intensely.

The work of Abayazid and Ghajari (2020) also analysed mechanical properties of PolyJet materials. The tensile strength and elongation at break found for Tango 30 and Agilus in Chapter 6 had values analogous to those reported by the authors. The materials were not the same in either hardness or chemistry, as they investigated pristine Agilus30 and TangoPlus. However, these materials are of the same family as the Agilus and Tango samples studied here. Dynamic mechanical analyses in the authors' publication with dual-cantilever clamps identified high glass transition temperatures as well as high energy absorption. This was consistent with the results from Chapter 10 in the uniaxial tensile mode. Their relaxation tests, although in compression at 20% strain, showed great stress decays from the maximal stress. The results reported in Section 8.2 for a tensile stress relaxation at 15% strain were comparable to some degree. The stress drops in the work of Abayazid and Ghajari were in the range of 50%-70%, while they were found to be around 30% for Tango 30 and 37% for Agilus. This suggests that the stress relaxation behaviour under compression of these families of PolyJet photopolymers are more pronounced, which requires studies in the future to validate this hypothesis.

All in all, the experimental investigations in this thesis showed the varied material behaviour among the studied photopolymers, TPUs and LSRs. Gathering the findings, Figures 11.2 and 11.3 were obtained with a comparative analysis of the evaluated material properties. With the quantities expressed in the respective thermomechanical and caloric test chapters, the figures provide a visual resource of material performance.

Although omitted in this chapter, it was verified in Chapter 6 that Arnitel (infill orientations at 45° and 0°) showed a large plasticity after the tensile tests. Therefore, this type of TPE is not primarily recommended as a 3D printed substitute for conventional rubber undergoing high elongations. The compressive strength, however, was not evaluated for the samples. The material Arnitel could be advantageous in this regard, being a topic for future studies. Due to the similarities with Tango 30, the transparent sample Tango 30 (t) was also not included in the following analysis.
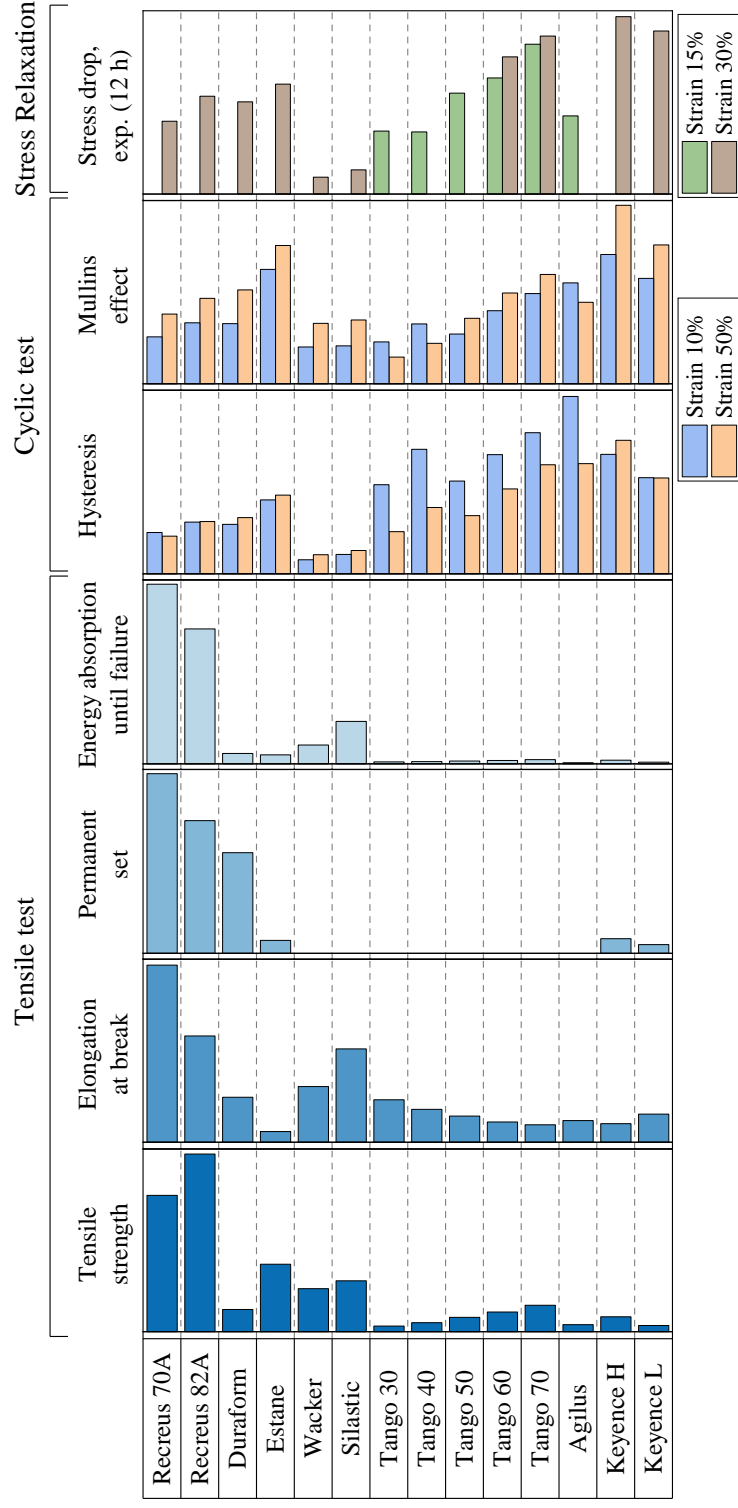
Figure 11.2: Summary of the properties assessed from the uniaxial tests.
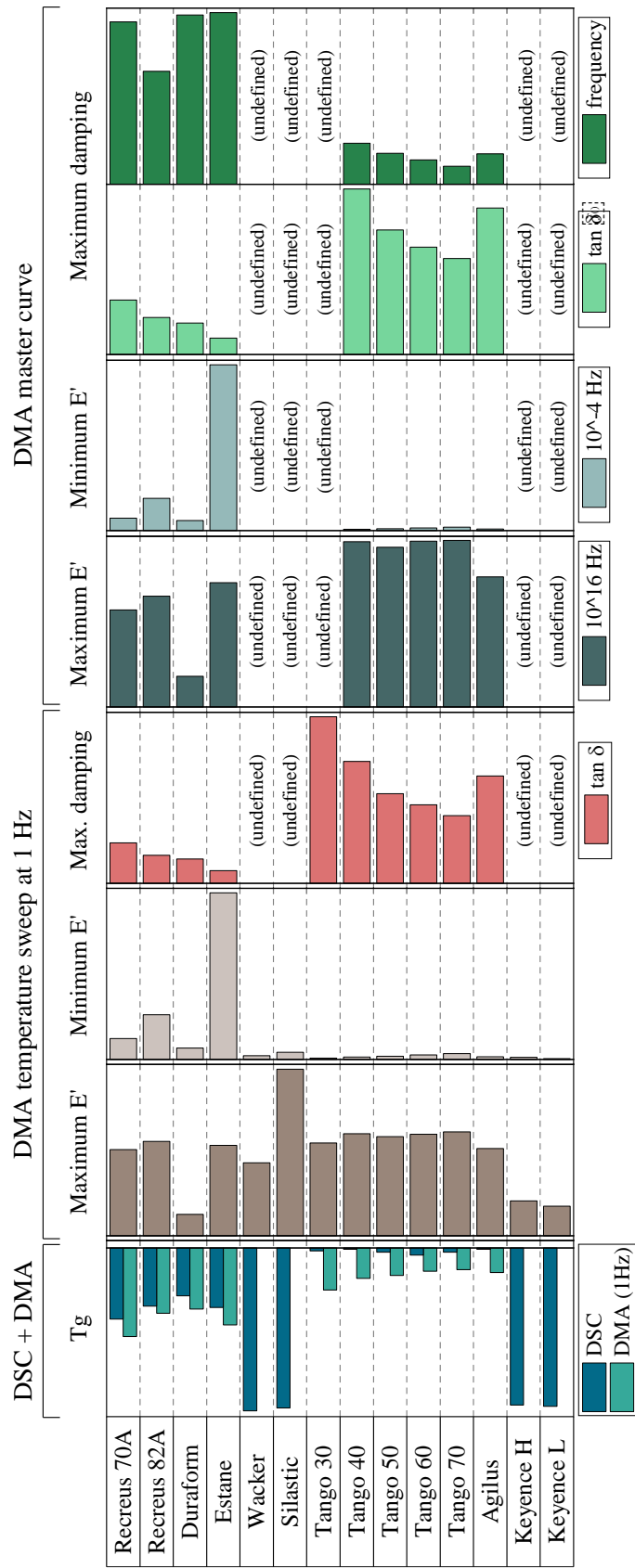
Figure 11.3: Summary of the properties assessed from the caloric and dynamic tests (frequency at maximum damping in logarithmic scale).

The inferior tensile strength of the photopolymers (Tango, Agilus and Keyence) was the most noticeable in Figure 11.2. Consequently, their total extensibility ranges from 143% for Tango 70 to 347% for Tango 30 (refer to Table 6.4). Excluding the premature failure of Estane due to the punching of the specimens, the performance of all studied photopolymers were below that of the other elastomeric materials, both in terms of tensile strength and elongation at break. Hence, these photopolymers are not appropriate for demanding tensile loading applications. Alternatives are the LSRs and TPUs for moderate and high stresses, respectively. In addition, the absence of residual deformations after unloading the PolyJet samples or the small permanent set in the Keyence samples was achieved after some time, unlike the Wacker and Silastic silicones. If a fast recovery, especially after high elongations, is of interest in the design of a component, the LSRs are the best alternatives.

On account of a large residual deformation after tensile testing, the TPU samples generally showed the highest tensile strength. However, after the uniaxial cyclic tests up to 50% strain, no plasticity was identified, except for a 2% permanent set of Estane. Furthermore, all four TPUs, submitted to a stress relaxation at 30% strain, recovered to their initial size. Likewise, the Keyence photopolymers had a residual deformation of only 1-2% after the cyclic and stress relaxation tests. Considering that rubbers are usually stretched up to 10% to 50% in technical applications, all materials investigated could be used. Nonetheless, the stress levels should also be kept in mind if there is a minimum tensile stress as a requirement in a specific application. According to Smith (1993), rubber parts such as belts, hoses, O-rings and mountings are hardly (if ever) submitted to tensile stresses above 1 MPa. If greater stresses are concerned, then Tango 30 and Keyence L would be unsuitable, while Tango 40 and Agilus would be in a critic situation as their tensile failure stresses were close to 1 MPa.

In addition, the rubber material is, as a rule, standardized in order to provide a guidance and specification to buyers and suppliers. For instance, the Standard ASTM D 2000-18 (ASTM, 2018) is a widely used industry specification for the properties of vulcanised rubber materials for automotive applications. The formulation of rubber compounds should meet the requirements of the standard depending on the desired application. The material specification, named line call-out, contains basic requirements of hardness and minimum tensile strength (and elongation), besides designations for heat resistance (*type*) and oil resistance (*class*). Table 11.1 presents basic requirements for some rubber materials and their corresponding polymer most frequently used. Table 11.2 recalls the results from Chapter 6.

Table 11.1: Basic requirements for the classification of elastomers from ASTM D 2000-18.

Material type and class	Corresponding polymers[1]	Hardness, ± 5 pt. (Shore A)	Min. tensile strength[2] (MPa)	Min. elongation at break[2] (%)
AA	NR, SBR, butyl rubber	30	7-14	400
		50	3-21	250-500
		70	3-21	150-350
		90	3-10	75-125
BA	EPDM, butyl	30	7-14	400
		50	7-17	300-400
		70	3-17	150-300
		90	3-10	75-125
BC	Neoprene	30	3-14	300-500
		50	3-24	300-500
		70	3-21	200-300
		90	3-14	50-150
BG	NBR, PU	50	3-21	300-400
		70	3-28	150-400
		90	3-10	50-100
FC	SiR	50	7-8	400-500
GE	SiR	50	3-8	200-400

[1]taken from Hutchinson (2023); [2]for several heat and oil resistance requirements, among others.

Table 11.2: Ultimate tensile stress-strain information of the studied samples, in ascending order of approximate hardness.

Sample	Tensile strength (MPa)	Elongation at break (%)	Hardness (Shore A)
Tango 30	0.784 ± 0.011	347	30
Keyence L	0.879 ± 0.014	231	35
Tango 40	1.276 ± 0.017	270	40
Tango 50	2.042 ± 0.056	215	50
Agilus	1.017 ± 0.026	177	50
Wacker	6.124 ± 0.095	457	50
Silastic	7.235 ± 0.058	766	50
Tango 60	2.794 ± 0.182	165	60
Duraform	3.147 ± 0.244	369	60
Keyence H	2.104 ± 0.082	152	65
Tango 70	3.740 ± 0.248	143	70
Recreus 70A	19.391 ± 0.351	1,451	70
Recreus 82A	25.290 ± 0.128	872	82
Estane	9.599 ± 0.337	88	95

Considering this standard, Tango 30 did not meet the minimum tensile strength requirements for any of the conventional materials in Table 11.1 with a hardness of 30 Shore A, nor did Keyence L (which has a hardness of 35 Shore A). As seen in Chapter 6, both photopolymers withstood stresses below 0.9 MPa. The same can be said for Keyence H, Tango 40, Tango 50, Tango 60 and Agilus, in the 30-70 Shore A hardness range. Their tensile strengths were below the minimum 3 MPa to 7 MPa required for all materials shown

here from the ASTM D 2000-18 standard. Additionally, Tango 70 is an unsuitable alternative since its elongation at break was insufficient in all cases of a 70 Shore A hardness. Regarding silicone rubbers, Wacker could be an alternative to the GE type/class material, while Silastic could substitute both GE and FC materials, depending on the remaining requirements.

With ultimate stress of 3.74 MPa and strain of circa 350%, Duraform has chances of replacing materials such as AA, BC and BG. Nevertheless, its porous nature may be a determining factor for its inadequacy for sealing purposes in contact with liquids. Finally, Recreus 70A, Recreus 82A and Estane met the minimum stress and strain requirements of materials of respective hardness, at least at the lower range limits. The same statement about porosity can be made for Estane, although the fusion quality of its powder particles seemed to be superior to that of Duraform. Furthermore, it should be noted that the claims above were made on the basis of mechanical performance only. Resistance to heat and oil still needs to be verified in further studies on the narrowed material alternatives for full compliance with the requirements of the ASTM standard presented.

Returning to Figure 11.2, the high resilience of the silicone samples can be seen by both the highest energy absorption until failure among the materials without permanent set after tensile testing and the lowest hysteresis in cyclic testing. Despite the typical resilience requirements for elastomers, a high hysteresis in dynamic loadings can on the other hand be advantageous. Materials with low resilience are desired in vibration absorption applications to limit the maximum developed amplitude of the operating part (Smith, 1993). For materials with the same hardness, it was seen in Chapter 7 that the hysteresis of Tango 70 was about 3 times higher than that of Recreus 70A, while Tango 50 and Agilus dissipated much more energy than Wacker and Silastic. Keyence H and Keyence L provided similar results to the PolyJet materials. Therefore, the photopolymers are preferable for the conversion of the kinetic energy of a mechanical system into thermal energy. In summary, if a resilient material is required, the 3D printed silicones are the most suitable alternative. For moderate energy dissipation, the choice goes to the TPUs. Additionally, in the case of large damping requirements, the photopolymers are suggested. Regarding Mullins effect, the Keyence samples as well as Estane stood out in the stress softening, which increased with the strain level. As this pronounced behaviour is expected from these materials, caution should be exercised when dealing with them in constitutive modelling, taking this effect into account as damage in the computations.

The damping response detected in the dynamic mechanical measurements of the PolyJet photopolymers in Figure 11.3 was in line with the hysteresis results of the cyclic tests (performed at a frequency close to 0.1 Hz) in Figure 11.2. The highest loss factors of these samples in the lower frequency range were observed in both the temperature sweeps at 1 Hz and the master curves. The optimal operating range of viscoelastic damping devices is in the vicinity of the maximum $\tan \delta$ (Menczel and Prime, 2009). Hence, the PolyJet photopolymers are the most recommended choice for shock absorption and noise control at frequencies of 10^{-1}-10^{4} Hz, as verified in the master curves at 20°C obtained in Chapter 10. Abayazid and Ghajari (2020) reported on the potential suitability of the PolyJet materials for applications where complex designs and viscoelastic properties for energy absorption are required, e.g. in helmets.

The maximum damping capacities of the TPUs occurred in the range of 10^5 Hz to 10^8 Hz. However, even in this case, they were lower than those of the photopolymers at low frequencies. Therefore, their performances were not equivalent in their $\tan\delta$ peak frequency ranges. At higher frequencies, though, the use of TPUs for damping requirements in technical systems is more suitable, as their vibration absorption was still higher than those of the PolyJet materials. Furthermore, the largest variation of the storage modulus with temperature in the master curves was found for the Tango and Agilus materials. If a 3D printed rubber-like part is used over a large frequency range, this fact should be regarded. If excessive heat build-up (not verified in this work) is produced in the dynamic loading, the use the more resilient TPU materials is recommended (Smith, 1993).

The stress relaxation behaviour of the materials under tensile loading in Figure 11.2 displayed the considerably smaller decay in peak stresses for the silicones. The photopolymers relaxed the most, particularly Keyence H and Keyence L. Consequently, the LSRs are a more appropriate choice for sealing applications. If during operation there is no need to maintain the tension on the component over time as much as possible, TPUs are an intermediate alternative, although their stress relaxations were closer to those of photopolymers than silicones.

The DSC results in Figure 11.3 revealed the substantially lower glass transition temperatures at circa -110°C of the Wacker and Silastic silicones as well as of Keyence H and Keyence L due to their silicone content. Therefore, components of two different types of 3D printed elastomers (in nature and in processing) can be operated over a wider negative temperature range. Although the mechanical behaviour at room temperature, especially the resilience observed in the cyclic tests, was very distinct for the LSRs and the Keyence photopolymers, mechanical investigations at lower temperatures are suggested for a further analysis of their mechanical properties.

In terms of thermal applications involving temperatures as low as -70°C, both the LSRs and the Keyence materials are recommended. However, it is important to consider the softening of Wacker and Silastic at around -45°C on heating from lower temperatures due to the melting of their crystalline phase (see Figure 9.6), limiting their temperature applicability. In the case of a temperature decrease during operation, parts printed with Silastic and Wacker can be cooled down to circa -65°C and -70°C, respectively. This is due to the crystallisation only taking place below these temperatures. The TPUs are an intermediate choice. They still presented a sufficiently low glass transition for cold weather applications, although they are not the best selection for extreme sub-zero temperatures. From both the DSC and DMA experiments performed, the TPU materials can be used down to -30°C. As for the studied photopolymers, their higher Tg, close to 0°C, makes them not appropriate for applications in cold environments.

Compared to conventional elastomers shown in Table 11.3, the LSRs would be suitable alternatives to all five natural and synthetic rubbers with respect to low service temperatures. Combined with the requirements of ASTM D 2000-18 of the automotive industry, Recreus 70A, Recreus 82A and Estane could be candidates to replace Natural Rubber, Neoprene, and EPDM (commonly used in type/class AA, BA and BC materials) in both tensile requirements and minimum operating temperature.

Table 11.3: Comparative properties of Du Pont elastomers (adapted from Smith, 1993).

Property	Natural rubber	Neoprene	VITON (fluoro-elastomer)	ELVAX (EVA)	NORDEL (EPDM)
Service Temperature (°C)	-50 to 70	-40 to 100	-20 to 200	-30 to 70	-50 to 145
Hardness range (Shore A)	30-90	40-95	55-95	40-95	40-90

The experiments performed in this thesis were focused on the tensile mode. However, the material properties under compression, which is a common service load for elastomers, were not studied. Their compressive performance may not be as limited as their tensile capabilities, with chances of being comparable to the other material options. Thus, investigating the material behaviour under compression is a relevant topic to be explored. Other aspects observed were related to some of the five human senses. The LSRs had a smooth tactile surface and the real feel of rubber, which was not noticed in the case of the other materials. Furthermore, the photopolymers had a strong, characteristic odour, which may be unpleasant for some people. In addition, the photopolymers from the PolyJet process had a gluey surface after printing. If human interactions with the 3D printed elastomers take place, these aspects may be unfavourable to their application. Silicones, for example, would be more suitable due to their biocompatibility.

Furthermore, the hygroscopicity of the materials Recreus 70A, Tango 50 and Tango 70 verified in independent publications does not make them suitable for applications in damp or wet environments. Instead, Silastic would be more appropriate. Moreover, the pronounced swelling of the TPU and the LSR by toluene absorption and their consequent low strength dismiss them for the manufacturing of functional parts in contact with this solvent during service. The situation is even more critical for the two Tango materials, since they broke before saturation. Additional investigations with different solvents are advisable for a thorough assessment of the behaviour and feasibility of 3D printed elastomers regarding oil resistance.

Finally, it is worth emphasising that the application requirements, including the desired geometry, will dictate the selection of the most suitable 3D printing elastomeric material. With the help of results such as those obtained and discussed in this work, this selection can be facilitated. Additionally, continuum mechanical modelling and numerical analyses, which are outside the scope of this thesis, can be conducted in the future with the results collected. This may allow the improvement of component design, as investigated and documented in the publication of Goularte et al. (2023).

12. Conclusions

The rapid manufacturing of elastomeric components by means of AM depends on technology improvement and associated material knowledge for obtaining parts with a satisfactory and reliable performance. Research in this field has focused on the development of new materials and printers, often for academic purposes only. Considering the deficiencies in studies of commercially available elastic materials processed by 3D printing and their mechanical behaviour, this work contributes with a database of the caloric and thermomechanical properties of the main types of accessible materials printed in several AM technologies.

In order to analyse the suitability of AM elastomers as alternatives for the fabrication of functional components, a review on additive manufacturing was initially conducted. The main technologies currently used with polymers were included, as well as a subsequent survey on 3D printing elastomers in the current market. Due to the operating mode, three of the basic groups appropriate for 3D printers were characterised. Unique attributes of conventional rubbers such as elasticity, resilience and vibration damping behaviour were investigated for thermoplastic polyurethanes, silicones and elastic photopolymers printed with the FFF, SLS, MJF, DOD, LAM, PolyJet and MJM technologies.

In a second stage, caloric, quasi-static and dynamic mechanical tests were performed to characterise the behaviour of the selected materials. The practice of printing in FFF and LAM machines allowed to better understand the nature of silicone and TPUs processed in these technologies, in addition to the effect of printing parameters on the final print. FFF has shown drawbacks with respect to extrusion failure issues arising from the process itself and the moisture absorption particularly associated with TPUs. The tendency to buckling as a result of the low elastic modulus of elastic filaments hinders the extrusion mechanism, frequently leading to under-extruded parts. The hygroscopic nature of this thermoplastic not only produces bubbles in the flow when printed moist but also eventually clogs the hotend. Furthermore, the deposition path impacts the strength of the part. However, the practicality of the less expensive and user-friendly filament printer has been its great advantage. One of the main challenges observed in LAM was the presence of voids in the prints, which were substantially reduced (and even eliminated to the naked eye) by modifying certain printing parameters. Other particularities of the LAM printer were also addressed, such as operational conditions. Its best benefit lies in printing with conventional, thermally cured silicone.

The thermomechanical experiments revealed the extensive range of properties of the three material types. The higher tensile strength and elongation at break achieved by TPUs were followed by significant residual deformation. Nevertheless, for strains up to 50% (often

used in technical applications), no permanent set was generally observed. They exhibited a moderate-to-high stress relaxation under tension, a somewhat hysteretic behaviour under cyclic loading, and greater damping capabilities at high frequencies above the order of 10^5 Hz. In addition, TPUs have shown the possibility of being operated at low temperatures. On the other hand, due to their thermoplastic nature, they cannot withstand temperatures above 90°C, depending on the softening point of the TPU in question. 3D printed TPUs have demonstrated great potential for use in the automotive field, for instance, since they have met some industry requirements.

Silicones were the distinction when it came to elasticity. They featured a highly resilient behaviour together with an instant recovery without permanent set. Consequently, they were not the best suited for vibration damping applications. They have proven to be appropriate for sealing applications, in view of their considerably low stress relaxation in comparison to the other studied materials. The lower glass transition temperatures of the LSRs enable thermal stability over a broad temperature range, although their behaviour at higher temperatures has not been assessed. An interesting fact was the similar results provided by both thermal and UV-cured silicones, which were also processed in different AM technologies.

The primary characteristic of all investigated photopolymers was their low mechanical performance in terms of tensile strength and elongation at break. These factors have been decisive for their inadequacy in the automotive industry according to a set of requirements considered. The high stress relaxation was also an attribute of the materials processed in PolyJet and MJM printers. The highlight was evidenced by their high damping capabilities, especially at low frequencies in the order of 10^0 Hz. With regard to minimum service temperatures, material chemistry played an important role. PolyJet photopolymers have shown glass transitions close to 0°C, whereas they have been much lower for MJM photopolymers due to their silicone content. Thus, MJM materials have combined the low operating temperature of LSRs with the hysteretic behaviour of PolyJet photopolymers under cyclic loading.

In summary, some of the current 3D printed elastomers available in the market are promising materials for the fabrication of functional parts, featuring varied advantages. 3D printing companies, however, still have a challenging task with regard to improving the tensile mechanical properties of elastic photopolymers through chemistry formulation in order to meet regular industry requirements. For a thorough evaluation of the performance and feasibility of using AM elastomers, several subjects need to be additionally investigated. Examples include analysing the material behaviour of 3D printed silicones and photopolymers at higher temperatures (as, unlike TPUs, they have a cross-linked network), as well as their resistance to abrasion and chemicals. Topics such as these are presented below as an outlook for further research.

13. Outlook for Future Works

Considering the material behaviour displayed and analysed in this work, some questions have emerged, which are worthy of attention in prospective studies. Investigations of additional physical properties are also provided as suggestions. They are as follows:

- The evaluation of temperature on the mechanical behaviour of 3D printed elastomers. The effect of various test temperatures on tensile strength, elongation and stress relaxation is essential for checking their applicability in working components. Equally relevant is the use of different (especially higher) temperature ranges in DSC and DMA experiments to determine the maximum service temperature of the materials;
- The impact of printing parameters on the mechanical response. In the FFF technology, optimisations with printing temperature and flow percentage were conducted, while infill angle orientation and contour lines were varied and assessed. In the LAM process, the parameters layer height, line width and flow were optimised by visual means to avoid the presence of air bubbles in the prints. The influence of the infill deposition path was not verified for the silicone printer, for instance. In addition, the prints in this work were restricted to 100% infill at low printing speeds. The use of lower infill percentages helps to save printing time, particularly in extrusion-based processes. The compromise between infill percentage and mechanical performance, as well as other printing parameters for faster and more dimensionally accurate parts, are worth investigating;
- Further material characterization. The analyses in this work can be complemented by TMA measurements to obtain the coefficient of thermal expansion, thermal conductivity calculations, evaluation of the degrees of crystallisation and if strain-induced crystallisation occurs, studies on resistance to several oils and chemicals, and the mechanical behaviour under compression. Long-term experiments investigating ageing, fatigue, oxidation and exposure to UV radiation of the 3D printed elastomers are also recommended.

References

3D Activation. (2022, October 28). *Liquid Additive Manufacturing Verfahren*. https://www.3d-activation.de/information/lexikon/liquid-additive-manufacturing-verfahren/.

3D Printing Industry (2019a, March 28). *Adidas unveils Carbon 3D printed shoe in collaboration with Stella McCartney*. https://3dprintingindustry.com/news/adidas-unveils-carbon-3d-printed-shoe-in-collaboration-with-stella-mccartney-152262/.

3D Printing Industry (2021a, June 17). *Voxel8 3d prints comfort-optimized insoles for Hush Puppies' latest shoes*. https://3dprintingindustry.com/news/voxel8-3d-prints-comfort-optimized-insoles-for-hush-puppies-latest-shoes-191669/.

3D Printing Industry (2022a, October 11). *Climbing made easier: HP, Sculpteo, and Athos launch world's first 3d printed climbing shoes*. https://3dprintingindustry.com/news/climbing-made-easier-hp-sculpteo-and-athos-launch-worlds-first-3d-printed-climbing-shoes-215645/.

3D Printing Industry (2022b, March 14). *Indian army builds its first green 3d printed houses*. https://3dprintingindustry.com/news/indian-army-builds-its-first-green-3d-printed-houses-205988/

3D Printing Media Network. (2021, December 27). *Wacker Chemie to shut down ACEO silicone 3D printing service*. https://www.3dprintingmedia.network/wacker-chemie-to-shut-down-aceo-silicone-3d-printing-service/.

3D Systems. (2022a, October 27). *3D-Printers*. https://www.3dsystems.com/3d-printers.

3D Systems. (2022b, November 2). *DuraForm TPU Elastomer (SLS)*. https://www.3dsystems.com/materials/duraform-flex-tpu?ind=truck-bus-rail.

3DR Holdings. (2018, November 2). *German RepRap to Present Liquid Additive Manufacturing and L280 3D Printer at Formnext*. https://3dprint.com/229102/german-reprap-presents-liquid-additive-manufacturing-and-l280/.

Abayazid, F. F., Ghajari, M. (2020). Material characterisation of additively manufactured elastomers at different strain rates and build orientations. *Additive Manufacturing*, 33, 101160. https://doi.org/10.1016/j.addma.2020.101160.

Afsana et al. (2018). 3D printing in personalized drug delivery. *Current pharmaceutical design*, 24, 5062-5071. https://doi.org/10.2174/1381612825666190215122208.

Agassant, J. F. et al. (2019). Flow analysis of the polymer spreading during extrusion additive manufacturing. *Additive Manufacturing*, 29, 100794. https://doi.org/10.1016/j.addma.2019.100794.

Ai, J. R., Vogt, B. D. (2022). Size and print path effects on mechanical properties of material extrusion 3D printed plastics. *Progress in Additive Manufacturing*, 7(5), 1009-1021. https://doi.org/10.1007/s40964-022-00275-w.

American Society for Testing and Materials. (2012). *Standard Terminology for Additive Manufacturing Technologies* (ASTM Standard No. F2792e12a).

American Society for Testing and Materials. (2018). *Standard Classification System for Rubber Products in Automotive Applications* (ASTM Standard No. D 2000 – 18).

Arruda, E.M., Boyce, M.C. (1993). A three-dimensional constitutive model for the large stretch behavior of rubber elastic materials. *Journal of the Mechanics and Physics of Solids*, 41, 389–412. https://doi.org/10.1016/0022-5096(93)90013-6.

Askeland, D.R. et al. (2011). *The science and engineering of materials*, 6th ed. Cengage Learning.

Ayrilmis, N. (2018). Effect of layer thickness on surface properties of 3D printed materials produced from wood flour/PLA filament. *Polymer testing*, 71, 163-166. https://doi.org/10.1016/j.polymertesting.2018.09.009.

Bagheri, A., Jin, J. (2019). Photopolymerization in 3D Printing. *ACS Applied Polymer Materials*, 1, 593-611.

Bakır, A.A. et al. (2021). Mechanical Properties of 3D-Printed Elastomers Produced by Fused Deposition Modeling. In: *Fused Deposition Modeling Based 3D Printing* (p. 107-130). Springer, Cham. https://doi.org/10.1007/978-3-030-68024-4_6.

Banjanin, B. et al. (2022). Global market structure. In: *Polymers for 3D Printing: Methods, Properties, and Characteristics* (p. 353-367). Elsevier. https://doi.org/10.1016/B978-0-12-818311-3.00013-6.

Bauman, J.T. (2008). *Fatigue, stress, and strain of rubber components: a guide for design engineers*. Carl Hanser Verlag.

Bergström, J. (2015). *Mechanics of Solid Polymers: Theory and Computational Modeling*. Elsevier.

Betten, J. (2001). *Kontinuumsmechanik: Elastisches und inelastisches Verhalten isotroper und anisotroper Stoffe*. Berlin, Germany: Springer.

Bhandari, S., Lopez-Anido, R. (2018). Finite element analysis of thermoplastic polymer extrusion 3D printed material for mechanical property prediction. *Additive Manufacturing*, 22, 187–196. https://doi.org/10.1016/j.addma.2018.05.009.

Bikas, H. et al. (2016). Additive manufacturing methods and modelling approaches: a critical review. *The International Journal of Advanced Manufacturing Technology*, 83, 389-405. https://doi.org/10.1007/s00170-015-7576-2.

Bose, S. et al. (2013). Bone tissue engineering using 3D printing. *Materials today*, 16, 496-504. https://doi.org/10.1016/j.mattod.2013.11.017.

Brinson, H. F., Brinson, L. C. (2008). Characteristics, Applications and Properties of Polymers. In: *Polymer engineering science and viscoelasticity: An introduction* (p.55-97). Springer.

Bruère, V.M. et al. (2022a). Under-extrusion challenges for elastic filaments: the influence of moisture on additive manufacturing. *Progress in Additive Manufacturing*, 7, 445-452. https://doi.org/10.1007/s40964-022-00300-y.

Bruère, V.M. et al. (2022b). An Overview on the 3D Printing of Elastomers and the Influence of Printing Parameters on Their Mechanical Properties. In: *Lectures Notes on Advanced Structured Materials, Advanced Structured Materials*, 153, 139-153. https://doi.org/10.1007/978-3-031-11589-9_9.

Bruère, V.M. et al. (2023). The influence of printing parameters on the mechanical properties of 3D printed TPU-based elastomers. *Progress in Additive Manufacturing*, 1-9. https://doi.org/10.1007/s40964-023-00418-7.

Brusa da Costa Linn, L. et al. (2022). Towards 4D Printing of Very Soft Heterogeneous Magnetoactive Layers for Morphing Surface Applications via Liquid Additive Manufacturing. *Polymers*, 14(9), 1684. https://doi.org/10.3390/polym14091684.

Butts, M. et al. (2000). Silicones. *Kirk-Othmer Encyclopedia of Chemical Technology*. John Wiley & Sons.

Callister, W.D. (2000). *Materials science and engineering: An introduction*. Wiley and Sons.

Carbon, Inc. (2022a, October 18). *EPU 40*. https://www.carbon3d.com/materials/epu-40

Carbon, Inc. (2022b, October 18). *FPU 50*. https://www.carbon3d.com/materials/fpu-50

Carbon. (2022c, October 27). *Breaking Down the Carbon Digital Light Synthesis Process*. https://www.carbon3d.com/resources/dls-101/breaking-down-carbon-digital-light-synthesis-process.

Collinson, D. W. et al. (2022). Direct evidence of interfacial crystallization preventing weld formation during fused filament fabrication of poly (ether ether ketone). *Additive Manufacturing*, 51, 102604. https://doi.org/10.1016/j.addma.2022.102604.

Colorfabb. (2022, November 2). *Arnitel ID2045 Natural*. https://colorfabb.com/arnitelr-id2045-natural?gclid=Cj0KCQjwqoibBhDUARIsAH2OpWi0NFsdkl6TDuvydOZIY7EzFMG-k8AHFrSY506amKBtcXOmGTD3TNUaAuz_EALw_wcB.

Coogan, T.J., Kazmer, D.O. (2020). Prediction of interlayer strength in material extrusion additive manufacturing. *Additive Manufacturing*, 35. https://doi.org/10.1016/j.addma.2020.101368.

Dadbakhsh, S. et al. (2016). Effect of powder size and shape on the SLS processability and mechanical properties of a TPU elastomer. *Physics Procedia*, 83, 971-980. https://doi.org/10.1016/j.phpro.2016.08.102.

Dargazany, R., Itskov, M. (2013). Constitutive modeling of the Mullins effect and cyclic stress softening in filled elastomers. *Physical Review E*, 88, 012602. http://dx.doi.org/10.1103/PhysRevE.88.012602.

Dassault Systèmes. (2022, October 27). *MJF - Multi Jet Fusion*. https://www.3ds.com/make/service/3d-printing-service/mjf-multi-jet-fusion.

Dill, E.H. (2007). *Continuum Mechanics: Elasticity, Plasticity, Viscoelasticity*. Boca Raton, USA: CRC Press.

DIN German Institute for Standardisation. (2017). *Prüfung von Kautschuk und Elastomeren – Bestimmung von Reißfestigkeit, Zugfestigkeit, Reißdehnung und Spannungswerten im Zugversuch* [Testing of rubber - determination of tensile strength at break, tensile stress at yield, elongation at break and stress values in a tensile test]. (DIN Standard No. 53504-S3A).

DIN German Institute for Standardisation. (2022). *Thermoplastische Elastomere – Nomenklatur und Kurzzeichen* [Thermoplastic elastomers – Nomenclature and abbreviated terms] (DIN EN ISO Standard No. 18064).

Dohmen, E. et al. (2020). Field-structured magnetic elastomers based on thermoplastic polyurethane for fused filament fabrication. *Philosophical Transactions of the Royal Society A*, 378(2171), 20190257. https://doi.org/10.1098/rsta.2019.0257.

Dow. (2022, November 2). *SILASTIC™ 3D 3335 Liquid Silicone Rubber (LSR)*. https://www.dow.com/en-us/pdp.silastic-3-d-3335-liquid-silicone-rubber-lsr.4137603z.html?productCatalogFlag=1#overview.

Drobny, J.G. (2014). *Handbook of Thermoplastic Elastomers*. Elsevier.

Duoss, E. B. et al. (2014). Three-dimensional printing of elastomeric, cellular architectures with negative stiffness. *Advanced Functional Materials*, 24(31), 4905-4913. https://doi.org/10.1002/adfm.201400451.

Ehrenstein, G. W. et al. (2004). *Thermal analysis of plastics: theory and practice*. Carl Hanser Verlag.

EnvisionTec. (2021). *Our Systems*. https://etec.desktopmetal.com/product/.

Fang, L. et al. (2020). Processing-structure-property relationships of bisphenol-A-polycarbonate samples prepared by fused filament fabrication. *Additive Manufacturing*, 35, 101285. https://doi.org/10.1016/j.addma.2020.101285.

Farashi, S., Vafaee, F. (2022). Effect of extruder temperature and printing speed on the tensile strength of fused deposition modeling (FDM) 3D printed samples: a meta-analysis study. *International Journal on Interactive Design and Manufacturing (IJIDeM)*, 16(1), 305-316. https://doi.org/10.1007/s12008-021-00827-4.

Farstad, J. M. G., Netland, Ø., & Welo, T. (2017). Surface friction of rapidly prototyped wheels from 3D-printed thermoplastic elastomers: An experimental study. *Procedia Cirp*, 60, 247-252. https://doi.org/10.1016/j.procir.2017.02.009.

Fast Radius, Inc. (2020, June 5). *An overview of photopolymers*. https://www.fastradius.com/resources/photopolymers/#:~:text=The%20term%20photopolymer%20refers%20to,light%20energy%20into%20chemical%20energy.

Ferry, J.D. (1980). *Viscoelastic Properties of Polymers*. John Wiley & Sons.

Fink, J.K. (2019). *Liquid Silicone Rubber: Chemistry, Materials, and Processing*. John Wiley & Sons.

Fitzharris, E. R. et al. (2018). Interlayer bonding improvement of material extrusion parts with polyphenylene sulfide using the Taguchi method. *Additive Manufacturing*, 24, 287-297. https://doi.org/10.1016/j.addma.2018.10.003.

Flory, P.J. (1953). *Principles of polymer chemistry*. Cornell University Press.

Ford, S., Despeisse, M. (2016). Additive manufacturing and sustainability: an exploratory study of the advantages and challenges. *Journal of Cleaner Production*, 137, 1573-1587. https://doi.org/10.1016/j.jclepro.2016.04.150.

Formlabs. (2022a, October 19). *Resin Family: Flexible and Elastic*. https://formlabs.com/materials/flexible-elastic/.

Formlabs. (2022b, October 27). *Guide to Stereolithography (SLA) 3D Printing*. https://formlabs.com/blog/ultimate-guide-to-stereolithography-sla-3d-printing/.

Formlabs. (2022c, October 27). *SLA vs. DLP: Guide to Resin 3D Printers*. https://formlabs.com/blog/resin-3d-printer-comparison-sla-vs-dlp/.

Gauthier, C. et al. (2004). Analysis of the non-linear viscoelastic behaviour of silica filled styrene butadiene rubber. *Polymer*, 45(8), 2761-2771.

Gent, A.N. (2013). Rubber Elasticity: Basic Concepts and Behavior. In: *The Science and Technology of Rubber* (p.1-26). Academic Press. http://dx.doi.org/10.1016/B978-0-12-394584-6.00001-7.

Georgopoulou, A. et al. (2021). Fabrication of a soft robotic gripper with integrated strain sensing elements using multi-material additive manufacturing. *Frontiers in Robotics and AI*, 8, 615991. https://doi.org/10.3389/frobt.2021.615991.

Gilmer, E. L. et al. (2018). Model analysis of feedstock behavior in fused filament fabrication: Enabling rapid materials screening. *Polymer*, 152, 51-61. https://doi.org/10.1016/j.polymer.2017.11.068.

Goularte, B.F. et al. (2023). Multiparametric optimisation of 3D printed aircraft door seals. *Proceedings of the Munich Symposium on Lightweight Design 2021*, 136–153. https://doi.org/10.1007/978-3-662-65216-9_13.

Grady, B.P. et al. (2013). Thermoplastic Elastomers. In: *The Science and Technology of Rubber* (p. 591-652). Academic Press. http://dx.doi.org/10.1016/B978-0-12-394584-6.00013-3.

Guessasma, S. et al. (2016). Anisotropic damage inferred to 3D printed polymers using fused deposition modelling and subject to severe compression. *European Polymer Journal*, 85, 324–340. http://dx.doi.org/10.1016/j.eurpolymj.2016.10.030.

Hacker, M.C et al. (2019). Synthetic Polymers. In: *Principles of regenerative medicine* (p. 559-590). Academic press. https://doi.org/10.1016/B978-0-12-381422-7.10033-1

Hamidi, A., Tadesse, Y. (2020). 3D printing of very soft elastomer and sacrificial carbohydrate glass/elastomer structures for robotic applications. *Materials & Design*, 187, 108324. https://doi.org/10.1016/j.matdes.2019.108324.

Hanon, M. M. et al. (2019). Anisotropy evaluation of different raster directions, spatial orientations, and fill percentage of 3D printed PETG tensile test specimens. In: *Key engineering materials*, 821. Trans Tech Publications Ltd, pp.167-173. https://doi.org/10.4028/www.scientific.net/KEM.821.167.

Hanon, M. M. et al. (2021). The influence of 3D printing process parameters on the mechanical performance of PLA polymer and its correlation with hardness. *Procedia Manufacturing*, 54, 244-249. https://doi.org/10.1016/j.promfg.2021.07.038.

Harper, C.A. (2002). *Handbook of plastics, elastomers and composites*. 4th ed. McGraw-Hill.

Haupt, P. (2002). *Continuum Mechanics and Theory of Materials*. Berlin, Germany: Springer.

He, Z. et al. (2021). Preparation and properties of styrene ethylene butylene styrene/polypropylene thermoplastic elastomer powder for selective laser sintering 3D printing. *Journal of Applied Polymer Science*, 138(36), 50908. https://doi.org/10.1002/app.50908.

Herzberger, J. et al. (2019). Polymer design for 3D printing elastomers: Recent advances in structure, properties, and printing. *Progress in Polymer Science*, 97, 101144. https://doi.org/10.1016/j.progpolymsci.2019.101144.

Hill, R.G. (2005). Biomedical polymers. In: *Biomaterials, artificial organs and tissue engineering* (p. 97-106). Woodhead Publishing. https://doi.org/10.1533/9781845690861.2.97

Holzapfel, G.A. (2000). *Nonlinear solid mechanics: a continuum approach for engineering*. Chichester, England: Wiley.

HP. (2022, October 27). *HP Multi Jet Fusion-Technology*. https://www.hp.com/uk-en/printers/3d-printers/products/multi-jet-technology.html.

Hu, Y. et al. (2022). Influence of Cooling Rate on Crystallization Behavior of Semi-Crystalline Polypropylene: Experiments and Mathematical Modeling. *Polymers*, 14(17), 3646. https://doi.org/10.3390/polym14173646.

Hutchinson, S. A. (2023, March 07). *What is an ASTM D2000 callout for elastomer material and what does it mean?* HUTCHINSON Aerospace & Industry. https://hutchinsonai.com/wp-content/uploads/2020/01/ASTDM_D2000.pdf.

innovatiQ. (2022, October 28). *LiQ 320*. https://www.innovatiq.com/en/products/3d-printers/liq-320/.

Izdebska-Podsiadły, J. (2022). Materials for 3D printing. In: *Polymers for 3D Printing: Methods, Properties, and Characteristics* (p.35-49). Elsevier. https://doi.org/10.1016/B978-0-12-818311-3.00012-4.

Jaksa, L. et al. (2022). Calibration Dependencies and Accuracy Assessment of a Silicone Rubber 3D Printer. *Inventions*, 7(2), 35. https://doi.org/10.3390/inventions7020035.

Janusziewicz, R. et al. (2016). Layerless fabrication with continuous liquid interface production. *Proceedings of the National Academy of Sciences*, 113(42), 11703-11708. https://doi.org/10.1073/pnas.1605271113.

Jiang, J. et al. (2018). Support Structures for Additive Manufacturing: A Review. *Journal of Manufacturing and Materials Processing*, 2, 64. https://doi.org/10.3390/jmmp2040064.

Jiao, Z. et al. (2018). Experimental research of drop-on-demand droplet jetting 3D printing with molten polymer. *Journal of Applied Polymer Science*, 135, 45933. https://doi.org/10.1002/app.45933.

Johlitz, M. et al. (2010). Modelling of thermo-viscoelastic material behaviour of polyurethane close to the glass transition temperature. *ZAMM-Journal of Applied Mathematics and Mechanics*/Zeitschrift für Angewandte Mathematik und Mechanik: Applied Mathematics and Mechanics, 90(5), 387-398. https://doi.org/10.1002/zamm.200900361.

Joseph, B. et al. (2022). Photopolymers for 3D printing. In: *Polymers for 3D Printing: Methods, Properties, and Characteristics* (p.145-154). Elsevier. https://doi.org/10.1016/B978-0-12-818311-3.00011-2.

Keyence. (2020, February 17). *Hochauflösender 3D Drucker, Modellreihe AGILISTA Serie 3000: Materialdatenblatt*. (Document obtained from the manufacturer).

Kilian, H.G. (1981). Equation of state of real networks. *Polymer*, 22, 209–217. https://doi.org/10.1016/0032-3861(81)90200-7.

Kilian, H.G., Enderle, H.F., Unseld, K. (1986). The use of the van der Waals model to elucidate universal aspects of structure-property relationships in simply extended dry and swollen rubbers. *Colloid and Polymer Science*, 264, 866–876. https://doi.org/10.1007/BF01410637.

Klahn, C. et al. (2015). Design Strategies for the Process of Additive Manufacturing. *Procedia Cirp*, 36, 230-235. https://doi.org/10.1016/j.procir.2015.01.082.

Kotlinski, J. (2014). Mechanical properties of commercial rapid prototyping materials. *Rapid Prototyping Journal*, 20, 499-510. https://doi.org/10.1108/RPJ-06-2012-0052.

Kumar, N. et al. (2018). Extrusion-based additive manufacturing process for producing flexible parts. *Journal of the Brazilian Society of Mechanical Sciences and Engineering*, 40, 1-12. https://doi.org/10.1007/s40430-018-1068-x.

Kummert, C. et al. (2018). Thermoplastic elastomer part color as function of temperature histories and oxygen atmosphere during selective laser sintering. *JOM*, 70, 425-430. https://doi.org/10.1007/s11837-017-2658-2.

Landers, R. et al. (2002). Fabrication of soft tissue engineering scaffolds by means of rapid prototyping techniques. *Journal of materials science*, 37, 3107-3116. https://doi.org/10.1023/A:1016189724389.

Landers, R., Mülhaupt, R. (2000). Desktop manufacturing of complex objects, prototypes and biomedical scaffolds by means of computer-assisted design combined with computer-guided 3D plotting of polymers and reactive oligomers. *Macromolecular Materials and Engineering*, 282, 17-21. https://doi.org/10.1002/1439-2054(20001001)282:1<17::AID-MAME17>3.0.CO;2-8.

Lederle, F. et al. (2016). Improved mechanical properties of 3D-printed parts by fused deposition modeling processed under the exclusion of oxygen. *Progress in Additive Manufacturing*, 1, 3-7. https://doi.org/10.1007/s40964-016-0010-y.

León-Calero, M. et al. (2021). 3D printing of thermoplastic elastomers: Role of the chemical composition and printing parameters in the production of parts with controlled energy absorption and damping capacity. *Polymers*, 13(20), 3551. https://doi.org/10.3390/polym13203551.

Lepoivre, A. et al. (2020). Heat transfer and adhesion study for the FFF additive manufacturing process. *Procedia manufacturing*, 47, 948-955. https://doi.org/10.1016/j.promfg.2020.04.291.

Ligon, S. C. et al. (2017). Polymers for 3D printing and customized additive manufacturing. *Chemical reviews*, 117, 10212-10290. https://doi.org/10.1021/acs.chemrev.7b00074.

Liravi, F. et al. (2017). Additive manufacturing of 3D structures with non-Newtonian highly viscous fluids: Finite element modeling and experimental validation. *Additive Manufacturing*, 13, 113-123. https://doi.org/10.1016/j.addma.2016.10.008.

Liravi, F., Toyserkani, E. (2018). Additive manufacturing of silicone structures: A review and prospective. *Additive Manufacturing*, 24, 232-242. https://doi.org/10.1016/j.addma.2018.10.002.

Liu, Z. et al. (2017). 3D printing: printing precision and application in food sector. Trends in Food Science & Technology, 69, 83-94. https://doi.org/10.1016/j.tifs.2017.08.018.

Loos, K. et al. (2021). Future-Oriented Experimental Characterization of 3D Printed and Conventional Elastomers Based on Their Swelling Behavior. *Polymer*, 13, 4402. https://doi.org/10.3390/polym13244402.

Lubrizol. (2022, November 3). *ESTANE® 3D TPU (Thermoplastic Polyurethane)*. https://www.lubrizol.com/Engineered-Polymers/Products/Estane-TPU/Estane-3D.

Lukić, M. et al. (2016). Printability of elastomer latex for additive manufacturing or 3D printing. *Journal of Applied Polymer Science*, 133, 42931. https://doi.org/10.1002/app.42931.

Machado, G. et al. (2010). Analysis of the isotropic models of the Mullins effect based on filled silicone rubber experimental results. *Mechanics of Materials*, 42, 841-851. https://doi.org/10.1016/j.mechmat.2010.07.001.

Mahmood, S. et al. (2017). Tensile strength of partially filled FFF printed parts: meta modelling. *Rapid Prototyping Journal*, 23(3), 524-533. https://doi.org/10.1108/RPJ-10-2015-0151.

Mark, J.E. et al. (2015). *The Polysiloxanes*. Oxford University Press.

Mark, J.E., Erman, B. (2007). *Rubberlike elasticity: a molecular primer*. Cambridge University Press.

Maruo, S., Fourkas, J. T. (2008). Recent progress in multiphoton microfabrication. *Laser & Photonics Reviews*, 2, 100-111. https://doi.org/10.1002/lpor.200710039.

McCoul, D. et al. (2017). Inkjet 3D printing of UV and thermal cure silicone elastomers for dielectric elastomer actuators. *Smart Materials and Structures*, 26(12), 125022. https://doi.org/10.1088/1361-665X/aa9695.

Mellor, S. et al. (2014). Additive manufacturing: A framework for implementation. *International Journal of Production Economics*, 149, 194-201. https://doi.org/10.1016/j.ijpe.2013.07.008.

Menard, K. P. (2008). *Dynamic Mechanical Analysis: A practical introduction*. CRC Press.

Menczel, J. D., Prime, R. B. (Eds.). (2009). *Thermal analysis of polymers: fundamentals and applications*. John Wiley & Sons.

Miriyev, A. et al. (2019). Additive manufacturing of silicone composites for soft actuation. *3D Printing and Additive Manufacturing*, 6(6), 309-318. https://doi.org/10.1089/3dp.2019.0116.

Mittermeier, C., Lion, A. (2020). Challenges in the experimental investigation of the caloric and thermomechanical behaviour of semi-crystalline polymers: a study on the example of polyethylene terephthalate (PET). Polymer Testing, 81, 106252. https://doi.org/10.1016/j.polymertesting.2019.106252.

Monzón, M. et al. (2017). Anisotropy of photopolymer parts made by digital light processing. *Materials*, 10, 64. https://doi.org/10.3390/ma10010064.

Mooney, M. (1940). A theory of large elastic deformation. *Journal of Applied Physics*, 11, 582–592. https://doi.org/10.1063/1.1712836.

Moore, J. P., Williams, C. B. (2012). Fatigue characterization of 3D printed elastomer material. In: *2012 International Solid Freeform Fabrication Symposium*. University of Texas at Austin. http://dx.doi.org/10.26153/tsw/15379.

Morettini, G. et al. (2022). Comprehensive characterization of mechanical and physical properties of PLA structures printed by FFF-3D-printing process in different directions. *Progress in Additive Manufacturing*, 7(5), 1111-1122. https://doi.org/10.1007/s40964-022-00285-8.

Mullins, L. (1948). Effect of stretching on the properties of rubber. *Rubber chemistry and technology*, 21, 281-300.

Mullins, L. (1969). Softening of rubber by deformation. *Rubber chemistry and technology*, 42, 339-362.

Nakamura, K. (2015). *Photopolymers: Photoresist Materials, Processes, and Applications*. CRC Press.

Nathan-Walleser, T. et al. (2014). 3D Micro-Extrusion of Graphene-based Active Electrodes: Towards High-Rate AC Line Filtering Performance Electrochemical Capacitors. *Advanced Functional Materials*, 24(29), 4706-4716. https://doi.org/10.1002/adfm.201304151.

Ngai, K.L. et al. (2013). The Viscoelastic Behavior of Rubber and Dynamics of Blends. In: *The Science and Technology of Rubber* (p.193-284). Academic Press. http://dx.doi.org/10.1016/B978-0-12-394584-6.00005-4.

Noll. W. (1968). *Chemistry and Technology of Silicones*. Academic Press.

Noor, N. et al. (2019). 3D Printing of Personalized Thick and Perfusable Cardiac Patches and Hearts. *Advanced Science*, 6, 1900344. https://doi.org/10.1002/advs.201900344.

Nouri, H. et al. (2016). Structural imperfections in additive manufacturing perceived from the X-ray micro-tomography perspective. *Journal of Materials Processing Technology* 234, 113–124. http://dx.doi.org/10.1016/j.jmatprotec.2016.03.019.

Oelsch, E. et al. (2021). Comparative investigation on the mechanical behavior of injection molded and 3D-printed thermoplastic polyurethane. *Journal of Rubber Research*, 24, 249-256. https://doi.org/10.1007/s42464-021-00092-w.

Ogden, R.W., Hill, R. (1972). Large deformation isotropic elasticity—on the correlation of theory and experiment for incompressible rubberlike solids. *Proceedings of the Royal Society of London. A. Mathematical and Physical Sciences*, 326, 565–584. https://doi.org/10.1098/rspa.1972.0026.

Optomec. (2020). *Aerosol Jet Technology*. https://optomec.com/printed-electronics/aerosol-jet-technology/.

Pagac, M. et al. (2021). A Review of Vat Photopolymerization Technology: Materials, Applications, Challenges, and Future Trends of 3D Printing. *Polymers*, 13, 598. https://doi.org/10.3390/polym13040598.

Patel, D. K. et al. (2017). Highly stretchable and UV curable elastomers for digital light processing based 3D printing. *Advanced Materials*, 29(15), 1606000. https://doi.org/10.1002/adma.201606000.

178

Payne, A. R. (1962). The dynamic properties of carbon black-loaded natural rubber vulcanizates. Part I. *Journal of applied polymer science*, 6, 57-63.

Payne, A. R., Whittaker, R. E. (1971). Low strain dynamic properties of filled rubbers. *Rubber chemistry and technology*, 44, 440-478.

Peiffer, R.W. (1997). Applications of Photopolymer Technology. In: *Photopolymerization: Fundamentals and Applications – ACS Symposium Series 673*. American Chemical Society.

Pitayachaval, P. et al. (2018). A review of 3D food printing technology. MATEC web of conferences, 213, 01012. https://doi.org/10.1051/matecconf/201821301012.

Płatek, P. et al. (2020). Deformation process of 3D printed structures made from flexible material with different values of relative density. *Polymers*, 12(9), 2120. https://doi.org/10.3390/polym12092120.

Plott, J., Shih, A. (2017). The extrusion-based additive manufacturing of moisture-cured silicone elastomer with minimal void for pneumatic actuators. *Additive Manufacturing*, 17, 1-14. http://dx.doi.org/doi:10.1016/j.addma.2017.06.009.

Plott, J. et al. (2018a). Voids and tensile properties in extrusion-based additive manufacturing of moisture-cured silicone elastomer. *Additive Manufacturing*, 22, 606-617. https://doi.org/10.1016/j.addma.2018.06.010.

Plott, J. et al. (2018b). Measurement and modeling of forces in extrusion-based additive manufacturing of flexible silicone elastomer with thin wall structures. *Journal of Manufacturing Science and Engineering*, 140(9). https://doi.org/10.1115/1.4040350.

Porter, D. A. et al. (2019). Additive manufacturing by material extrusion with medical grade silicone elastomers and IR laser curing. *Rapid Prototyping Journal*, 26(1), 145-155. https://doi.org/10.1108/RPJ-10-2018-0279.

Protiq. (2022, October 27). *Multi Jet Fusion*. https://www.protiq.com/en/3d-printing/processes/multi-jet-fusion/.

Putra, K. B. et al. (2020). Biaxial test and hyperelastic material models of silicone elastomer fabricated by extrusion-based additive manufacturing for wearable biomedical devices. *Journal of the mechanical behavior of biomedical materials*, 107, 103733. https://doi.org/10.1016/j.jmbbm.2020.103733.

Rajpurohit, S. R., Dave, H. K. (2018). Effect of process parameters on tensile strength of FDM printed PLA part. *Rapid Prototyping Journal*, 24(8), 1317-1324. https://doi.org/10.1108/RPJ-06-2017-0134.

Rayna, T., Striukova, L. (2016). From rapid prototyping to home fabrication: How 3D printing is changing business model innovation. *Technological Forecasting and Social Change*, 102, 214-224. https://doi.org/10.1016/j.techfore.2015.07.023.

Recreus (2021, August 31). *Moisture vs. flexible filaments*. https://recreus.com/gb/noticias/learn-with-recreus/moisture-vs-flexible-filaments.

Recreus. (2022a, November 2). *Filaflex 70A*. https://recreus.com/gb/filaments/6-31-filaflex-70a.html#/1-colour-black/2-diameter-175_mm/3-weight-500_gr.

Recreus. (2022b, November 2). *Filaflex 82A*. https://recreus.com/gb/filaments/9-684-filaflex-82a.html#/1-colour-black/2-diameter-175_mm/3-weight-500_gr.

Riande, E. et al. (2000). *Polymer viscoelasticity: Stress and strain in practice*. CRC Press.

Rivlin, R.S. (1948). Large elastic deformations of isotropic materials IV. further developments of the general theory. *Philosophical Transactions of the Royal Society of London. Series A, Mathematical and Physical Sciences*, 241, 379–397. https://doi.org/10.1098/rsta.1948.0024.

Rize Inc. (2019). *Rize Additive Manufacturing Helps Soldiers Get Parts Faster; Builds Trust into Critical Parts*. AM. https://additivemanufacturing.com/2019/02/25/rize-additive-manufacturing-helps-soldiers-get-parts-faster-builds-trust-into-critical-parts/.

Robinson, M. et al. (2019). Mechanical characterisation of additively manufactured elastomeric structures for variable strain rate applications. *Additive Manufacturing*, 27, 398-407. https://doi.org/10.1016/j.addma.2019.03.022.

Rodgers, B., Waddell, W. (2013). The Science of Rubber Compounding. In: *The Science and Technology of Rubber* (p.417-472). Academic Press. http://dx.doi.org/10.1016/B978-0-12-394584-6.00009-1.

Rodriguez, N. et al. (2021). 3D printing of high viscosity reinforced silicone elastomers. *Polymers*, 13(14), 2239. https://doi.org/10.3390/polym13142239.

Roland, C.M. (2013). Structure Characterization in the Science and Technology of Elastomers. In: *The Science and Technology of Rubber* (p.115-166). Academic Press. http://dx.doi.org/10.1016/B978-0-12-394584-6.00003-0.

Rösler, J. et al. (2007). *Mechanical behaviour of engineering materials*. Springer.

Selbertinger, E. et al. (2019). *Method for producing silicone elastomer parts* (U.S. Patent No. 10,471,653, assigned to Wacker Chemie AG). U.S. Patent and Trademark Office.

Shaukat, U. et al. (2022). A Review of Multi-Material 3D Printing of Functional Materials via Vat Photopolymerization. *Polymers*, 14, 2449. https://doi.org/10.3390/polym14122449.

Sheoran, A. J., Kumar, H. (2020). Fused Deposition modeling process parameters optimization and effect on mechanical properties and part quality: Review and reflection on present research. *Materials Today: Proceedings*, 21, 1659-1672. https://doi.org/10.1016/j.matpr.2019.11.296.

Sinh, L. H. et al. (2016). Novel photo-curable polyurethane resin for stereolithography. *RSC advances*, 6(56), 50706-50709. https://doi.org/10.1039/C6RA05045J.

Smith, L. P. (1993). *The Language of Rubber: An Introduction to the Specification and Testing of Elastomers*. Butterworth-Heinemann.

Stratasys. (2017). *Digital Materials Data Sheet*. (Document obtained from the manufacturer).

Stratasys. (2022a, October 19). *Agilus30*. https://www.stratasys.com/en/materials/materials-catalog/polyjet-materials/agilus30/.

Stratasys. (2022b, October 19). *Tango*. https://www.stratasys.com/en/materials/materials-catalog/polyjet-materials/tango/

Stratasys. (2022c, October 27). *Pioneering the future*. https://www.stratasys.com/en/about-us/history/.

TA Instruments. (2021, June 6). *Determining the Linear Viscoelastic Region in Oscillatory Measurements*. https://www.tainstruments.com/pdf/literature/RH107.pdf

Tayeb, A. et al. (2022). 3D printing of soft thermoplastic elastomers: Effect of the deposit angle on mechanical and thermo-mechanical properties. *Mechanics of Materials*, 165, 104155. https://doi.org/10.1016/j.mechmat.2021.104155.

Thrasher, C. J. et al. (2017). Modular elastomer photoresins for digital light processing additive manufacturing. *ACS applied materials & interfaces*, 9(45), 39708-39716. https://doi.org/10.1021/acsami.7b13909.

Toki, S. et al. (2000). Strain-induced crystallization of natural rubber as detected real-time by wide-angle X-ray diffraction technique. *Polymer*, 41, 5423-5429. https://doi.org/10.1016/S0032-3861(99)00724-7.

Treloar, L. R. G. (1943a). The elasticity of a network of long-chain molecules. I. *Transactions of the Faraday Society*, 39, 36-41. https://doi.org/10.1039/TF9433900036.

Treloar, L.R.G. (1943b). The elasticity of a network of long-chain molecules—II. *Transactions of the Faraday Society*, 39, 241–246. https://doi.org/10.1039/TF9433900241.

Treloar, L.R.G. (1975). *The physics of rubber elasticity*. Oxford University Press.

Tumbleston, J. R. et al. (2015). Continuous liquid interface production of 3D objects. *Science*, 347, 1349-1352. https://doi.org/10.1126/science.aaa2397.

Upcraft, S., Fletcher, R. (2003). The rapid prototyping technologies. *Assembly Automation*, 23, 318-330. https://doi.org/10.1108/01445150310698634.

Valanis, K.C., Landel, R.F. (1967). The strain-energy function of a hyperelastic material in terms of the extension ratios. *Journal of Applied Physics*, 38, 2997–3002. https://doi.org/10.1063/1.1710039.

Volkswagen AG (2019, April 08). *Audi expands polymer 3D printing in Production*. https://www.volkswagenag.com/en/news/2019/04/Audi_expands_polymer_3D_printing_in_Production.html.

Wacker. (2019, October 15). *ACEO® Silicone GP Shore A 50*. (Document obtained from the manufacturer).

Wallin, T. J. et al. (2018). 3D printing of soft robotic systems. *Nature Reviews Materials*, 3(6), 84-100. https://doi.org/10.1038/s41578-018-0002-2.

Wellen, R. et al. (2015). Melting and crystallization of poly (3-hydroxybutyrate): effect of heating/cooling rates on phase transformation. *Polímeros*, 25, 296-304. https://doi.org/10.1590/0104-1428.1961.

Williams, M. L. et al. (1955). The temperature dependence of relaxation mechanisms in amorphous polymers and other glass-forming liquids. *Journal of the American Chemical society*, 77, 3701-3707.

Wu, W. et al. (2015). Influence of layer thickness and raster angle on the mechanical properties of 3D-printed PEEK and a comparative mechanical study between PEEK and ABS. *Materials*, 8(9), 5834-5846. https://doi.org/10.3390/ma8095271.

Xiao, J., Gao, Y. (2017). The manufacture of 3D printing of medical grade TPU. *Progress in Additive Manufacturing*, 2, 117-123. https://doi.org/10.1007/s40964-017-0023-1.

Yeoh, O.H. (1990). Characterization of elastic properties of carbon-black-filled rubber vulcanizates. *Rubber Chemistry and Technology*, 63, 792–805. https://doi.org/10.5254/1.3538289.

Yu, K. et al. (2019). Additive manufacturing of self-healing elastomers. *NPG Asia Materials*, 11(1), 7. https://doi.org/10.1038/s41427-019-0109-y.

Yuan, S. et al. (2016). Characterization of creeping and shape memory effect in laser sintered thermoplastic polyurethane. *Journal of Computing and Information Science in Engineering*, 16(4). https://doi.org/10.1115/1.4034032.

Zhou, L. Y. et al. (2020). A review of 3D printing technologies for soft polymer materials. *Advanced Functional Materials*, 30(28), 2000187. https://doi.org/10.1002/adfm.202000187.

Appendix A: FFF Printing Optimizations

A.1 Printing Optimization for Recreus 70A

The optimisations began with Recreus 70A, as it was the softest and thus the most difficult filament to print. Square plates of 60x60x2 mm³ were printed and dumbbell specimens with a 90° infill angle were punched. In this way, the most critical condition for line adhesion was studied. Subsequently, five specimens per sample were subjected to uniaxial tensile tests. The following printing parameters were optimised: printing temperature, extruder gripping pressure (called here *spring*) and flow rate at which the printer extrudes the material (also called *extrusion multiplier*, or simply *flow*).

The x500 innovatiQ printer has an adjusting screw that compresses a spring to regulate the extruder pressure applied onto the filament. There are 12 specific positions (see Figure A.1, where the number on the bottom corresponds to the pressure applied). The larger the number, the higher the pressure. The standard position is 7, while for elastic filaments it is recommended to use it at 3-4.
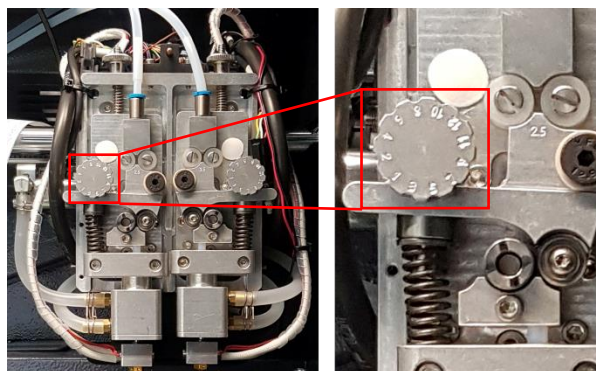
Figure A.1: Stress-strain curves for the printing temperature optimisation of Recreus 70A.

Initially, a flow of 130% was applied with the extruder spring in position 3. Plates were printed at different temperatures between 230°C and 250°C, with a 5°C increment within this range. The tensile stress-strain curves of the samples for each temperature are seen in Figure A.2 and the ultimate stresses and strains in Table A.1. The samples at the three highest temperatures presented a similar appearance. During testing, the 230°C and 235° samples exhibited premature delamination. The ones at 240°C and 245°C showed equivalent performances. The samples at 250°C provided the highest tensile strength, but it was only 10% above those of 240°C and 245°C. In addition, the printing temperature was closer to degradation. Considering this and the almost equal results of the prints at 240°C

and 245°C, 240°C was chosen since it was further away from the degradation temperature of the filament.
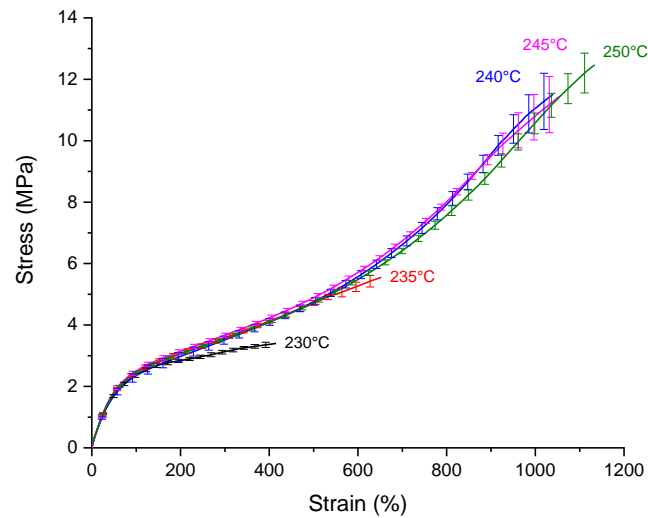
Figure A.2: Stress-strain curves for the printing temperature optimisation of Recreus 70A.

Table A.1: Ultimate tensile stresses for the temperature optimisation of Recreus 70A.

Temperature (°C)	Tensile strength (MPa)
230	3.40 ± 0.10
235	5.55 ± 0.25
240	11.51 ± 1.08
245	11.43 ± 1.03
250	12.46 ± 0.68

Excessive pressure can compromise the grip of the filament for extrusion due to its elastic nature. Hence, the extruder pressure (*spring*) was varied from 3 to 1. The optimised printing temperature of 240°C was applied and the flow was once more 130%. Results shown in Figure A.3 and Table A.2 evidence a significant improvement in tensile strength with less pressure on the filament. Therefore, the spring at position 1 was selected.
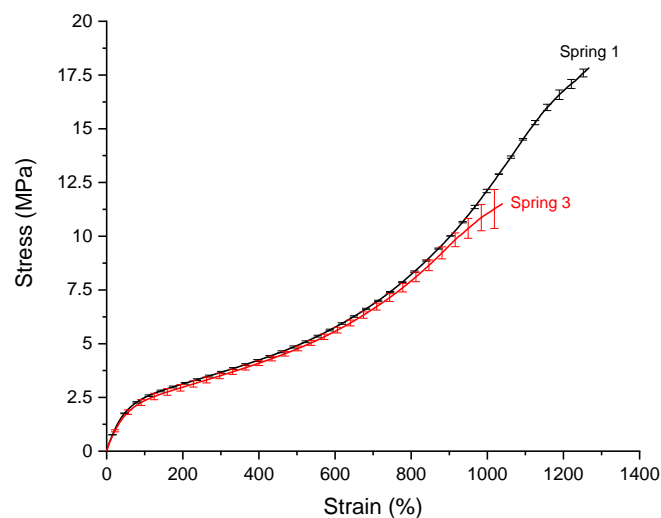
Figure A.3: Stress-strain curves for the extruder pressure optimisation of Recreus 70A.

Table A.2: Ultimate tensile stresses for extruder pressure optimisation of Recreus 70A.

Spring	Tensile strength (MPa)
3	11.51 ± 1.08
1	17.84 ± 0.15

At last, the material flow of plates printed at 240°C with the spring at 1 was increased to 135% and 140%. The tensile strengths from Figure A.4 and Table A.3 showed a better performance for the intermediate flow. Consequently, the final optimised parameters consisted of a printing temperature of 240°, a minimal extruder pressure (spring at position 1) and a flow of 135%, which were used in the printings of Recreus 70A in this thesis.
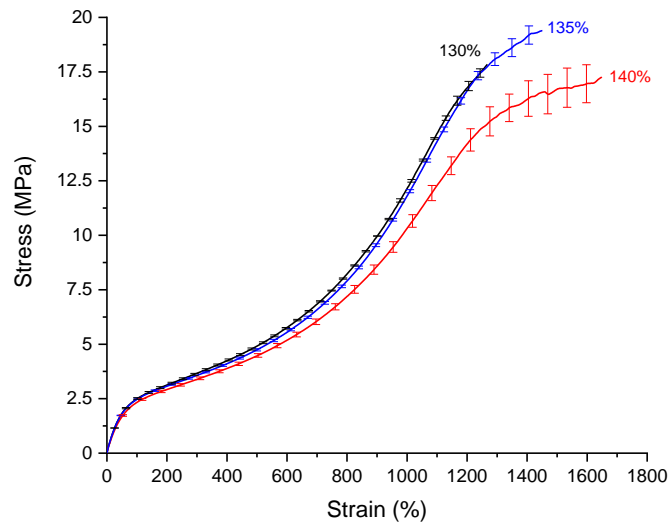
Figure A.4: Stress-strain curves for the flow optimisation of Recreus 70A.

Table A.3: Ultimate tensile stresses for the flow optimisation of Recreus 70A.

Flow (%)	Tensile strength (MPa)
130	17.84 ± 0.15
135	19.39 ± 0.35
140	17.26 ± 1.07

A.2 Printing Optimization for Recreus 82A

Based on the printing optimisation for the softer filament, the same extruder pressure was used in the printing of Recreus 82A. Its optimisation was simplified. Only printing temperature and flow were evaluated. For plates with poor appearance, only one specimen per sample was tested. This was enough to corroborate the low quality due to easy delamination. These included 220°C with a flow of 130%, and 230°C with a flow of 130%, with tensile strengths of circa 9 MPa and 12 MPa, respectively. With promising results, three combinations were printed, and five specimens per sample were tested. These are detailed in Table A.4 below.

Table A.4: Ultimate tensile stresses for the optimisation of Recreus 82A.

Temperature (°C)	Flow (%)	Tensile strength (MPa)
230	135	26.19 ± 0.51
230	140	25.29 ± 0.13
235	130	21.35 ± 1.32

The performance of the 235°C sample was inferior to those of the samples printed with 5°C less. The 230°C samples printed at flows of 135% and 140% showed similar tensile strengths, with a deviation of less than 4% of the latter from the former. Furthermore, the thickness of the specimens with a 140% flow was higher, and closer to the tolerances of the tensile testing standard. Thus, the best option for Recreus 82A was a printing temperature of 230°C and a flow of 135%.

Appendix B: Printing files and images

B.1 G-Code settings for FFF and LAM Prints

Table B.1: G-Code settings for the Arnitel plates of infill at 0° [or 45°].

; G-Code generated by Simplify3D(R) Version 4.1.2	; raftSeparationDistance,0.15
; Oct 28, 2020 at 5:08:48 PM	; raftTopInfill,100
; Settings Summary	; aboveRaftSpeedMultiplier,0.3
; processName,Process1	; useSkirt,1
; applyToModels,geometry_plate	; skirtExtruder,0
; profileName,Default (modified)	; skirtLayers,1
; profileVersion,2020-01-24 10:44:32	; skirtOutlines,12
; baseProfile,German RepRap X350 Dual Extruder	; skirtOffset,0
; printMaterial,ABS	; usePrimePillar,0
; printQuality,Medium	; primePillarExtruder,0
; printExtruders,Left Extruder Only	; primePillarWidth,12
; extruderName,Left Extruder,Right Extruder	; primePillarLocation,2
; extruderToolheadNumber,0,1	; primePillarSpeedMultiplier,1
; extruderDiameter,0.4,0.4	; useOozeShield,0
; extruderAutoWidth,1,1	; oozeShieldExtruder,0
; extruderWidth,0.48,0.48	; oozeShieldOffset,4
; extrusionMultiplier,1.2,1	; oozeShieldOutlines,2
; extruderUseRetract,1,1	; oozeShieldSidewallShape,0
; extruderRetractionDistance,3.5,0.7	; oozeShieldSidewallAngle,30
; extruderExtraRestartDistance,0,0	; oozeShieldSpeedMultiplier,1
; extruderRetractionZLift,0,0	; outlineOverlapPercentage,40
; extruderRetractionSpeed,2400,5100	; infillExtrusionWidthPercentage,100
; extruderUseCoasting,1,0	; minInfillLength,2
; extruderCoastingDistance,2,0.2	; infillLayerInterval,1
; extruderUseWipe,1,0	; internalInfillAngles,0 [45]
; extruderWipeDistance,2.5,5	; overlapInternalInfillAngles,0
; primaryExtruder,0	; externalInfillAngles,0
; layerHeight,0.2	; generateSupport,0
; topSolidLayers,0	; supportExtruder,0
; bottomSolidLayers,0	; supportInfillPercentage,25
; perimeterOutlines,1	; supportExtraInflation,1
; printPerimetersInsideOut,0	; supportBaseLayers,3
; startPointOption,1	; denseSupportExtruder,0
; startPointOriginX,0	; denseSupportLayers,3
; startPointOriginY,0	; denseSupportInfillPercentage,100
; sequentialIslands,0	; supportLayerInterval,1
; spiralVaseMode,0	; supportHorizontalPartOffset,0.6
; firstLayerHeightPercentage,130	; supportUpperSeparationLayers,1
; firstLayerWidthPercentage,130	; supportLowerSeparationLayers,1
; firstLayerUnderspeed,1	; supportType,0
; useRaft,0	; supportGridSpacing,4
; raftExtruder,0	; maxOverhangAngle,45
; raftTopLayers,2	; supportAngles,45
; raftBaseLayers,1	; temperatureName,Left Extruder,Right
; raftOffset,3	Extruder,Heated Bed,Heated chamber

```
;    temperatureNumber,0,1,2,2
;    temperatureSetpointCount,1,1,1,1
;    temperatureSetpointLayers,1,1,1,1
;    temperatureSetpointTemperatures,230,0,45,25
;    temperatureStabilizeAtStartup,1,1,1,0
;    temperatureHeatedBed,0,0,1,0
;    fanLayers,1,3
;    fanSpeeds,0,0
;    blipFanToFullPower,0
;    adjustSpeedForCooling,0
;    minSpeedLayerTime,25
;    minCoolingSpeedSlowdown,20
;    increaseFanForCooling,0
;    minFanLayerTime,45
;    maxCoolingFanSpeed,100
;    increaseFanForBridging,0
;    bridgingFanSpeed,100
;    use5D,1
;    relativeEdistances,0
;    allowEaxisZeroing,1
;    independentExtruderAxes,0
;    includeM10123,0
;    stickySupport,1
;    applyToolheadOffsets,0
;    gcodeXoffset,0
;    gcodeYoffset,0
;    gcodeZoffset,0
;    overrideMachineDefinition,1
;    machineTypeOverride,0
;    strokeXoverride,500
;    strokeYoverride,400
;    strokeZoverride,450
;    originOffsetXoverride,0
;    originOffsetYoverride,0
;    originOffsetZoverride,0
;    homeXdirOverride,-1
;    homeYdirOverride,-1
;    homeZdirOverride,-1
;    flipXoverride,-1
;    flipYoverride,1
;    flipZoverride,1
;    toolheadOffsets,0,0|0,0|0,0|0,0|0,0|0,0
;    overrideFirmwareConfiguration,1
;    firmwareTypeOverride,RepRap
(Marlin/Repetier/Sprinter)
;    GPXconfigOverride,r2
;    baudRateOverride,115200
;    overridePrinterModels,1
;    printerModelsOverride
;    startingGcode,G1 Z240 F3000,M140
S[bed2_temperature],M104 S[extruder2_temperature]
T2,M109 S[extruder2_temperature] T2,M190
S[bed2_temperature],G1 X-20 Y70 F3000,M104
S[extruder0_temperature] T0,M109
S[extruder0_temperature] T0,G1 Y10,G1 Y70
;    layerChangeGcode,
;    retractionGcode,
;    toolChangeGcode,
;    endingGcode,G28 X0 ; home X axis,G28 Y0 ; home
Y axis,M104 S0 T0 ; turn off extruder,M104 S0 T1 ;
turn off extruder,M104 S0 T2 ; turn off extruder,M140
S0 ; turn off bed,M106 S0 ; turn off fan,M806 S0 ; turn
of housing fan,M84 ; disable motors
;    exportFileFormat,gcode
;    celebration,0
;    celebrationSong,Star Wars
```

```
;    postProcessing,
;    defaultSpeed,600
;    outlineUnderspeed,1
;    solidInfillUnderspeed,1
;    supportUnderspeed,1
;    rapidXYspeed,10800
;    rapidZspeed,300
;    minBridgingArea,50
;    bridgingExtraInflation,2
;    bridgingExtrusionMultiplier,0.8
;    bridgingSpeedMultiplier,1.3
;    useFixedBridgingAngle,0
;    fixedBridgingAngle,0
;    applyBridgingToPerimeters,0
;    filamentDiameters,1.75|1.75|1.75|1.75|1.75|1.75
;    filamentPricesPerKg,33|33|33|33|33|33
;    filamentDensities,1.25|1.25|1.25|1.25|1.25|1.25
;    useMinPrintHeight,0
;    minPrintHeight,0
;    useMaxPrintHeight,0
;    maxPrintHeight,0
;    useDiaphragm,0
;    diaphragmLayerInterval,20
;    robustSlicing,1
;    mergeAllIntoSolid,0
;    onlyRetractWhenCrossingOutline,1
;    retractBetweenLayers,0
;    useRetractionMinTravel,1
;    retractionMinTravel,0.02
;    retractWhileWiping,1
;    onlyWipeOutlines,0
;    avoidCrossingOutline,1
;    maxMovementDetourFactor,3
;    toolChangeRetractionDistance,0.7
;    toolChangeExtraRestartDistance,0
;    toolChangeRetractionSpeed,5100
;    externalThinWallType,0
;    internalThinWallType,0
;    thinWallAllowedOverlapPercentage,10
;    singleExtrusionMinLength,1
;    singleExtrusionMinPrintingWidthPercentage,50
;    singleExtrusionMaxPrintingWidthPercentage,200
;    singleExtrusionEndpointExtension,0.2
;    horizontalSizeCompensation,0
```

Table B.2: G-Code settings for the Recreus 70A plates.

```
; G-Code generated by Simplify3D(R) Version 4.1.2
; Jun 27, 2022 at 12:11:03 PM
; Settings Summary
;   processName,250
;   applyToModels,geometry_plate(2)
;   profileName,Default (modified)
;   profileVersion,2020-01-24 10:44:32
;   baseProfile,German RepRap X350 Dual Extruder
;   printMaterial,ABS
;   printQuality,Medium
;   printExtruders,Left Extruder Only
;   extruderName,Left Extruder,Right Extruder
;   extruderToolheadNumber,0,1
;   extruderDiameter,0.4,0.4
;   extruderAutoWidth,1,1
;   extruderWidth,0.48,0.48
;   extrusionMultiplier,1.35,1
;   extruderUseRetract,1,1
;   extruderRetractionDistance,3.5,0.7
;   extruderExtraRestartDistance,0,0
;   extruderRetractionZLift,0,0
;   extruderRetractionSpeed,2400,5100
;   extruderUseCoasting,1,0
;   extruderCoastingDistance,2,0.2
;   extruderUseWipe,1,0
;   extruderWipeDistance,2.5,5
;   primaryExtruder,0
;   layerHeight,0.2
;   topSolidLayers,0
;   bottomSolidLayers,0
;   perimeterOutlines,0
;   printPerimetersInsideOut,0
;   startPointOption,3
;   startPointOriginX,150
;   startPointOriginY,200
;   sequentialIslands,0
;   spiralVaseMode,0
;   firstLayerHeightPercentage,130
;   firstLayerWidthPercentage,130
;   firstLayerUnderspeed,1
;   useRaft,0
;   raftExtruder,0
;   raftTopLayers,2
;   raftBaseLayers,1
;   raftOffset,3
;   raftSeparationDistance,0.15
;   raftTopInfill,100
;   aboveRaftSpeedMultiplier,0.3
;   useSkirt,1
;   skirtExtruder,0
;   skirtLayers,1
;   skirtOutlines,5
;   skirtOffset,5
;   usePrimePillar,0
;   primePillarExtruder,0
;   primePillarWidth,12
;   primePillarLocation,2
;   primePillarSpeedMultiplier,1
;   useOozeShield,0
;   oozeShieldExtruder,0
;   oozeShieldOffset,4
;   oozeShieldOutlines,2
;   oozeShieldSidewallShape,0
;   oozeShieldSidewallAngle,30
;   oozeShieldSpeedMultiplier,1
;   infillExtruder,0
;   internalInfillPattern,Rectilinear
;   externalInfillPattern,Rectilinear
;   infillPercentage,100
;   outlineOverlapPercentage,40
;   infillExtrusionWidthPercentage,100
;   minInfillLength,2
;   infillLayerInterval,1
;   internalInfillAngles,0
;   overlapInternalInfillAngles,0
;   externalInfillAngles,45,-45
;   generateSupport,0
;   supportExtruder,0
;   supportInfillPercentage,25
;   supportExtraInflation,1
;   supportBaseLayers,3
;   denseSupportExtruder,0
;   denseSupportLayers,3
;   denseSupportInfillPercentage,100
;   supportLayerInterval,1
;   supportHorizontalPartOffset,0.6
;   supportUpperSeparationLayers,1
;   supportLowerSeparationLayers,1
;   supportType,0
;   supportGridSpacing,4
;   maxOverhangAngle,45
;   supportAngles,45
;   temperatureName,Left Extruder,Right
Extruder,Heated Bed,Heated chamber
;   temperatureNumber,0,1,2,2
;   temperatureSetpointCount,1,1,1,1
;   temperatureSetpointLayers,1,1,1,1
;   temperatureSetpointTemperatures,240,0,30,30
;   temperatureStabilizeAtStartup,1,1,1,0
;   temperatureHeatedBed,0,0,1,0
;   fanLayers,1,3
;   fanSpeeds,0,0
;   blipFanToFullPower,0
;   adjustSpeedForCooling,0
;   minSpeedLayerTime,25
;   minCoolingSpeedSlowdown,20
;   increaseFanForCooling,0
;   minFanLayerTime,45
;   maxCoolingFanSpeed,100
;   increaseFanForBridging,0
;   bridgingFanSpeed,100
;   use5D,1
;   relativeEdistances,0
;   allowEaxisZeroing,1
;   independentExtruderAxes,0
;   includeM10123,0
;   stickySupport,1
;   applyToolheadOffsets,0
;   gcodeXoffset,0
;   gcodeYoffset,0
;   gcodeZoffset,0
;   overrideMachineDefinition,1
;   machineTypeOverride,0
;   strokeXoverride,500
;   strokeYoverride,400
;   strokeZoverride,450
```

;   originOffsetXoverride,0
;   originOffsetYoverride,0
;   originOffsetZoverride,0
;   homeXdirOverride,-1
;   homeYdirOverride,-1
;   homeZdirOverride,-1
;   flipXoverride,-1
;   flipYoverride,1
;   flipZoverride,1
;   toolheadOffsets,0,0|0,0|0,0|0,0|0,0|0,0
;   overrideFirmwareConfiguration,1
;   firmwareTypeOverride,RepRap
(Marlin/Repetier/Sprinter)
;   GPXconfigOverride,r2
;   baudRateOverride,115200
;   overridePrinterModels,1
;   printerModelsOverride
;   startingGcode,G1 Z240 F3000,M140
S[bed2_temperature],M104 S[extruder2_temperature]
T2,M109 S[extruder2_temperature] T2,M190
S[bed2_temperature],G1 X-20 Y70 F3000,M104
S[extruder0_temperature] T0,M109
S[extruder0_temperature] T0,G1 Y10,G1 Y70
;   layerChangeGcode,
;   retractionGcode,
;   toolChangeGcode,
;   endingGcode,G28 X0 ; home X axis,G28 Y0 ; home
Y axis,M104 S0 T0 ; turn off extruder,M104 S0 T1 ;
turn off extruder,M104 S0 T2 ; turn off extruder,M140
S0 ; turn off bed,M106 S0 ; turn off fan,M806 S0 ; turn
of housing fan,M84 ; disable motors
;   exportFileFormat,gcode
;   celebration,0
;   celebrationSong,Star Wars
;   postProcessing,
;   defaultSpeed,600
;   outlineUnderspeed,1
;   solidInfillUnderspeed,1
;   supportUnderspeed,1
;   rapidXYspeed,10800
;   rapidZspeed,300
;   minBridgingArea,50
;   bridgingExtraInflation,2
;   bridgingExtrusionMultiplier,0.8
;   bridgingSpeedMultiplier,1.3
;   useFixedBridgingAngle,0
;   fixedBridgingAngle,0
;   applyBridgingToPerimeters,0
;   filamentDiameters,1.75|1.75|1.75|1.75|1.75|1.75
;   filamentPricesPerKg,33|33|33|33|33|33
;   filamentDensities,1.25|1.25|1.25|1.25|1.25|1.25
;   useMinPrintHeight,0
;   minPrintHeight,0
;   useMaxPrintHeight,0
;   maxPrintHeight,1
;   useDiaphragm,0
;   diaphragmLayerInterval,20
;   robustSlicing,1
;   mergeAllIntoSolid,0
;   onlyRetractWhenCrossingOutline,1
;   retractBetweenLayers,0
;   useRetractionMinTravel,1
;   retractionMinTravel,0.02
;   retractWhileWiping,1
;   onlyWipeOutlines,0

;   avoidCrossingOutline,1
;   maxMovementDetourFactor,3
;   toolChangeRetractionDistance,0.7
;   toolChangeExtraRestartDistance,0
;   toolChangeRetractionSpeed,5100
;   externalThinWallType,0
;   internalThinWallType,0
;   thinWallAllowedOverlapPercentage,10
;   singleExtrusionMinLength,1
;   singleExtrusionMinPrintingWidthPercentage,50
;   singleExtrusionMaxPrintingWidthPercentage,200
;   singleExtrusionEndpointExtension,0.2
;   horizontalSizeCompensation,0

Table B.3: G-Code settings for the Recreus 82A plates.

```
; G-Code generated by Simplify3D(R) Version 4.1.2
; Jul 8, 2022 at 10:57:42 AM
; Settings Summary
;   processName,Process1
;   applyToModels,geometry_plate
;   profileName,Default (modified)
;   profileVersion,2020-01-24 10:44:32
;   baseProfile,German RepRap X350 Dual Extruder
;   printMaterial,ABS
;   printQuality,Medium
;   printExtruders,Left Extruder Only
;   extruderName,Left Extruder,Right Extruder
;   extruderToolheadNumber,0,1
;   extruderDiameter,0.4,0.4
;   extruderAutoWidth,1,1
;   extruderWidth,0.48,0.48
;   extrusionMultiplier,1.35,1
;   extruderUseRetract,1,1
;   extruderRetractionDistance,3.5,0.7
;   extruderExtraRestartDistance,0,0
;   extruderRetractionZLift,0,0
;   extruderRetractionSpeed,2400,5100
;   extruderUseCoasting,1,0
;   extruderCoastingDistance,2,0.2
;   extruderUseWipe,1,0
;   extruderWipeDistance,2.5,5
;   primaryExtruder,0
;   layerHeight,0.2
;   topSolidLayers,0
;   bottomSolidLayers,0
;   perimeterOutlines,0
;   printPerimetersInsideOut,1
;   startPointOption,1
;   startPointOriginX,0
;   startPointOriginY,0
;   sequentialIslands,0
;   spiralVaseMode,0
;   firstLayerHeightPercentage,130
;   firstLayerWidthPercentage,130
;   firstLayerUnderspeed,1
;   useRaft,0
;   raftExtruder,0
;   raftTopLayers,2
;   raftBaseLayers,1
;   raftOffset,3
;   raftSeparationDistance,0.15
;   raftTopInfill,100
;   aboveRaftSpeedMultiplier,0.3
;   useSkirt,1
;   skirtExtruder,0
;   skirtLayers,1
;   skirtOutlines,3
;   skirtOffset,5
;   usePrimePillar,0
;   primePillarExtruder,0
;   primePillarWidth,12
;   primePillarLocation,2
;   primePillarSpeedMultiplier,1
;   useOozeShield,0
;   oozeShieldExtruder,0
;   oozeShieldOffset,4
;   oozeShieldOutlines,2
;   oozeShieldSidewallShape,0
;   oozeShieldSidewallAngle,30
;   oozeShieldSpeedMultiplier,1
;   infillExtruder,0
;   internalInfillPattern,Rectilinear
;   externalInfillPattern,Rectilinear
;   infillPercentage,100
;   outlineOverlapPercentage,40
;   infillExtrusionWidthPercentage,100
;   minInfillLength,2
;   infillLayerInterval,1
;   internalInfillAngles,0
;   overlapInternalInfillAngles,0
;   externalInfillAngles,0
;   generateSupport,0
;   supportExtruder,0
;   supportInfillPercentage,25
;   supportExtraInflation,1
;   supportBaseLayers,3
;   denseSupportExtruder,0
;   denseSupportLayers,3
;   denseSupportInfillPercentage,100
;   supportLayerInterval,1
;   supportHorizontalPartOffset,0.6
;   supportUpperSeparationLayers,1
;   supportLowerSeparationLayers,1
;   supportType,0
;   supportGridSpacing,4
;   maxOverhangAngle,45
;   supportAngles,45
;   temperatureName,Left Extruder,Right
Extruder,Heated Bed,Heated chamber
;   temperatureNumber,0,1,2,2
;   temperatureSetpointCount,1,1,1,1
;   temperatureSetpointLayers,1,1,1,1
;   temperatureSetpointTemperatures,230,0,30,25
;   temperatureStabilizeAtStartup,1,1,1,0
;   temperatureHeatedBed,0,0,1,0
;   fanLayers,1,3
;   fanSpeeds,0,0
;   blipFanToFullPower,0
;   adjustSpeedForCooling,0
;   minSpeedLayerTime,25
;   minCoolingSpeedSlowdown,20
;   increaseFanForCooling,0
;   minFanLayerTime,45
;   maxCoolingFanSpeed,100
;   increaseFanForBridging,0
;   bridgingFanSpeed,100
;   use5D,1
;   relativeEdistances,0
;   allowEaxisZeroing,1
;   independentExtruderAxes,0
;   includeM10123,0
;   stickySupport,1
;   applyToolheadOffsets,0
;   gcodeXoffset,0
;   gcodeYoffset,0
;   gcodeZoffset,0
;   overrideMachineDefinition,1
;   machineTypeOverride,0
;   strokeXoverride,500
;   strokeYoverride,400
;   strokeZoverride,450
```

; originOffsetXoverride,0
; originOffsetYoverride,0
; originOffsetZoverride,0
; homeXdirOverride,-1
; homeYdirOverride,-1
; homeZdirOverride,-1
; flipXoverride,-1
; flipYoverride,1
; flipZoverride,1
; toolheadOffsets,0,0|0,0|0,0|0,0|0,0|0,0
; overrideFirmwareConfiguration,1
; firmwareTypeOverride,RepRap
(Marlin/Repetier/Sprinter)
; GPXconfigOverride,r2
; baudRateOverride,115200
; overridePrinterModels,1
; printerModelsOverride
; startingGcode,G1 Z240 F3000,M140
S[bed2_temperature],M104 S[extruder2_temperature]
T2,M109 S[extruder2_temperature] T2,M190
S[bed2_temperature],G1 X-20 Y70 F3000,M104
S[extruder0_temperature] T0,M109
S[extruder0_temperature] T0,G1 Y10,G1 Y70
; layerChangeGcode,
; retractionGcode,
; toolChangeGcode,
; endingGcode,G28 X0 ; home X axis,G28 Y0 ; home
Y axis,M104 S0 T0 ; turn off extruder,M104 S0 T1 ;
turn off extruder,M104 S0 T2 ; turn off extruder,M140
S0 ; turn off bed,M106 S0 ; turn off fan,M806 S0 ; turn
of housing fan,M84 ; disable motors
; exportFileFormat,gcode
; celebration,0
; celebrationSong,Star Wars
; postProcessing,
; defaultSpeed,600
; outlineUnderspeed,1
; solidInfillUnderspeed,1
; supportUnderspeed,1
; rapidXYspeed,10800
; rapidZspeed,300
; minBridgingArea,50
; bridgingExtraInflation,2
; bridgingExtrusionMultiplier,0.8
; bridgingSpeedMultiplier,1.3
; useFixedBridgingAngle,0
; fixedBridgingAngle,0
; applyBridgingToPerimeters,0
; filamentDiameters,1.75|1.75|1.75|1.75|1.75|1.75
; filamentPricesPerKg,33|33|33|33|33|33
; filamentDensities,1.25|1.25|1.25|1.25|1.25|1.25
; useMinPrintHeight,1
; minPrintHeight,0
; useMaxPrintHeight,1
; maxPrintHeight,35
; useDiaphragm,0
; diaphragmLayerInterval,20
; robustSlicing,1
; mergeAllIntoSolid,0
; onlyRetractWhenCrossingOutline,1
; retractBetweenLayers,0
; useRetractionMinTravel,1
; retractionMinTravel,0.02
; retractWhileWiping,1
; onlyWipeOutlines,0

; avoidCrossingOutline,1;
maxMovementDetourFactor,3;
toolChangeRetractionDistance,0.7
; toolChangeExtraRestartDistance,0
; toolChangeRetractionSpeed,5100
; externalThinWallType,0
; internalThinWallType,0
; thinWallAllowedOverlapPercentage,10
; singleExtrusionMinLength,1
; singleExtrusionMinPrintingWidthPercentage,50
; singleExtrusionMaxPrintingWidthPercentage,200
; singleExtrusionEndpointExtension,0.2
; horizontalSizeCompensation,0

Table B.4: G-Code settings for the Silastic plates.

```
; G-Code generated by Simplify3D(R) Version 4.1.2        ;   oozeShieldSidewallAngle,30
; Jul 30, 2021 at 10:03:22 AM                            ;   oozeShieldSpeedMultiplier,1
; Settings Summary                                       ;   infillExtruder,0
;   processName,Process1                                 ;   internalInfillPattern,Rectilinear
;   applyToModels,Platte 100x100x2mm(2)                  ;   externalInfillPattern,Rectilinear
;   profileName,Default (modified)                       ;   infillPercentage,100
;   profileVersion,2019-03-14 11:10:12                   ;   outlineOverlapPercentage,40
;   baseProfile,GRR_2K_Helix (modified)                  ;   infillExtrusionWidthPercentage,100
;   printMaterial,                                       ;   minInfillLength,1
;   printQuality,                                        ;   infillLayerInterval,1
;   printExtruders,                                      ;   internalInfillAngles,90
;   extruderName,Extruder 1                              ;   overlapInternalInfillAngles,0
;   extruderToolheadNumber,0                             ;   externalInfillAngles,120
;   extruderDiameter,0.42                                ;   generateSupport,0
;   extruderAutoWidth,0                                  ;   supportExtruder,0
;   extruderWidth,0.41                                   ;   supportInfillPercentage,100
;   extrusionMultiplier,1.45                             ;   supportExtraInflation,0
;   extruderUseRetract,1                                 ;   supportBaseLayers,0
;   extruderRetractionDistance,10                        ;   denseSupportExtruder,0
;   extruderExtraRestartDistance,-1                      ;   denseSupportLayers,0
;   extruderRetractionZLift,5                            ;   denseSupportInfillPercentage,70
;   extruderRetractionSpeed,1002                         ;   supportLayerInterval,1
;   extruderUseCoasting,1                                ;   supportHorizontalPartOffset,0
;   extruderCoastingDistance,1                           ;   supportUpperSeparationLayers,0
;   extruderUseWipe,0                                    ;   supportLowerSeparationLayers,0
;   extruderWipeDistance,2                               ;   supportType,0
;   primaryExtruder,0                                    ;   supportGridSpacing,1
;   layerHeight,0.4                                      ;   maxOverhangAngle,10
;   topSolidLayers,0                                     ;   supportAngles,40,-50
;   bottomSolidLayers,0                                  ;   temperatureName,Primary Extruder,Heated Bed
;   perimeterOutlines,0                                  ;   temperatureNumber,0,0
;   printPerimetersInsideOut,0                           ;   temperatureSetpointCount,1,1
;   startPointOption,3                                   ;   temperatureSetpointLayers,1,1
;   startPointOriginX,100                                ;   temperatureSetpointTemperatures,0,0
;   startPointOriginY,100                                ;   temperatureStabilizeAtStartup,0,0
;   sequentialIslands,0                                  ;   temperatureHeatedBed,0,1
;   spiralVaseMode,0                                     ;   fanLayers,2
;   firstLayerHeightPercentage,100                       ;   fanSpeeds,100
;   firstLayerWidthPercentage,100                        ;   blipFanToFullPower,0
;   firstLayerUnderspeed,1                               ;   adjustSpeedForCooling,0
;   useRaft,0                                            ;   minSpeedLayerTime,15
;   raftExtruder,0                                       ;   minCoolingSpeedSlowdown,20
;   raftTopLayers,1                                      ;   increaseFanForCooling,0
;   raftBaseLayers,2                                     ;   minFanLayerTime,45
;   raftOffset,3                                         ;   maxCoolingFanSpeed,100
;   raftSeparationDistance,0                             ;   increaseFanForBridging,0
;   raftTopInfill,100                                    ;   bridgingFanSpeed,100
;   aboveRaftSpeedMultiplier,0.3                         ;   use5D,1
;   useSkirt,1                                           ;   relativeEdistances,0
;   skirtExtruder,0                                      ;   allowEaxisZeroing,1
;   skirtLayers,300                                      ;   independentExtruderAxes,0
;   skirtOutlines,1                                      ;   includeM10123,0
;   skirtOffset,3                                        ;   stickySupport,1
;   usePrimePillar,0                                     ;   applyToolheadOffsets,0
;   primePillarExtruder,999                              ;   gcodeXoffset,0
;   primePillarWidth,12                                  ;   gcodeYoffset,0
;   primePillarLocation,7                                ;   gcodeZoffset,0
;   primePillarSpeedMultiplier,1                         ;   overrideMachineDefinition,1
;   useOozeShield,0                                      ;   machineTypeOverride,0
;   oozeShieldExtruder,999                               ;   strokeXoverride,327
;   oozeShieldOffset,5                                   ;   strokeYoverride,465
;   oozeShieldOutlines,1                                 ;   strokeZoverride,156
;   oozeShieldSidewallShape,0                            ;   originOffsetXoverride,81
```

; originOffsetYoverride,10
; originOffsetZoverride,0
; homeXdirOverride,-1
; homeYdirOverride,-1
; homeZdirOverride,-1
; flipXoverride,-1
; flipYoverride,1
; flipZoverride,1
; toolheadOffsets,0,0|0,0|0,0|0,0|0,0|0,0
; overrideFirmwareConfiguration,0
; firmwareTypeOverride,RepRap
(Marlin/Repetier/Sprinter)
; GPXconfigOverride,r2
; baudRateOverride,115200
; overridePrinterModels,0
; printerModelsOverride
; startingGcode,;,;,;,;START-SCRIPT BEGIN,G21
    ;metric values,G28 ;home all axes,G1 X0 Y0
Z0 F1000 ;Zero all Axis for relative conversion,,G92 E0
    ;zero the extruded length,;G1 X10.0 Y150.0
F3000,;G1 E1.0 F1000,;START-SCRIPT END,;,;,;,
; layerChangeGcode,;,;,; LCSB -1 LAYER-
CHANGE-SCRIPT BEGIN,,G91 ; relative
movement,g1 z+5,G90; absolute movement,,; Fahre u
Lampenstart,G1 X0 Y120.0 F3000,G4 S300,,; --
LAMPE EIN 0---,G4 P0,M104 S800 T2,; ----------------
,G1 Y320.0 F500,G1 Y120.0 F500,,,; -- LAMPE
AUS,G4 P0,M104 S0 T2,,G1 X100.0 Y100.0
F3000,,;G91,;G1 z-5,;G90,,; LCSE -1 LAYER-
CHANGE-SCRIPT END,;,;,;
; retractionGcode,;RETRACTION-SCRIPT
BEGIN,;RETRACTION-SCRIPT END
; toolChangeGcode,,;TOOL-CHANGE-SCRIPT
BEGIN,;TOOL-CHANGE-SCRIPT END
; endingGcode,,,,;ENDING-SCRIPT BEGIN,G91,G1
Z10,G90,; Fahre u Lampenstart,G1 X1.0 Y120.0
F3000,,; -- LAMPE EIN 0---,G4 P0,M104 S800 T2,; ---
--------------,G1 Y320.0 F600,G1 Y120.0 F600,;G1
Y250 F900,,; -- LAMPE AUS,G4 P0,M104 S0 T2,,; ----
--,G1 X5 F3000,G1 Y70 F3000,,G91,G1 Z40,G90,,G1
X150 Y0 F3000,G4 P5000,,;ENDING-SCRIPT END,,,,
; exportFileFormat,gcode
; celebration,0
; celebrationSong,Star Wars
; postProcessing,
; defaultSpeed,402
; outlineUnderspeed,1
; solidInfillUnderspeed,1
; supportUnderspeed,1
; rapidXYspeed,3000
; rapidZspeed,3000
; minBridgingArea,50
; bridgingExtraInflation,0
; bridgingExtrusionMultiplier,1
; bridgingSpeedMultiplier,1
; useFixedBridgingAngle,0
; fixedBridgingAngle,0
; applyBridgingToPerimeters,0
; filamentDiameters,1.75|1.75|1.75|1.75|1.75|1.75
; filamentPricesPerKg,46|46|46|46|46|46
; filamentDensities,1.25|1.25|1.25|1.25|1.25|1.25
; useMinPrintHeight,0
; minPrintHeight,0.47
; useMaxPrintHeight,1
; maxPrintHeight,1.6
; useDiaphragm,0

; diaphragmLayerInterval,1
; robustSlicing,0
; mergeAllIntoSolid,0
; onlyRetractWhenCrossingOutline,0
; retractBetweenLayers,1
; useRetractionMinTravel,1
; retractionMinTravel,1
; retractWhileWiping,0
; onlyWipeOutlines,0
; avoidCrossingOutline,0
; maxMovementDetourFactor,100
; toolChangeRetractionDistance,12
; toolChangeExtraRestartDistance,-0.5
; toolChangeRetractionSpeed,600
; externalThinWallType,0
; internalThinWallType,0
; thinWallAllowedOverlapPercentage,0
; singleExtrusionMinLength,1
; singleExtrusionMinPrintingWidthPercentage,90
; singleExtrusionMaxPrintingWidthPercentage,110
; singleExtrusionEndpointExtension,0.2
; horizontalSizeCompensation,0

B.2 Surface topography images (3D Laser Scanning Microscope VK-X3000, Keyence)
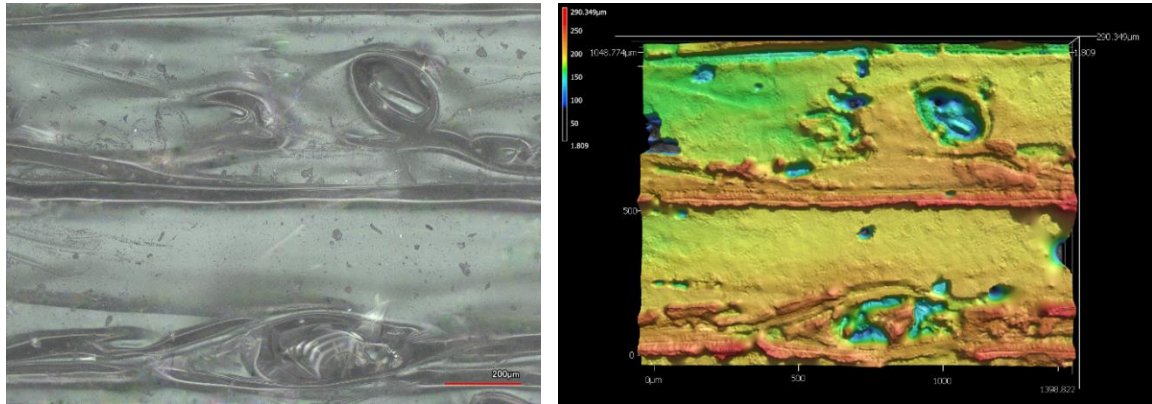

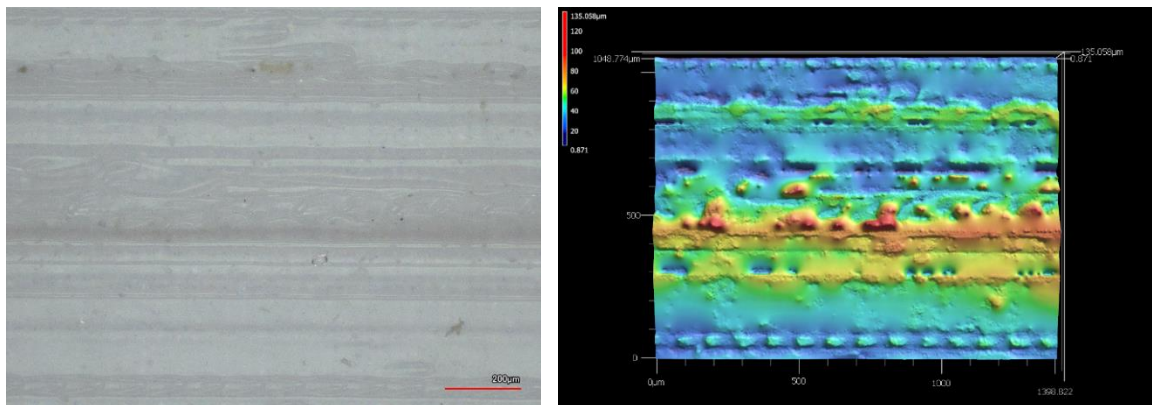Figure B.1: Surface optical and topographic images for Recreus 70A.

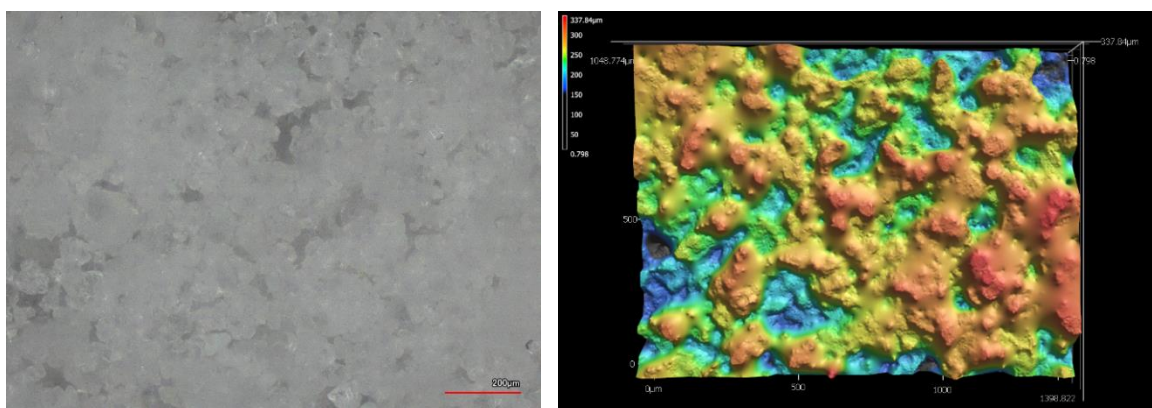Figure B.2: Surface optical and topographic images for Recreus 82A.

Figure B.3: Surface optical and topographic images for Duraform.

Figure B.4: Surface optical and topographic images for Estane.

Figure B.5: Surface optical and topographic images for Wacker.

Figure B.6: Surface optical and topographic images for Silastic.
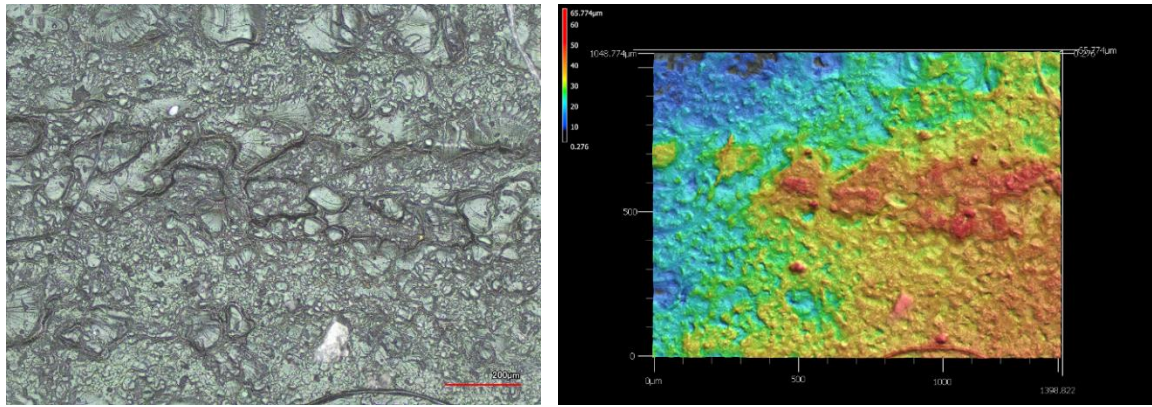
Figure B.7: Surface optical and topographic images for Tango 30.
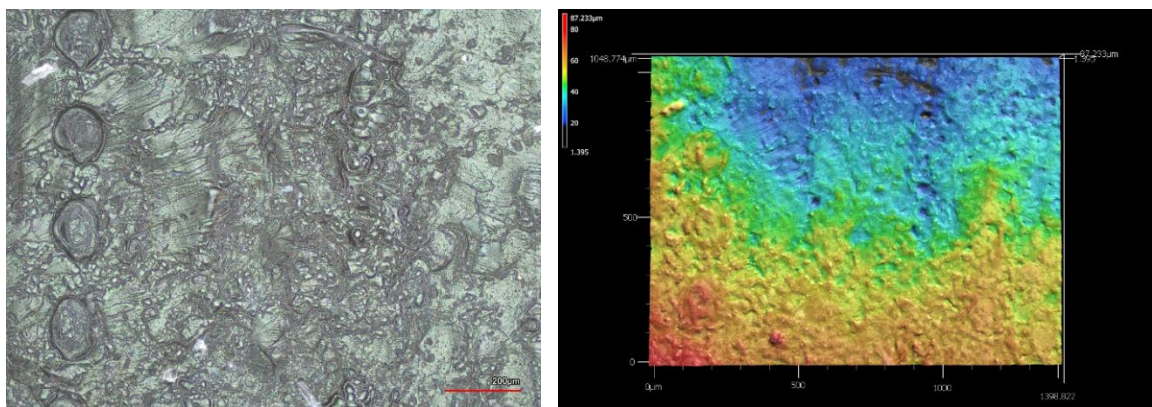
Figure B.8: Surface optical and topographic images for Tango 40.
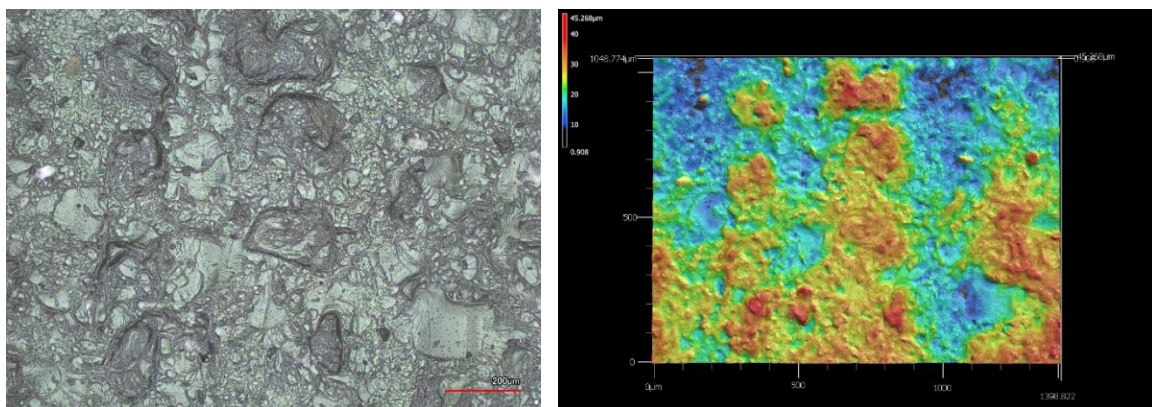
Figure B.9: Surface optical and topographic images for Tango 50.
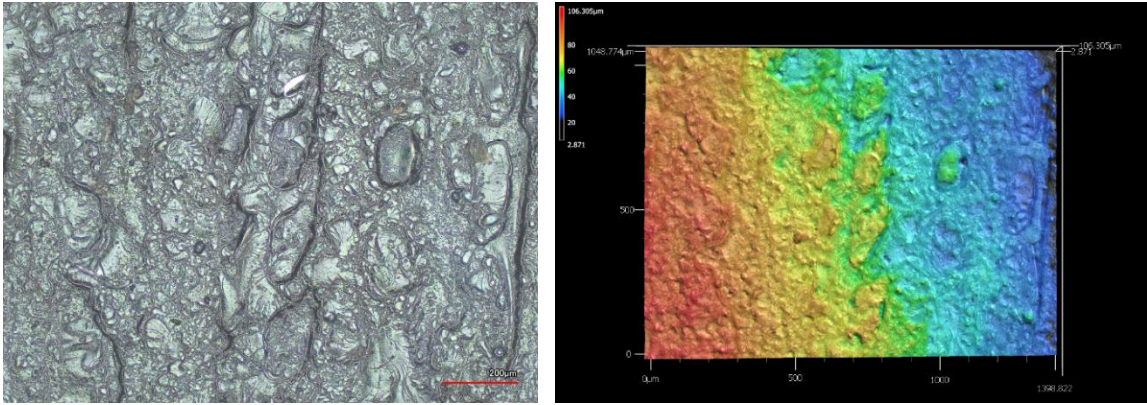
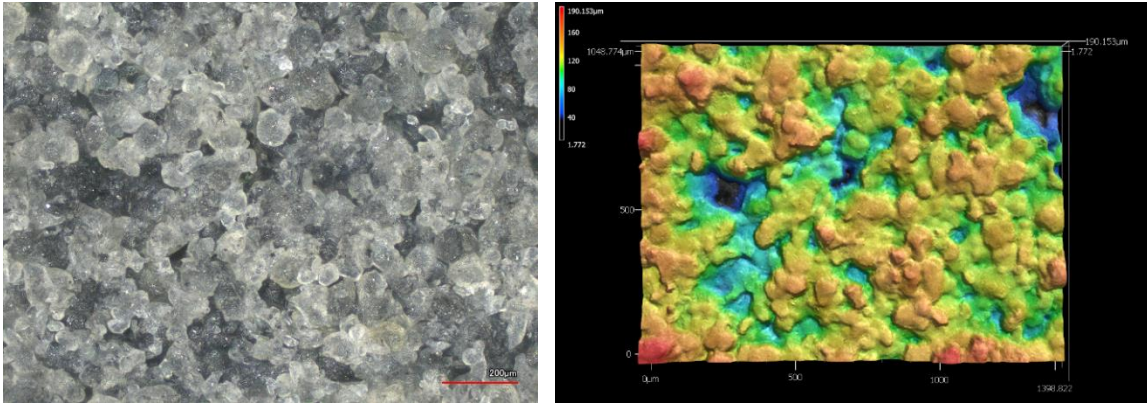Figure B.10: Surface optical and topographic images for Tango 60.
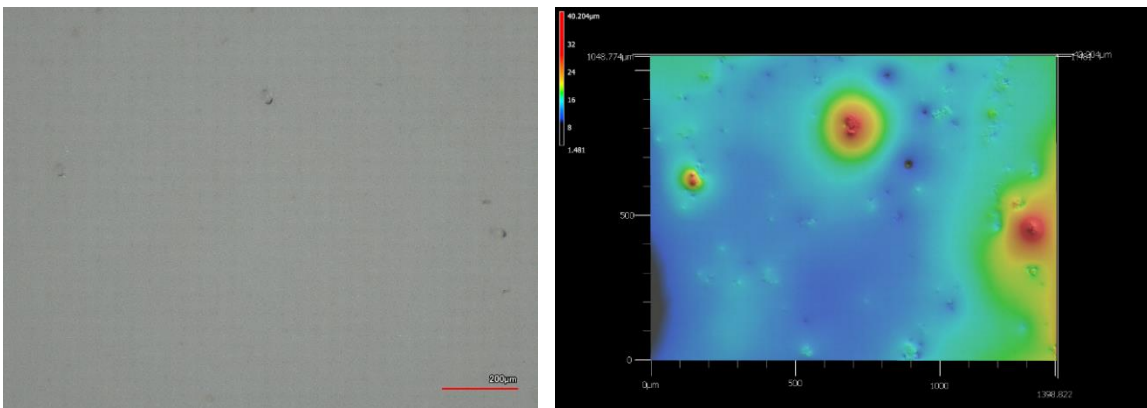

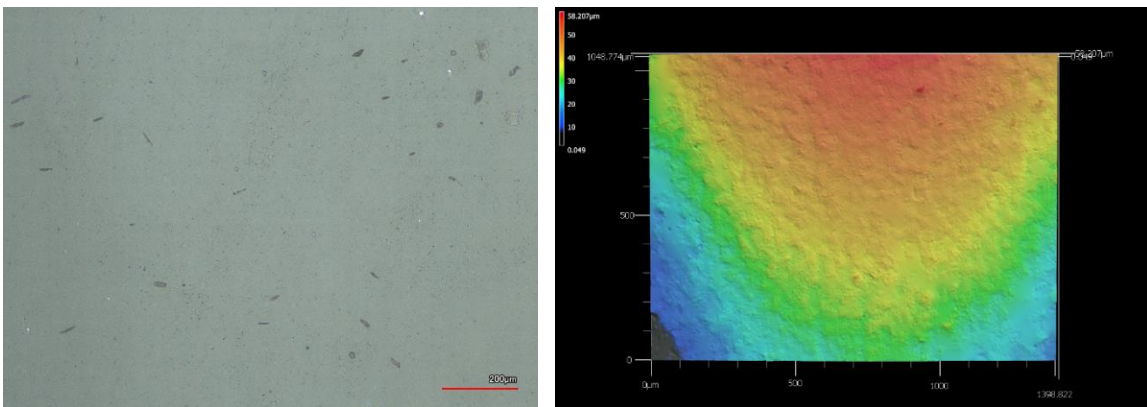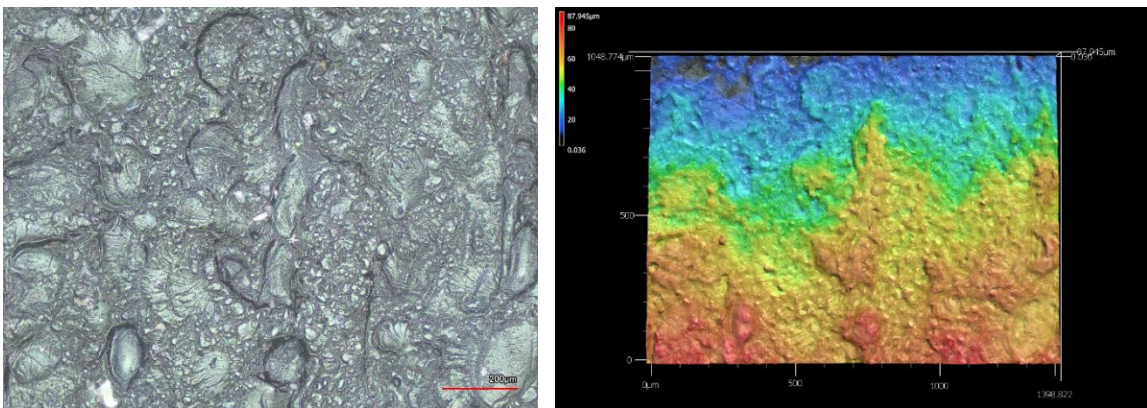Figure B.11: Surface optical and topographic images for Tango 70.
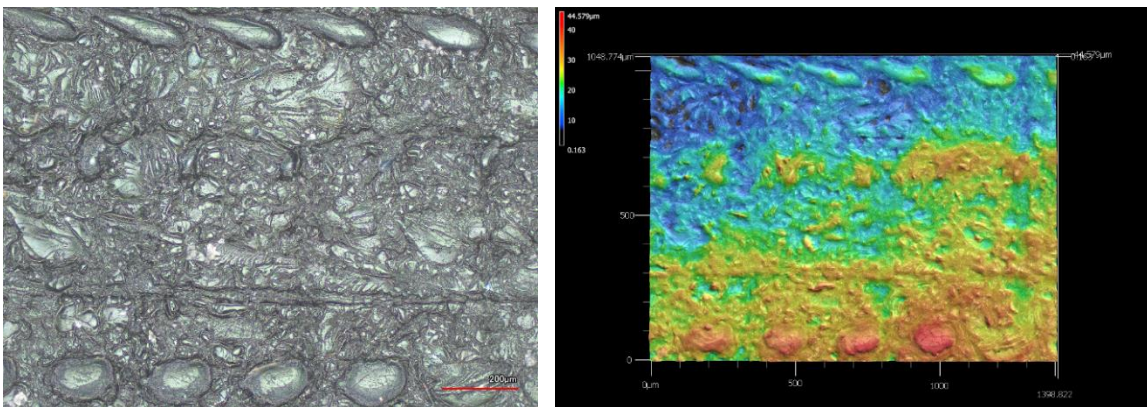
Figure B.12: Surface optical and topographic images for Agilus.
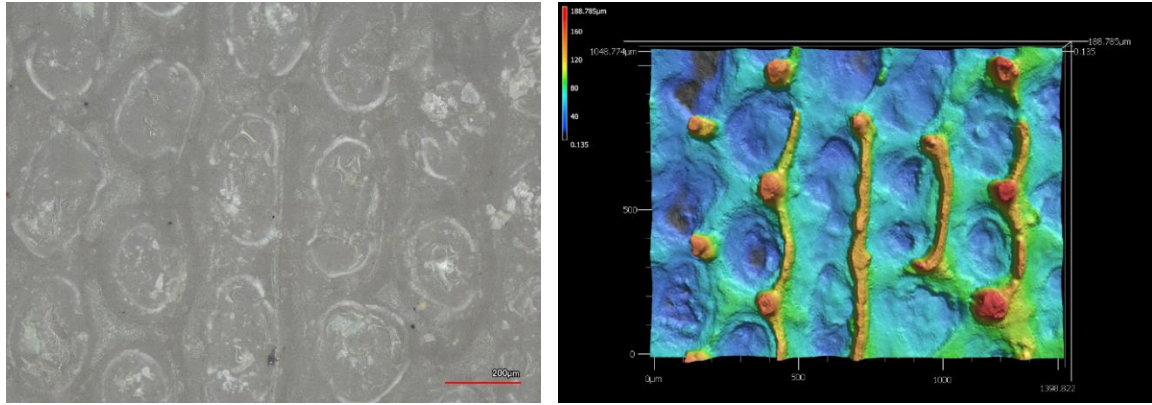
Figure B.13: Surface optical and topographic images for Keyence H.
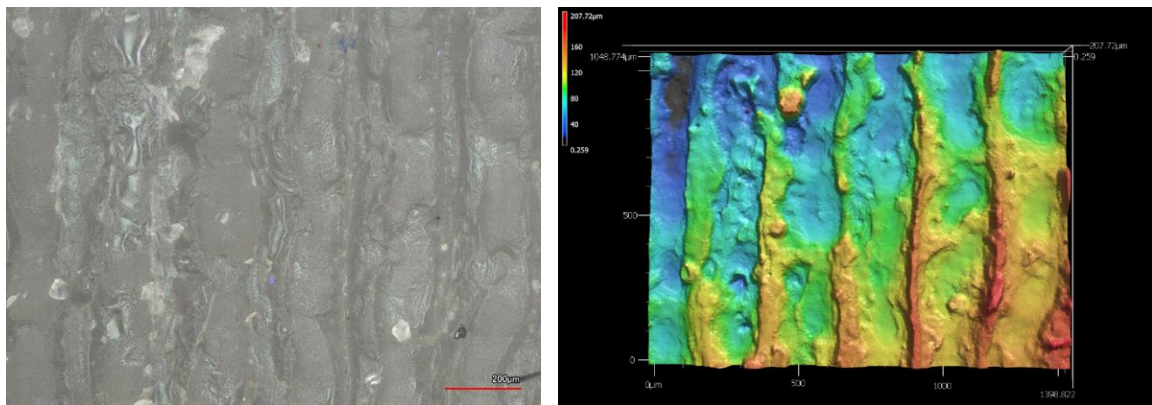
Figure B.14: Surface optical and topographic images for Keyence L.

200

Appendix C: Additional Testing Information

C.1 DMA Strain Amplitude Test Plots
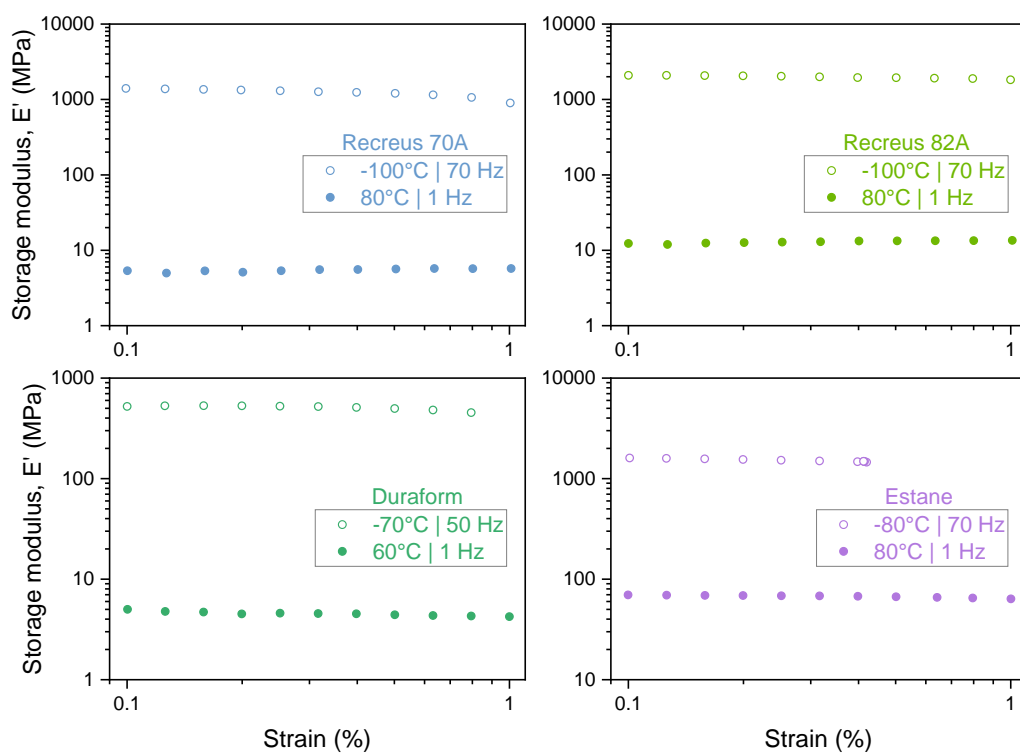
Figure C.1: Dynamic strain amplitude test plots for the TPUs.
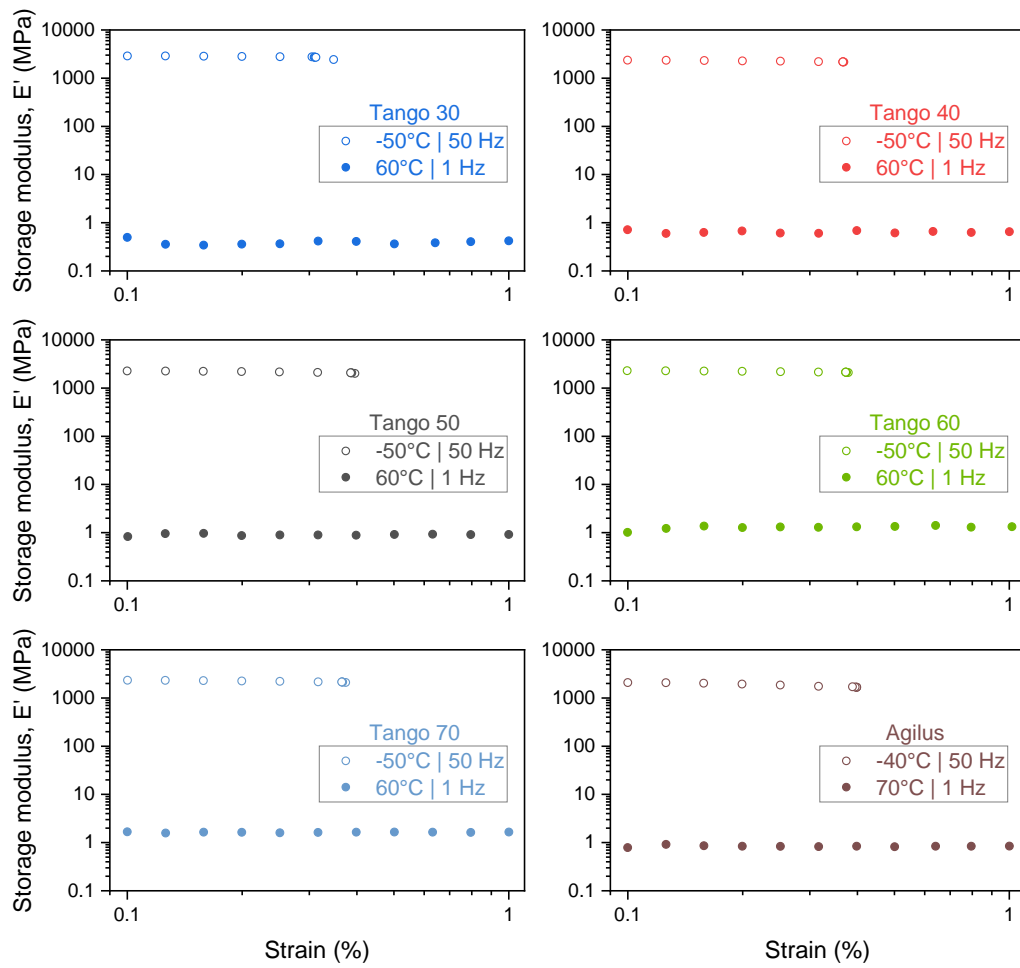
Figure C.2: Dynamic strain amplitude test plots for the PolyJet photopolymers.
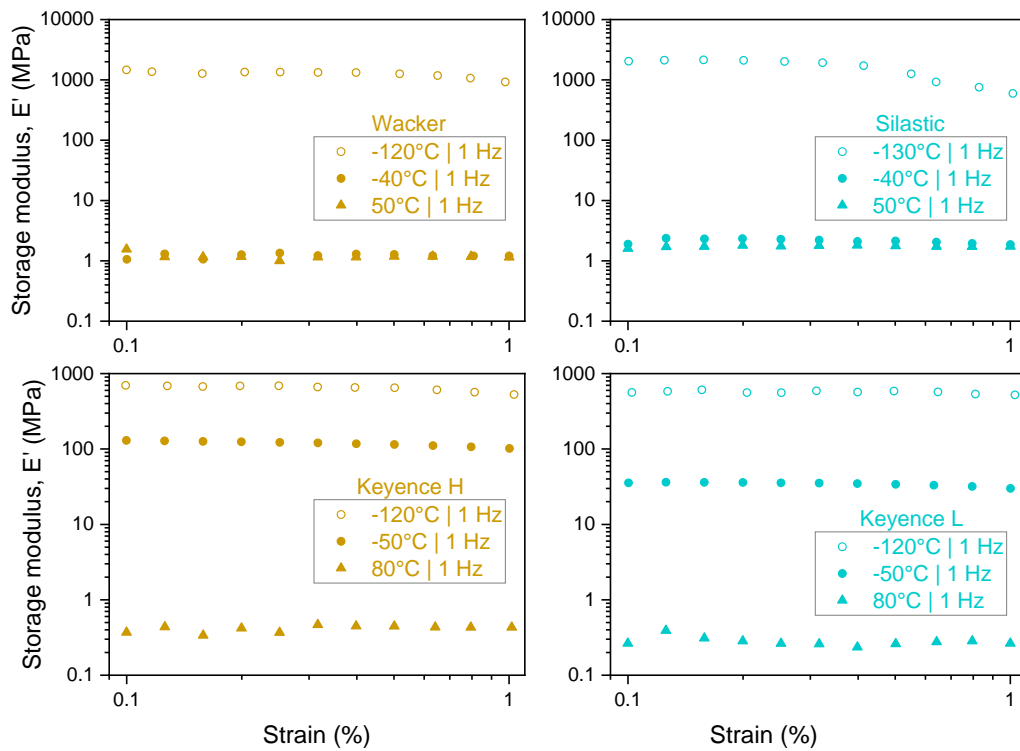
Figure C.3: Dynamic strain amplitude test plots for the LSRs and Keyence materials.

C.2 DMA Input Parameters

Table C.1: DMA testing conditions of the temperature-frequency sweeps.

Temperature increments (°C)	Min. frequency (Hz)	Frequency steps/decade	Soak time (s)
5	1	5	300

Sample	Temperatures (°C)		Max. frequency (Hz)	Load (%)		Contact force (N)	Force sensor (N)
	Min.	Max.		Static	Dynamic		
Recreus 70A	-100	80	70	3.00	0.35	0.50	500
Recreus 82A	-100	80	70	3.00	0.35	0.50	500
Duraform	-70	60	50	2.00	0.30	0.20	500
Estane	-80	80	70	2.00	0.15	0.30	500
Tango 30	-50	60	50	2.00	0.80	0.50	150
Tango 40	-50	60	50	2.00	0.32	0.20	150
Tango 50	-50	60	50	2.00	0.25	0.20	150
Tango 60	-50	60	50	2.00	0.25	0.20	150
Tango 70	-50	60	50	2.00	0.25	0.20	150
Agilus	-40	70	50	2.00	0.27	0.30	150

Table C.2: DMA testing conditions of the temperature sweeps.

Temperature increments (°C)		Frequency (Hz)		Frequency steps/decade		
5		1		5		

Sample	Temperatures (°C)		Load (%)		Contact force (N)	Force sensor (N)	Soak time (s)
	Min.	Max.	Static	Dynamic			
Wacker (c)	-120	-40	5.00	0.50	0.30	500	240
Wacker (h)	-40	50	5.00	0.50	0.30	500	180
Silastic (c)	-130	-40	5.00	0.20	0.30	500	240
Silastic (h)	-40	50	5.00	0.20	0.30	150	240
Keyence H (c)	-120	-50	4.00	0.25	0.10	150	240
Keyence H (h)	-50	80	4.00	0.30	0.10	150	240
Keyence L (c)	-120	-50	4.00	0.25	0.10	150	240
Keyence L (h)	-50	80	4.00	0.80	0.10	150	240

Appendix D: Stress Relaxation Fitting Viscoelastic Parameters

D.1 Parameters of the Maxwell Elements from Preliminary Assessments

Table D.1: R-Squared from fitting and Maxwell elements stress-like constants from preliminary assessments.

Sample	R-Squared	σ_1	σ_2	σ_3	σ_4	σ_5	σ_6	σ_7	σ_8
Recreus 70A	0.999965	9.769E-02	1.579E-01	1.660E-01	1.424E-01	1.045E-01	2.109E-01		
Recreus 82A	0.999995	2.332E-01	2.694E-01	2.685E-01	2.438E-01	2.278E-01	2.132E-01	2.002E-01	3.608E-01
Duraform	0.999945	1.051E-01	1.046E-01	9.036E-02	7.038E-02	5.557E-02	8.064E-02		
Estane	0.999980	7.964E-01	6.398E-01	5.359E-01	4.530E-01	3.965E-01	3.501E-01	6.300E-01	
Wacker	0.999741	2.283E-02	1.992E-02	1.742E-02	1.548E-02	9.722E-03	2.539E-02		
Silastic	0.999802	3.869E-02	3.624E-02	3.241E-02	2.464E-02	1.915E-02	3.862E-02		
Keyence H	0.999823	4.753E-01	3.267E-01	2.629E-01	1.955E-01	1.104E-01	7.577E-02	6.876E-02	
Keyence L	0.999876	9.842E-02	7.134E-02	5.466E-02	4.313E-02	3.276E-02	2.941E-02	2.824E-02	

Table D.2: Maxwell elements relaxation times from preliminary assessments.

Sample	τ_1	τ_2	τ_3	τ_4	τ_5	τ_6	τ_7	τ_8
Recreus 70A	4.112E-01	4.062E+00	3.686E+01	3.291E+02	2.714E+03	2.678E+04		
Recreus 82A	3.201E-01	1.647E+00	7.830E+00	3.749E+01	1.781E+02	8.725E+02	4.144E+03	3.308E+04
Duraform	3.357E-01	2.984E+00	2.881E+01	2.920E+02	2.316E+03	2.178E+04		
Estane	2.310E-01	1.427E+00	8.137E+00	4.936E+01	3.152E+02	1.949E+03	1.566E+04	
Wacker	5.292E-01	5.302E+00	4.703E+01	3.928E+02	2.381E+03	1.946E+04		
Silastic	3.592E-01	4.310E+00	5.285E+01	5.381E+02	3.889E+03	5.206E+04		
Keyence H	3.209E-01	2.198E+00	1.289E+01	8.521E+01	5.817E+02	3.296E+03	2.269E+04	
Keyence L	4.674E-01	3.363E+00	1.504E+01	6.840E+01	3.302E+02	1.666E+03	2.270E+04	

D.2 Parameters of the Maxwell Elements from PolyJet Photopolymers at 15% Strain

Table D.3: R-Squared from fitting and Maxwell elements stress-like constants from PolyJet photopolymers at 15% strain.

Sample	R-Squared	σ_1	σ_2	σ_3	σ_4	σ_5
Tango 30	0.966768	1.479E-02	5.029E-03	3.730E-03	1.038E-03	
Tango 40	0.984420	7.551E-03	1.240E-02	5.780E-03	4.094E-03	2.697E-03
Tango 50	0.998543	4.374E-02	2.676E-02	1.374E-02	9.740E-03	6.038E-03
Tango 60	0.998949	6.794E-02	4.288E-02	2.200E-02	1.841E-02	8.938E-03
Tango 70	0.998819	2.158E-01	1.030E-01	5.220E-02	3.060E-02	2.145E-02
Agilus	0.995023	3.248E-02	1.613E-02	5.391E-03	1.902E-03	9.842E-03

Table D.4: Maxwell elements relaxation times from PolyJet photopolymers at 15% strain.

Sample	τ_1	τ_2	τ_3	τ_4	τ_5
Tango 30	6.36E-01	1.275E+02	1.630E+03	2.286E+04	
Tango 40	2.630E-01	4.580E+00	1.150E+02	1.512E+03	2.223E+04
Tango 50	1.258E+00	1.164E+01	1.430E+02	1.454E+03	2.078E+04
Tango 60	9.074E-01	1.600E+01	1.532E+02	1.257E+03	1.085E+04
Tango 70	7.847E-01	9.599E+00	2.297E+02	1.873E+03	1.827E+04
Agilus	6.987E-01	5.622E+00	1.010E+02	1.270E+03	3.068E+05

D.3 Parameters of the Maxwell Elements from Stress Relaxation at 30% Strain

Table D.5: R-Squared from fitting and Maxwell elements stress-like constants from stress relaxation at 30% strain.

Sample	R-Squared	σ_1	σ_2	σ_3	σ_4	σ_5	σ_6	σ_7
Recreus 70A	0.999988	7.164E-02	9.450E-02	9.431E-02	8.414E-02	7.449E-02	6.253E-02	1.489E-01
Recreus 82A	0.999994	2.135E-01	2.138E-01	2.339E-01	1.888E-01	1.652E-01	1.372E-01	2.132E-01
Duraform	0.999968	8.109E-02	7.529E-02	6.658E-02	5.557E-02	4.277E-02	3.704E-02	7.458E-02
Estane	0.999980	7.964E-01	6.398E-01	5.359E-01	4.530E-01	3.965E-01	3.501E-01	6.301E-01
Wacker	0.878743	7.650E-03	6.336E-03	3.555E-03	3.052E-03	3.202E-03		
Silastic	0.995591	1.157E-02	5.991E-03	5.502E-03	6.285E-03	7.129E-03	7.208E-03	
Tango 60	0.997934	2.193E-01	9.384E-02	5.009E-02	2.852E-02	2.093E-02		
Tango 70	0.998489	4.612E-01	1.996E-01	1.116E-01	5.886E-02	4.872E-02		
Keyence H	0.999872	4.086E-01	2.938E-01	2.436E-01	1.905E-01	1.088E-01	6.186E-02	6.314E-02
Keyence L	0.999866	7.484E-02	5.626E-02	4.158E-02	3.203E-02	2.025E-02	2.304E-02	2.240E-02

Table D.6: Maxwell elements relaxation times from stress relaxation at 30% strain.

Sample	τ_1	τ_2	τ_3	τ_4	τ_5	τ_6	τ_7
Recreus 70A	4.326E-01	3.392E+00	2.640E+01	2.026E+02	1.446E+03	8.409E+03	5.846E+04
Recreus 82A	3.612E-01	2.479E+00	1.285E+01	8.939E+01	6.097E+02	3.639E+03	2.761E+04
Duraform	2.876E-01	1.901E+00	1.230E+01	8.162E+01	4.627E+02	2.080E+03	1.718E+04
Estane	2.310E-01	1.427E+00	8.137E+00	4.936E+01	3.152E+02	1.949E+03	1.566E+04
Wacker	6.064E-01	4.775E+00	3.292E+01	2.262E+02	3.714E+03		
Silastic	4.708E-01	2.696E+00	1.105E+01	6.764E+01	6.396E+02	5.883E+03	
Tango 60	1.239E+00	1.404E+01	1.535E+02	1.320E+03	1.254E+04		
Tango 70	1.360E+00	1.463E+01	1.718E+02	1.716E+03	1.558E+04		
Keyence H	2.786E-01	1.840E+00	1.066E+01	7.048E+01	6.201E+02	3.454E+03	2.120E+04
Keyence L	5.169E-01	3.000E+00	1.420E+01	6.518E+01	2.753E+02	1.145E+03	9.362E+03

Appendix E: Specific Heat Capacity Trendlines

Table E.1: Linear trendline $c_p = \alpha_1 T + \alpha_0$ and its valid range of the measured specific heat capacity.

Sample	α_1	α_0	R-Squared	Range (°C)	Sample	α_1	α_0	R-Squared	Range (°C)
Recreus 70A	0.0014	1.8091	0.9891	[-27.5, 12.7]	Tango 40	0.0020	2.0351	0.9774	[46.1, 95.6]
	0.0032	1.8261	0.9955	[42.2, 78.9]					
Recreus 82A	0.0036	0.8317	0.9971	[-22.3, 27.5]	Tango 50	0.0020	1.6403	0.9160	[53.8, 94.8]
	0.0038	0.8706	0.9978	[34.7, 79.0]					
Duraform	0.0015	1.0599	0.9352	[-18.8, 23.2]	Tango 60	0.0024	1.9828	0.9891	[52.8, 94.8]
	0.0032	1.1484	0.9964	[62.7, 119.0]					
Estane	0.0023	1.3891	0.9912	[-22.1, 20.1]	Tango 70	0.0022	1.7439	0.9893	[47.8, 94.8]
	0.0028	1.4727	0.9985	[51.9, 118.9]					
Wacker	0.0014	1.2701	0.9888	[-34.8, 18.4]	Agilus	0.0028	1.7517	0.9977	[50.7, 99.0]
	0.0009	1.3645	0.9364	[32.3, 48.4]					
Silastic	0.0010	1.3885	0.9278	[-32.1, 28.6]	Keyence H	0.0029	1.4350	0.9974	[-93.7, 32.8]
						0.0024	1.4949	0.9944	[50.8, 99.0]
Tango 30	0.0021	1.9603	0.9796	[44.2, 95.2]	Keyence L	0.0006	0.3017	0.9996	[-98.4, 40.0]
						0.0004	0.3127	0.9983	[51.6, 98.7]

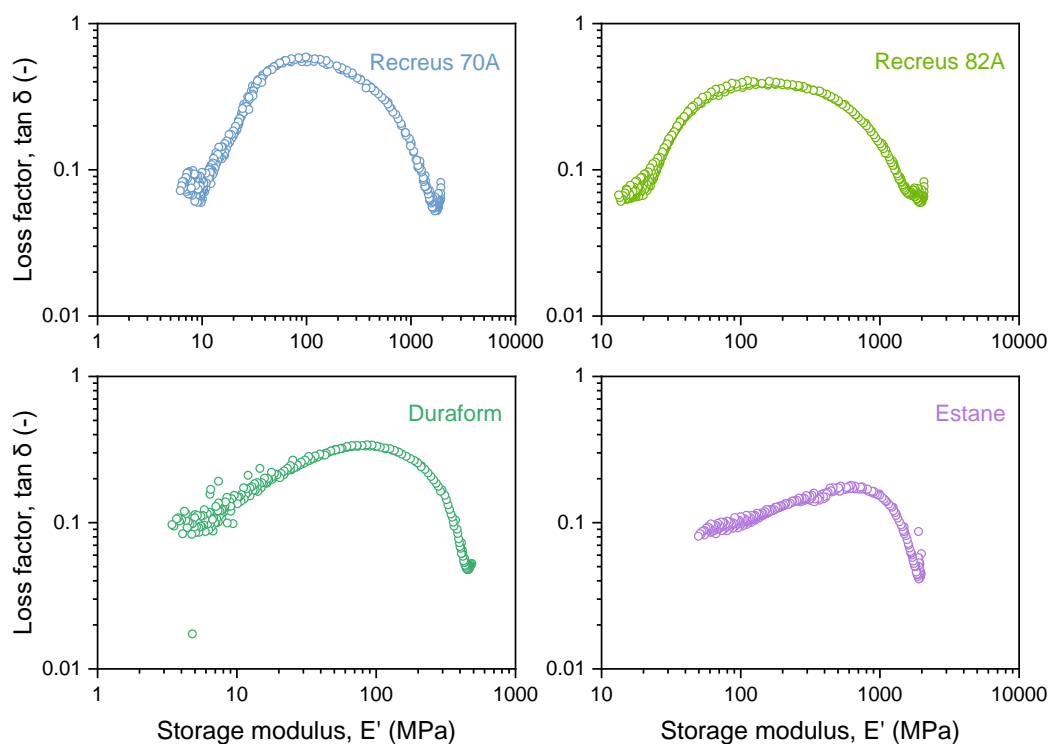# Appendix F: Supplementary Data from DMA

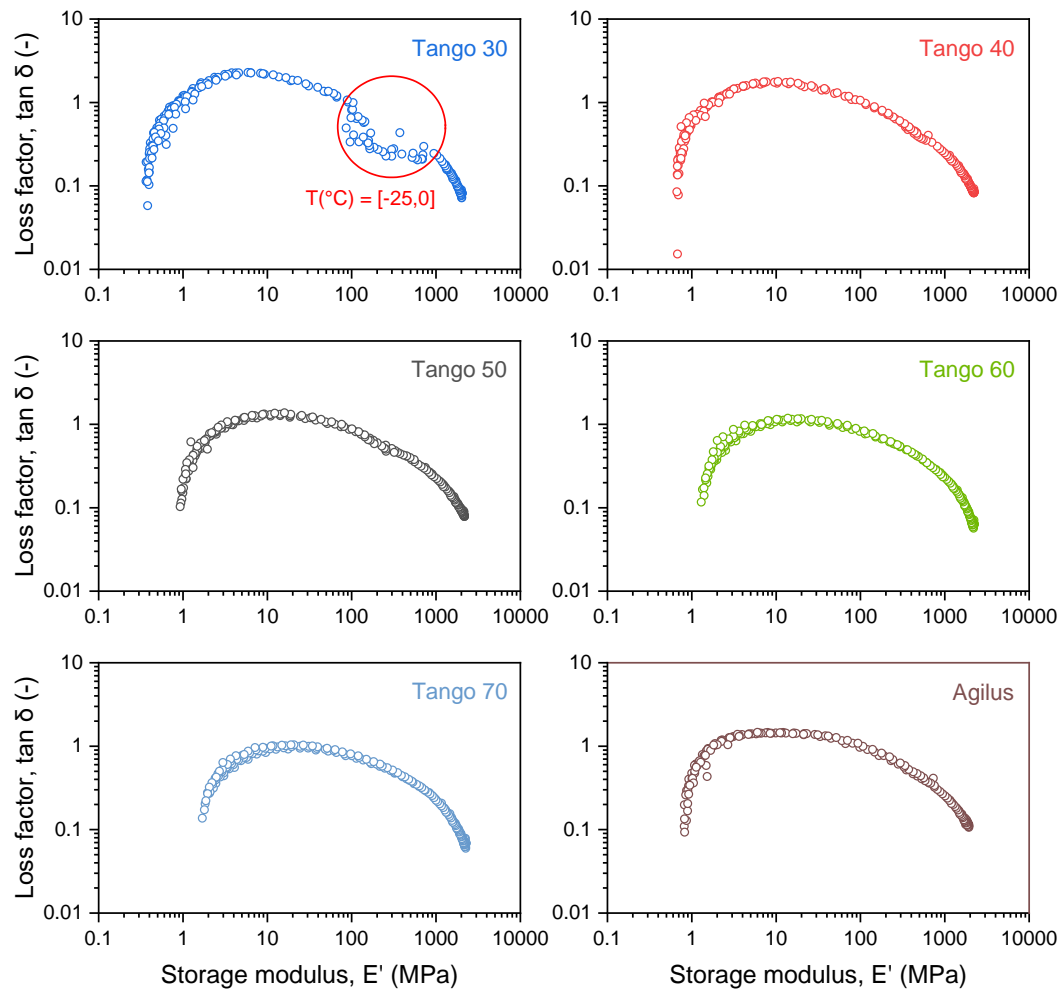## F.1 Wicket Plots

Figure F.1: Wicket plots for the TPUs.

Figure F.2: Wicket plots for the PolyJet photopolymers.
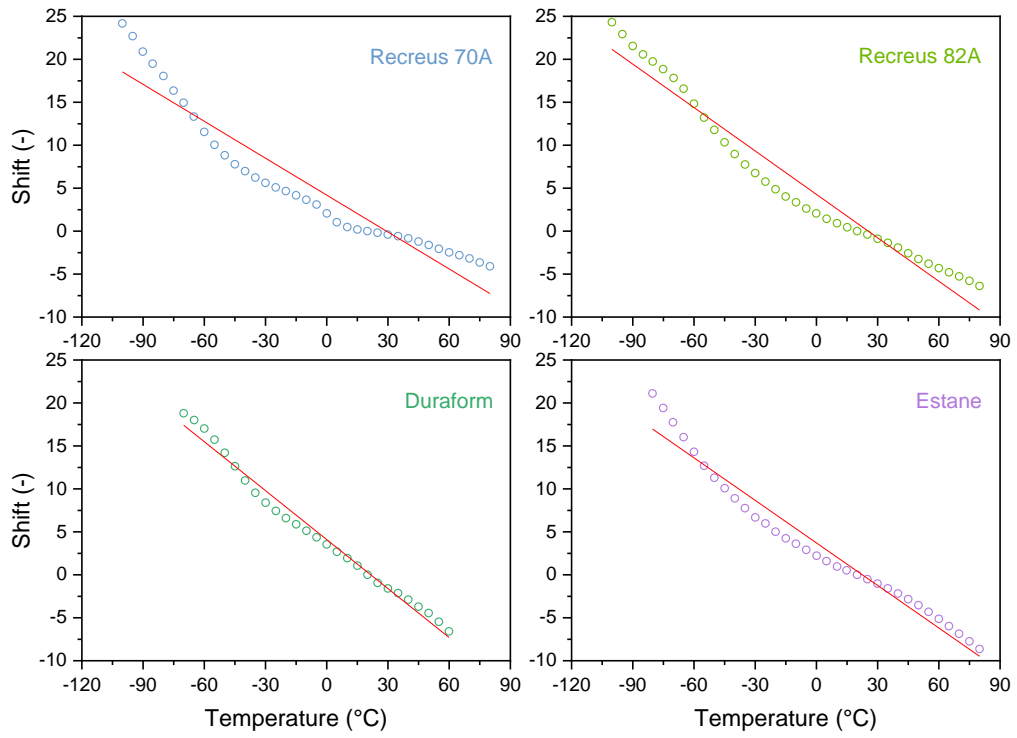
F.2 Master Curve Shift Factor Plots

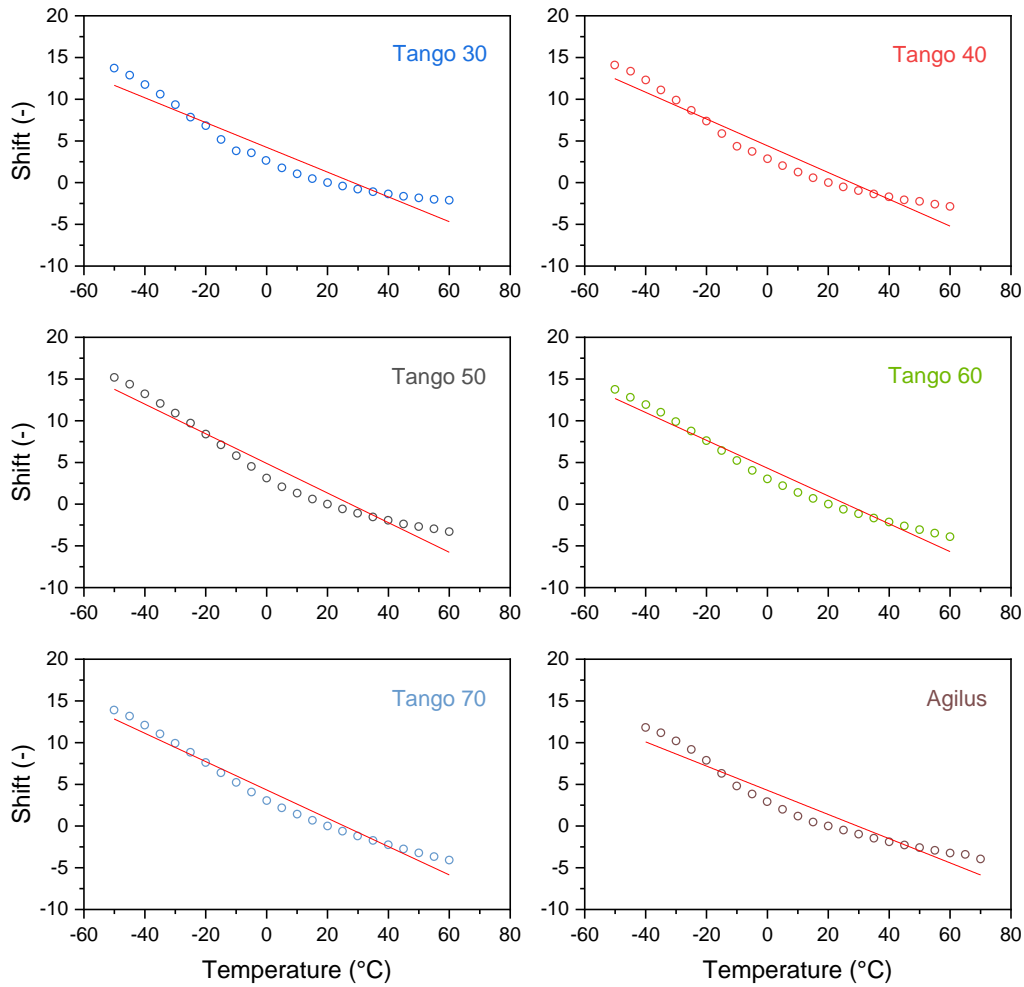Figure F.3: Shift factors plotted against the temperature for the TPUs.

Figure F.4: Shift factors plotted against the temperature for the PolyJet photopolymers.

F.3 Time-Temperature Superposition Parameters (WLF Equation)

Table F.1: Calculated shifting parameters at $T_R = 20°C$.

Sample	C_1	C_2 (K)	Sample	C_1	C_2 (K)
Recreus 70A	22.59	235.43	Tango 40	14.32	129.92
Recreus 82A	23.02	216.97	Tango 50	14.30	121.51
Duraform	71.41	437.47	Tango 60	20.91	162.85
Estane	33.25	265.47	Tango 70	20.75	160.55
Tango 30[*]	10.49	113.61	Agilus	11.29	105.41

[*]failed TTS

Appendix G: Publications from Additional Studies

Future-Oriented Experimental Characterization of 3D Printed and Conventional Elastomers Based on Their Swelling Behavior

Authors: Klara Loos, Vivianne Marie Bruère, Benedikt Demmel, Yvonne Ilmberger, Alexander Lion and Michael Johlitz

Abstract: The present study investigates different elastomers with regard to their behavior towards liquids such as moisture, fuels, or fuel components. First, four additively manufactured materials are examined in detail with respect to their swelling in the fuel component toluene as well as in water. The chemical nature of the materials is elucidated by means of infrared spectroscopy. The experimentally derived absorption curves of the materials in the liquids are described mathematically using Fick's diffusion law. The mechanical behavior is determined by uniaxial tensile tests, which are evaluated on the basis of stress and strain at break. The results of the study allow for deriving valuable recommendations regarding the printing process and post-processing. Second, this article investigates the swelling behavior of new as well as thermo-oxidatively aged elastomers in synthetic fuels. For this purpose, an analysis routine is presented using sorption experiments combined with gas chromatography and mass spectrometry and is thus capable of analyzing the swelling behavior multifaceted. The transition of elastomer constituents into the surrounding fuel at different aging and sorption times is determined precisely. The change in mechanical properties is quantified using density measurements, micro Shore A hardness measurements, and the parameters stress and strain at break from uniaxial tensile tests.

Under-extrusion challenges for elastic filaments: the influence of moisture on additive manufacturing

Authors: Vivianne Marie Bruère, Alexander Lion, Jens Holtmannspötter, Michael Johlitz

Abstract: The applicability of Additive Manufacturing for operational parts expands with the availability of new materials with specific properties. For elastomeric components produced with Fused Filament Fabrication, challenges associated with the printing process due to the nature of the material are faced. This paper investigates the effect of under-extrusion in this process regarding the feeding system and, predominantly, the moisture for thermoplastic polyurethanes with 3D printing experiments and thermomechanical testing. In particular, the filament flow control with a Bowden extruder provides a challenge. A microscopic analysis reveals the signs of under-extrusion, along with the influence of material drying to reduce the moisture content. The drying may depend not only on time and temperature, but also on mass and surface effects. Water uptake measurements exhibit absorptions up to 1.89% in weight, most of which take place during the first 24 h of the experiments. Tensile tests performed on samples with different moisture contents show their influence in the ultimate stresses. The moisture in the material causes under-extrusion induced failures. Those failures are less likely to happen at lower moisture levels, resulting in occasional higher tensile strengths. Overall, the importance of proper storage of the material throughout printing is verified, even under moderate humidity conditions due to its hygroscopic nature.

Multiparametric Design Optimisation of 3D Printed Aircraft Door Seals

Authors: Bruno Franke Goularte, Vivianne Marie Bruère, Alexander Lion, and Michael Johlitz

Abstract: Additive Manufacturing is a young, promising manufacturing method that is currently coming into focus for its faster and relatively cheaper fabrication of complex, custom-made parts in comparison to conventional manufacturing methods. Prototyping is one of the most favoured fields, as on-demand 3D printing of components can be particularly beneficial at the Research & Development stage. Among the employed materials, one can find elastomer alternatives as traditional liquid silicone rubber and photopolymers. This work deals with mechanical investigation of four silicone technologies, with emphasis on the material characterization. Hyperelastic laws were fitted to tensile tests for Finite Element Method simulations of aircraft door seals. A proposal for multiparametric design optimisation of the seal geometry through genetic algorithms (NSGA-II) is presented based on analysis results. The potential application of each 3D printing technology in seals prototyping is highlighted and evaluated according to the collapse criteria under cabin pressure. Results indicate the variability of the optimal parametric designs according to both the silicone behaviour and the material model stability limitations. The impact of the material model is also underlined as a way to enable seal design improvements.

An Overview on the 3D Printing of Elastomers and the Influence of Printing Parameters on Their Mechanical Properties

Authors: Vivianne Marie Bruère, Alexander Lion, Jens Holtmannspötter, Michael Johlitz

Abstract: Additive manufacturing (AM) technologies show a great potential to revolutionize the fabrication and logistics of components. However, the field of elastomers is a rather unexplored topic regarding 3D printing compared to other types of materials. To enlarge the scientific knowledge of 3D printing of elastomeric parts, this work starts with a literature overview and a discussion of AM in general. Subsequently, AM of elastomers is presented with the focus on fused filament fabrication (FFF) particularities. Characteristics and limitations as well as relevant aspects to be considered when dealing with thermoplastic elastomers in FFF printers are addressed. A quantitative analysis follows, investigating the primary effect of the infill raster orientation on the tensile behavior of samples printed in a FFF printer using thermoplastic polyurethane. A minor influence of unidirectional (0°, 45°, 90°) and alternating (45°–135°) orientations was verified for strains below 400%, which becomes more significant for the higher strain range and the resulting ultimate tensile stress.

The influence of printing parameters on the mechanical properties of 3D printed TPU-based elastomers

Authors: Vivianne Marie Bruère, Alexander Lion, Jens Holtmannspötter, Michael Johlitz

Abstract: Additive Manufacturing (AM) becomes more and more the focus of studies in the scientific community. Nevertheless, elastomers in 3D printing are still a relatively understudied topic despite their extensive use in machine components. The further understanding of the technologies and knowledge acquirement are fundamental steps towards the improvement of the printing process and the broadening of feasible applications of 3D printed elastomers. This work focused on thermoplastic polyurethanes printed with Fused Filament Fabrication (FFF) and investigated the effect of infill deposition angle and contour lines on the tensile and the stress relaxation behavior. Samples were printed in alternating as well as unidirectional infill orientations, the latter without and with outlines. Tensile tests revealed that alternating orientations of 0°-90° and 45°-135° have a similar behavior and benefit the integrity of the part. The fully unidirectional orientation at 90° hindered the tensile strength due to the absence of outlines and consequent delamination. All comparative analyses displayed a low influence of the raster angle at lower strains. Stress relaxation results showed similar behavior for samples with outlines, without a clear effect of the infill orientations. In summary, contour lines are essential and an alternating orientation is recommended for better part integrity.